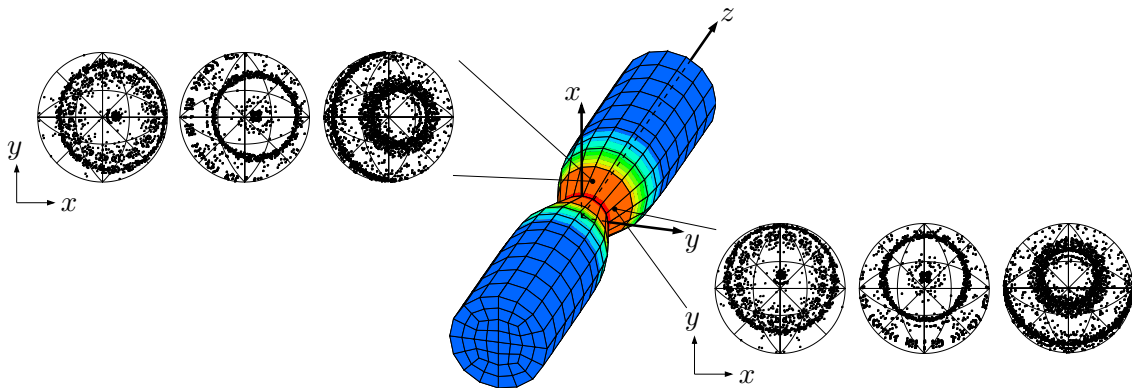


Hybrid Micro-Macro Modeling of Texture Evolution in Polycrystal Plasticity Based on Microstructural Reorientation Continua

Ilona Andrea Zimmermann



$$\bar{\Phi}(\dot{\bar{\mathbf{q}}}^r; \bar{\mathbf{c}}^m) = \sup_{\bar{\mathbf{p}}^r} \left\{ \bar{\mathbf{p}}^r \cdot \dot{\bar{\mathbf{q}}}^r - \frac{1}{2\bar{\eta}} \langle \bar{\chi}(\bar{\mathbf{p}}^r; \bar{\mathbf{c}}^m) \rangle^2 \right\} \quad \text{with} \quad \bar{\mathbf{c}}^m = \frac{(2m+1)}{E^h} \sum_{e=1}^{E^h} \mathbf{b}^m(\boldsymbol{\theta}, t)$$

Bericht Nr.: I-27 (2013)
 Institut für Mechanik (Bauwesen), Lehrstuhl I
 Professor Dr.-Ing. C. Miehe
 Stuttgart 2013

Hybrid Micro-Macro Modeling of Texture Evolution in Polycrystal Plasticity Based on Microstructural Reorientation Continua

Von der Fakultät Bau- und Umweltingenieurwissenschaften
der Universität Stuttgart zur Erlangung der Würde
eines Doktor-Ingenieurs (Dr.-Ing.)
genehmigte Abhandlung

vorgelegt von

Ilona Andrea Zimmermann

aus Ellwangen/Jagst

Hauptberichter: Prof. Dr.-Ing. Christian Miehe
Mitberichter: Prof. Dr.-Ing. Thomas Böhlke
Tag der mündlichen Prüfung: 14. Dezember 2012

Herausgeber:

Prof. Dr.-Ing. habil. C. Miehe

Organisation und Verwaltung:

Institut für Mechanik (Bauwesen)

Lehrstuhl I

Universität Stuttgart

Pfaffenwaldring 7

D-70550 Stuttgart

Tel.: ++49-(0)711/685-66378

Fax : ++49-(0)711/685-66347

© Ilona Zimmermann

Institut für Mechanik (Bauwesen)

Lehrstuhl I

Universität Stuttgart

Pfaffenwaldring 7

D-70550 Stuttgart

Alle Rechte, insbesondere das der Übersetzung in fremde Sprachen, vorbehalten. Ohne Genehmigung des Autors ist es nicht gestattet, dieses Heft ganz oder teilweise auf fotomechanischem Wege (Fotokopie, Mikrokopie) zu vervielfältigen.

ISBN 3-937859-15-2 (D 93 Stuttgart)

Abstract

The present work deals with the modeling of evolving crystal orientation microstructures in finite polycrystal plasticity and its impact on the macroscopic material behavior by means of a two-scale approach. A micro-mechanical plasticity model is developed that locally accounts for microscopic structural changes in the form of grain reorientations. The algorithmic treatment captures in a numerically efficient manner the crystal reorientation for evolving face- and body-centered cubic textures. Thereby, the parametrization of rotations is carried out in the Rodrigues space. The performance is demonstrated by means of representative numerical examples. As a key ingredient the crystallographic texture is responsible for the development of macroscopic anisotropy, entailing the necessity of a multiscale approach for appropriately predicting the material behavior. Crystal orientation distribution functions govern the evolution of structural tensors, representing in a homogenized sense the crystal reorientation within a model-inherent scale bridging technique. The texture estimation is incorporated in a modular format into a micro-macro model resulting in a computationally manageable approach compared to straightforward homogenization-based multiscale methods, such as e.g. FE². A macro-mechanical model of anisotropic finite plasticity is based on evolving structural tensors accounting for the texture-induced macroscopic anisotropy. The general framework for the micro-macro modeling is a purely phenomenological setting of anisotropic plasticity in the logarithmic strain space. The capabilities and computational efficiency of this hybrid two-scale model of finite polycrystalline plasticity is demonstrated by means of a variety of numerical examples including the comparison with benchmark analyses and experimental observations.

Zusammenfassung

Inhalt der vorliegenden Arbeit ist die Modellierung von Mikrostruktur-Entwicklungen in der finiten Kristallplastizität sowie deren Einfluss auf das makroskopische Materialverhalten im Rahmen einer Zweiskalenmodellierung. Ein mikromechanisches Plastizitätsmodell, das die lokale Orientierungsänderung der mikroskopischen Kornstruktur abbildet, wird entwickelt. Dazu wird ein Algorithmus vorgeschlagen, mit dem die Orientierungsänderung in kubisch-flächen- und kubisch-raumzentrierten Kristallen numerisch effizient beschreibbar ist. Die Parametrisierung der Rotationen erfolgt dabei im Rodrigues Raum. Repräsentative numerische Beispiele zeigen die Leistungsfähigkeit dieses Modells. Die Textur, d.h. die Orientierungsverteilung der Mikrostruktur, ist entscheidende Ursache für das Entstehen makroskopischer Anisotropie, für deren genaue Modellierung ein Mehrskalenansatz sinnvoll ist. Strukturtenoren, die mit Hilfe von Orientierungsverteilungsfunktionen berechnet werden, beschreiben in einem homogenisierten Sinn den Reorientierungsvorgang von Kristallen in einem modellinhärenten Skalenübergang. Dazu werden die Strukturtenoren in modularer Weise in ein Mikro-Makro-Modell eingebaut, das -im Vergleich zu homogenisierungsbasierten Mehrskalenmethoden, wie z.B. FE²- einen numerisch effizienten Ansatz darstellt. Die durch mikrostrukturelle Effekte induzierte makroskopische Anisotropie wird durch diese Strukturtenoren in ein makroskopisches, anisotropes Plastizitätsmodell integriert. Den übergeordneten Rahmen dieses hybriden Mikro-Makro-Ansatzes bildet ein phänomenologisches, anisotropes Plastizitätsmodell im logarithmischen Verzerrungsraum. Die Leistungsfähigkeit und die numerische Effizienz des vorgeschlagenen Zweiskalenmodells der finiten Kristallplastizität werden anhand einiger numerischer Beispiele, die einen Vergleich mit experimentellen Ergebnissen und mit Benchmark-Untersuchungen beinhalten, gezeigt.

Acknowledgements

The work presented in this thesis was elaborated in the years between 2007 and 2012 during my employment as research associate at the Institute of Applied Mechanics (Civil Engineering) at the University of Stuttgart. At the end of this stage I feel grateful to many people.

First, I want to thank my academic teacher Prof. Christian Miehe. During my studies he inspired me for engineering mechanics and finally he gave me the opportunity to work as an assistant lecturer in his research group. I would like to express my gratitude for his support to achieve this work, his guidance and his support with regard to my familiar situation.

In addition, I offer my thanks to Prof. Thomas Böhlke for being interested in my work and for acting as co-referee of this doctoral thesis.

Next, I want to thank all my colleagues at the Institute of Applied Mechanics for fruitful discussions, collaborations and friendship. In particular, I would like to accentuate Dr. Daniele Rosato for the great support, the close cooperation and the true friendship. Additionally, I want to thank Dr. Felix Hildebrand for the friendly atmosphere in room 3.165 and Dipl.-Ing. Dominic Zäh for the administrative cooperation with computer issues. Furthermore, I want to mention the friendship and support in scientific as well as personal questions of Gautam Ethiraj, M.Sc., Dipl.-Ing. Lisa Schänzel, Prof. Nikolas Apel, Dr. Gerald Scheday, Dr. Fabian Welschinger and Anja Konietzny.

I am very grateful to Simon Bove and Daniel Vallicotti who provided me significant support through their bachelor theses. The supervision of these theses was a true pleasure.

Moreover, I thank my parents Helene and Josef, my sister Sonja with family, my brother Tobias with family, my parents-in-law Rita and Joachim and my brother-in-law Benedikt for their everlasting sympathy, support and backing.

Last but not least, I want to give my deep gratitude to my beloved husband Dominik for his inspiration to computational mechanics and everlasting motivation, for fruitful discussions and intense proofreading, his support in all subjects and for his true love of our cute daughter Anna.

Stuttgart, January 2013

Ilona Zimmermann

Contents

1. Introduction	1
1.1. Motivation and State of the Art	1
1.2. Overview and Outline	5
2. General Aspects of Material Modeling	9
2.1. Basics of Continuum Mechanics	9
2.1.1. Kinematics	9
2.1.2. Notion of Stresses and Heat Flux	13
2.1.3. Balance Principles	14
2.1.4. Modeling of Standard Dissipative Materials	18
2.2. Modeling Aspects in Crystal Plasticity	18
2.2.1. Hierarchical Methods for Textured Aggregates	19
2.2.2. Macroscopic Anisotropy Modeling of Textured Aggregates	21
3. Fundamentals of Polycrystalline Materials	25
3.1. Ideal Crystalline Structure	26
3.1.1. Space Lattice Composition and Symmetry Properties	26
3.1.2. Miller Indices. Crystallographic Planes and Directions	28
3.2. Real Crystalline Structure	31
3.2.1. Defects in Crystalline Materials	32
3.2.2. Dislocations	32
3.2.3. Slip Systems	37
3.2.4. Classical Flow Rule of Crystal Plasticity	37
3.3. Description of Crystallographic Texture	39
3.3.1. Representation of Crystal Orientations	39
3.3.2. Graphical Representation of Orientations	44
3.3.3. Experimental Determination of Textures	48
3.3.4. Orientation Distribution Function	48
4. Texture Modeling in Rigid Crystal Plasticity	51
4.1. Rigid-Plastic Deformation of Polycrystalline Microstructures	52
4.1.1. Taylor-Type Micro-Macro Linking	52
4.1.2. Rigid-Plastic Decomposition of Crystal Deformation	53
4.1.3. Rate Equations of Rigid Crystal Plasticity	54
4.2. Constitutive Formulation for the Determination of the Slip	54
4.2.1. Non-Uniqueness of Plastic Slip in Fcc and Bcc Crystals	54

4.2.2.	Standard Power-Type Formulation	55
4.2.3.	Purely Geometric Approach	55
4.3.	Fast Incremental Updates of Crystal Orientation	58
4.3.1.	Incremental Macroscopic Deformation	58
4.3.2.	Incremental Equations of Rigid Crystal Plasticity	60
4.3.3.	Algorithmic Determination of Plastic Slip	60
4.3.4.	Incremental Update of Orientation	61
4.4.	Representative Numerical Examples	63
4.4.1.	Texture Development in Planar Crystals	63
4.4.2.	Texture Development in Fcc Crystals	65
4.4.3.	Texture Development in Bcc Polycrystals	73
5.	Reorientation Continuum and Fourier Expansion	81
5.1.	Kinematics of an Orientation Continuum	82
5.1.1.	Orientation Continuum of Crystals	82
5.1.2.	Crystal Reorientation Map, Gradient and Velocity	83
5.1.3.	Parameterization of Rotations by Rodrigues Vectors	84
5.1.4.	Spatial Discretization of Orientation Space	87
5.1.5.	Constitutive Formulation of Crystal Reorientations	88
5.2.	Evolution of Crystal Orientation Distribution Function	88
5.2.1.	Eulerian Formulation of Crystal Fraction Conservation	88
5.2.2.	Lagrangian Formulation of Crystal Fraction Conservation	90
5.2.3.	Discrete Formulation of Crystal Fraction Conservation	91
5.3.	Numerical Examples	93
5.3.1.	Evolution of Codf in Planar Polycrystals	93
5.3.2.	Evolution of Codf in Fcc Crystals	96
5.4.	Orientation Averages and Homogenization	99
5.4.1.	Continuous Formulation	99
5.4.2.	Discrete Formulation	100
5.4.3.	Evolution of Texture-Induced Anisotropy. Definition of Anisotropy Coefficients	101
5.4.4.	Numerical Study	101
6.	Hybrid Modeling of Texture-Induced Anisotropy	105
6.1.	Framework for Hybrid Micro-Macro Modeling in Finite Crystal Plasticity .	106
6.1.1.	Kinematic Approach in terms of a Plastic Metric	107
6.1.2.	Geometric Preprocessing into the Logarithmic Strain Space	107
6.1.3.	Hybrid Constitutive Model the Logarithmic Strain Space	108

6.1.4. Geometric Postprocessing from the Logarithmic Strain Space	113
6.2. Algorithmic Formulation at Frozen Texture	114
6.3. Representative Numerical Examples	117
6.3.1. Localization of a rectangular strip in tension	118
6.3.2. Necking of a 3D rod in tension	121
6.3.3. Circular Deep Drawing of a Metallic Sheet	123
6.3.4. Square Deep Drawing of a Metallic Sheet	127
7. Conclusion	131
A. Planar Crystals undergoing Double Slip	133
A.1. Continuous Formulation	133
A.2. Discrete Algorithmic Formulation	135
References	137

1. Introduction

The overall objective of this work is the modeling of anisotropic material behavior, which physically originates from a heterogeneous microstructure. This task is a wide area of current research with active interest over the last decades as the modeling of developing anisotropies in materials undergoing finite elastic-plastic strains has a high importance for industrial applications. In particular, the work is concerned with the modeling of texture evolution in polycrystalline materials and its influence on the macroscopic material behavior. An efficient model with regard to the grain reorientation mechanism of an idealized reorientation continuum is incorporated by a model-inherent scale bridging technique in a hybrid micro-macro approach.

1.1. Motivation and State of the Art

For many engineering applications such as beverage or food can manufacturing and deep drawing or folding processes of thin-walled materials in the automotive, aircraft, civil engineering or household industry, illustrated in Figure 1.1, the simulation of the production progress is notably reasonable. Prediction of material rupture and fatigue, mechanical



Figure 1.1: Engineering applications. a) Beverage can manufacturing, forming of b) front lids in the automotive and c) kitchen sinks in the household industry. (Sources of pictures: www.aluminium.matter.org.uk [1], www.schulergroup.com [2], www.thomasnet.com [3])

properties, material shape, springback and thickness distribution after forming are main objectives of computer simulations. By means of these simulations experimental costs are avoided and moreover a better understanding of the process development is obtained, which may result in an improved fabrication design. For instance, the earing formation during a deep drawing process could be reduced and a post-trimming might be eliminated. On the one hand material can be saved, on the other hand production costs can be reduced and the production rate can be increased by an omitting finishing process. The finite element method is a very successful tool for the simulation of deformation processes, but the preciseness of the simulation results critically depends on the constitutive material formulation and the accompanying parameter identification. Induced by a rising request with regard to a qualitative and quantitative prediction of computer simulations, an accurate modeling of the material and structural properties is necessary. Therefore, additional, so-called internal variables as for instance the plastic strains, need to be taken into account. A crucial perspective towards the description of macroscopic visible effects, such as anisotropy, is provided by multiscale approaches which account for the evolution of the material on a lower scale by model-inherent scale bridging techniques. The physical source of macroscopic anisotropic, i.e. direction dependent material behavior originates in general from the heterogeneous constitution of the microstructure. The prediction of anisotropy in polycrystalline materials such as metals, polymers or minerals due to the crystallographic texture evolution is very complicated to describe within a direct macro-

scopic approach. Most macroscopic material models are therefore restricted to isotropic response or cover an initial, non-evolving texture by an anisotropic initial yield surface. Nevertheless, effects of the macroscopic deformation influencing the evolving microstructure need to be taken into account. This explains a phenomenological description of the material on different scales, each defined by its dimension and characteristic structural effects: Atomistic effects on the quantumscale, atom or molecular interaction on the

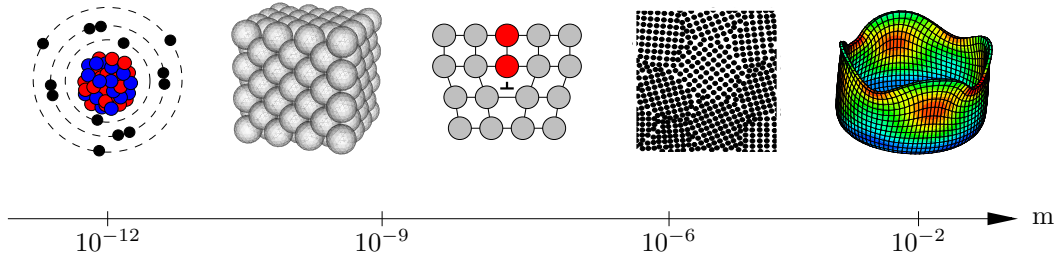


Figure 1.2: Multiscale modeling on different length-scales.

nanoscale, dislocation dynamics on the microscale, grain interaction on the mesoscale and visible phenomena, such as necking or earing development on the macroscale. An approximative link of scale clusters to length scales is shown in Figure 1.2. Note, that this link is only an indicative classification which varies in the literature. Micromechanical models are proved to provide better predictions compared to purely macroscopic models. In a top-down modeling the macroscopic description of polycrystalline materials can be based on two phenomenological scales, denoted in this contribution macroscale and microscale, governing effects taking place on the crystalline structure such as dislocation movement or crystal reorientation. An essential ingredient is the link between the different scales representing the influence of the effects on one scale to a higher or lower scale, respectively.

In order to incorporate microstructural effects of polycrystalline aggregates into a multiscale formulation, physically occurring processes need to be understood and put into a mathematical continuum description. For many deformation processes of polycrystalline materials at large strains and in a large range of temperature the plastic deformation is alleviated by the movement of dislocations and the reorientation of crystals comprising the underlying microstructure, see for instance HULL & BACON [60], HONEYCOMBE [55], WASSERMANN & GREWEN [141] and BUNGE [36]. The movement of dislocations takes place on given crystallographic planes and hardening effects occur if dislocations hinder each other. This induces a direction-dependent plastic flow and hence, anisotropic material response on the macroscale is caused by the crystalline microstructure of polycrystalline materials. Hardening effects, e.g. isotropic, kinematic or distortional hardening can be modeled by internal variables in continuum mechanics, which influence the size, position and shape of the yield surface. The modeling of the well-known Bauschinger effect of kinematic hardening is anisotropic in nature. It covers a displacement of the yield surface but not a change of its shape. In this work, the focus is put on the distortional hardening with the yield surface changing its shape during the deformation process. This distortional hardening originates from the reorientation of crystals with the polycrystalline microstructure developing preferential orientations or texture.

Many publications exist with regard to the constitutive modeling of single crystals. The phenomenological description of plastic strains in single crystals bases on the pioneering works of TAYLOR [133, 134], SCHMID & BOAS [127], NYE [107] and KRÖNER [71].

Hereby, the inelastic distortion of single crystals is governed by the movement of dislocations resulting in plastic slip on crystallographic slip systems. This dislocation movement is caused by shear stresses reaching a critical value. Hardening effects influence the relation between shear stresses and plastic slip. A rate formulation for the modeling of slip resistance due to hardening was suggested by HILL [51] with e.g. isotropic, weighted self-latent or saturation-type approaches for the hardening, cf. TAYLOR [134], HUTCHINSON [61] or PEIRCE, ASARO & NEEDLEMAN [111], among others. The elastic-plastic deformations of crystals at small and finite strains is cast in a mathematical formulation by HILL [51], TEODOSIU [135], RICE [123] and MANDEL [82], respectively. It is assumed, that the overall deformation of single crystals consists of two independent atomic mechanisms representing on the one hand the elastic distortion of the crystal lattice and on the other hand a plastic deformation preserving the lattice geometry and implying an overall effect of dislocation motion on active slip systems. In the macroscopic continuum slip theory of finite elasto-plasticity this decoupling is modeled by a multiplicative decomposition of the local deformation gradient. This ansatz is widely used for the simulation of texture evolution. For a comprehensive overview with regard to the micromechanics and the modeling of single crystals and polycrystals the reader is referred e.g. to the publications of ASARO [14] and CUITIÑO & ORTIZ [39].

A central cause for the evolution of macroscopic anisotropy is the texture development induced by the response of individual crystals. In this sense, many existing models are based on the characterization of a polycrystal by a discrete aggregate of single crystals. Under a deformation, individual crystals deform and reorient, which is characterized through (i) a micro-macro linking hypothesis and (ii) a single crystal model, cf. ASARO & NEEDLEMAN [15], HARREN & ASARO [47], MATHUR & DAWSON [84], BRONKHORST, KALIDINDI & ANAND [33], MIEHE, SCHRÖDER & SCHOTTE [98] and MIEHE & SCHOTTE [95]. These works apply the widely used Taylor ansatz, describing a uniform deformation gradient to all grains, cf. TAYLOR [134]. The assumption of a rigid-plastic decomposition of the deformation gradient neglects elastic contributions, which is often reasonable according to BUNGE [36] and was applied by several authors such as MATHUR & DAWSON [84], RASHID [122] and DAFALIAS [40]. Alternative polycrystalline models describe the texture evolution by crystal orientation distribution functions governed by (i) a model of crystal plasticity and (ii) a crystal fraction conservation equation, cf. RASHID [122], DAFALIAS [40], KUMAR & DAWSON [72] and BÖHLKE, RISY & BERTRAM [30]. In many publications, the crystal orientations are parametrized by Eulerian angles. A parametrization of crystal orientations by Rodrigues vectors was first discussed by FRANK [42] and applied to texture simulations e.g. by BECKER & PANCHANADEESWARAN [22], KUMAR & DAWSON [73, 74, 75] and RANDLE & ENGLER [121].

The constitutive relationship between macroscopic quantities as a function of the microstructure is called homogenization. Here, the macroscale is associated with a homogenized continuum and the microscale is often characterized by a statistically representative set of crystal grains, cf. Figure 1.3. Typical material properties on the microscale are for instance the orientation distribution of crystal grains, the morphology, the hardening of the crystal grains or the distribution of any defects such as cracks, pores, voids or inclusions. Based on the works of e.g. HILL [53] and SUQUET [132] the homogenization is characterized by a volume average of a certain quantity across a representative volume element. In the work of MIEHE, SCHRÖDER & SCHOTTE [98] a computational homogenization takes place in each integration point of a macro-continuum furnished by a microstructure

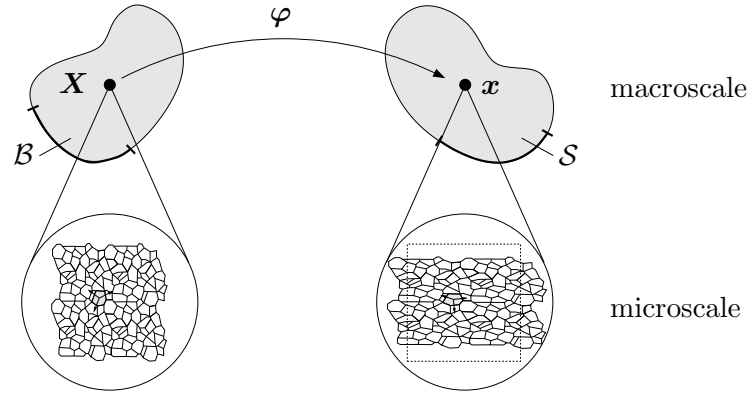


Figure 1.3: Homogenized continuum on the macroscale with locally, i.e. pointwise, attached polycrystalline aggregates on the microscale in both the undeformed state \mathcal{B} as well as the deformed state \mathcal{S} .

consisting of a finite amount of crystal grains represented by another finite element mesh, known as FE^2 method. An averaging procedure of micro-stresses in polycrystalline aggregates gives a homogenized macroscopic stress-state, cf. HARREN & ASARO [47], MATHUR & DAWSON [84], BRONKHORST, KALIDINDI & ANAND [33], ANAND & KOTHARI [10] and BÖHLKE & BERTRAM [28], among others. Based on homogenization, the overall response of a polycrystalline material is described by micro-macro-transitions, where the computational effort is extremely high. Therefore, these approaches can barely be used for large-scale applications and stronger idealizations for micro-macro approaches are necessary. The rootage of homogenization techniques in recently developed energy-minimization-based incremental homogenization and relaxation methods of ORTIZ & REPETTO [109], ORTIZ & STAINIER [110], MIEHE [87] and MIEHE, SCHOTTE & LAMBRECHT [96] provide an important new perspective for the analysis of plastic microstructures in single crystals and polycrystals. However, many of the scale bridging techniques developed so far are computationally extremely demanding. Thus, they are only of restricted applicability to large-scale computations, such as two-scale descriptions of texture-induced anisotropy in polycrystals based on microstructures with a large amount of discretized grains. As these scenarios are more and more to be incorporated to capture all the requirements within the afore mentioned industrial applications, there is in deed a need for the construction of multiscale-based constitutive models. These models need to be able to deliver predictive and trustable results at manageable numerical effort.

With regard to a numerically efficient realization of evolving texture-induced anisotropy, RAABE & ROTERS [118] introduced a texture component method based on a reduced set of orientations, approximating the crystal orientation distribution function. An important step towards a manageable micro-macro theory of texture evolution is provided by BÖHLKE & BERTRAM [28] and BÖHLKE [25]. This approach bases on the description of the crystal orientation distribution function by a tensorial Fourier series, cf. ADAMS, BOEHLER, GUIDI & ONAT [8], GUIDI, ADAMS & ONAT [45], ZHENG & ZOU [146] and ZHENG & FU [145]. It is equivalent to the representation of the crystal orientation distribution function by generalized spherical harmonics, cf. BUNGE [35] and ROE [126]. In contrast to the representation by generalized spherical harmonics, the Fourier series representation has the advantage of being coordinate-independent and the coefficients can be interpreted as internal variables which govern the distortion of the yield surface, cf. MAN [80, 81] and BÖHLKE & BERTRAM [28]. The challenge of these models is the de-

velopment of efficient material models which describe a macroscopic anisotropy resulting from both initial and evolving texture. A rational approach to the quantification of these texture effects can only be realized by multiscale methods which derive the macroscopic response of a polycrystal by explicitly linking the response of individual crystals. Hybrid micro-macro models mix ingredients of a purely macroscopic modeling with those of full two-scale models. In the particular approach of the underlying contribution the hybrid model is characterized by the coupling of a macroscopic plasticity model with a microscopic plasticity model, where the latter describes in a simplified manner a key microstructural mechanism such as grain reorientation. The coupling is provided by a linking hypothesis governed by specific homogenization assumptions, defining the evolution of effective structural anisotropy tensors entering the macro model based on the micro-mechanism described by the micro-model. Thereby, the present work conceptually follows the recent publications of MIEHE & ROSATO [93], MIEHE, ROSATO & FRANKENREITER [94] and MIEHE, FRANKENREITER & ROSATO [91]. Following the structure of this thesis, the content of these publications is reorganized and supplemented with additional comments and more detailed numerical examples.

1.2. Overview and Outline

The first part of **Chapter 2** is devoted to the introduction of the basic notation of this thesis and the key equations of continuum mechanics for the mathematical description of large deformations. By means of the motion of a material body, fundamental mappings and main quantities such as the deformation gradient, metric tensors and strain measures are introduced. With the definition of stress tensors generally accepted balance principles are formulated. As this thesis is concerned with the texture-induced anisotropy in polycrystalline materials, in the second part of this chapter a rough overview concerning modeling aspects in crystal plasticity is given. To be specific, this concerns the hierarchical modeling and microstructure-based anisotropy of textured aggregates.

In **Chapter 3** some fundamentals of polycrystalline materials are reviewed. By means of an ideal crystalline structure the common indication of crystallographic planes and directions with Miller indices is introduced. Shortly, defects in real crystalline materials are listed and a closer discussion is concerned with line defects, so-called dislocations, which are the dominant origin for the plastic deformation of polycrystalline materials. The movement of dislocations on crystallographic planes involves the introduction of slip systems for face-centered and body-centered cubic crystals. These slip systems are governed by a slip plane normal and slip plane direction included with the plastic slip in the flow rule of crystal plasticity. Polycrystalline materials are composed by a finite amount of crystal grains, each characterized by a certain orientation. The distribution of orientations and its evolution towards preferential directions is known as the crystallographic texture. Therefore, different parameterizations of crystal orientations are presented, where the one with Rodrigues parameters is favored in this contribution. The graphical representation by means of pole figures and in the Rodrigues space as well as the experimental determination of textures are shortly discussed. A measure for the volume fraction of grains having a certain orientation is the so-called orientation distribution function. Its representation as Fourier series expansion defines structural tensors, which turn out to be interpreted as homogenized quantities characterizing the anisotropy effect of the microstructure.

Discrete reorientations are obtained by the fast updates of rigid crystal plasticity outlined in **Chapter 4**. A Taylor-type approach where the lattice rotation is driven by the

macroscopic deformation of the polycrystalline aggregate is considered. For fully developed plastic flow at large strains, the assumption of a rigid-plastic decomposition of the deformation is reasonable. In the rate-independent setting, the update of the active set of slip systems is governed by a purely kinematic criterion. As the computation of the plastic slip on these active slip systems for face-centered and body-centered cubic crystals is not unique, a supplementary optimization condition is solved. The numerical integration is performed in terms of an incrementally objective mid-point-type scheme. Closed-form algorithmic representations for the current Rodrigues parameters of discrete orientations are derived. The formulation is applied to planar crystals undergoing double slip, which gives a simple linear differential equation for the crystal reorientation. By means of representative numerical examples the reorientation process is demonstrated for planar crystals, face-centered cubic crystals and body-centered cubic crystals under different characteristic deformation modes. These are associated with typical industrial processes such as wire drawing, extrusion and rolling. The texture evolution is analyzed and compared qualitatively to experimental and numerical results. The computational speed of the proposed update algorithm is demonstrated and offers an important ingredient with regard to a hybrid micro-macro modeling.

In **Chapter 5**, the polycrystalline microstructure is idealized as a crystal orientation continuum, with the single crystal grains being represented by material points of the orientation continuum. A deformation of the orientation continuum is described by a crystal reorientation map as mapping between Lagrangian and Eulerian configuration. The parametrization of rotations by Rodrigues vectors induces the definition of a metric which relates volume elements of the Rodrigues space to volume elements of the orientation space. The evolution of the reorientation map is governed by a constitutive assumption for the lattice spin providing the link to the macroscopic deformation of the polycrystalline aggregate. A so-called crystal orientation distribution function describes the orientation texture of the polycrystalline aggregates. Its evolution in time is governed by the crystal reorientation map. The underlying concept is a mass-type conservation of crystal fractions, which describes the probability that orientations fall into certain control orientation sectors. In detail, the Eulerian and Lagrangian representations of these conservation statements are outlined and their discretization is considered. With regard to a fast implementation into homogenization methods over the orientation space, rough estimates of the crystal orientation distribution function are developed. Within an Eulerian geometric setting, discrete reorientations are projected onto control spaces. The current discrete crystal orientation distribution function is then simply determined by the number of current orientations in the control space. In the Lagrangian geometric setting, the crystal orientation distribution function update is based on the deformation of the tetrahedral cells in the orientation space. Clearly, such an approach is restricted to smooth reorientation processes at moderate deformations. The crystal orientation distribution function is analyzed for planar crystals and face-centered cubic crystals. With these formulations at hand, orientation averages based on the homogenization over the current orientation space are introduced. These averages are defined in the Eulerian setting in terms of the crystal orientation distribution function. However, the pull-back to the Lagrangian setting gives a representation where the current crystal orientation distribution function is not needed. That is of particular importance for the discrete setting. It is shown that an orientation average in the discrete setting with cells of equal size is essentially determined by an arithmetic average of discrete quantities which depend on the current orientation.

For a simple Hill-type yield function including distortional hardening, the influence of the crystalline microstructure on the yield surface, on the normalized yield stress and on the Lankford coefficient is discussed.

In **Chapter 6** a hybrid micro-macro model is proposed. It concerns a purely macroscopic plasticity model with structural tensors accounting for an evolving macroscopic anisotropy. This macro model is coupled to an accompanying microscopic plasticity model that accounts locally for the microscopic structural changes in the form of grain reorientations, motivated by a crystal fraction conservation of a polycrystalline aggregate. The macroscopic model of anisotropic plasticity is framed by a plastic-spin free metric-type plasticity model in the logarithmic strain space. In a preprocessing step logarithmic strains are computed from the current and plastic metric. This makes it possible to formulate the constitutive model in a framework similar to the geometrically linear theory of plasticity. In a postprocessing step nominal stresses and moduli are obtained by a purely geometric transformation from the logarithmic counterparts. The texture-induced anisotropy enter the macroscopic plasticity model in the anisotropic parts of the elasticity modulus and the Hill tensor, solved by an operator splitting of the micro-macro problem convenient with regard to its numerical implementation. By means of representative examples the texture evolution within a shearband development of a two-dimensional strip and within the necking region of a three-dimensional rod is analyzed. Furthermore, deep drawing simulations relevant for industrial applications including texture-induced anisotropy effects are examined demonstrating the high predictive capabilities as well as the computational efficiency of the proposed model.

2. General Aspects of Material Modeling

2.1. Basics of Continuum Mechanics

The aim of this section is to give a short introduction to continuum mechanics and the notation used in this work, based on the lecture notes MIEHE [88, 89]. For a more detailed discussion the reader is referred to the textbooks of TRUESDELL & NOLL [138], MALVERN [79] and MARSDEN & HUGHES [83] or the recent publications of CHADWICK [37], HOLZAPFEL [54] and HAUPT [48], among others.

2.1.1. Kinematics. This subsection is dedicated to the geometrical description of the deformation of material bodies on the basis of dual bases and metric tensors. The deformation gradient, its meaning as a tangent, area and volume map and its decomposition into stretch and rotation is discussed. Furthermore, strain measures are derived and material and spatal velocities are introduced.

2.1.1.1. Motion of a Body and Dual Bases. Consider a material body B as a physical object occupied with specific properties such as density, texture, stiffness, etc. B is defined as an entity of material points $P \in B$ which are mapped to a subset of the Euclidean space \mathbb{E}^3 , i.e.

$$\chi : \begin{cases} B \times \mathbb{R} \rightarrow \mathbb{E}^3 \\ (P, t) \mapsto \mathbf{x} = \chi(P, t) . \end{cases} \quad (2.1)$$

The coordinates $\mathbf{x} \in \mathbb{E}^3$ represent the current, spatial or Eulerian configuration $\mathcal{S} = \mathcal{S}_t$ of the body B with respect to a global Cartesian coordinate system, see Figure 2.1. Here, the consecutive configurations at time t define the motion of the body B along its path, where the stress-free state at $t = t_0$ is denoted by the reference, material or Lagrangian

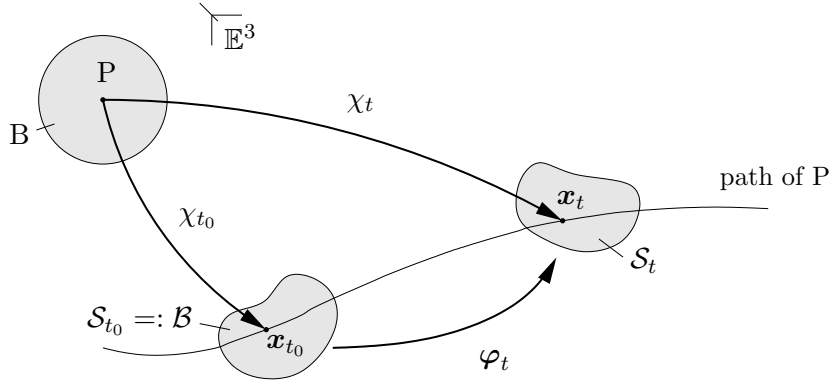


Figure 2.1: Motion of a material body B . The map χ defines the current configuration \mathcal{S}_t of the body B within the Euclidean space \mathbb{E}^3 . The motion of the material body is described by a sequence of configurations, usually related to the reference configuration \mathcal{B} .

configuration \mathcal{B} with the mapping

$$\chi_{t_0} : \begin{cases} B \rightarrow \mathcal{B} \subset \mathbb{E}^3 \\ P \mapsto \mathbf{X} = \chi_{t_0}(P) . \end{cases} \quad (2.2)$$

The Lagrangian coordinates are indicated by $\mathbf{X} \in \mathcal{B} \subset \mathbb{E}^3$ with respect to the global Cartesian coordinate system. This global frame can be represented by covariant and contravariant material and spatial base vectors $\{\mathbf{E}_i, \mathbf{E}^i\}_{i=1,2,3}$ and $\{\mathbf{e}_i, \mathbf{e}^i\}_{i=1,2,3}$, which are

related through the orthogonality relation

$$\delta^i_j = \mathbf{E}^i \cdot \mathbf{E}_j \quad \text{and} \quad \delta^i_j = \mathbf{e}^i \cdot \mathbf{e}_j \quad \text{with} \quad \delta^i_j = \begin{cases} 1 & \text{if } i = j \\ 0 & \text{if } i \neq j \end{cases} \quad (2.3)$$

representing the Kronecker-Delta δ . Covariant elements are denoted with superscript indices and contravariant elements with subscript indices. For now, the differentiation is maintained, but as curvilinear coordinates are not considered in this work, the base vectors coincide.

2.1.1.2. Deformation Gradient and Jacobi Determinant. By means of the above introduced mappings, the spatial coordinates can be represented by $\mathbf{x} = \chi(\mathbf{P}, t) = \chi \circ \chi_{t_0}^{-1} = \boldsymbol{\varphi}(\mathbf{X}, t)$, where the nonlinear deformation map

$$\boldsymbol{\varphi}_t : \begin{cases} \mathcal{B} \rightarrow \mathcal{S} \\ \mathbf{X} \mapsto \mathbf{x} = \boldsymbol{\varphi}_t(\mathbf{X}) \end{cases} \quad (2.4)$$

describes the relative motion between \mathcal{B} and \mathcal{S} parametrized in the position \mathbf{X} and the time t . Variation in time describes the path $\boldsymbol{\varphi}_{\mathbf{X}}$ of a material point and $\boldsymbol{\varphi}_t$ describes the configuration for a specific time t . A key quantity for the description of finite deformations is the deformation gradient, defined by the Fréchet derivative

$$\mathbf{F}(\mathbf{X}) := \nabla_{\mathbf{X}} \boldsymbol{\varphi}_t(\mathbf{X}) = \frac{\partial \boldsymbol{\varphi}(\mathbf{X}, t)}{\partial \mathbf{X}}. \quad (2.5)$$

It is a linear map between tangent vectors $\mathbf{T} \in \mathcal{B}$ to material curves and $\mathbf{t} \in \mathcal{S}$ to spatial curves

$$\mathbf{F} : \begin{cases} T_{\mathbf{X}}\mathcal{B} \rightarrow T_{\mathbf{x}}\mathcal{S} \\ \mathbf{T} \mapsto \mathbf{t} = \mathbf{F}\mathbf{T} \end{cases} \quad (2.6)$$

in the tangent spaces $T_{\mathbf{X}}\mathcal{B}$ and $T_{\mathbf{x}}\mathcal{S}$. A relation between material and spatial normal vectors $d\mathbf{A}$ and $d\mathbf{a}$ is found by Nansons formula

$$d\mathbf{a} = d\mathbf{x}_1 \times d\mathbf{x}_2 = \mathbf{F}d\mathbf{X}_1 \times \mathbf{F}d\mathbf{X}_2 = \det[\mathbf{F}]\mathbf{F}^{-T}(d\mathbf{X}_1 \times d\mathbf{X}_2) =: \text{cof}[\mathbf{F}]d\mathbf{A}, \quad (2.7)$$

where $\text{cof}[\mathbf{F}]$ represents the cofactor of the deformation gradient. With $d\mathbf{A} = \mathbf{N}dA$ and $d\mathbf{a} = \mathbf{n}da$, it is clear, that \mathbf{F}^{-T} is a linear map between normal vectors $\mathbf{N} \in \mathcal{B}$ to material area elements and $\mathbf{n} \in \mathcal{S}$ to spatial area elements

$$\mathbf{F}^{-T} : \begin{cases} T_{\mathbf{X}}^*\mathcal{B} \rightarrow T_{\mathbf{x}}^*\mathcal{S} \\ \mathbf{N} \mapsto \mathbf{n} = \mathbf{F}^{-T}\mathbf{N} \end{cases} \quad (2.8)$$

in the cotangent spaces $T_{\mathbf{X}}^*\mathcal{B}$ and $T_{\mathbf{x}}^*\mathcal{S}$. In order to ensure invertibility, $\det[\mathbf{F}] \neq 0$ must hold. By means of the tangent and normal mappings (2.6) and (2.8) the deformation gradient links the Lagrangian covariant and contravariant bases to the Eulerian covariant and contravariant bases via

$$\mathbf{e}^a = \mathbf{F}\mathbf{E}^A \quad \text{and} \quad \mathbf{e}_a = \mathbf{F}^{-T}\mathbf{E}_A. \quad (2.9)$$

Similar to area elements, a relation for material and spatial volume elements can be given. The volume element is spanned by $d\mathbf{x}_1$, $d\mathbf{x}_2$ and $d\mathbf{x}_3$, i.e.

$$dv = d\mathbf{x}_1 \cdot (d\mathbf{x}_2 \times d\mathbf{x}_3) = \mathbf{F}d\mathbf{X}_1 \cdot (\mathbf{F}d\mathbf{X}_2 \times \mathbf{F}d\mathbf{X}_3) = \det[\mathbf{F}]dV. \quad (2.10)$$

Hence, the determinant of the deformation gradient is a linear map between material volume elements and spatial volume elements

$$J := \det[\mathbf{F}] : \begin{cases} \mathbb{R} \rightarrow \mathbb{R} \\ dV \mapsto dv = J dV \end{cases}, \quad (2.11)$$

with the constraints $J \neq 0$ of a bijective deformation and $J > 0$ in order to avoid penetration of the material. The covariant and contravariant bases $\{\mathbf{E}^i\}$, $\{\mathbf{E}_i\}$, $\{\mathbf{e}^i\}$ and $\{\mathbf{e}_i\}$ defined above span the tangent and cotangent spaces, illustrated in Figure 2.2.

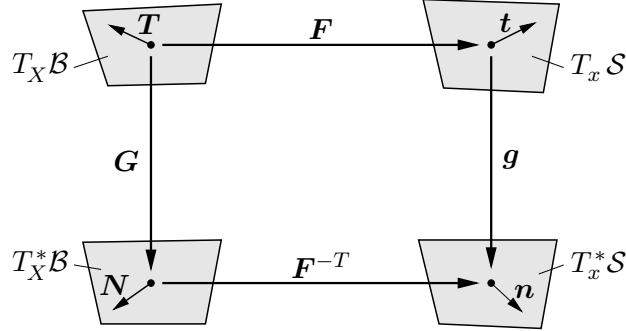


Figure 2.2: Fundamental mappings between vector spaces. \mathbf{F} maps elements between the tangent spaces $T_X \mathcal{B}$, $T_x \mathcal{S}$ and \mathbf{F}^{-T} maps elements between the cotangent spaces $T_X^* \mathcal{B}$, $T_x^* \mathcal{S}$. The metric tensors \mathbf{G} and \mathbf{g} govern the mappings between the tangent and cotangent spaces.

2.1.1.3. Metric Tensors and Strain Measures. The Lagrangian and Eulerian metric tensors \mathbf{G} and \mathbf{g}

$$\begin{aligned} \mathbf{G} &= \delta_{AB} \mathbf{E}^A \otimes \mathbf{E}^B & \text{and} & & \mathbf{g} &= \delta_{ab} \mathbf{e}^a \otimes \mathbf{e}^b \\ \mathbf{G}^{-1} &= \delta^{AB} \mathbf{E}_A \otimes \mathbf{E}_B & \text{and} & & \mathbf{G}^{-1} &= \delta^{ab} \mathbf{e}_a \otimes \mathbf{e}_b \end{aligned} \quad (2.12)$$

can be interpreted as index lowering or raising, i.e. mappings between the tangent and cotangent spaces

$$\mathbf{G} : \begin{cases} T_X \mathcal{B} \rightarrow T_X^* \mathcal{B} \\ \mathbf{T} \mapsto \mathbf{N} = \mathbf{G}\mathbf{T} \end{cases} \quad \text{and} \quad \mathbf{g} : \begin{cases} T_x \mathcal{S} \rightarrow T_x^* \mathcal{S} \\ \mathbf{t} \mapsto \mathbf{n} = \mathbf{g}\mathbf{t} \end{cases}. \quad (2.13)$$

Note, that these metric tensors do not contain any information with regard to the deformation state. Metric tensors are used for the computation of the length of a vector with respect to a certain basis. The length of a material and a spatial vector

$$\begin{aligned} |\mathbf{T}|_{\mathbf{G}} &= [\mathbf{T} \cdot (\mathbf{G}\mathbf{T})]^{\frac{1}{2}} = [\mathbf{F}^{-1}\mathbf{t} \cdot (\mathbf{G}\mathbf{F}^{-1}\mathbf{t})]^{\frac{1}{2}} = [\mathbf{t} \cdot (\mathbf{c}\mathbf{t})]^{\frac{1}{2}} = |\mathbf{t}|_{\mathbf{c}} \\ |\mathbf{t}|_{\mathbf{g}} &= [\mathbf{t} \cdot (\mathbf{g}\mathbf{t})]^{\frac{1}{2}} = [\mathbf{F}\mathbf{T} \cdot (\mathbf{g}\mathbf{F}\mathbf{T})]^{\frac{1}{2}} = [\mathbf{T} \cdot (\mathbf{C}\mathbf{T})]^{\frac{1}{2}} = |\mathbf{T}|_{\mathbf{C}} \end{aligned} \quad (2.14)$$

is defined as the scalar product of a covariant vector with its contravariant counterpart. Herein, the so-called right and left Cauchy Green tensors

$$\mathbf{C} = \varphi^*(\mathbf{g}) = \mathbf{F}^T \mathbf{g} \mathbf{F} \quad \text{and} \quad \mathbf{c} = \varphi_*(\mathbf{G}) = \mathbf{F}^{-T} \mathbf{G} \mathbf{F}^{-1} \quad (2.15)$$

are introduced. They can be interpreted as linear maps between tangent and cotangent spaces, i.e. dual to \mathbf{g} and \mathbf{G} . Similar to metric tensors, the Cauchy Green tensors are

symmetric and positive definite, but depend on the deformation state. $\varphi^*(\mathbf{g})$ represent a pull-back operation of the Eulerian metric \mathbf{g} and $\varphi_*(\mathbf{G})$ a push-forward operation of the Lagrangian metric \mathbf{G} . A measure for the strains is half the quadratic change in length compared either in the material or in the spatial configuration, i.e.

$$\delta := \frac{1}{2} [|d\mathbf{x}|_{\mathbf{g}}^2 - |d\mathbf{X}|_{\mathbf{G}}^2] = d\mathbf{X}\mathbf{E} \cdot d\mathbf{X} = d\mathbf{x}\mathbf{e} \cdot d\mathbf{x} . \quad (2.16)$$

Therefore, the Lagrangian Green and Eulerian Almansi strain tensors

$$\mathbf{E} = \frac{1}{2} (\mathbf{C} - \mathbf{G}) \quad \text{and} \quad \mathbf{e} = \frac{1}{2} (\mathbf{g} - \mathbf{c}) , \quad (2.17)$$

both comparing current and reference metric, are defined. A general representation of strain tensors is given by the Seth-Hill family, cf. SETH [129] and HILL [52], of strain measures

$$\mathbf{E}^{(m)} = \begin{cases} \frac{1}{m} [\mathbf{C}^{\frac{m}{2}} - \mathbf{G}] & \text{if } m \neq 0 \\ \frac{1}{2} \ln[\mathbf{C}] & \text{if } m = 0 \end{cases} \quad \text{and} \quad \mathbf{e}^{(m)} = \begin{cases} \frac{1}{m} [\mathbf{g} - \mathbf{c}^{\frac{m}{2}}] & \text{für } m \neq 0 \\ \frac{1}{2} \ln[\mathbf{c}] & \text{für } m = 0 \end{cases} \quad (2.18)$$

giving the Green and Almansi tensor (2.17) for $m = 2$ and the logarithmic Hencky strains for $m = 0$, used in Section 6.

2.1.1.4. Polar Decomposition of the Deformation Gradient. The deformation gradient (2.5) can be multiplicatively decomposed

$$\mathbf{F} = \mathbf{R}\mathbf{U} = \mathbf{v}\mathbf{R} \quad (2.19)$$

into a stretch and a rotation. The orthogonal rotation tensor \mathbf{R} with $\det[\mathbf{R}] = 1$ either follows a stretch \mathbf{U} or is followed by a stretch \mathbf{v} . The symmetric and positive definite tensors \mathbf{U} and \mathbf{v} are denoted Lagrangian right or Eulerian left stretch tensor. With the polar decomposition and the symmetry property of the stretch tensors, the right and left Cauchy Green tensor can be rewritten according to

$$\begin{aligned} \mathbf{C} &= \mathbf{F}^T \mathbf{g} \mathbf{F} = \mathbf{U}^T (\mathbf{R}^T \mathbf{g} \mathbf{R}) \mathbf{U} = \mathbf{U}^T \mathbf{G} \mathbf{U} = \mathbf{U}^2 \\ \mathbf{c}^{-1} &= \mathbf{F} \mathbf{G}^{-1} \mathbf{F}^T = \mathbf{v}^T (\mathbf{R} \mathbf{G}^{-1} \mathbf{R}^T) \mathbf{v} = \mathbf{v} \mathbf{g}^{-1} \mathbf{v}^T = \mathbf{v}^2 \end{aligned} \quad (2.20)$$

Hence it is clear, that strain measures do not include any rotational information. The stretch tensors can be computed by means of a spectral decomposition.

2.1.1.5. Time Derivatives of Material and Spatial Objects. As the nonlinear deformation map φ_t is a function of the Lagrangian coordinates \mathbf{X} and the time, the material velocity is defined as the partial derivative of the deformation of fixed material points with respect to the time t . A parameterization by the Eulerian coordinates \mathbf{x} is obtained by a composition with the inverse deformation map. Hence, material and spatial velocities are defined as

$$\mathbf{V}(\mathbf{X}, t) = \frac{\partial}{\partial t} \varphi(\mathbf{X}, t) \quad \text{and} \quad \mathbf{v}(\mathbf{x}, t) = \frac{\partial}{\partial t} \varphi(\mathbf{X}, t) \circ \varphi_t^{-1}(\mathbf{x}) \quad (2.21)$$

and represent both the same quantity but in different parametrizations. The temporal changes of a material field $F(\mathbf{X}, t)$ and a spatial field $f(\mathbf{x}, t)$

$$\frac{d}{dt} F = \frac{\partial}{\partial t} F \quad \text{and} \quad \frac{d}{dt} f = \frac{\partial}{\partial t} f + \nabla_x f \cdot \mathbf{v} \quad (2.22)$$

are given by the total time derivative consisting of a local part $\partial f / \partial t$ and a convective part $\nabla_x f \cdot \mathbf{v}$ for the spatial field, whereas for the material field $F(\mathbf{X}, t)$ the total time derivative is equal to the partial time derivative.

2.1.2. Notion of Stresses and Heat Flux. An arbitrary part \mathcal{P} is cut out of the material body \mathcal{S} and phenomenological quantities such as the surface traction \mathbf{t} and the heat flux q_n representing the effect of the cut-off part of the body on \mathcal{P} are introduced, see Figure 2.3.

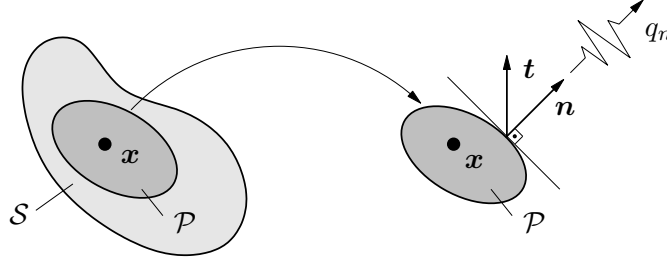


Figure 2.3: Eulers cut principle. A part \mathcal{P} is cut out of the deformed material body and the effects on \mathcal{P} are represented by the surface traction \mathbf{t} and the heat flux q_n .

2.1.2.1. Stress Tensors. The surface traction \mathbf{t} represents the mechanical effect on \mathcal{P} as an infinitesimal force vector $d\mathbf{f} = \mathbf{t}da$ acting on an infinitesimal area element of the cut surface $\partial\mathcal{P}$. According to Cauchy's theorem, the surface traction \mathbf{t} is a linear function of the normal \mathbf{n} to the cut-surface

$$\mathbf{t}(\mathbf{x}, t, \mathbf{n}) = \boldsymbol{\sigma}(\mathbf{x}, t)\mathbf{n} , \quad (2.23)$$

with the true Cauchy stress tensor $\boldsymbol{\sigma}$ giving a relation of the actual force acting on the cut-surface and the deformed area element. The Cauchy stress tensor as a covariant Eulerian tensor can be interpreted as a mapping between cotangent space $T_x^*\mathcal{S}$ and tangent space $T_x\mathcal{S}$ according to

$$\boldsymbol{\sigma} : \begin{cases} T_x^*\mathcal{S} \rightarrow T_x\mathcal{S} \\ \mathbf{n} \mapsto \mathbf{t} = \boldsymbol{\sigma}\mathbf{n} . \end{cases} \quad (2.24)$$

Multiplication of the Cauchy stresses $\boldsymbol{\sigma}$ with the determinant J of the deformation gradient defines the Kirchhoff stress tensor $\boldsymbol{\tau} = J\boldsymbol{\sigma}$. Relating the force $d\mathbf{f}$ to a Lagrangian surface element dA , the traction vector acting on the undeformed cut-surface is called nominal surface traction vector $\tilde{\mathbf{t}}$. A Cauchy-type relation gives the linear relation between the nominal traction and the Lagrangian normal \mathbf{N}

$$\tilde{\mathbf{t}} = \mathbf{P}\mathbf{N} \quad (2.25)$$

in terms of the nominal or first Piola-Kirchhoff stress tensor \mathbf{P} . It can be interpreted as a mapping between the cotangent space $T_X^*\mathcal{B}$ of the reference configuration and the tangent space $T_x\mathcal{S}$ of the current configuration

$$\mathbf{P} : \begin{cases} T_X^*\mathcal{B} \rightarrow T_x\mathcal{S} \\ \mathbf{N} \mapsto \tilde{\mathbf{t}} = \mathbf{P}\mathbf{N} . \end{cases} \quad (2.26)$$

The alternative representation of the resultant force yields the identity $d\mathbf{f} = \mathbf{t}da = \tilde{\mathbf{t}}dA$. With Nanson's formula (2.7) a relation between the true and nominal stresses is given by

$$\mathbf{P} = J\boldsymbol{\sigma}\mathbf{F}^{-T} = \boldsymbol{\tau}\mathbf{F}^{-T} . \quad (2.27)$$

The second Piola-Kirchhoff stress tensor \mathbf{S} is the Lagrangian counterpart of the Eulerian Kirchhoff stresses $\boldsymbol{\tau}$. It can be interpreted as a mapping between the cotangent space $T_X^*\mathcal{B}$ and the tangent space $T_X\mathcal{B}$ of the reference configuration

$$\mathbf{S} := \mathbf{F}^{-1} \boldsymbol{\tau} \mathbf{F}^{-T} . \quad (2.28)$$

In Figure 2.4 the alternative representations of the introduced stresses are visualized.

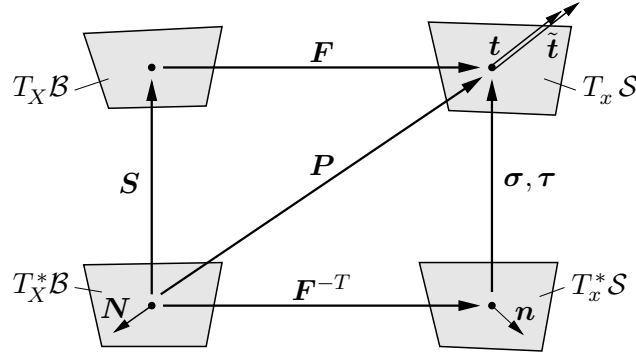


Figure 2.4: Definition of stress tensors. The second Piola-Kirchhoff stress tensor \mathbf{S} and the Kirchhoff stress tensor $\boldsymbol{\tau}$ are purely contravariant Lagrangian and Eulerian objects, whereas the first Piola-Kirchhoff stress tensor \mathbf{P} is a mixedvariant two-field tensor.

2.1.2.2. Heat Flux. As shown in Figure 2.3, the thermal effects onto the part \mathcal{P} are described by the scalar heat flux q_n , characterizing the heat flux through the surface in the direction of the normal \mathbf{n} . Analogously to Cauchy's theorem for the stresses, Stokes' heat flux theorem

$$q_n(\mathbf{x}, t, \mathbf{n}) = \mathbf{q}(\mathbf{x}, t) \cdot \mathbf{n} \quad (2.29)$$

assumes a linear dependence of the heat flux on the normal with \mathbf{q} representing the true heat flux vector defined per unit deformed area. Through $\mathbf{q} \cdot \mathbf{n} da = \mathbf{Q} \cdot \mathbf{N} dA$, the Lagrangian counterpart of \mathbf{q} is introduced which yields with Nanson's formula (2.7) the identity

$$\mathbf{Q} = J \mathbf{F}^{-1} \mathbf{q} \quad (2.30)$$

in terms of the Lagrangian or nominal heat flux vector \mathbf{Q} .

2.1.3. Balance Principles. In this subsection the classical balance principles, conservation of mass, balance of linear and angular momentum, balance of energy and balance of entropy are discussed. These principles are generally admitted and can be applied to any material. A part \mathcal{P} is cut out of the body \mathcal{B} for which integral balances must hold. These global balances can be transformed by application of the Gauss and localization theorem into local balances valid at every point $\mathbf{x} \in \mathcal{P}$. The Reynolds transport theorem

$$\frac{d}{dt} \int_{\mathcal{P}} f(\mathbf{x}, t) dv = \int_{\mathcal{P}} \dot{f} + f \operatorname{div}[\dot{\mathbf{x}}] dv = \int_{\mathcal{P}} \dot{f} dv + \int_{\partial \mathcal{P}} f \dot{\mathbf{x}} \cdot \mathbf{n} da \quad (2.31)$$

is used for the derivation of the following balance laws.

2.1.3.1. Balance of Mass. For the part \mathcal{P} the material density is defined by $\rho_0 = dm/dV$ and the spatial density by $\rho = dm/dv$. The balance of mass states that the temporal change of the mass is equal to zero, presumed that there is no transport of mass

$$\frac{d}{dt}m_{\mathcal{P}} = 0 \quad \text{with} \quad m_{\mathcal{P}} = \int_{\mathcal{P}} dm = \int_{\mathcal{P}} \rho dv = \int_{\mathcal{P}} \rho_0 dV = M_{\mathcal{P}} \quad (2.32)$$

which is the global form of the balance of mass. Either reformulating (2.32)₂ or taking the time derivative of (2.32)₁ and application of the localization theorem $dV \rightarrow 0$ yields the local forms of the balance of mass

$$\rho_0 - J\rho = 0 \quad \text{and} \quad \dot{\rho} + \rho \operatorname{div} \mathbf{v} = 0 . \quad (2.33)$$

These equations represent the Lagrangian (material) and Eulerian (spatial) formats of the balance equations being valid for the limit $\mathcal{P} \rightarrow \mathcal{B}; \mathcal{S}$ for all material points $\mathbf{X} \in \mathcal{B}$ or $\mathbf{x} \in \mathcal{S}$, respectively.

2.1.3.2. Balance of Linear Momentum. The global balance of linear momentum postulates that the temporal change of the momentum $\mathbf{I}_{\mathcal{P}}$ of the part $\mathcal{P} \in \mathcal{B}$ is identical to the resultant forces $\mathbf{F}_{\mathcal{P}}$ acting on \mathcal{P}

$$\frac{d}{dt}\mathbf{I}_{\mathcal{P}} = \mathbf{F}_{\mathcal{P}} \quad (2.34)$$

with the linear momentum and the resultant forces

$$\mathbf{I}_{\mathcal{P}} = \int_{\mathcal{P}} \mathbf{v} dm = \int_{\mathcal{P}} \rho \mathbf{v} dv \quad \text{and} \quad \mathbf{F}_{\mathcal{P}} = \int_{\partial\mathcal{P}} \mathbf{t} da + \int_{\mathcal{P}} \boldsymbol{\gamma} dv , \quad (2.35)$$

containing a surface and a volume part. \mathbf{t} is the contact traction acting on the boundary $\partial\mathcal{P}$ of the part \mathcal{P} and $\boldsymbol{\gamma}$ out of $\boldsymbol{\gamma} = \rho\mathbf{b}$ is the gravitational acceleration. With the Cauchy theorem $\mathbf{t} = \boldsymbol{\sigma}\mathbf{n}$ and the Gauss integration theorem the boundary integral is converted into a volume integral. Furthermore, the local balance of mass is used and with the fact that \mathcal{P} is not a function of the time, the limit $dV \rightarrow 0$ results in the local form of the balance of linear momentum

$$\operatorname{Div} \mathbf{P} + \boldsymbol{\gamma}_0 = \rho_0 \dot{\mathbf{v}} \quad \text{and} \quad \operatorname{div} \boldsymbol{\sigma} + \boldsymbol{\gamma} = \rho \dot{\mathbf{v}} , \quad (2.36)$$

again in the dual Lagrangian and Eulerian formats.

2.1.3.3. Balance of Angular Momentum. This axiom states that the change in time of the angular momentum of the part $\mathcal{P} \subset \mathcal{B}$ with regard to the origin o is equal to the resultant moment $\mathbf{M}_{\mathcal{P}}^o$ acting on \mathcal{P} with respect to o

$$\frac{d}{dt}\mathbf{D}_{\mathcal{P}}^o = \mathbf{M}_{\mathcal{P}}^o \quad (2.37)$$

in terms of the angular momentum and the definition of the moment $\mathbf{M}_{\mathcal{P}}^o$, composed in a surface and a volume part,

$$\mathbf{D}_{\mathcal{P}}^o = \int_{\mathcal{P}} \mathbf{x} \times \mathbf{v}(\mathbf{x}, t) dm. \quad \text{and} \quad \mathbf{M}_{\mathcal{P}}^o = \int_{\partial\mathcal{P}} \mathbf{x} \times \mathbf{t} da + \int_{\mathcal{P}} \mathbf{x} \times \rho \mathbf{b} dv . \quad (2.38)$$

Application of the local balance of mass, the local balance of linear momentum, the Cauchy, Gauss and localization theorem yields the local forms of the balance of angular momentum

$$\mathbf{S} = \mathbf{S}^T \quad \text{and} \quad \boldsymbol{\sigma} = \boldsymbol{\sigma}^T, \quad (2.39)$$

which claims the symmetry of the second Piola-Kirchhoff stress tensor \mathbf{S} and the Cauchy stress tensor $\boldsymbol{\sigma}$. The latter demands the symmetry of the Kirchhoff stress tensor $\boldsymbol{\tau} = \boldsymbol{\tau}^T$. Note, that this symmetry property does not hold for the first Piola-Kirchhoff stress tensor \mathbf{P} .

2.1.3.4. Balance of Energy. First Axiom of Thermodynamics. The total energy $E_{\mathcal{P}}$ of a part $\mathcal{P} \subset \mathcal{B}$

$$E_{\mathcal{P}} = \int_{\mathcal{P}} \rho e \, dv = \int_{\mathcal{P}} \frac{1}{2} \rho \mathbf{v} \cdot \mathbf{v} \, dv + \int_{\mathcal{P}} \rho u \, dv = K + U \quad (2.40)$$

is defined in terms of the specific energy e per unit mass and can be split in a kinetic part K and a potential part U with the specific internal energy u per unit mass. Restriction to thermo-mechanical problems means, that temporal change of the energy is identical to the sum of external mechanical and thermal power

$$\frac{d}{dt} (K + U) = \mathcal{P}_{\mathcal{P}} + \mathcal{Q}_{\mathcal{P}}, \quad (2.41)$$

which is also named the global balance of energy or the first axiom of thermodynamics. Herein, the external mechanical power as well as the external thermal power

$$\mathcal{P}_{\mathcal{P}} = \int_{\mathcal{P}} \mathbf{v} \cdot \boldsymbol{\gamma} \, dv + \int_{\partial \mathcal{P}_t} \mathbf{v} \cdot \mathbf{t} \, da \quad \text{and} \quad \mathcal{Q}_{\mathcal{P}} = \int_{\mathcal{P}} \rho r \, dv + \int_{\partial \mathcal{P}_h} -q_n \, da \quad (2.42)$$

consist of a volume and a surface term. r is the heat supply and $q_n = \mathbf{q} \cdot \mathbf{n}$ the heat flux with the heat flux vector \mathbf{q} , see Figure 2.3. With these definitions at hand, a local balance of energy can be derived. Application of the Cauchy theorem, the local balance of angular momentum and the Gauss integration theorem are necessary to reformulate both the mechanical and the thermal surface terms. The localization theorem finally yields

$$\rho_0 \dot{e} = \text{Div} [\mathbf{v} \mathbf{P} - \mathbf{Q}] + \mathbf{v} \cdot \boldsymbol{\gamma}_0 + \rho_0 r \quad \text{and} \quad \rho \dot{e} = \text{div} [\mathbf{v} \cdot \boldsymbol{\sigma} - \mathbf{q}] + \mathbf{v} \cdot \boldsymbol{\gamma} + \rho r. \quad (2.43)$$

Substituting the balance of mass and linear momentum, the energy balance boils down to the dual local forms of the balance of internal energy

$$\rho_0 \dot{u} = \rho_0 r - \text{div} [\mathbf{Q}] + \mathbf{P} : \mathbf{g} \dot{\mathbf{F}} \quad \text{and} \quad \rho \dot{u} = \rho r - \text{div} [\mathbf{q}] + \boldsymbol{\sigma} : \mathbf{g} \nabla_x \mathbf{v} \quad (2.44)$$

With this balance at hand, the local energy balance reduces to the local form of the balance of the kinetic energy

$$\frac{d}{dt} \left(\frac{1}{2} \rho \mathbf{v} \cdot \mathbf{v} \right) = \mathbf{v} \cdot \text{div} \boldsymbol{\sigma} + \mathbf{v} \cdot \boldsymbol{\gamma}, \quad (2.45)$$

corresponding to the balance of linear momentum. By consideration of the corresponding global balances of internal and kinetic energy

$$\frac{d}{dt} U = \mathcal{Q}_{\mathcal{P}} + \int_{\mathcal{B}} \boldsymbol{\sigma} : \mathbf{g} \nabla_x \mathbf{v} \, dv \quad \text{and} \quad \frac{d}{dt} K = \mathcal{P}_{\mathcal{P}} - \int_{\mathcal{B}} \boldsymbol{\sigma} : \mathbf{g} \nabla_x \mathbf{v} \, dv \quad (2.46)$$

it is clear, that neither the internal energy nor the kinetic one are conservation quantities due to the production term $\int_{\mathcal{B}} \boldsymbol{\sigma} : \mathbf{g} \nabla_x \mathbf{v} \, dV$, referred to as the stress power. The velocity gradient $\mathbf{g} \nabla_x \mathbf{v} = \mathbf{gl}$ can be replaced by the symmetric rate of deformation $\mathbf{d} = \frac{1}{2}(\mathbf{gl} + \mathbf{l}^T \mathbf{g})$ due to the Cauchy stress being symmetric. Nevertheless, the balance of total energy is fulfilled, as the temporal change of the kinetic energy is equal to the mechanical power *minus* the stress power and the temporal change of the internal energy is equal to the thermal power *plus* the stress power.

2.1.3.5. Balance of Entropy. Second Axiom of Thermodynamics. Entropy is a state variable which measures microscopic randomness and disorder and determines the direction of a thermodynamical process. It is defined in terms of the specific entropy η per unit mass

$$H = \int_{\mathcal{P}} \rho \eta \, dv . \quad (2.47)$$

The total entropy production $\Gamma = \int_{\mathcal{B}} \rho \gamma \, dv$ depends on the entropy production γ per unit mass and time as difference between the temporal change of the entropy and the rate of entropy input \mathcal{Q} , with

$$\mathcal{Q} = \int_{\mathcal{P}} \rho \frac{\tilde{r}}{\theta} \, dv - \int_{\partial \mathcal{P}_h} \frac{1}{\theta} \mathbf{q} \cdot \mathbf{n} \, da . \quad (2.48)$$

The second law of thermodynamics states that the entropy production is always positive, i.e.

$$\Gamma = \frac{d}{dt} H - \mathcal{Q} \geq 0 , \quad (2.49)$$

which can be interpreted as the global form of the balance of entropy. Without any entropy production, $\Gamma = 0$, the thermodynamical process is reversible whereas in an irreversible process energy dissipates. The rate of entropy input is the external thermal power written in terms of entropy sources and fluxes instead of heat sources and fluxes. A relation of the entropy sources $\tilde{r} = r/\theta$ and the entropy fluxes $\tilde{q} = q_n/\theta$ to the heat sources r and the heat fluxes q_n is given through the temperature θ . With these definitions at hand and with the local form of the balance of energy, the local material and spatial forms of the so-called Clausius-Duhem inequality read

$$\begin{aligned} \rho_0 \gamma &= \rho_0 \dot{\eta} - \rho_0 \frac{\tilde{r}}{\theta} + \frac{1}{\theta} \text{Div} \mathbf{Q} - \frac{1}{\theta^2} \mathbf{Q} \cdot \nabla_X \theta \geq 0 \\ \rho \gamma &= \rho \dot{\eta} - \rho \frac{\tilde{r}}{\theta} + \frac{1}{\theta} \text{div} \mathbf{q} - \frac{1}{\theta^2} \mathbf{q} \cdot \nabla_x \theta \geq 0 . \end{aligned} \quad (2.50)$$

Via a Legendre transformation the Helmholtz free energy Ψ per unit mass is defined as $\Psi = u - \theta \eta$, which yields the alternative representation of the Clausius-Duhem inequality

$$\begin{aligned} \rho_0 \theta \gamma &= \mathbf{gP} : \dot{\mathbf{F}} - \rho_0 \dot{\Psi} - \rho_0 \dot{\theta} \eta - \frac{1}{\theta} \mathbf{Q} \cdot \nabla_X \theta \geq 0 \\ \rho \theta \gamma &= \boldsymbol{\sigma} : \mathbf{g} \nabla_x \mathbf{v} - \rho \dot{\Psi} - \rho \dot{\theta} \eta - \frac{1}{\theta} \mathbf{q} \cdot \nabla_x \theta \geq 0 . \end{aligned} \quad (2.51)$$

With the mechanical dissipation $\mathcal{D} = \theta \gamma$ the Clausius-Duhem inequality for isothermal processes reduces to the so-called Clausius-Planck inequality

$$\rho_0 \mathcal{D} = \mathbf{gP} : \dot{\mathbf{F}} - \rho_0 \dot{\Psi} \geq 0 \quad \text{and} \quad \rho \mathcal{D} = \boldsymbol{\sigma} : \mathbf{g} \nabla_x \mathbf{v} - \rho \dot{\Psi} \geq 0 . \quad (2.52)$$

2.1.4. Modeling of Standard Dissipative Materials. Many materials are characterized by an inelastic material behavior represented by a nonlinear relation between stresses and strains. The so-called standard dissipative materials can be described mathematically by two scalar-valued tensor functions. The Helmholtz free energy

$$\Psi = \Psi(\mathbf{F}, \mathbf{\Omega}) \quad (2.53)$$

depends on the deformation gradient \mathbf{F} and a set of internal variables $\mathbf{\Omega}$, characterizing the internal state of the material, as for instance the plastic deformation gradient or variables describing hardening effects. By means of the dissipation inequality (2.52)₁ and the so-called Coleman's exploitation method, this ansatz for the free energy governs the constitutive function for the first Piola-Kirchhoff stress tensor

$$\mathbf{gP} := \rho_0 \partial_{\mathbf{F}} \Psi \quad (2.54)$$

and yields with the definition of the internal forces $\mathfrak{P} := -\partial_{\mathbf{\Omega}} \Psi$ dual to the internal variables $\mathbf{\Omega}$ the reduced dissipation inequality

$$\mathcal{D} = \mathfrak{P} : \dot{\mathbf{\Omega}} \geq 0 . \quad (2.55)$$

The dissipation function is assumed to depend on the internal variables and the flux of the internal variables, i.e.

$$\Phi = \Phi(\dot{\mathbf{\Omega}}, \mathbf{\Omega}) \quad (2.56)$$

and needs to be convex and homogeneous of degree one with respect to the flux. This function determines the evolution of the internal variables by the well-known Biot equation of standard dissipative materials

$$\mathbf{0} \in \partial_{\mathbf{\Omega}} \Psi(\mathbf{F}, \mathbf{\Omega}) + \partial_{\dot{\mathbf{\Omega}}} \Phi(\dot{\mathbf{\Omega}}, \mathbf{\Omega}) . \quad (2.57)$$

The free energy and dissipation function determine the stress response of standard dissipative materials in a deformation-driven scenario.

With these phenomenological models an exact solution or the general trend with regard to the stress-strain response can be predicted. Nevertheless, there remain discrepancies for many materials as their response is critically determined by physical processes on lower length scales inside the material. Therefore, phenomenological models are often not sufficient. More advanced models take into account these microstructural effects of the material by means of so-called multiscale methods.

2.2. Modeling Aspects in Crystal Plasticity

Solids, fluids and structures can be considered at the engineering scale, called macroscale, as continuous bodies described successfully by the above discussed continuum mechanics. To gain a better understanding of the visible and measurable material response, in recent years more and more questions about meso-, micro-, nanostructural and atomistic effects appeared. Clearly, it is impossible to formulate a single macroscopic theory including all these effects. Effects on the macroscale are driven by microscopic effects taking place on the microstructure of the material. Advanced techniques are needed, which directly take into account effects of the material on a lower scale, called the microscale of the material. The scale bridging between the microstructure and the macroscopic response can be covered by homogenization methods entailing an increase in complexity and data storage.

Therefore, numerical efficient approaches both of microstructure modeling and linking the microstructural response to the macroscale need to be designed, related to computational multiscale models. Multiscale models are applied among others in processes in environmental and biomechanical, automotive and aircraft engineering and in the forming industry. Phenomena such as developing anisotropies, size effects or phase transitions on the macroscale need to take into account microstructural mechanisms. In metal plasticity effects on the atomistic scale, dislocation dynamics on the microscale, crystal plasticity simulations on the mesoscale and polycrystal simulations on the macroscale illustrated in Figure 2.5 need to be covered. Hierarchical top-down multiscale methods serve for a quantitatively accurate material modeling where micro mechanisms are directly incorporated in existing macroscopic models. An exact modeling of the micro mechanisms alleviate the understanding of the macroscopic behavior driven by these microscopic effects. A combination of a purely macroscopic model including micro mechanisms by scale bridging scenarios is called hybrid micro-macro modeling.

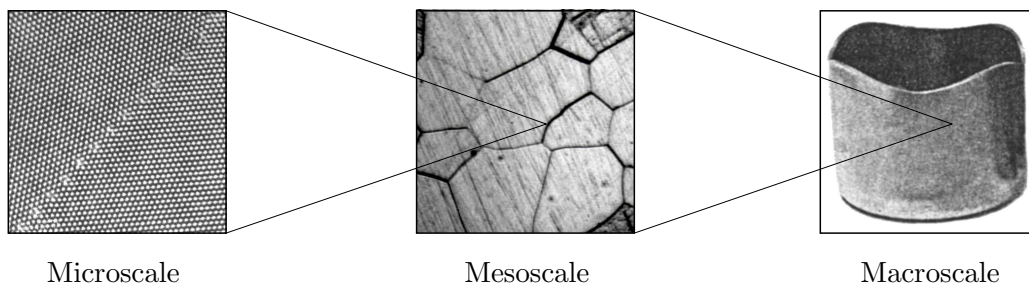


Figure 2.5: Micro-, meso- and macroscale. Dislocation movement on the micro-scale, grain interaction on the meso-scale and deep drawing on the macro-scale. (Sources of pictures: www-hrem.msm.cam.ac.uk [4], www.en.wikipedia.org [5], WILSON & BUTLER [143])

2.2.1. Hierarchical Methods for Textured Aggregates. Crystalline materials are characterized by grains of different orientation, shape and size. The distribution of grain orientations in polycrystalline materials is named crystallographic texture. Some fundamental aspects of polycrystalline materials are outlined in Section 3. During deformation preferred grain orientations develop which entail an overall anisotropic response of the polycrystalline material. For engineering applications it makes sense to rather simulate the texture and anisotropy development by means of computational models in order to avoid the enormous experimental costs. Furthermore, additional information of the polycrystalline materials, e.g. concerning dislocation density, energy storage or plastic strain, is provided by simulations which cannot or hardly be measured in experiments. The deformation of a polycrystalline material is a complex, heterogeneous process with moving dislocations which interact and accumulate at the grain boundaries. Thereby, the grains reorient and interact with neighboring grains. The arising local stresses and strains cause material hardening. Despite the local heterogeneity of the microstructure stress equilibrium and strain compatibility between the crystal grains need to be sustained. With regard to the modeling of texture and anisotropy at large plastic strains, homogenization models are developed describing the polycrystalline response by averaging the individual behavior of a collection of single crystals. With regard to the numerical treatment of multiscale methods in polycrystal plasticity, the finite element method is an indispensable tool. At each integration point a microstructure consisting of a discrete set of crystals is attached. Herefore, two main ingredients need to be specified:

- a certain micro-macro linking hypothesis, representing the chain between microscale and macroscale and
- a single crystal model, describing the microscopic material behavior including among others the number, size, shape and kind of crystals.

Note, that the number of crystals directly influences on the one hand the accuracy of the texture and on the other hand the computational effort, i.e. data storage and especially computation time.

With regard to the micro-macro linking hypothesis in 1928 Sachs proposed a polycrystalline model with homogeneous external stresses for all grains representing a lower bound for the stresses. Here, stress equilibrium is fulfilled, whereas strain compatibility is violated due to all crystals deforming independently. A homogenized global strain is obtained by an averaging over the grains. The deformation is often concentrated in some grains and only the most loaded slip system is activated. This results in partly wrong texture predictions and hence this model did not establish. In 1938, TAYLOR [134] suggested a polycrystalline model with homogeneous strains for all grains representing an upper bound for the strains. Contrarily to the Sachs model, strain compatibility is assured in the Taylor model, but stress equilibrium is violated. Averaging the stress over all grains gives a homogenized global stress

$$\bar{\mathbf{P}} = \frac{1}{V} \int_{\mathcal{B}} \mathbf{P} dV \approx \frac{1}{N} \sum_i^N \mathbf{P}_i . \quad (2.58)$$

For materials where the strength of many slip systems is comparable, the Taylor assumption yields reasonable results regarding the texture. Note, that the Sachs and Taylor models base on the elastic counterparts of Voigt (1910) and Reuss (1929). For arbitrary deformations with a large number of slip systems, Taylor-type models yield in general good results for fcc and bcc crystals. Therefore, it was applied by several authors such as e.g. ASARO & NEEDLEMAN [15], HARREN & ASARO [47], BRONKHORST, KALIDINDI & ANAND [33] and KUMAR & DAWSON [73]. It is well-known that such an approach tends to overpredict peak texture intensities and to shift the position of texture components, especially at large strains, see HARREN & ASARO [47] and BRONKHORST, KALIDINDI & ANAND [33], and in cases where experiments show evidence of inhomogeneous deformation inside grains, see MOLINARI, CANOVA & AZHI [100]. It yields an upper bound for the stiffness of the microstructure due to the rigorous kinematic constraint and provides good estimates for the macroscopic texture of fcc polycrystalline materials, see for instance MIEHE, SCHRÖDER & SCHOTTE [98], MIEHE, SCHOTTE & LAMBRECHT [96]. Nevertheless, the activation of too many slip systems, too sharp textures and the negligence of the volume, position and interaction of grains caused several authors to suggest modified Taylor models. Relaxed constraint models, discussed e.g. by HONNEF & MECKING [56], VAN HOUTTE [58], to name but a few, use a strain relaxation between grains, i.e. shear strains at the grain scale are allowed and not prescribed. In the so-called lath model, the shear component rolling-normal direction is not prescribed and in the pancake model, the one in transverse-normal direction. A change in the reorientation rate and hence the texture development is obtained by a relaxation of different strain components. This method is not appropriate for any arbitrary deformation state but for modes with flat or elongated grains resulting e.g. from plane compression modes. In order to take into

account the interaction between grains and the grain shape, self-consistent models in the small and large strain context were proposed, see for instance MOLINARI, CANOVA & AHZI [100], LEBENSOHN & TOMÉ [77], among others. Here, each crystal is treated as an elastic-plastic inclusion within a homogeneous elastic or an elastic-plastic matrix satisfying strain compatibility and stress equilibrium. Despite the higher accuracy, for each crystal a boundary value problem needs to be solved to compute the active slip systems which makes this method computationally expensive. Variations of the relaxed constraint and self-consistent models were proposed. For a detailed discussion, see the monographs MÜLLER [103], RISY [124] as well as the indicated literature, respectively. In HARREN & ASARO [47] the crystal grains are modeled by the elements of a finite element mesh, which was enhanced to three-dimensional problems and to the large strain context. Here, the crystalline aggregate is treated as continuum with stress equilibrium as well as strain compatibility being fulfilled automatically. E.g. MIEHE, SCHRÖDER & SCHOTTE [98, 97] and MIEHE [86, 87] attach to each material point a local microstructure, i.e. a representative volume element (RVE) with single crystal grains. By means of a finite element discretization of the RVE, with the grains assumed to be cubic, a volume average of the micro stresses relate the microscopic and macroscopic scales. Each finite element represents one crystal grain, whereas e.g. ACHARYA & BEAUDOIN [7] discretize one grain by several finite elements. KUMAR & DAWSON [75, 76] use Rodrigues parameters to describe the crystal orientations. By a finite element discretization of the Rodrigues space with each element representing a crystal orientation, a crystal orientation distribution function is calculated, being the link between microstructure and macrostructure. The finite element modeling of the microstructure is superior compared to Taylor-type models, due to the kinematic constraint of the Taylor models. Nevertheless, the computational effort of the so-called FE^2 ansatz is enormous when being applied in large-scale applications. Furthermore, the deformed meshes clearly show, that claiming a homogeneous deformation of the microstructure is a strong restriction.

2.2.2. Macroscopic Anisotropy Modeling of Textured Aggregates. The description of macroscopic anisotropy is based for most materials on the heterogeneous microstructure, which makes the modeling of the microstructure obvious for the simulation of macroscopic anisotropy. For polycrystalline materials the movement of dislocations on the microscale and the grain interaction on the mesoscale induce an anisotropic material behavior on the macroscale. Taking a polycrystalline material with initially isotropic distributed orientations, the preferred texture and the corresponding plastic anisotropy are caused by a defined pre-deformation such as the rolling to a flat sheet, which serves as input for a forming process, see Figure 2.6. This crystallographic texture is the main source of anisotropy, resulting e.g. in the appearance of ears within a deep drawing process. As is well-known, the amount of pre-texture, i.e. the degree of anisotropy, is directly related to the height of the ears, the thickness distribution and formability of a metal sheet. Several approaches exist for the modeling of macroscopic anisotropic material behavior induced by the crystalline microstructure, see e.g. the review articles of RAABE, ZHAO & ROTERS [119] and RAABE, KLOSE, ENGL, IMLAU, FRIEDEL & ROTERS [117]. Mainly, the approaches can be divided in two categories: anisotropic yield surfaces within a phenomenological ansatz and crystallographic texture models.

Anisotropic yield surface formulations date back to MISES [99] for the anisotropy description of single crystals. His quadratic yield criterion corresponds to the orthotropic yield

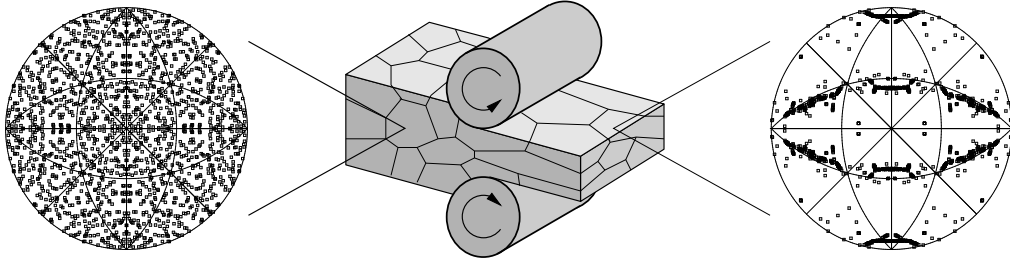


Figure 2.6: Rolling of an initial isotropic polycrystalline material yields grains with preferred orientations accounting for earing development in deep drawing processes.

function of the generalized yield criterion proposed by HILL [50] in the form

$$2f = F(\sigma_{yy} - \sigma_{zz})^2 + G(\sigma_{yy} - \sigma_{xx})^2 + H(\sigma_{xx} - \sigma_{yy})^2 + 2L\sigma_{yz}^2 + 2M\sigma_{zx}^2 + 2N\sigma_{xy}^2 = 1. \quad (2.59)$$

Herein, $\{\sigma_{ij}\}_{i,j=x,y,z}$ represent the stresses and the set of parameters $\{F, G, H, L, M, N\}$ characterizes the anisotropy. Main drawback of the Hill criterion is that certain effects cannot be modeled due to its particular quadratic form. For instance the simulation of six ears, resulting either from the pre-production process or the type of material of a metal sheet, is not possible. However, many commercially processed metal sheets exhibit four ears, which can be modeled with the quadratic Hill criterion. In HABRAKEN [46] and BANABIC [19] a detailed description of advanced yield criteria can be found. Phenomenological yield surfaces have several advantages, such as the simplicity with regard to their interpretation and implementation, the computational efficiency and the availability in several commercial software packages. They yield in general reasonable results, especially for moderate strains. In empirical or phenomenological yield surface approaches, the anisotropy coefficients in (2.59) are determined by simple mechanical tests such as the calculation of the so-called Lankford coefficient. The Lankford coefficient is a measure for the planar sheet anisotropy. It can be measured by uniaxial tension tests relating the strains in width and thickness direction, which is correlated to the drawability of a sheet. Another possibility is the formulation of anisotropic yield surfaces based on texture data, see e.g. KOCKS, TOMÉ & WENK [69], VAN HOUTTE, MOLS, VAN BAELE & AERNOUDT [59]. Here, the anisotropy coefficients are calculated from experimentally obtained orientation distributions extracted from X-ray or electron diffraction. In contrast to empirical yield surfaces, six-dimensional yield loci can be obtained. Note, that the experimental determination of anisotropy coefficients takes additional time and is rather tedious. Recapitulatory, the main advantages of anisotropy incorporation by yield surfaces are short calculation times and robust results. Nevertheless, only an initial texture is accounted for, whereas a texture evolution is disregarded. The rotation of crystal grains induced by the crystal slip during the deformation, e.g. a forming process, influences the skew part of the velocity gradient. This results in an evolving texture and anisotropy by means of an expansion, contraction, translation and distortion of the yield surface, which needs to be accounted for.

The microstructural behavior can also be incorporated in the constitutive approach by crystallographic texture models. For the simulation of forming processes the finite element method is proved to be successful. Nevertheless, the accurate description of macroscopic anisotropy depends on the constitutive microscopic material law and an exact parameter identification. Taylor-type homogenization models use a finite element simulation with a discrete set of grain orientations at each integration point, which all undergo the

same deformation. Herein, texture, hardening and anisotropy evolve during the deformation process. Differences occur in the single crystal modeling. With this approach at hand, an accurate simulation of texture evolution during complex deformation processes is possible. This requires a large number of crystal orientations (internal variables) being directly related to the computation time. Otherwise, i.e. with a small number of crystal orientations, the macroscopic anisotropy is overestimated. For the modeling of the crystal orientation distribution functions, which models the texture effect of the microstructure, RAABE, ZHAO & ROTERS [119] suggest a so-called texture component crystal plasticity method. The motivation originates from the fact, that more texture information as necessary is obtained by experimental techniques, see Section 3.3.3, with regard to the modeling of plastic anisotropy. Furthermore, the macroscopic anisotropy should be described accurately with a small number of representative orientations. Each texture component is described by one discrete crystal orientation corresponding to a maximum in the crystal orientation distribution. This means that the small amount of representative orientation components reduces the computational effort enormously. The overestimation of the plastic anisotropy is in average reduced by RAABE & ROTERS [118] through a scattering of the crystallites around the ideal texture components. The idea bases on the isotropic or anisotropic decrease of the crystal orientation distribution function around the representative texture components modeled by a Gauss distribution. BÖHLKE, RISY & BERTRAM [29, 30] suggest two Taylor-type models to overcome the overestimation of anisotropy. In the continuous model the earing height is adopted by a varying half-width of the Mises-Fisher distribution, whereas in the discrete model the sharpness is reduced by means of an additional isotropic orientation distribution. An important step towards a manageable micro-macro theory of texture evolution is provided by BÖHLKE & BERTRAM [28] and BÖHLKE [25, 26] based on a tensorial Fourier approximation of the crystal orientation distribution function and its incorporation in the macroscopic yield criterion.

3. Fundamentals of Polycrystalline Materials

Before starting with the main development of this contribution, some fundamentals of polycrystalline materials are reviewed. Various materials, as metals for instance, possess a crystalline structure formed by a regular distribution of atoms or molecules, with the finite neighborhood of all atoms being identical. They exhibit completely different characteristics compared to so-called amorphous materials, as for instance fluids, glass or some polymers, e.g. with regard to fracture mechanisms. A crystal, i.e. an ideal crystalline structure, discussed in Section 3.1, can be abstractly described by a regular, three-dimensional space lattice. The corners of this space lattice pose the atoms. A single crystal is characterized by its orientation. This property of a distinctive orientation dependence makes a crystal a priori anisotropic, i.e. some physical properties are orientation dependent. For the determination of the orientation the arrangement of atoms is crucial. Crystallographic planes or directions are formed by layers or lines of closest packed atoms. The introduction of a notation for crystallographic planes and directions is necessary as loading of a material with a crystalline structure results in shearing on such planes. In the majority of materials found in nature the regular crystalline structure is discontinuous as the material features defects, see Section 3.2. The most important defects in crystals are dislocations, whose movement is caused by loading of a material and which yields slip on crystallographic planes. A real crystalline structure with dislocations is inhomogeneous and the orientations of neighboring crystals differ. Regions with the same crystal orientation are called grains and are separated by so-called grain boundaries from each other. Therefore, a material consisting of several crystal grains is called polycrystalline. The distribution of those crystallographic orientations is named the texture of a polycrystalline material. The large amount of grains forming a polycrystalline material provides a statistically uniform contribution of crystal orientations. Under certain production processes, such as rolling, textures develop, i.e. the single crystals orient in a certain manner and an anisotropic behavior of the material evolves. Section 3.3 deals with the mathematical description and graphical representation of crystallographic textures. Several possibilities for the representation of crystal orientations exist. In this work mainly the representation by Rodrigues vectors is used. Following FRANK [42], this is a particular form of the representation by quaternions based on an axis-angle description. With regard to the graphical representation of crystallographic texture, a stereographic projection is needed for the visualization with pole figures. This visualization method is well-established in the literature and most suitable for the qualitative comparison with experimental results. Nevertheless, a representation of texture in the Rodrigues space is discussed as it is compared to simulation results of KUMAR & DAWSON [75]. Drawback of this texture representation is the direct or tedious experimental determination of Rodrigues vectors, see BECKER & PANCHANADEESWARAN [22]. The orientation distribution of a material can be described by continuous crystal orientation distribution functions (codf), introduced by BUNGE [35] and ROE [126]. It is a measurement for the volume fraction of crystals having a certain orientation. In contrast to pole figures, the visualization of crystal orientation distribution functions has the advantage of being a quantitative representation. The function can be approximated by a tensorial Fourier expansion where the coefficients of this expansion can be identified as homogenized quantities representing the crystallographic texture of the material. These evolving texture coefficients are used later in this contribution in order to describe the microscopic texture effect on the macroscopic behavior of the material. A lot of research is done on the subject of polycrystalline materials with regard to special

topics. In the following, some selected key literature is given, which, to the authors opinion, provides a comprehensive overview of this subject. For a more detailed discussion on the basic description of polycrystalline materials with a view to the crystalline structure see e.g. BARGEL & SCHULZE [20], ILSCHNER & SINGER [63] and TROOST [137]. Moreover the reader is referred for instance to BUERGER [34], JAGODZINSKI [64], RAAZ & TERTSCH [120] and KLEBER, BAUTSCH & BOHM [68] for an emphasis on symmetry properties of crystal structures. Several publications treat the stereographic projection, especially BARRETT & MASSALSKI [21]. A discussion on dislocations and plastic deformation in crystalline materials can be found in HULL & BACON [60], HONEYCOMBE [55], HOSFORD [57] or NEMAT NASSER [105]. An extended overview on texture is given among others in WASSERMANN & GREWEN [141], BUNGE [36] and KOCKS, TOMÉ & WENK [69]. With regard to the experimental techniques for the texture determination, the reader is referred to RANDLE & ENGLER [121] and SCHWARTZ, KUMAR, FIELD & ADAMS [128].

3.1. Ideal Crystalline Structure

3.1.1. Space Lattice Composition and Symmetry Properties. A regular lattice is obtained by an infinite repetition of a point in three non-coplanar directions, see Figure 3.1. Translations of a point \mathbf{x}_0 with $\{i\mathbf{a}\}_{i \in \mathbb{Z}}$, $\{j\mathbf{b}\}_{j \in \mathbb{Z}}$ and $\{k\mathbf{c}\}_{k \in \mathbb{Z}}$ gives the coordinates

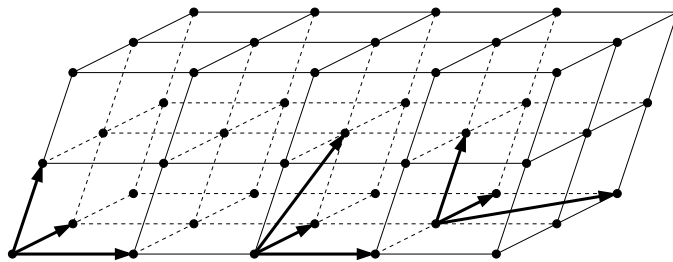


Figure 3.1: Regular space lattice. Different possibilities of linear independent translation vectors for the generation of the same lattice.

of the lattice points

$$\mathbf{x} = \mathbf{x}_0 + i\mathbf{a} + j\mathbf{b} + k\mathbf{c} \quad \text{with } i, j, k \in \mathbb{Z} \quad (3.1)$$

of a three-dimensional lattice. Here, \mathbf{a} , \mathbf{b} and \mathbf{c} are linear independent vectors and \mathbb{Z} is the set of all integers. As can be seen in Figure 3.1, there are different possibilities of linear independent translation vectors \mathbf{a} , \mathbf{b} and \mathbf{c} for the generation of the same lattice. An important characterization for space lattices are the symmetry properties of the lattice. Symmetry operations are translations, rotations around an axis, inversions with respect to a point, reflections with respect to a plane or a combination of two operations. A n -rotation symmetry exists if a rotation with $2\pi/n$ gives an equivalent arrangement, i.e.

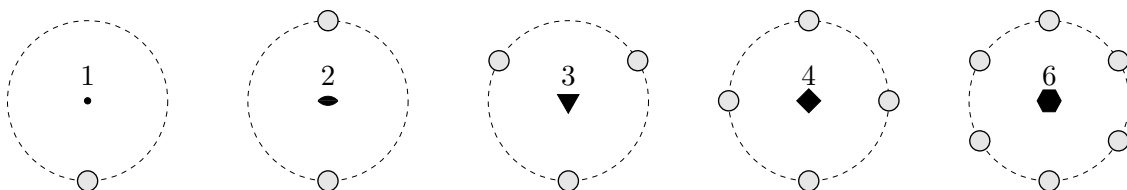


Figure 3.2: Space lattice symmetry. Rotation with $2\pi/n$ for $n \in \{1, 2, 3, 4, 6\}$ gives an equivalent arrangement, with the rotation axis normal to the drawing plane.

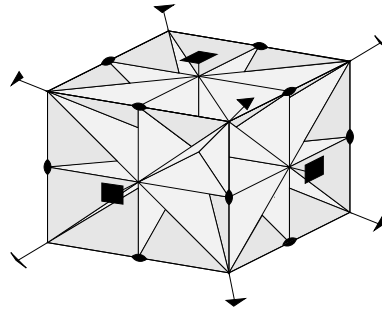


Figure 3.3: Space lattice symmetry. Rotation axis and mirroring planes of a cube taken from KLEBER, BAUTSCH & BOHM [68]. 4-fold rotation symmetry ■ for the six cube faces, 3-fold rotation symmetry ▼ for the eight long body diagonals and a 2-fold symmetry ● for the twelve short body diagonals.

all material properties remain unchanged. Common graphical symbols for rotation symmetry are shown in Figure 3.2. For a rectangular cube with equal side lengths the rotation symmetry axes and reflection planes are shown in Figure 3.3. A 4-fold rotation symmetry exists for the six cube faces, a 3-fold rotation symmetry for the eight long body diagonals and a 2-fold symmetry for the twelve short body diagonals. For the exact definition of a space lattice, one considers primitive unit cells as illustrated in Figure 3.4. By successive, periodic arrangement of such unit cells in three linear independent directions a regular space lattice, as depicted in Figure 3.1, is produced, where all unit cells are of the same size, shape and orientation. The unit cell is uniquely described by the three grid vectors \mathbf{a} , \mathbf{b} and \mathbf{c} or equivalently the grid constants a , b , c with corresponding angles α , β and γ for the lattice itself. These parameters define the size and shape of the unit cell formed as parallelepiped. For most of the metals a , b , c are in the range 0.25 – 0.5nm. With specific choices of the grid constants a , b , c and α , β , γ seven different types of unit cells can be defined:

- Triclinic cell: $a \neq b \neq c$, $\alpha \neq 90^\circ, \beta \neq 90^\circ, \gamma \neq 90^\circ$. $n = 1$.
- Monoclinic cell: $a \neq b \neq c$, $\alpha \neq 90^\circ, \beta = \gamma = 90^\circ$. $n = 2$.
- Orthorhombic cell: $a \neq b \neq c$, $\alpha = \beta = \gamma = 90^\circ$. $n = 2$.
- Tetragonal cell: $a = b \neq c$, $\alpha = \beta = \gamma = 90^\circ$. $n = 4$.
- Cubic cell: $a = b = c$, $\alpha = \beta = \gamma = 90^\circ$. $n = 4$.
- Trigonal cell: $a = b = c$, $\alpha = \beta = \gamma \neq 90^\circ$. $n = 3$.
- Hexagonal cell: $a = b \neq c$, $\alpha = \beta = 90^\circ, \gamma = 120^\circ$. $n = 6$.

For crystalline materials the cubic, tetragonal and hexagonal cells are the important ones.

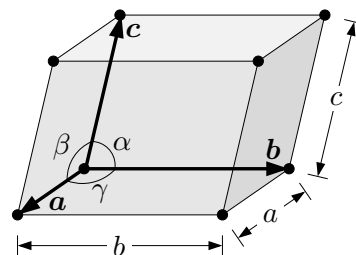


Figure 3.4: Primitive unit cell. The grid vectors \mathbf{a} , \mathbf{b} , \mathbf{c} or the grid parameters a , b , c and $\alpha \angle(\mathbf{b}, \mathbf{c})$, $\beta \angle(\mathbf{c}, \mathbf{a})$, $\gamma \angle(\mathbf{a}, \mathbf{b})$ characterize size and shape of the unit cell.

Primitive unit cells consist of eight atoms at the lattice points. The lattice point density of each unit cell is one, as one eighth of the volume of each atom belongs to a single unit cell. As mentioned above, there are several possibilities for a space lattice assembly with regard to the translation vectors. Hence, the election of a unit cell is also arbitrary. Preferential is an orthogonal unit cell with minimal volume under short base vectors with the same symmetry properties as the lattice itself. These preferences cause, that most unit cells are not primitive, i.e. they have additional atoms, see Figure 3.5 for a two-dimensional representation. The unit cell in Figure 3.5a) is orthogonal, of smallest area and the base

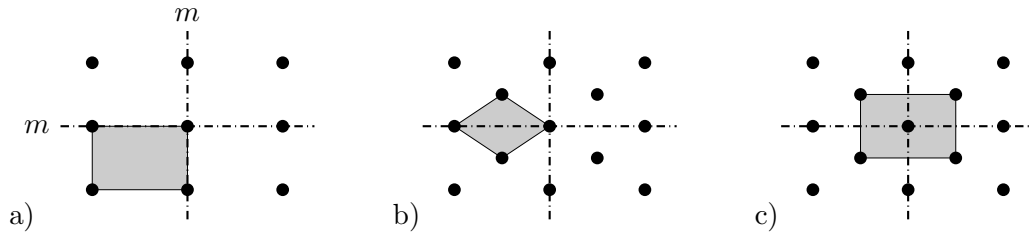


Figure 3.5: Unit cell. a) Primitive unit cell with the preferred properties of orthogonality, minimal volume under short base vectors and symmetry according to the lattice symmetry. b) Primitive unit cell with neither orthogonal axis nor symmetry corresponding to the lattice symmetry. Therefore, c) a centered unit cell with additional atom in the center is preferred.

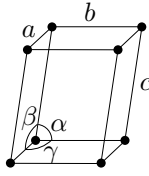
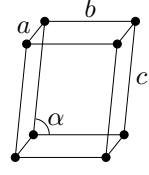
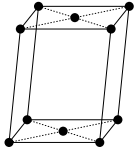
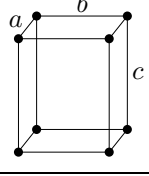
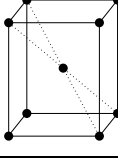
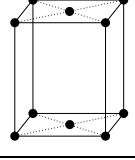
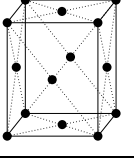
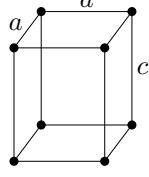
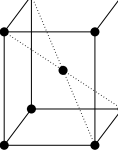
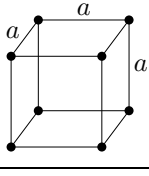
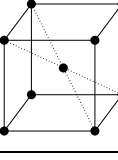
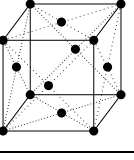
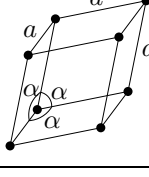
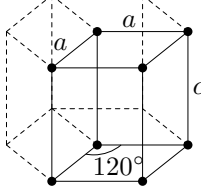
vectors coincide with symmetry axes of the lattice resulting in a primitive unit cell. The symmetry does not change in Figure 3.5b), but for a unit cell with smallest area the base vectors are not orthogonal. Therefore, a unit cell according to Figure 3.5c) is favored due to the higher symmetry and the orthogonal base vectors although it contains more lattice points. Additional atoms in the center of either the faces or the body give face-centered, body-centered or base-centered cells. The seven primitive unit cells are supplemented with the seven centered unit cells to the so-called 14 Bravais cells according to BRAVAIS [32]. They are summarized in Table 3.1.

3.1.2. Miller Indices. Crystallographic Planes and Directions. As the grid constants a , b and c are in general not equal, the distance between the atoms differ for the primitive as well as for the so-called centered unit cells. For the face-centered cell the body diagonal is the largest distance, whereas the face diagonal is the smallest and for the body-centered cell it is the other way round. This results in the evolution of so-called crystallographic planes and directions. For the indication of the crystallographic directions as well as the crystallographic planes in a characteristic coordinate system so-called Miller indices are used. A crystallographic plane is uniquely defined by three points, e.g. the three intersections A , B and C with the coordinate axes corresponding to the grid triad, see Figure 3.6a). As introduced above \mathbf{a} , \mathbf{b} and \mathbf{c} are the known vectors characterizing the unit cell. Hence, the components m , n and p are enough for the characterization of the crystallographic plane. The Miller indices

$$(hkl) = \left(\frac{N}{m} \frac{N}{n} \frac{N}{p} \right) \quad (3.2)$$

can be computed with N being the common denominator of the values $\frac{1}{m}$, $\frac{1}{n}$ and $\frac{1}{p}$. For the crystallographic planes the Miller indices (hkl) are written in round brackets and in curly brackets $\{hkl\}$ for a set of crystallographic planes, see Table 3.2. E.g. the crystallographic planes (100) , (010) , (001) , $(\bar{1}00)$, $(0\bar{1}0)$ and $(00\bar{1})$ can be summarized by the set $\{100\}$

Table 3.1: The 14 Bravais unit cells according to BRAVAIS [32].

unit cell	primitive	body-centered	base-centered	face-centered
triclinic				
monoclinic				
orthorhombic				
tetragonal				
cubic				
trigonal				
hexagonal				

of crystallographic planes which is useful for equivalent planes due to symmetry. Herein, negative coordinates are marked by a bar. In addition to planes, Miller indices are used for the indication of directions, see Figure 3.6b). Here, the Miller indices

$$[uvw] = [NrNsNt] \quad (3.3)$$

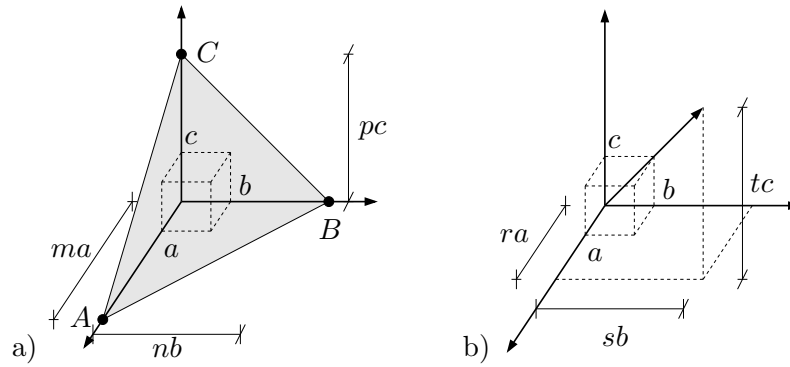


Figure 3.6: Miller indices. a) Specification of a plane (hkl) and b) description of a direction $[uvw]$ by means of Miller indices.

are obtained by multiplication of the coefficients r , s and t characterizing the crystallographic direction with the smallest common factor N . Respectively, for directions the

Table 3.2: Equivalent crystallographic directions and planes in the cubic lattice.

	set	elements
direction	$\langle 100 \rangle$	$[100]$, $[010]$, $[001]$, $[\bar{1}00]$, $[0\bar{1}0]$, $[00\bar{1}]$
plane	$\{100\}$	(100) , (010) , (001) , $(\bar{1}00)$, $(0\bar{1}0)$, $(00\bar{1})$
direction	$\langle 110 \rangle$	$[011]$, $[101]$, $[110]$, $[0\bar{1}1]$, $[\bar{1}01]$, $[\bar{1}10]$, $[0\bar{1}\bar{1}]$, $[\bar{1}0\bar{1}]$, $[\bar{1}\bar{1}0]$, $[01\bar{1}]$, $[10\bar{1}]$, $[1\bar{1}0]$
plane	$\{110\}$	(011) , (101) , (110) , $(0\bar{1}1)$, $(\bar{1}01)$, $(\bar{1}10)$, $(0\bar{1}\bar{1})$, $(\bar{1}0\bar{1})$, $(\bar{1}\bar{1}0)$, $(01\bar{1})$, $(10\bar{1})$, $(1\bar{1}0)$
direction	$\langle 111 \rangle$	$[111]$, $[\bar{1}11]$, $[1\bar{1}1]$, $[11\bar{1}]$, $[\bar{1}\bar{1}\bar{1}]$, $[1\bar{1}\bar{1}]$, $[\bar{1}1\bar{1}]$, $[\bar{1}\bar{1}1]$
plane	$\{111\}$	(111) , $(\bar{1}11)$, $(1\bar{1}1)$, $(11\bar{1})$, $(\bar{1}\bar{1}\bar{1})$, $(1\bar{1}\bar{1})$, $(\bar{1}1\bar{1})$, $(\bar{1}\bar{1}1)$

Miller indices $[uvw]$ are written in square brackets, whereas for a set of directions $\langle uvw \rangle$ angle brackets are used. Equivalent planes/directions are listed in Table 3.2 and selected planes/directions are illustrated in Figure 3.7 for a cubic lattice with the corresponding Miller indices. Miller indices specify equivalent planes and directions relative to the crystal axes without giving the position with respect to a global origin. In Figure 3.8 packed

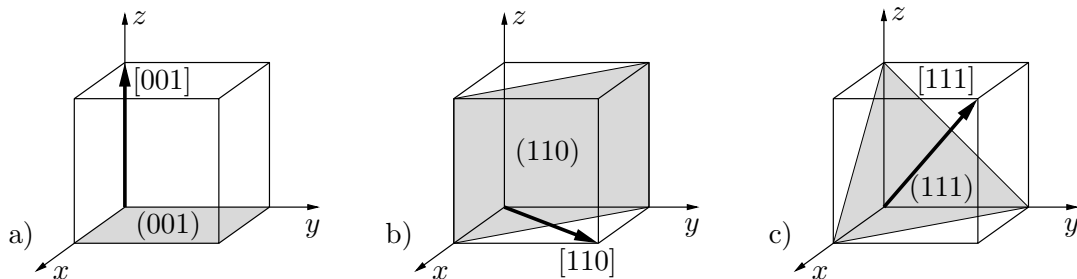


Figure 3.7: Crystallographic planes and directions in the cubic lattice. Selected directions $[001]$, $[110]$, $[111]$ and equivalent planes (001) , (110) , (111) can be described by the sets $\langle 100 \rangle$, $\langle 110 \rangle$, $\langle 111 \rangle$ and $\{100\}$, $\{110\}$, $\{111\}$, for directions and planes, respectively.

cubic primitive, face centered cubic and body centered cubic unit cells and corresponding closest packed planes are shown. The packing density in percent can be calculated by the ratio of the volume of atoms within the unit cell with respect to the volume of the unit

cell itself. Alternatively, the ratio of the area of atoms within a crystallographic plane with respect to the area of the crystallographic plane itself gives the packing density. As for the primitive cells the packing density is very low and hence the structure is unstable, most materials form face centered cubic (fcc) or body centered cubic (bcc) cells. Materials for face centered cubic, body centered cubic or hexagonal closest packed cells (not further considered) are

- face centered cubic (fcc): Al, Cu, Ni, Ag, Pt, Au, Pb, γ -Fe
- body centered cubic (bcc): Na, Li, Cr, Nb, Ta, W, α -Fe, Mo, β -Ti
- hexagonal closest packed (hcp): Mg, Be, Zr, Co, Zn, Cd, α -Ti .

Plastic slip mainly occurs in the direction of highest packing density within the closest packed crystal plane. For the cubic primitive cell these directions are $\langle 100 \rangle$, for the body centered cubic cell $\langle 111 \rangle$ and for the face centered cubic cell $\langle 110 \rangle$. These closest packed planes are arranged in a certain manner, called stacking order, see Figure 3.8. For a cubic

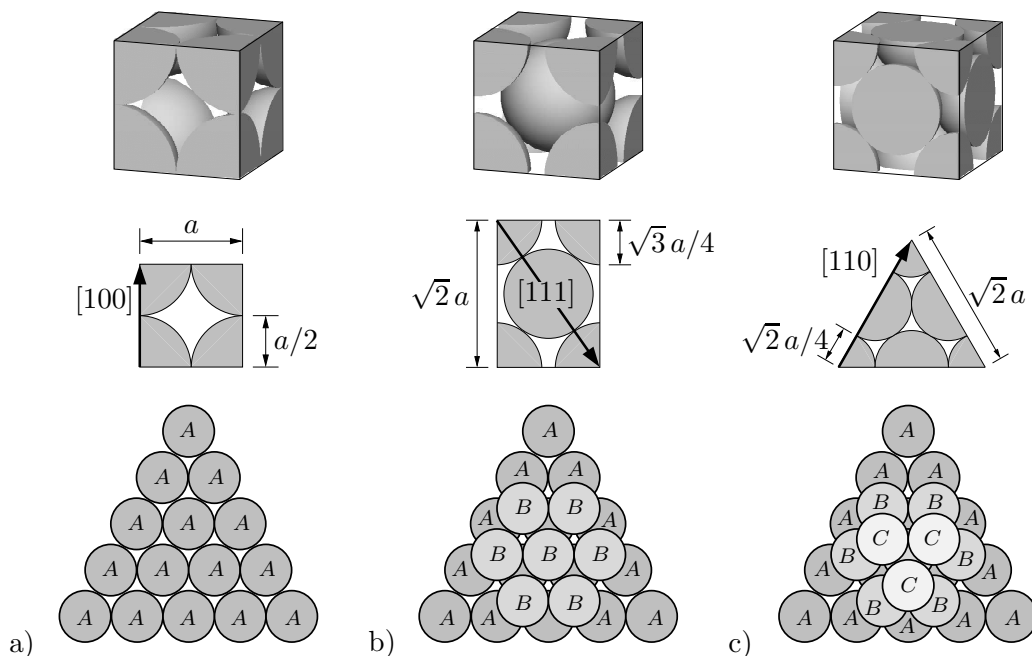


Figure 3.8: Packed unit cells, closest packed planes and stacking order of closest packed planes. Packing density for a) cubic primitive cells is 52%(79%), b) for body centered cubic cells 68%(83%) and c) for face centered cells 74%(91%) based on volume (area) ratios. Closest packed planes play a crucial role for the slip within a crystal lattice.

primitive arrangement the atoms of two closest packed atom rows A lie on top of each other indicated by the stacking order $AA \dots$. Here, the structure can be sheared off relatively easy. In the bcc arrangement the atoms of each second closest packed atom row B are shifted with respect to the other atom rows A . Hence, the stacking order is $ABAB \dots$. For the fcc arrangement the stacking order is $ABCABC \dots$.

3.2. Real Crystalline Structure

In contrast to ideal crystal structures considered so far, in real crystal structures several types of imperfections may appear. In this contribution, structural imperfections such as deviations from the ideal crystal lattice are considered.

3.2.1. Defects in Crystalline Materials. One differentiates between 0-dimensional point defects, 1-dimensional line defects, 2-dimensional surface defects and 3-dimensional volume defects. Possible point defects are shown in Figure 3.9. Intrinsic point defects are

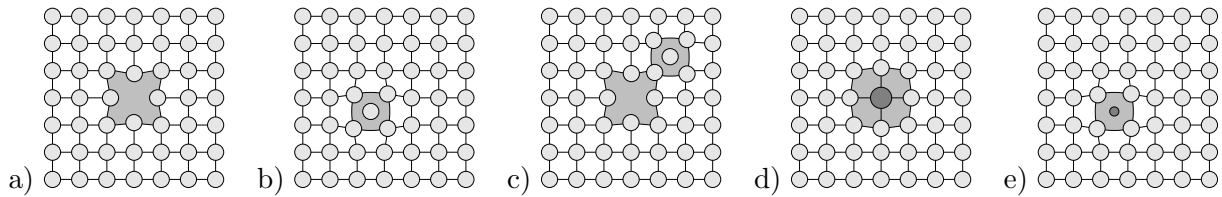


Figure 3.9: Point defects. Intrinsic defects such as a) vacancies, b) interstitial atoms or c) Frenkel pairs and extrinsic defects such as d) substitutional or e) interstitial impurity atom.

e.g. vacancies or interstitial atoms, leaving their regular place and accumulating somewhere in-between the lattice. The amount of voids increases with temperature and is about 10^{-12} at room temperature, implying one void for one billion lattice points or 1mm^2 lattice area. A combination of a close lying pair of vacancy and interstitial atom is called Frenkel pair. Extrinsic point defects are substitutional or interstitial impurity atoms, which are atoms of a different type or size replacing a regular atom or occupying a place in-between the lattice, respectively. Line defects, called dislocations, are the most important defects and will be discussed in detail in Section 3.2.2. Surface defects are grain boundaries, phase boundaries, twin boundaries or stacking faults, shown in Figure 3.10. A

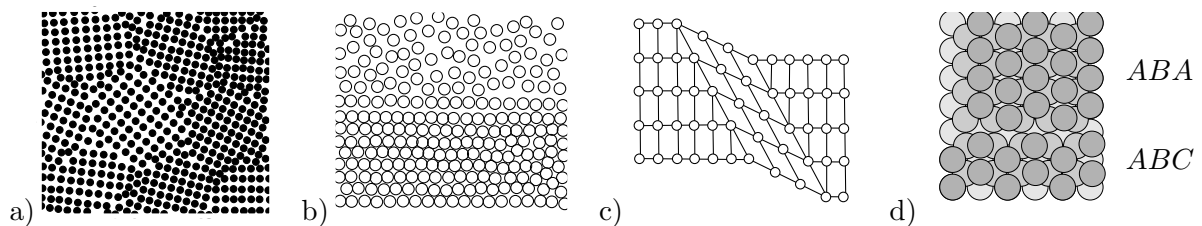


Figure 3.10: Surface defects. a) Grain boundary, b) phase boundary consisting of a solid and a liquid phase, c) twin boundary and d) stacking fault.

real material consists of a large amount of single crystals where the characteristic orientations of all unit cells vary and hence grain boundaries occur if the orientation of a grain is rotated with respect to neighboring grains. One distinguishes between small angle grain boundaries and large angle grain boundaries. The length and motion of dislocations is limited by grain boundaries and hence, a material with smaller grains is stiffer due to the larger grain boundary surface area. Phase boundaries are interfaces between two separate phases. Twin boundaries appear if two crystals reflect or mirror at a grain boundary. A stacking fault is an interruption in the stacking sequence. Finally, volume defects are voids or precipitates. Voids occur, if a larger number of atoms is missing within a certain region resulting from the production process. Precipitates are several impurity atoms of a different phase forming a small region.

3.2.2. Dislocations. The shearing of crystallographic glide planes is micromechanically motivated by the movement of dislocations through the crystal. Dislocations appear by growth or due to local deformations. There are two types of dislocations: edge dislocations and screw dislocations, illustrated in Figure 3.11. Edge dislocations are lattice planes ending within the crystal, whereas screw dislocations are spiral-like shifted lattice planes. In

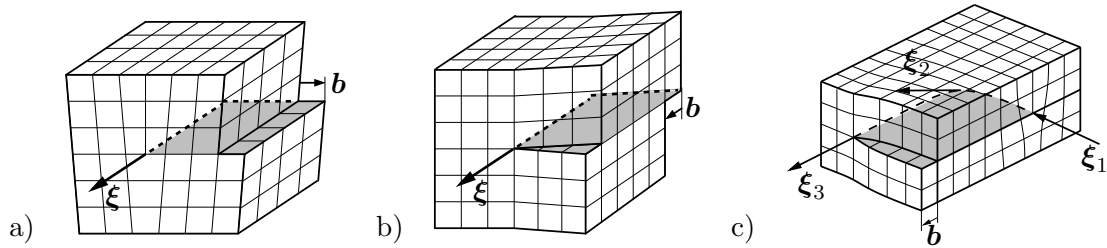


Figure 3.11: Line defects - dislocations. a) Pure edge dislocation, b) pure screw dislocation and c) mixed dislocation.

addition a combination of both exists. Either the dislocations start and end at the boundary of the crystal or they form a closed line within the crystal. The dislocation density is measured as dislocation length per volume. For soft-annealed and cold-rolled metals it ranges from $10^8/\text{cm}^2$ to $10^{12}/\text{cm}^2$, respectively. From a thermodynamical perspective a certain amount of derangement is required. This induces, that crystals intrinsically include point defects in order to fulfill the thermodynamical balance. By occurrence of dislocations, however, the energetic state of the lattice is raised and hence, there is never a thermodynamical balance in a real crystal with dislocations. Therefore, the effort of dislocation movement through the crystal is comparatively small resulting in a good plastic deformability of metals. In the following subchapters some characteristics of dislocations are summarized.

3.2.2.1. Dislocation Movement. Shear stresses cause glide deformations on crystallographic planes. A reversible elastic deformation with changing lattice angle results from small shear stresses, whereas an irreversible plastic deformation occurs above a critical shear stress. Here, an atom within a certain lattice plane gets into the field of the next atom within a neighboring lattice plane whereby crystallographic glide planes develop. By reversal of the elastic strains, the geometrical form of the lattice is similar to the initial lattice, but the upper atom row moves about one lattice point, see Figure 3.12 for a visualization. In 1926 FRENKEL [43] calculated stresses necessary for plastic deformations.

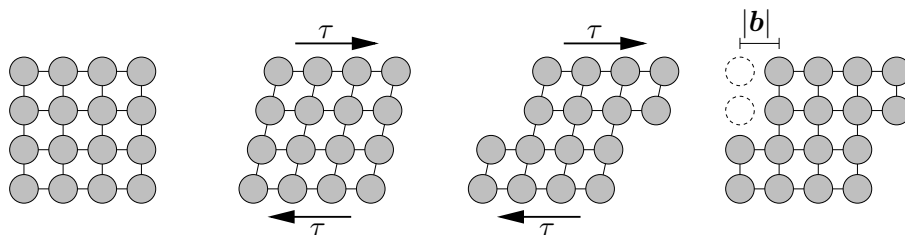


Figure 3.12: Sliding of crystallographic planes. Sliding about one atom interval occurs after reaching a critical shear stress.

But as the theoretical limit was higher than in the experimental observations, the idea of an ideal crystal structure was clear to be wrong. OROWAN [108], POLANYI [113] and TAYLOR [133] independently suggested a concept for the movement of dislocations, visualized in Figure 3.13. Herein, the symbol \perp represents the dislocation line corresponding to the ξ axis in Figure 3.11. A dislocation enters an ideal structure under a shear loading and moves consecutively through the crystal structure. This results in the same configuration as in Figure 3.12, but the necessary stresses are much lower. As mentioned above, the dislocation line is a closed curve or it moves until it reaches the grain boundary and a slip

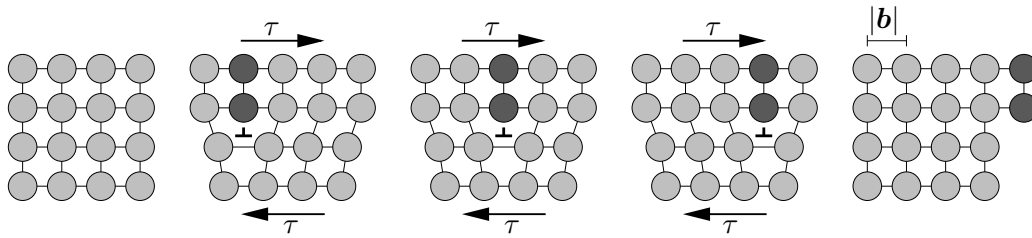


Figure 3.13: Dislocation movement. Dislocation enters an ideal structure under a shear loading and moves through the crystal structure. Elastic deformation is neglected.

step with the length $|\mathbf{b}|$ of the so-called Burgers vector, see Section 3.2.2.2, is microscopically visible. The dislocation movement with regard to an edge and screw dislocation is shown in Figure 3.14. The shear stress τ causes a force F perpendicular to the dislocation

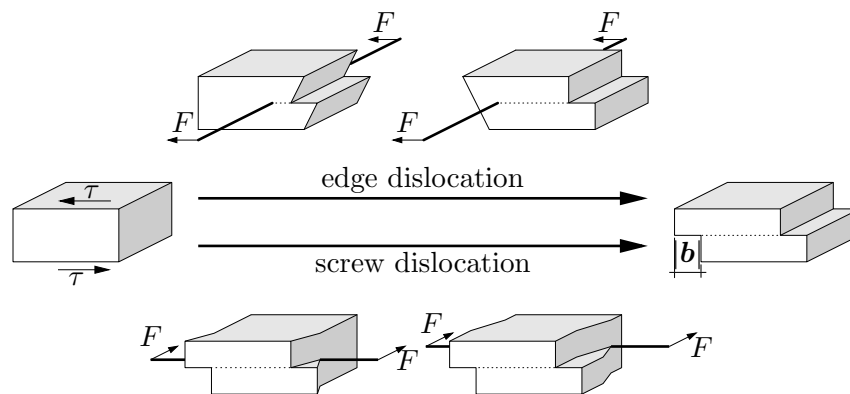


Figure 3.14: Dislocation movement of edge and screw dislocation.

line in the direction of the Burgers vector, driving the dislocation line through the material in the case of an edge dislocation. An edge dislocation is characterized by a unique slip plane spanned by the Burgers vector \mathbf{b} and the dislocation line axis $\boldsymbol{\xi}$, illustrated in Figure 3.11. Reaching the boundary the length $|\mathbf{b}|$ of the Burgers vector is visible, as explained above. If the dislocation meets a barrier such as an interstitial atom or another dislocation line, it changes to a parallel glide plane, called climbing. For a screw dislocation the two parts glide in the direction of the shear stress, which causes a force F perpendicular to the dislocation line. The result is the same as for an edge dislocation as it only depends on the Burgers vector and not on the type of dislocation. Reaching a barrier, the screw dislocation changes its direction, called cross gliding. This is due to the fact, that the Burgers vector and the dislocation line axis point in the same direction and do not span a unique slip plane. A mixed dislocation can always be decomposed into an edge and a screw dislocation by splitting the Burgers vector in a part perpendicular and parallel to the dislocation line axis. If a dislocation forms a closed line within the crystal it is called dislocation loop.

3.2.2.2. Burgers Vector. The Burgers vector \mathbf{b} , already introduced above, characterizes the direction and size of a lattice distortion caused by a dislocation. For the determination of the Burgers vector a closed circuit surrounding a dislocation in a real crystal is run in discrete steps from lattice point to lattice point following the right hand rule. Taking the same path in an ideal, same orientated crystal without dislocation, the circuit does not close, see Figure 3.15. The vector required to close the circuit between end and starting point in the ideal crystal is called the Burgers vector. As the Burgers vector is defined in an

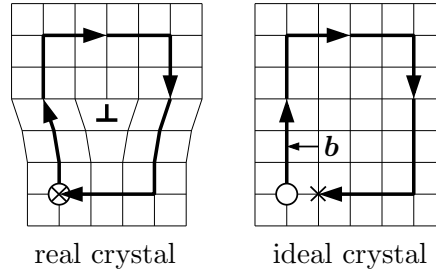


Figure 3.15: Definition of the Burgers vector. A closed circuit in a real crystal containing a dislocation does not close in an ideal crystal.

undistorted lattice, it is a vector with length of an interatomic spacing, which is common practice in most metallic materials. The Burgers vector \mathbf{b} lies in the crystallographic plane of closest packed atoms with $\mathbf{b} = \langle 100 \rangle$, $|\mathbf{b}| = a$ for primitive cells, $\mathbf{b} = \frac{1}{2} \langle 110 \rangle$, $|\mathbf{b}| = \frac{a}{\sqrt{2}}$ for fcc and $\mathbf{b} = \frac{1}{2} \langle 111 \rangle$, $|\mathbf{b}| = \frac{\sqrt{3}}{2}a$ for bcc in a cubic lattice with the lattice parameter a .

3.2.2.3. Plastic Deformation and Critical Schmid Stress. As discussed before, a plastic deformation takes place if a certain shear stress is applied. This limit stress τ_c is called critical resolved shear stress or Schmid stress. FRENKEL [43] calculated this stress based on the simplified model depicted in Figure 3.12. He thought about two interdig-

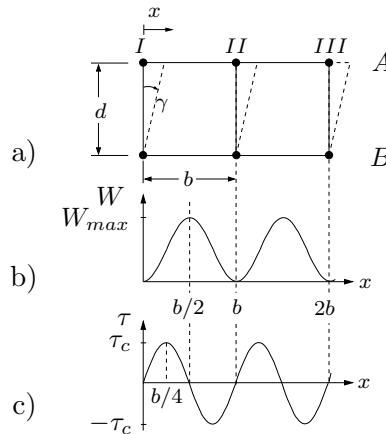


Figure 3.16: Critical resolved shear stress, adopted from TROOST [137]. a) Simplified ideal crystal structure, b) work W and c) shear stress τ as a function of the deformation x .

itating saws with equal teeth representing two whole atom rows which are sheared off. In order to find the critical resolved shear stress, consider a simplified crystal structure pictured in Figure 3.16 with two atom rows A and B being arranged in stable states I , II and III with interatomic spacing b corresponding to the length $|\mathbf{b}|$ of the Burgers vector \mathbf{b} and glide plane distance $d = b$ of a cubic primitive structure. A shear stress τ results in a shear strain $\gamma = x/d$. The shear stress τ and its corresponding work

$$W = \frac{W_{max}}{2} \left[1 - \cos \left(2\pi \frac{x}{b} \right) \right] \quad (3.4)$$

are periodic functions of the deformation x , see Figure 3.16. For the unstable deformation state $x = b/2$ the work reaches a maximum and an excess of W_{max} results in an irreversible plastic deformation. The atom falls in the neighboring equilibrium state II , whereas the

neighboring atom moves from *II* to *III*. Hence, the two atom rows are sheared off about one atom spacing corresponding to the deformation in Figure 3.12. The shear stress

$$\tau = \frac{W_{max}}{2} \frac{2\pi}{b} \sin\left(2\pi \frac{x}{b}\right) = \tau_c^{Frenkel} \sin\left(2\pi \frac{x}{b}\right). \quad (3.5)$$

follows by derivation of the work W with respect to the deformation x . Furthermore, for linear elastic material response the shear stress $\tau = \mu\gamma$ is written in terms of the shear strain $\gamma = x/d$ and the shear modulus μ . With the assumption of small deformations $x \ll b$, i.e. $\sin(\cdot) = (\cdot)$, the critical shear stress reads

$$\tau_c^{Frenkel} = \frac{\mu b}{2\pi d}. \quad (3.6)$$

The critical shear stress and hence the glide mechanism depends on the ratio b/d of the interatomic spacing with respect to the glide plane distance. Consider the atom sample depicted in Figure 3.17. It contains a body centered cubic structure with glide plane

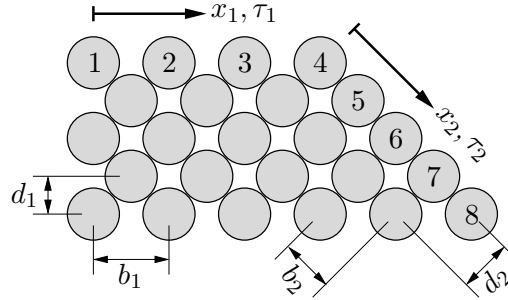


Figure 3.17: Critical resolved shear stress. Sliding on the closest packed 4-5-6-7-8-plane is preferred compared to the 1-2-3-4-plane.

1-2-3-4 in the direction $x_1 \in [0, b_1]$ caused by the shear stress τ_1 and a cubic primitive structure with glide plane 4-5-6-7-8 in the direction $x_2 \in [0, b_2]$ caused by the shear stress τ_2 . Obviously, for the first glide plane, $x_1 = 0$ and $x_1 = b_1$ are stable and $x_1 = b_1/2$ unstable equilibrium states, whereas for the second glide plane $x_2 = 0, x_2 = b_2$ are unstable and $x_2 = b_2/2$ stable equilibrium states. As the ratio b/d for the glide plane 4-5-6-7-8 in Figure 3.17 is smaller, the critical stress is lower and sliding on this plane is preferred compared to glide plane 1-2-3-4. However, the critical shear stress $\tau_c^{Frenkel}$ evaluated according to (3.6) is 10^4 times higher compared to experimental results. Motivated by this discrepancy, the idea of a corrugated sheet model goes back to OROWAN [108], POLANYI [113] and TAYLOR [133] for the movement of dislocations illustrated in Figure 3.13. Here, the atoms close to a dislocation are progressively in an unstable equilibrium state where less energy is necessary for their movement. See Figure 3.18 for a representation of the equilibrium

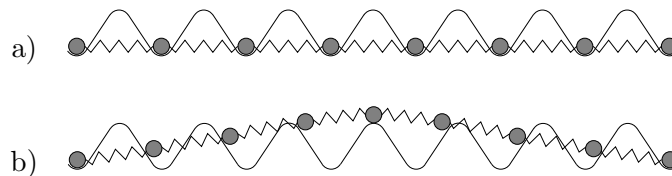


Figure 3.18: Critical resolved shear stress. Representation of one atom row of an a) ideal and a b) real crystal, taken from Troost [137].

states of an ideal and a real crystalline structure. In an ideal crystal each atom lays in a sink, i.e. a stable equilibrium state, with one atom per sink ensured by the springs representing interatomic bonds. A large amount of energy is necessary to lift all atoms to the top, representing a plastic deformation. Contrarily in a real crystal the atoms are partly in an unstable equilibrium state due to the lattice defects and therefore a plastic deformation is achieved at less shear stresses. As mentioned above, the plastic shearing, i.e. the motion of e.g. an edge dislocation, can be expressed by the shear strain $\gamma = b/d$, if the dislocation reaches a grain boundary. The total shearing of n dislocations reaching the crystal boundary adds up to $\gamma = nb/h$ with h being the height of the crystal. However, if dislocations cover only a fraction x_i of the distance, the shear strain is

$$\gamma = \frac{b(\sum_i^n x_i)/w}{h} = \frac{bx}{wh}. \quad (3.7)$$

Here, $x = \sum_i^n x_i$ is the total length of dislocation movement and w is the width of the crystal. With the definitions of an average dislocation length $\bar{x} = (\sum_i^n x_i)/n$ and a dislocation density $\rho_d = n/(wh)$ the strain follows to

$$\gamma = b\rho_d\bar{x}. \quad (3.8)$$

For a constant dislocation density $\rho_d = const.$, time differentiation of (3.8) yields the Orowan equation

$$\dot{\gamma} = b\rho_d\bar{v} \quad (3.9)$$

for the macroscopically visible shear velocity $\dot{\gamma}$ as a function of the average dislocation velocity $\bar{v} = \dot{\bar{x}}$. This equation is considered as the main relation between dislocation and continuum mechanics in crystal plasticity.

3.2.3. Slip Systems. Basic properties such as slip on closest packed planes and directions can be explained by the ansatz of FRENKEL [43]. The critical resolved shear stress τ decreases with a decreasing length b of the Burgers vector \mathbf{b} at a glide plane distance d . A small magnitude of the Burgers vector is achieved by a lattice direction which is closest packed. Again, this is clear in Figure 3.17 for plane 4-5-6-7-8 compared to plane 1-2-3-4 due to the reduced ratio of interatomic spacing b to glide plane distance d . All closest packed planes and directions form the possible slip systems and are crucial for the plastic deformation of a crystal. There are 12 slip systems for the fcc crystal, i.e. four planes $\{111\}$ with three directions $\langle 110 \rangle$ each, see Figure 3.19. There are 48 slip systems for the bcc crystal with the planes $\{110\}$, $\{112\}$, $\{123\}$ and directions $\langle 111 \rangle$. These slip systems are characterized by a slip direction \mathbf{s}^α and a slip normal \mathbf{n}^α . The slip directions \mathbf{s}^α and slip normals \mathbf{n}^α with $\alpha = 1, \dots, m$ and m being the number of slip systems are listed in Table 3.3 for fcc and Table 3.4 for bcc crystals, respectively.

3.2.4. Classical Flow Rule of Crystal Plasticity. The macroscopic shear rate (3.9) can be related to the plastic deformation \mathbf{F}^p as part of the total deformation of the body, characterized by the deformation gradient (2.5). \mathbf{F}^p describes the plastic slip on given crystallographic slip systems with the slip plane normal \mathbf{n}^α and the slip direction \mathbf{s}^α of the $\alpha = 1, \dots, m$ slip systems, see Figure 3.20. A continuous macroscopic plastic deformation

$$\mathbf{p} : \begin{cases} \mathcal{B} \rightarrow \mathcal{B}^p \\ \bar{\mathbf{X}} \mapsto \mathbf{p}(\bar{\mathbf{X}}) = \mathbf{F}^p \bar{\mathbf{X}} \end{cases} \quad (3.10)$$

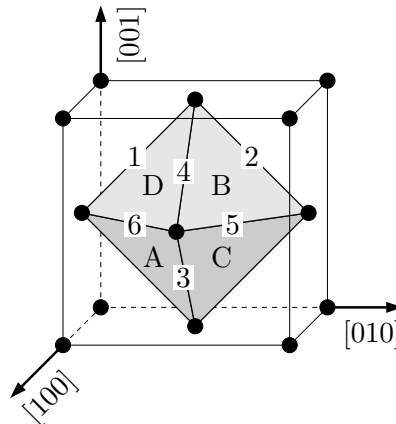
Table 3.3: Slip directions \mathbf{s}^α and planes \mathbf{n}^α for fcc crystals

α	\mathbf{s}^α	\mathbf{n}^α	α	\mathbf{s}^α	\mathbf{n}^α	α	\mathbf{s}^α	\mathbf{n}^α
1	$[\bar{1}10]$	(111)	5	$[101]$	$(\bar{1}11)$	9	$[\bar{1}0\bar{1}]$	$(\bar{1}\bar{1}1)$
2	$[0\bar{1}1]$	(111)	6	$[01\bar{1}]$	$(\bar{1}11)$	10	$[110]$	$(1\bar{1}1)$
3	$[10\bar{1}]$	(111)	7	$[1\bar{1}0]$	$(\bar{1}\bar{1}1)$	11	$[\bar{1}01]$	$(1\bar{1}1)$
4	$[\bar{1}\bar{1}0]$	$(\bar{1}11)$	8	$[011]$	$(\bar{1}\bar{1}1)$	12	$[0\bar{1}\bar{1}]$	$(1\bar{1}1)$

Table 3.4: Slip directions \mathbf{s}^α and planes \mathbf{n}^α for bcc crystals

α	\mathbf{s}^α	\mathbf{n}^α	α	\mathbf{s}^α	\mathbf{n}^α	α	\mathbf{s}^α	\mathbf{n}^α	α	\mathbf{s}^α	\mathbf{n}^α
1	$[1\bar{1}\bar{1}]$	(110)	13	$[\bar{1}\bar{1}1]$	(112)	25	$[\bar{1}\bar{1}1]$	(123)	37	$[\bar{1}1\bar{1}]$	(231)
2	$[\bar{1}1\bar{1}]$	(110)	14	$[1\bar{1}1]$	$(\bar{1}12)$	26	$[1\bar{1}1]$	$(\bar{1}23)$	38	$[11\bar{1}]$	$(\bar{2}31)$
3	$[111]$	$(1\bar{1}0)$	15	$[\bar{1}11]$	$(1\bar{1}2)$	27	$[\bar{1}11]$	$(1\bar{2}3)$	39	$[111]$	$(2\bar{3}1)$
4	$[11\bar{1}]$	$(1\bar{1}0)$	16	$[111]$	$(11\bar{2})$	28	$[111]$	$(12\bar{3})$	40	$[\bar{1}11]$	$(23\bar{1})$
5	$[\bar{1}\bar{1}1]$	(101)	17	$[\bar{1}1\bar{1}]$	(121)	29	$[\bar{1}1\bar{1}]$	(132)	41	$[1\bar{1}\bar{1}]$	(312)
6	$[\bar{1}11]$	(101)	18	$[11\bar{1}]$	$(\bar{1}21)$	30	$[11\bar{1}]$	$(\bar{1}32)$	42	$[111]$	$(\bar{3}12)$
7	$[\bar{1}\bar{1}\bar{1}]$	$(10\bar{1})$	19	$[111]$	$(1\bar{2}1)$	31	$[111]$	$(1\bar{3}2)$	43	$[11\bar{1}]$	$(3\bar{1}2)$
8	$[1\bar{1}1]$	$(10\bar{1})$	20	$[\bar{1}11]$	$(12\bar{1})$	32	$[\bar{1}11]$	$(13\bar{2})$	44	$[1\bar{1}1]$	$(31\bar{2})$
9	$[11\bar{1}]$	(011)	21	$[1\bar{1}\bar{1}]$	(211)	33	$[\bar{1}\bar{1}1]$	(213)	45	$[1\bar{1}\bar{1}]$	(321)
10	$[1\bar{1}1]$	(011)	22	$[111]$	$(\bar{2}11)$	34	$[1\bar{1}1]$	$(\bar{2}13)$	46	$[111]$	$(\bar{3}21)$
11	$[111]$	$(01\bar{1})$	23	$[11\bar{1}]$	$(2\bar{1}1)$	35	$[\bar{1}11]$	$(2\bar{1}3)$	47	$[11\bar{1}]$	$(3\bar{2}1)$
12	$[\bar{1}11]$	$(01\bar{1})$	24	$[1\bar{1}1]$	$(21\bar{1})$	36	$[111]$	$(21\bar{3})$	48	$[1\bar{1}1]$	$(32\bar{1})$

describes as a homogenized quantity the macroscopic impact of multiple moving dislocations. \mathbf{F}^p maps points $\bar{\mathbf{X}} \in \mathcal{B}$ of the reference configuration \mathcal{B} onto points $\mathbf{p} \in \mathcal{B}_p$ in a purely plastically deformed configuration \mathcal{B}_p . Following RICE [123], \mathbf{F}^p is chosen such, that the orientation of the slip system remains unchanged. He determines the plastic

**Figure 3.19:** 12 slip systems of a face centered cubic crystal.

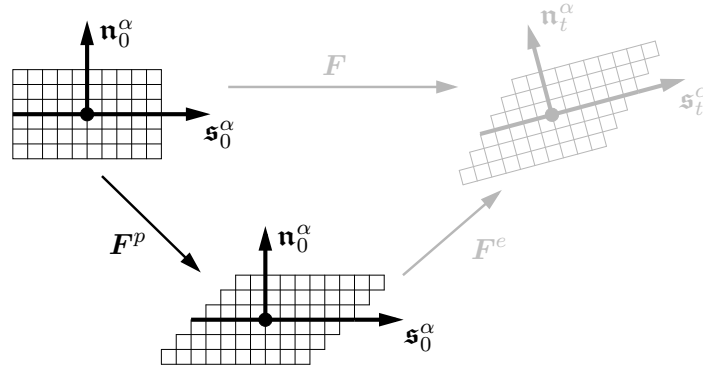


Figure 3.20: Plastic deformation. The plastic map $\mathbf{F}^p \in SL(3)$ describes the plastic slip on given slip systems.

velocity

$$\dot{\mathbf{p}} = \sum_{\alpha=1}^m \dot{\gamma}^{\alpha} \mathbf{s}^{\alpha} (\mathbf{n}^{\alpha} \cdot \mathbf{p}) \quad (3.11)$$

in terms of the shearing rates $\dot{\gamma}^{\alpha}$, also called plastic slip, of the m slip systems which can be related to the Orowan equation (3.9). Time differentiation of $\mathbf{F}^p = \mathbf{p} \bar{\mathbf{X}}^{-1}$ yields $\dot{\mathbf{F}}^p = \dot{\mathbf{p}} \bar{\mathbf{X}}^{-1}$ due to $\bar{\mathbf{X}} = \text{const.}$ in the reference configuration. The plastic velocity gradient reads

$$\dot{\mathbf{F}}^p \mathbf{F}^{p-1} = \dot{\mathbf{p}} \mathbf{p}^{-1} = \sum_{\alpha=1}^m \dot{\gamma}^{\alpha} \mathbf{s}^{\alpha} (\mathbf{n}^{\alpha} \cdot \mathbf{p}) \mathbf{p}^{-1}. \quad (3.12)$$

By means of index notation, it follows the classical flow rule of crystal plasticity

$$\dot{F}_{il}^p F_{lj}^{p-1} = \sum_{\alpha=1}^m \dot{\gamma}^{\alpha} \mathbf{s}_i^{\alpha} (\mathbf{n}_k^{\alpha} \cdot \mathbf{p}_k) \mathbf{p}_j^{-1} = \sum_{\alpha=1}^m \dot{\gamma}^{\alpha} \mathbf{s}^{\alpha} \otimes \mathbf{n}^{\alpha}, \quad (3.13)$$

describing the evolution problem for the plastic deformation in terms of the dislocation mechanism.

3.3. Description of Crystallographic Texture

A polycrystalline material consists of a large number of crystal grains. The orientation distribution of these grains is called the orientation texture of the polycrystal. Hence, the crucial purpose is to determine the crystal orientation. As an orientation is the result of a sequence of rotations, first the different possibilities for the representation of rotations are outlined. A discussion on the graphical representation and the experimental determination of textures follows. The distribution of crystal orientations of a polycrystalline material can be described by the crystal orientation distribution function, which can be approximated by a Fourier series. As described in Section 5.4, the coefficients of the Fourier series are the key quantities to describe the influence of the microscopic mechanism of crystal reorientation on the macroscopic behavior of the material.

3.3.1. Representation of Crystal Orientations. In order to describe the orientation of crystals, two coordinate systems with three orthonormal directions need to be introduced. One system is attached to the crystal lattice where e.g. in a cubic, tetragonal or orthorhombic lattice the three axes coincide with the base vectors, introduced in Section 3.1. These base vectors of this lattice frame are in the following denoted by $\{\mathbf{g}_i\}_{i=1,2,3}$. The

global sample system $\{\mathbf{e}_i\}_{i=1,2,3}$ is chosen according to the shape or loading of the macroscopic specimen, e.g. in a metallic sheet the three axes point in the rolling, transverse and normal directions of the sheet. The two coordinate systems $\mathbf{g}_i = \mathbf{R}\mathbf{e}_i$ are related by a rotation \mathbf{R} . In the following subsections equivalent possibilities for the representation of rotations by a proper orthogonal tensor, by Eulerian axis angles and an alternative series expansion, by Eulerian angles, by quaternions and by Rodrigues vectors as a specific form of quaternions are discussed. For a detailed discussion on rotations the reader is referred among others to ANGELES [11], ARGYRIS [13], ALTMANN [9] and MORAWIEC [102].

3.3.1.1. Rotation Matrix. A rotation of an arbitrary vector \mathbf{a} onto a vector \mathbf{b} can be described by a linear map

$$\mathbf{b} = \mathbf{R}\mathbf{a} \quad (3.14)$$

in terms of the second-order rotation tensor \mathbf{R} . The length of the vector needs to be invariant under such an operation, i.e. $|\mathbf{a}|^2 = |\mathbf{b}|^2$. Therefore, the rotation tensor \mathbf{R} needs to be orthogonal according to

$$\mathbf{a}^T \{ \mathbf{R}^T \mathbf{R} - \mathbf{1} \} \mathbf{a} = 0 \quad (3.15)$$

for an arbitrary vector \mathbf{a} . Consider furthermore a set of three unit vectors $\{\mathbf{e}_1, \mathbf{e}_2, \mathbf{e}_3\}$ and a corresponding rotated set $\{\mathbf{g}_1 = \mathbf{R}\mathbf{e}_1, \mathbf{g}_2 = \mathbf{R}\mathbf{e}_2, \mathbf{g}_3 = \mathbf{R}\mathbf{e}_3\}$, with the three vectors being orthonormal, i.e.

$$\mathbf{e}_1 \times \mathbf{e}_2 \cdot \mathbf{e}_3 = 1 \quad \text{and} \quad \mathbf{R}\mathbf{e}_1 \times \mathbf{R}\mathbf{e}_2 \cdot \mathbf{R}\mathbf{e}_3 = 1. \quad (3.16)$$

As introduced above, these two sets of unit vectors will be used as the axes of the crystal lattice and sample frame, respectively. For the two matrices $\mathbf{E} := [\mathbf{e}_1, \mathbf{e}_2, \mathbf{e}_3]$ and $\mathbf{G} := [\mathbf{g}_1, \mathbf{g}_2, \mathbf{g}_3]$ the determinants are $\det \mathbf{E} = 1$ and $\det \mathbf{G} = 1$. From tensor algebra it follows

$$\mathbf{G} = \mathbf{R}\mathbf{E} \quad \Rightarrow \quad \det \mathbf{G} = \det (\mathbf{R}\mathbf{E}) = \det \mathbf{R} \det \mathbf{E} \quad \Rightarrow \quad \det \mathbf{R} = 1. \quad (3.17)$$

Hence, the rotation is characterized as an element of the proper orthogonal group $\mathcal{SO}(3)$

$$\mathbf{R} \in \mathcal{SO}(3) := \{ \mathbf{R} \mid \mathbf{R}^T \mathbf{R} = \mathbf{1} \text{ and } \det \mathbf{R} = 1 \}. \quad (3.18)$$

The nine entries, so-called direction cosines, of the rotation tensor consist of only three degrees of freedom, as a consequence of *Eulers Rotation Theorem*. As it is simple to rotate a vector or to combine sequenced rotations, the parameterization of an orientation by a rotation tensor is quite popular, but not very compact and rather difficult to visualize.

3.3.1.2. Rotation Representation in terms of Eulerian Angles. A well established representation of a rotation is done by the three independent Eulerian angles. Here, the rotation is decomposed into three sequenced rotations about a prescribed axis. There are several conventions for specifying Eulerian angles, where the one introduced in BUNGE [36] is the most common. Starting point is that the axes of the sample $\{X, Y, Z\}$ and the crystal coordinate system $\{X', Y', Z'\}$ coincide. First, the crystal coordinate system is rotated with the angle φ_1 about the Z' -axis, second about the rotated X' -axis with Φ and third about the rotated Z' -axis with φ_2 , see Figure 3.21. Hence a rotation

$$\mathbf{R} = \mathbf{R}_{\varphi_1} \mathbf{R}_{\Phi} \mathbf{R}_{\varphi_2} = \begin{bmatrix} \cos \varphi_1 & -\sin \varphi_1 & 0 \\ \sin \varphi_1 & \cos \varphi_1 & 0 \\ 0 & 0 & 1 \end{bmatrix} \begin{bmatrix} 1 & 0 & 0 \\ 0 & \cos \Phi & -\sin \Phi \\ 0 & \sin \Phi & \cos \Phi \end{bmatrix} \begin{bmatrix} \cos \varphi_2 & -\sin \varphi_2 & 0 \\ \sin \varphi_2 & \cos \varphi_2 & 0 \\ 0 & 0 & 1 \end{bmatrix} \quad (3.19)$$

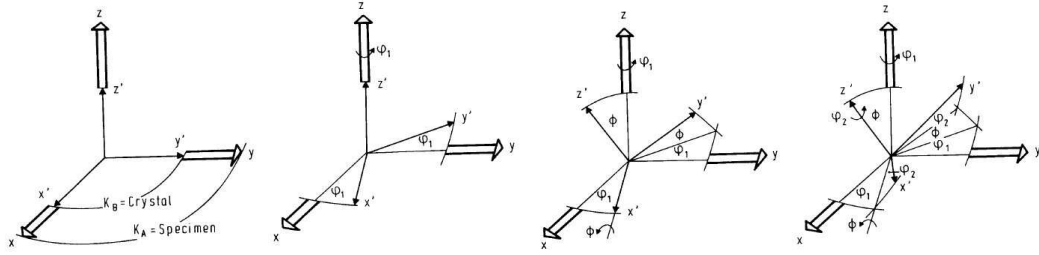


Figure 3.21: Eulerian angle representation. Definition of rotation by Eulerian angles according to BUNGE[36].

is represented by the three Eulerian angles $\varphi_1, \Phi, \varphi_2$. As pointed out in FRANK [42] due to some disadvantages, an axis angle representation is preferred for the description of rotations compared to Eulerian angles. Eulerian angles are asymmetric relative to the sample frame and behave pathological for small rotations. Furthermore, the fundamental region obtained through a highly distorted metric from the Eulerian angle space is bounded by curved surfaces. Therefore, Eulerian angles are used rarely in this work and the reader is referred to the literature for further details.

3.3.1.3. Axis Angle Representation of a Rotation. According to Eulers Theorem the displacement of a sphere with a fixed point can equivalently be described by a rotation about a certain axis comprising the fixed point and a certain angle. I.e. the nine linear dependent direction cosines can be reduced to two components of an axis \mathbf{e} of rotation, with $|\mathbf{e}| = 1$ and a scalar rotation angle ϑ about this axis. The rotation can be described by the so-called axial pseudo vector

$$\mathbf{w} = \vartheta \mathbf{e} . \quad (3.20)$$

In general, this axis angle parameterization has four coordinates $[\vartheta, e_1, e_2, e_3]$. However, due to the normalization $|\mathbf{e}| = 1$ it can be reduced to \mathbb{R}^3 . The pseudo vector \mathbf{w} can fully describe a rotation, but the standard vector algebra cannot be applied, e.g. application of two sequenced rotations does not give the same result if the multiplication order is changed. Instead, the algebra of quaternions has to be used, see Section 3.3.1.4. Consider

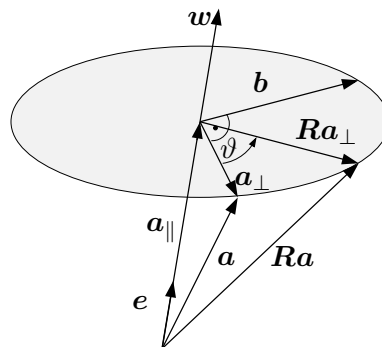


Figure 3.22: Axis angle parametrization.

a rotation \mathbf{R} about a unit axis \mathbf{e} . The vector \mathbf{a} starts from an origin which lays on the rotation axis and is rotated to \mathbf{Ra} , see Figure 3.22. It can be decomposed

$$\mathbf{a} = \mathbf{a}_{\parallel} + \mathbf{a}_{\perp} \quad \text{with} \quad \mathbf{a}_{\parallel} = (\mathbf{a} \cdot \mathbf{e})\mathbf{e} \quad \text{and} \quad \mathbf{a}_{\perp} = \mathbf{a} - (\mathbf{a} \cdot \mathbf{e})\mathbf{e} \quad (3.21)$$

in a part parallel and a part perpendicular to the rotation axis. The vector $\mathbf{b} = \mathbf{e} \times \mathbf{a}_\perp = \mathbf{e} \times \mathbf{a}$ is perpendicular to \mathbf{a} and \mathbf{e} as $\mathbf{e} \times \mathbf{a}_\parallel = \mathbf{0}$. With $\mathbf{Ra} = \mathbf{a}_\parallel + \mathbf{Ra}_\perp$ and $\mathbf{Ra}_\perp = \cos \vartheta \mathbf{a}_\perp + \sin \vartheta \mathbf{b}$ it follows

$$\mathbf{Ra} = (\mathbf{a} \cdot \mathbf{e})\mathbf{e} + \cos \vartheta (\mathbf{a} - (\mathbf{a} \cdot \mathbf{e})\mathbf{e}) + \sin \vartheta (\mathbf{e} \times \mathbf{a}) \quad (3.22)$$

as the Rodrigues rotation formula. Usage of the vector triple product $\mathbf{e} \times (\mathbf{e} \times \mathbf{a}) = \mathbf{e}(\mathbf{e} \cdot \mathbf{a}) - \mathbf{a}$, the trigonometric identity $\cos \vartheta = 1 - 2 \sin^2(\vartheta/2)$, equation (3.20) and $|\mathbf{w}| = \vartheta$ yields

$$\mathbf{Ra} = \mathbf{a} + \frac{\sin |\mathbf{w}|}{|\mathbf{w}|} (\mathbf{w} \times \mathbf{a}) + \frac{1}{2} \left[\frac{\sin(|\mathbf{w}|/2)}{|\mathbf{w}|/2} \right]^2 \mathbf{w} \times (\mathbf{w} \times \mathbf{a}) \quad (3.23)$$

as an equivalent representation. The Rodrigues rotation formula represents a rotation from an initial vector \mathbf{a} to a rotated vector \mathbf{Ra} in terms of the axial pseudo vector \mathbf{w} . In order to find a relation between the axial pseudo vector \mathbf{w} and the rotation tensor \mathbf{R} introduced in Section 3.3.1.1 consider a skew second-order tensor \mathbf{W} with $\mathbf{W} = -\mathbf{W}^T$. \mathbf{W} has the properties

$$\mathbf{W}\mathbf{a} = \mathbf{w} \times \mathbf{a} \quad \text{and} \quad \mathbf{W}\mathbf{w} = \mathbf{0} \quad \text{where} \quad \mathbf{w} = -\frac{1}{2} \boldsymbol{\epsilon} : \mathbf{W}, \quad w_k = -\frac{1}{2} W_{ij} \epsilon_{ijk} \quad (3.24)$$

with an arbitrary vector \mathbf{a} , the axial vector $\mathbf{w} = \text{vect } \mathbf{W}$ and the Levi-Civita permutation tensor $\boldsymbol{\epsilon}$. \mathbf{W} applied to \mathbf{a} corresponds to a rotation about the axial vector \mathbf{w} . Writing (3.24)₁ in index notation and eliminating \mathbf{a} gives

$$W_{ik} a_k = -\epsilon_{ijk} w_j a_k \quad \rightarrow \quad W_{ik} = -\epsilon_{ijk} w_j, \quad \mathbf{W} = \mathbf{1} \times \mathbf{w} = \mathbf{w} \times \mathbf{1}, \quad (3.25)$$

in terms of the second-order identity $\mathbf{1}$. The skew tensor and corresponding axial vector have the coordinate representation

$$\mathbf{W} = \begin{bmatrix} 0 & -w_3 & w_2 \\ w_3 & 0 & -w_1 \\ -w_2 & w_1 & 0 \end{bmatrix} \quad \text{and} \quad \mathbf{w} = \begin{bmatrix} W_{32} \\ W_{13} \\ W_{21} \end{bmatrix}. \quad (3.26)$$

Replacing \mathbf{a} in equation (3.24)₁ by $\mathbf{w} \times \mathbf{a}$ yields

$$\mathbf{w} \times (\mathbf{w} \times \mathbf{a}) = \mathbf{W}^2 \mathbf{a} \quad \text{with} \quad \mathbf{W}^2 = W_{ij} W_{jk}. \quad (3.27)$$

Substitution of (3.24)₁, (3.25) and (3.27) in (3.23) gives the Rodrigues representation

$$\mathbf{R}(\mathbf{w}) = \mathbf{1} + \frac{\sin |\mathbf{w}|}{|\mathbf{w}|} \mathbf{1} \times \mathbf{w} + \frac{1}{2} \left[\frac{\sin(|\mathbf{w}|/2)}{|\mathbf{w}|/2} \right]^2 (\mathbf{1} \times \mathbf{w})^2 \quad (3.28)$$

of the rotation matrix in terms of the axial pseudo vector \mathbf{w} . ARGYRIS [13] managed to obtain the same result by a series expansion of \mathbf{W} . First, he expanded the trigonometric function

$$\sin |\mathbf{w}| = |\mathbf{w}| - \frac{|\mathbf{w}|^3}{3!} + \frac{|\mathbf{w}|^5}{5!} - \dots + (-1)^n \frac{|\mathbf{w}|^{2n+1}}{(2n+1)!} + \dots \quad (3.29)$$

and second, he observed relations for the powers of \mathbf{W} . Therefore, one can write $\mathbf{W}^2 = W_{is}W_{sk} = (-\epsilon_{ist}w_t)(-\epsilon_{skl}w_l) = \dots = \mathbf{w} \otimes \mathbf{w} - (\mathbf{w} \cdot \mathbf{w})\mathbf{1}$. Multiplying both sides with \mathbf{W} , \mathbf{W}^2 and so on, gives the relations

$$\mathbf{W}^3 = -|\mathbf{w}|^2\mathbf{W}, \quad \mathbf{W}^4 = -|\mathbf{w}|^2\mathbf{W}^2, \quad \mathbf{W}^5 = +|\mathbf{w}|^4\mathbf{W}, \quad \mathbf{W}^6 = +|\mathbf{w}|^4\mathbf{W}^2, \quad \dots \quad (3.30)$$

for the powers of \mathbf{W} . Putting the expansion of the trigonometric function (3.29) and the relations for the powers of \mathbf{W} (3.30) in the Rodrigues formula (3.28) yields the expansion of the rotation

$$\mathbf{R} = \mathbf{1} + \mathbf{W} + \frac{1}{2!}\mathbf{W}^2 + \frac{1}{3!}\mathbf{W}^3 + \frac{1}{4!}\mathbf{W}^4 + \dots + \frac{1}{n!}\mathbf{W}^n = \exp(\mathbf{W}) \quad (3.31)$$

which corresponds to the Taylor series expansion of the exponential tensor function $\exp(\mathbf{W})$. I.e. a rotation can be expressed by the exponential map of a skew second-order tensor \mathbf{W} .

3.3.1.4. Quaternion representation of a Rotation. A rotation \mathbf{R} can be represented by a quaternion

$$\mathbb{Q} := (q, \mathbf{q}) = q + q_1i + q_2j + q_3k \quad (3.32)$$

consisting of a real number q and a pseudo vector \mathbf{q} with the imaginary directions i, j, k . Some basics of quaternion algebra are reviewed. For a more detailed description see e.g. ALTMANN [9]. For the three quaternion units i, j, k the Hamilton rules

$$ij = -ji = k, \quad jk = -kj = i, \quad ki = -ik = j \quad (3.33)$$

follow from the fundamental formula for quaternion multiplication

$$i^2 = j^2 = k^2 = ijk = -1, \quad (3.34)$$

which Hamilton scratched 1843 in a bridge in Dublin. The multiplication of the quaternion units is similar to complex numbers. Hence for the multiplication of two quaternions $\bar{\mathbb{Q}}$ and $\hat{\mathbb{Q}}$ it follows

$$\bar{\mathbb{Q}}\hat{\mathbb{Q}} = (\bar{q}, \bar{\mathbf{q}})(\hat{q}, \hat{\mathbf{q}}) = (\bar{q}\hat{q} - \bar{\mathbf{q}} \cdot \hat{\mathbf{q}}, \bar{q}\hat{\mathbf{q}} + \hat{q}\bar{\mathbf{q}} + \bar{\mathbf{q}} \times \hat{\mathbf{q}}). \quad (3.35)$$

The multiplication of quaternions is associative, but not commutative. The so-called real quaternion $(q, \mathbf{0})$ multiplies like real numbers and for the product of two pure quaternions

$$(0, \bar{\mathbf{q}})(0, \hat{\mathbf{q}}) = (\bar{\mathbf{q}} \cdot \hat{\mathbf{q}}, \bar{\mathbf{q}} \times \hat{\mathbf{q}}) \quad (3.36)$$

holds. Hence, a quaternion $(q, \mathbf{q}) = (q, \mathbf{0}) + (0, \mathbf{q})$ can always be decomposed in a real and a pure quaternion. A quaternion of the form $(0, \mathbf{n})$ with $|\mathbf{n}| = 1$ being a unit vector is called unit quaternion. With the definition of the conjugate $\mathbb{Q}^* := (q, -\mathbf{q})$ of a quaternion the norm of the quaternion can be identified by

$$\mathbb{Q}\mathbb{Q}^* = (q, \mathbf{q})(q, -\mathbf{q}) = (q^2 + \mathbf{q} \cdot \mathbf{q}, \mathbf{0}) =: |\mathbb{Q}|^2. \quad (3.37)$$

A quaternion with $|\mathbb{Q}|^2 = (1, \mathbf{0})$, i.e. $q^2 + q_1^2 + q_2^2 + q_3^2 = 1$ is called normalized quaternion, which holds e.g. for the Hamilton quaternion $(\cos \vartheta, \sin \vartheta \mathbf{e})$. The likewise normalized Rodrigues quaternion

$$\mathbb{Q} = (q, \mathbf{q}) = (\cos(\vartheta/2), \sin(\vartheta/2)\mathbf{e}), \quad (3.38)$$

with the rotation angle ϑ and the axis of rotation \mathbf{e} was introduced earlier than Hamilton's quaternion. Therein, the four coordinates of the quaternion are called Euler-Rodrigues parameters. In order to get the rotation tensor in terms of Rodrigues quaternions (3.38) the axial pseudo vector

$$\mathbf{w} = \vartheta \mathbf{e} = \frac{\vartheta}{\sin(\vartheta/2)} \mathbf{q} \quad (3.39)$$

can be inserted in (3.28). With the trigonometric identity $\sin \vartheta = 2 \sin(\vartheta/2) \cos(\vartheta/2)$ and $\mathbf{q} \cdot \mathbf{q} = 1 - q^2$ a rotation

$$\mathbf{R}(\mathbb{Q}) = \mathbf{1} + 2q(\mathbf{1} \times \mathbf{q}) + 2(\mathbf{1} \times \mathbf{q})^2 = (2q^2 - 1)\mathbf{1} + 2q(\mathbf{1} \times \mathbf{q}) + 2\mathbf{q} \otimes \mathbf{q} \quad (3.40)$$

can be represented in terms of the Rodrigues quaternion \mathbb{Q} .

3.3.1.5. Rodrigues Parameters. As a specific form of the axial vector, the Rodrigues vector

$$\mathbf{r} := \tan(\vartheta/2) \mathbf{e} \quad (3.41)$$

is introduced, as e.g. discussed in FRANK [42]. The vector \mathbf{r} is coaxial to the axial vector \mathbf{w} but scales the rotation with $\tan(\vartheta/2)$ about this axis. With the definition of the Rodrigues quaternion (3.38) the Rodrigues vector

$$\mathbf{r} = \frac{\mathbf{q}}{q} \quad (3.42)$$

can be formulated in terms of quaternions $(q, \mathbf{q}) = (\cos(\vartheta/2), \sin(\vartheta/2)\mathbf{e})$. Despite the singularity at $\vartheta = \pi$, the parameterization with Rodrigues vectors is a quite simple representation. Proceed as in the previous subsection by replacing the axial vector

$$\mathbf{w} = \vartheta \mathbf{e} = \frac{\vartheta}{\tan(\vartheta/2)} \mathbf{r} \quad (3.43)$$

in (3.28) yields with the trigonometric identities $\sin \vartheta = 2 \tan(\vartheta/2)/[1 + \tan^2(\vartheta/2)]$ and $\cos^2(\vartheta/2) = 1/[1 + \tan^2(\vartheta/2)]$ the rotation

$$\mathbf{R}(\mathbf{r}) = \mathbf{1} + \frac{2[(\mathbf{1} \times \mathbf{r}) + (\mathbf{1} \times \mathbf{r})^2]}{1 + \mathbf{r} \cdot \mathbf{r}} = \frac{(1 - \mathbf{r} \cdot \mathbf{r})\mathbf{1} + 2(\mathbf{1} \times \mathbf{r}) + \mathbf{r} \otimes \mathbf{r}}{1 + \mathbf{r} \cdot \mathbf{r}} \quad (3.44)$$

in terms of the Rodrigues parameter \mathbf{r} .

3.3.2. Graphical Representation of Orientations. Several possibilities exist for the visualization of textures, such as pole figures, inverse pole figures, orientation distribution by means of Eulerian angles or a representation in the Rodrigues space. The most popular one is the representation by pole figures using a stereographic or equal-area projection. The visualization of rotations by means of Eulerian angles does not have an immediate physical interpretation, hence it must be compared to calculations of reference deformation modes. A representation through an axis angle parameterization, Section 3.3.1.3, is unique if the symmetry of the material is taken into account. In this contribution, pole figures and a representation in the Rodrigues space are used.

3.3.2.1. Stereographic Projection and Pole Figures. As discussed in Section 3.1.2, Miller indices describe crystal planes/orientations with respect to the local coordinate system of the unit cell. Contrarily, pole figures describe the crystallographic directions with respect to an arbitrary global coordinate system, chosen according to the shape or loading of a macroscopic specimen. For the construction of a pole figure, the unit cell is attached to the origin of the coordinate system and surrounded by a unit sphere, see Figure 3.23. The vectors of all crystallographic directions belonging to a desired set of

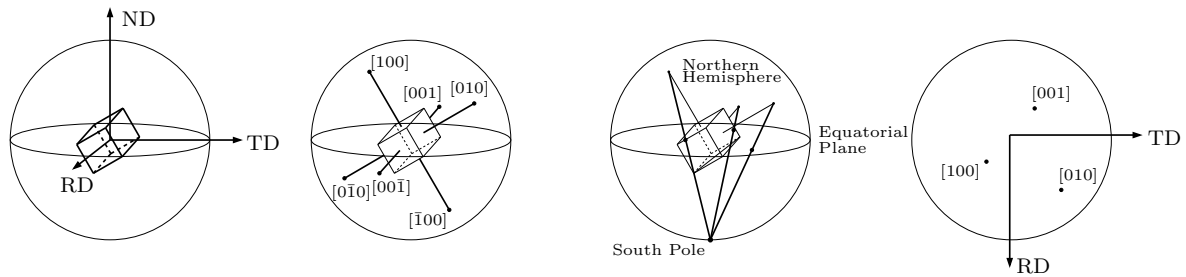


Figure 3.23: Concept of the stereographic projection, exemplarily shown for $\langle 100 \rangle$ set of directions. ND, TD and RD represent the normal, transverse and rolling direction, respectively.

directions are elongated until they intersect the unit sphere. In Figure 3.23 the procedure is shown for $\langle 100 \rangle$. A convenient projection of the three-dimensional points on the unit sphere is desired for a two-dimensional representation. Therefore, the intersections on the northern hemisphere are connected to the south pole of the unit sphere. Finally, the intersections of these lines with the equatorial plane represent the orientations of the unit cell in space on a two-dimensional plane. The orthogonal view of the equatorial plane is called the stereographic projection, see e.g. BARRETT & MASSALSKI [21]. Two-dimensional pole figures provide incomplete informations with regard to the texture of a material as it only shows the orientation of selected planes/directions. But in some cases it is sufficient to know only a portion of the orientation information, e.g. for fiber textures with respect to a certain axis, which makes a projection with respect to this axis reasonable. Although providing incomplete information, the representation of orientations by pole figures is the most popular as people are familiar with this representation and it is straightforward to handle with regard to its physical interpretation. Despite the symmetry, it is common in the literature to represent the entire pole figure. The stereographic projection of a standard cubic lattice is exemplarily shown in Figure 3.24 with the corners representing the

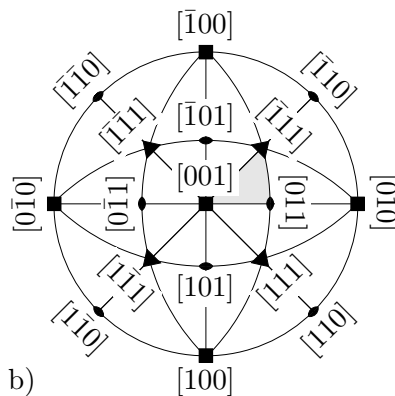


Figure 3.24: Standard stereographic cubic projection.

directions $\langle 100 \rangle$, $\langle 110 \rangle$ and $\langle 111 \rangle$. Here, the projection plane is divided into 24 unit stereographic triangles of varying area. As pointed out e.g. in KOCKS, TOMÉ & WENK [69] a uniform point density on a hemisphere, results in a more or less uniform distribution in the equal area mapping, whereas in the stereographic projection, which is equal of angle and equal of circle, the distribution is more dense near the center. Stereographic projection of a polycrystalline material results in a large amount of points in the equatorial plane. Typical experimental $\langle 100 \rangle$ pole figures for a rolling deformation are shown in Figure 3.25. Drawback of the graphical representation by pole figures is, that the points

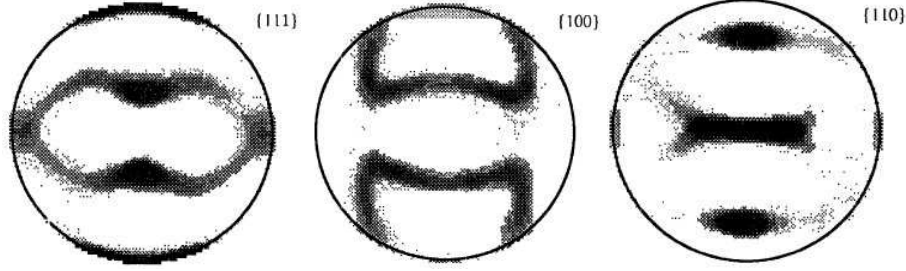


Figure 3.25: Pole figure representation. Experimental pole figures for rolling deformation taken from BRONKHORST, KALIDINDI & ANAND [33].

do not account for the volume fraction of the grains. In pole figures the crystal orientation in a crystal lattice system is represented with respect to the sample coordinate system. Another possibility is the projection of the sample system on the crystal system, called inverse pole figure. Due to the crystal symmetry, an inverse pole figure e.g. for a cubic system contains 24 equal areas, where usually only one is pictured.

3.3.2.2. Representation in Rodrigues Space. As discussed in Section 3.3.1.5 a rotation can be described by the Rodrigues vector

$$\mathbf{r} := \tan(\vartheta/2)\mathbf{e} \quad (3.45)$$

as a mathematical entity built up of the direction of the unit vector \mathbf{e} and the magnitude $\tan(\vartheta/2)$ describing the rotation axis and angle, respectively. The vector lies in a Cartesian coordinate system with the axes corresponding either to the sample or the crystal axes. For the representation of orientations possessing symmetries, the infinite space for Rodrigues vectors can be reduced. For all possible orientations the tip of the Rodrigues vector is a point lying within a polyhedron around the origin, which FRANK [42] named fundamental zone. Hence, each point lying outside the fundamental zone of the Rodrigues space has an equivalent point inside this fundamental zone representing the same orientation. Proved by HEINZ & NEUMANN [49], all bounding surfaces of the fundamental zone are planes in the Rodrigues space obtained by a geodesic projection. HEINZ & NEUMANN [49] discussed the size and shape of the fundamental zone for different crystals according to its symmetry. In order to find the bounds of the fundamental zone, consider a symmetry rotation $\mathbf{H} \in \mathcal{SO}(3)$ giving an identical structure, if

$$\bar{\mathbf{R}} = \mathbf{R} \cdot \mathbf{H} \quad (3.46)$$

with the two rotations $\mathbf{R} \in \mathcal{SO}(3)$ and $\bar{\mathbf{R}} \in \mathcal{SO}(3)$. Parameterizing the rotations by Quaternions $\mathbb{Q} = (q, \mathbf{q})$ and $\mathbb{H} = (h, \mathbf{h})$, the multiplication rule (3.35) gives

$$\bar{\mathbb{Q}} = (qh - \mathbf{q} \cdot \mathbf{h}, q\mathbf{h} + h\mathbf{q} + \mathbf{q} \times \mathbf{h}) . \quad (3.47)$$

Herein, $qh - \mathbf{q} \cdot \mathbf{h}$ represents the angle of rotation and $q\mathbf{h} + h\mathbf{q} + \mathbf{q} \times \mathbf{h}$ the direction of the rotation axis. For materials with symmetry, there eventually exist several rotation angles in the same direction giving an identical structure. E.g. for a cube, rotations with 0° , 90° , 180° and 360° with respect to a face normal give the same configuration. As a rotation axis representing the direction of the Rodrigues vector is a straight line passing through the origin of the Rodrigues space, the smallest rotation angle bounds the fundamental region, i.e.

$$q \leq \pm(qh - \mathbf{q} \cdot \mathbf{h}) \quad (3.48)$$

in the Quaternion space. With the geodesic projection (3.42), i.e. $\mathbf{q} = q\mathbf{r}$, it follows

$$\pm \mathbf{r} \cdot \mathbf{h} - (1 \pm h) \geq 0. \quad (3.49)$$

With the Rodrigues parameters $h = \cos(\vartheta/2)$, $\mathbf{h} = \sin(\vartheta/2)\mathbf{e}$ for the symmetry rotation and the trigonometrical half angle formulas $(1 - \cos \vartheta)/\sin \vartheta = \tan(\vartheta/2)$, $(1 + \cos \vartheta)/\sin \vartheta = \cot(\vartheta/2)$, (3.49) results in the two conditions

$$\pm \mathbf{r} \cdot \mathbf{e} \leq \tan\left(\frac{\vartheta}{4}\right) \quad \text{and} \quad \pm \mathbf{r} \cdot \mathbf{e} \leq \cot\left(\frac{\vartheta}{4}\right). \quad (3.50)$$

As $\cot(\vartheta/4) \geq \tan(\vartheta/4)$ in the range $0 \leq \vartheta \leq \pi$, condition (3.50)₁ is the relevant one. It defines an opposite pair of planes with the normal \mathbf{e} at a distance $\tan(\vartheta/4)$ from the origin of the Rodrigues space. Points lying on such a bounding face represent the same orientation as points on the opposite face. According to NEUMANN [106], orientations with a common direction such as ideal fiber textures are represented by straight lines in the Rodrigues space. For a cubic crystals, the Rodrigues space reduces to a truncated cube with six octagonal and eight triangular faces, illustrated in Figure 3.26. Equivalent

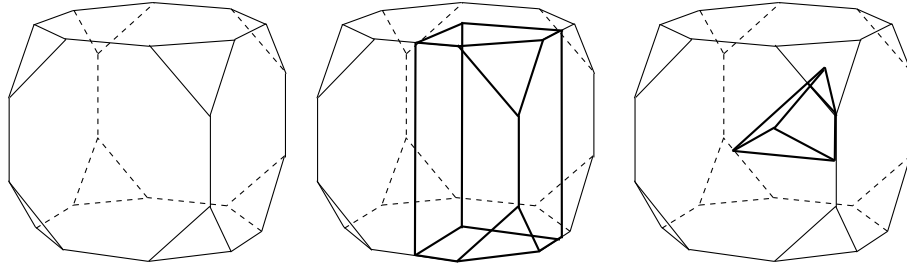


Figure 3.26: Rodrigues truncated cube for cubic crystals. Reduction of the sample without symmetry for orthorhombic and cubic samples, see NEUMANN[106].

structures are obtained (i) by a $\vartheta = \pi/2$ rotation about the $\langle 100 \rangle$ directions and (ii) by a $\vartheta = 2\pi/3$ rotation about the $\langle 111 \rangle$ directions. These conditions result in a truncated cube formed by six planes perpendicular to the $\langle 100 \rangle$ directions and eight planes perpendicular to the $\langle 111 \rangle$ direction with

$$\tan \frac{\pi}{8} = \sqrt{2} - 1 \quad \text{and} \quad \tan \frac{\pi}{6} = \frac{1}{\sqrt{3}} \quad (3.51)$$

distance from the origin, respectively. With regard to the graphical representation of the fundamental zone of the Rodrigues space, one avoids the three-dimensional plotting by cutting equidistant sections through the truncated cube. Here, all orientations within a specific slice are plotted, but this method is usually used for plotting the orientation distributions, see Section 3.3.4. The main drawback of the parameterization with Rodrigues parameters is the inability of the determination of Rodrigues vectors directly from experiments.

3.3.3. Experimental Determination of Textures. In the past, optical methods were applied for the determination of grain orientations. Nowadays, textures are measured by diffraction techniques such as X-ray, neutron or electron diffraction. For X-ray diffraction texture goniometers are used to measure angles, which the physicist Max von Laue used to prove the existence of a lattice structure of crystals. 1914 he won the Nobel Prize in Physics for the discovery of the X-ray diffraction. Ideally, a thick plate with a flat surface is clamped into a cradle, where it can be rotated about three axes in order to investigate all orientations of the sample. A detector receives the reflected or transmitted X-rays giving a reflection intensity as a function of the orientation. With X-ray diffraction a quite large area and a large penetration depth with a large number of grains being analyzed at once can be scanned. Disadvantage is the poor spatial resolution of X-ray diffraction. Electron backscatter diffraction (EBSD) is another diffraction technique

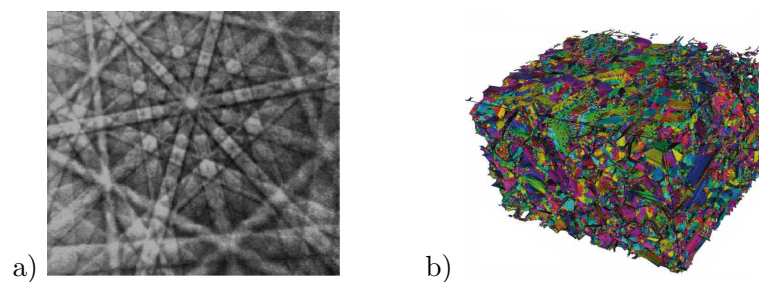


Figure 3.27: a) Electron backscatter pattern (EBSP) taken from SCHWARTZ, KUMAR, FIELD & ANAND [128] and b) 3D electron backscatter diffraction (EBSD) interface according to KHORASHADIZADEH, RAABE, ZAEFFERER, ROHRER, ROLLETT & WINNING [67]

to measure the crystallographic orientation by means of scanning (SEM) or transmission (TEM) electron microscopes. Here, diffracted electrons form an electron backscatter pattern (EBSP), shown in Figure 3.27a), on a phosphor screen. It includes the angular relationship between crystallographic planes and crystal symmetries. The pattern is recorded digitally by a camera and an orientation imaging microscopy (OIM) is produced providing information about grain size, grain and phase distribution, grain boundaries and crystal orientations. Nowadays, it is possible to generate three-dimensional images from EBSD as a map of the grain orientations on the surface of the specimen, indicated by different colors, see Figure 3.27b). Contrarily to X-ray diffraction, the orientation distribution function, important for the quantitative description of textures, can be calculated directly. The good spatial and angular resolution makes it possible to relate texture measurements and microstructural parameters. Two phase materials can be easily measured and through thickness measurements are possible. Disadvantage is, that the microscope is expensive and small samples are required, which implies more effort on the sample preparation. For heavily deformed grains or particular slip directions the texture calculation may be incorrect. RANDLE & ENGLER [121] distinguish between microtexture and macrotexture. They use X-ray diffraction for the determination of macrotexture, as it efficiently provides an overview. For their belief EBSD is the most suitable and widely used technique for the determination of texture.

3.3.4. Orientation Distribution Function. A polycrystal consists of a large number of grains and its orientation distribution is a key microstructural feature with regard to the overall response of a macroscopic specimen. The orientation distribution of a polycrystal can be described by a continuous crystal orientation distribution function (codf) f , which

is a quantitative measure with respect to the texture representation of polycrystalline materials. This function is a measurement for the volume fraction $dv(\mathbf{R})$ of crystals having a certain orientation

$$\frac{dv(\mathbf{R})}{v} = f(\mathbf{R})dR, \quad (3.52)$$

which evolves during the deformation due to distortions and rigid rotations of the grains. For the volume average \bar{A} of a quantity $A(\mathbf{R})$, which depends on the orientation \mathbf{R} , (3.52) yields

$$\bar{A} = \frac{1}{v} \int_v A(\mathbf{R})dv = \int_{\mathcal{SO}(3)} f(\mathbf{R})A(\mathbf{R})dR. \quad (3.53)$$

The codf is restricted to be positive and normalized, i.e.

$$f(\mathbf{R}) \geq 0 \quad \text{and} \quad \int_{\mathcal{SO}(3)} f(\mathbf{R})dR = 1. \quad (3.54)$$

Furthermore, it reflects both crystal and sample symmetry

$$f(\mathbf{R}) = f(\mathbf{R}\mathbf{R}^C) \quad \forall \mathbf{R}^C \in \mathcal{G}^C \quad \text{and} \quad f(\mathbf{R}) = f(\mathbf{R}^S\mathbf{R}) \quad \forall \mathbf{R}^S \in \mathcal{G}^S, \quad (3.55)$$

where $\mathcal{G}^C \in \mathcal{SO}(3)$ and $\mathcal{G}^S \in \mathcal{SO}(3)$ are the crystal and sample symmetry groups. The codf is assumed to be square integrable, i.e. it can be approximated in a Fourier series

$$f(\mathbf{R}) = 1 + \sum_{m=0}^{\infty} f_m(\mathbf{R}) \quad (3.56)$$

by means of generalized spherical harmonics as tensorial base functions, introduced by ADAMS, BOEHLER, GUIDI & ONAT [8] and GUIDI, ADAMS & ONAT [45]. Their ansatz for cubic symmetry was adopted for arbitrary crystal and sample symmetries by ZHENG & ZOU [146] and ZHENG & FU [145]. For a cubic lattice symmetry the codf

$$f(\mathbf{R}) = 1 + f_4(\mathbf{R}) + f_6(\mathbf{R}) + f_8(\mathbf{R}) + \dots \quad \text{with} \quad f_m(\mathbf{R}) = \mathbf{c}^m \cdot \mathbf{b}^m \quad (3.57)$$

can be reduced with m being the rank of the irreducible base tensor \mathbf{b}^m reflecting the cubic symmetry and the irreducible coefficient tensor \mathbf{c}^m reflecting the sample symmetry. The base tensor

$$\mathbf{b}^m(\mathbf{R}) = \mathbf{R} \star \mathbf{t}^m = t_{i_1, \dots, i_m}^m (\mathbf{R}e_{i_1}) \otimes \dots \otimes (\mathbf{R}e_{i_m}) \quad (3.58)$$

can be calculated by the Rayleigh product \star of the base coefficient tensor \mathbf{t}^m with $|\mathbf{t}^m| = 1$ with the orthogonal tensor \mathbf{R} . The tensorial coefficients \mathbf{c}^m of the Fourier representation can be expressed in terms of the base tensor \mathbf{b}^m and are used in Section 5.4. Therefore, first the base coefficient tensor \mathbf{t}^m and the base tensor \mathbf{b}^m need to be determined.

3.3.4.1. Base Coefficient Tensor. The irreducible, i.e. symmetric and traceless, base coefficient tensor \mathbf{t}^m of rank m satisfies the condition

$$t_{i_1 i_2 \dots i_m}^m = t_{p\{i_1 i_2 \dots i_m\}}^m, \quad t_{p\{i_k i_k \dots i_m\}}^m = 0, \quad (3.59)$$

where the indices $i_k \in \{1, 2, 3\}$ for $k = 1, \dots, m$ and $p\{i_1 i_2 \dots i_m\}$ represents the permutation of the sequence $\{i_1 i_2 \dots i_m\}$. In (3.59)₂ the Einstein summation convention is used. According to this condition, an irreducible tensor of order m features $2m + 1$ independent

components, see GELFAND, MINLOS & SHAPIRO [44]. All other entries of the irreducible tensor can be expressed by these independent components. The base coefficient tensor \mathbf{t}^m reflects the lattice symmetry like the base tensor \mathbf{b}^m , i.e.

$$t_{i_1 \dots i_m}^m = t_{j_1 \dots j_m}^m R_{i_1 j_1} \cdot \dots \cdot R_{i_m j_m} \quad \forall \mathbf{R} \in \mathcal{G}^c, \quad (3.60)$$

with \mathcal{G}^c representing the lattice symmetry group. Herewith, the number of non-zero elements of \mathbf{t}^m reduces drastically. The independent elements of cubic symmetric irreducible tensors up to rank 21 are given in GUIDI, ADAMS & ONAT [45]. According to the condition $|\mathbf{t}^m| = 1$, the components need to be normalized. Due to the cubic symmetry, many entries of the base coefficient tensor are zero. The tensor is filled according to the irreducibility conditions (3.59), i.e. being symmetric and traceless.

3.3.4.2. Base Tensor. With the base coefficient tensor \mathbf{t}^m at hand, the base tensor \mathbf{b}^m of same rank m is obtained by the rotation (3.58). As the base tensor is also irreducible, the rotation has to be performed only on the independent components of the base coefficient tensor. Furthermore, the nonzero entries of \mathbf{t}^m are ignored. The full base tensor follows from the irreducibility conditions

$$b_{i_1 i_2 \dots i_m}^m = b_{p\{i_1 i_2 \dots i_m\}}^m, \quad b_{p\{i_k i_k \dots i_m\}}^m = 0, \quad (3.61)$$

i.e. \mathbf{b}^m is symmetric and traceless. For the fourth-order base tensor the closed form expression is

$$b_{1111}^4 = R_{11}^4 t_{1111}^4 + 6 R_{11}^2 R_{12}^2 t_{1122}^4 + 6 R_{11}^2 R_{13}^2 t_{1133}^4 + R_{12}^4 t_{2222}^4 + 6 R_{12}^2 R_{13}^2 t_{2233}^4 + R_{13}^4 t_{3333}^4 \quad (3.62)$$

in terms of the six non-zero components $\{t_{1111}, t_{1122}, t_{1133}, t_{2222}, t_{2233}, t_{3333}\}$ of the base coefficient tensor \mathbf{t}^4 .

3.3.4.3. Coefficient Tensor. As the representation of the codf is of tensorial character and coordinate-independent, the tensorial quantities \mathbf{c}^m can be considered as internal state variables characterizing the crystallographic texture, see BÖHLKE [25] or BÖHLKE & BERTRAM [28]. By means of the orthogonality relation

$$\int_{SO(3)} \mathbf{b}^m(\mathbf{R}) \otimes \mathbf{b}^n(\mathbf{R}) dR = \begin{cases} \mathbf{0} & m \neq n \\ \frac{1}{2m+1} \mathbb{I} & m = n \end{cases} \quad (3.63)$$

and a given orientation distribution $f(\mathbf{R})$ the coefficient tensor can be computed according to

$$\mathbf{c}^m = (2m+1) \int_{SO(3)} f(\mathbf{R}) \mathbf{b}^m(\mathbf{R}) dR. \quad (3.64)$$

\mathbb{I} is the fourth order identity on irreducible tensors. For a polycrystalline material with n discrete orientations the codf can be approximated by the summation

$$f(\mathbf{Q}) \approx \sum_{k=1}^n \nu_k \delta_{\mathbf{R}_k} \quad (3.65)$$

with the set $\{\mathbf{R}_k, \nu_k\}$ of discrete crystal orientation \mathbf{R}_k and corresponding volume fraction ν_k . δ represents the Dirac distribution. Hence, the coefficient tensor is

$$\mathbf{c}^m = (2m+1) \sum_{k=1}^n \nu_k \mathbf{b}^m(\mathbf{R}_k). \quad (3.66)$$

In this contribution the coefficient tensor \mathbf{c}^m is used to describe the texture influence on the macroscopic behavior of the material.

4. Texture Modeling in Rigid Crystal Plasticity

The aim of this section is the modeling of texture evolution in rigid-plastic crystal plasticity. The content of this section is in accordance to parts of the recent publications of MIEHE & ROSATO [93], MIEHE, FRANKENREITER & ROSATO [91] and an extension from fcc to bcc crystals is outlined in MIEHE, ROSATO & FRANKENREITER [94]. In the current work, some additional comments and explanations are given and a more extensive part of numerical examples especially with regard to the comparison with experimental results is presented.

The modeling of a crystal reorientation process is characterized through (i) a micro-macro linking hypothesis and (ii) a single crystal model. Such discrete models for polycrystalline aggregates have found a wide range of applications, see for example ASARO & NEEDLEMAN [15], MATHUR & DAWSON [84], BRONKHORST, KALIDINDI & ANAND [33, 65], MIEHE, SCHRÖDER & SCHOTTE [98], MIEHE & SCHOTTE [95], ROTERS & RAABE [118]. These formulations are critically based on computationally efficient models of single crystal plasticity that govern the reorientation of the grains. Standard approaches to crystal plasticity with rate-dependent power laws are discussed for instance by PEIRCE, ASARO & NEEDLEMAN [111] and the advanced computational settings based on active set definitions by CUITIÑO & ORTIZ [39], ANAND & KOTHARI [10] and MIEHE, SCHOTTE & LAMBRECHT [96], among others. The latter are conceptually applicable in a rate-independent limit. Micro-macro linking hypotheses drawn for a general theory of homogenization are outlined e.g. in MIEHE, SCHRÖDER & SCHOTTE [98] and MIEHE, SCHOTTE & LAMBRECHT [96]. Comparative investigations outlined in these works showed that the classical Taylor-type micro-macro-linking ansatz, TAYLOR [134], provides reasonable approximations of the macroscopic texture of fcc polycrystalline aggregates, see Section 2.2. Here, it is assumed that all grains have equal volume and the deformation gradient within each grain has a uniform value throughout the aggregate. Deformation producing mechanisms of twinning, diffusion and grain boundary sliding are not considered, and other sources of anisotropy due to the morphological effects of grain shape, size and arrangement are not taken into account. Following e.g. RASHID [122], DAFALIAS [40], KUMAR & DAWSON [75] and BÖHLKE, RISY & BERTRAM [30] the applied model of crystal plasticity neglects elastic contributions and is considered as rigid-plastic, see Section 4.1. As mentioned in the classical work on texture development by BUNGE [36], this assumption is reasonable for the determination of crystal reorientations in the range of fully developed plastic flow at large strains. A kinematic condition determines the plastic slip and the so-called lattice spin $\mathbf{W}^l(\mathbf{R}^l, t)$ at time t . \mathbf{W}^l describes the plastic slip mechanism of single crystal grains, governed by the crystal reorientation process which is represented by the lattice rotation \mathbf{R}^l . For idealized plane crystals undergoing double slip as treated by RASHID [122], DAFALIAS [40] the lattice reorientation is purely geometric in nature and the kinematic condition yields a unique solution for the plastic slip. In contrast, for three-dimensional formulations of fcc and bcc crystals this is not the case. As a consequence, the intention of Section 4.2 is to develop a fast reorientation model for fcc and bcc crystals. Basic elements of such an estimate were recently proposed in MIEHE & ROSATO [93], where an algorithm for the update of the lattice spin of fcc crystals was developed based on geometric arguments. Similar to results of planar double slip, the most simple setting is a linear differential equation that estimates the crystal reorientation in terms of the macroscopic deformation of the aggregate. A closed-form linear differential equation is derived for the lattice spin of fcc and bcc crystals that is based on purely geometric considerations

combined with some optimality conditions. The first key step is a distinct estimation of the active set of slip systems in fcc and bcc crystals based on the introduction of fictitious pseudo-stresses, which are directly related to the incremental macro-deformation. Arithmetic means of these fictitious stresses result in a closed-form representation that determines the current active set as a function of the rate of deformation tensor. Still, the computation of the slip on these active system is not unique, which is solved by an optimization condition. This scheme minimizes the Euclidean norm of all slips and provides a robust unique solution in terms of a penalty functional. Due to consistency conditions, the active set needs to be enlarged. The key result is a linear formula for the active plastic slip. Finally, this geometric estimate results in a linear differential equation for the lattice spin of the crystal. In Section 4.3, the numerical implementation for a finite-step-sized incremental reorientation process is developed in terms of an incrementally objective mid-point-type scheme. This setting is based on the exploitation of exponential updates for the incremental rotations. It results in a precise update algorithm for the crystal lattice rotation, i.e. the Rodrigues parameters. In contrast to standard formulations based on power-type laws, the proposed purely geometric algorithm does not need iterations in deformation-driven scenarios of single crystals and polycrystals. It provides in combination with the exponential updates an optimal and fast estimate of the orientation texture for large deformation increments. In Section 4.4 representative numerical examples are presented. A simple representation is discussed for the closed-form solution of the reorientation of planar crystals and validated for single crystals and polycrystals undergoing pure and simple shear deformations. Furthermore, the performance of the rigid-plastic active-set model is compared with experimental results and simulations for a discussed standard power-type model of rigid-plasticity as well as an advanced elastic-plastic crystal plasticity model according to MIEHE & SCHOTTE [95]. It turns out that the geometric approach produces excellent texture estimates for a wide spectrum of deformation processes. It does this at a computational cost that is only a fraction of that of the other models. Taking this into account, the proposed scheme provides a sound basis for further development of polycrystal models.

4.1. Rigid-Plastic Deformation of Polycrystalline Microstructures

4.1.1. Taylor-Type Micro-Macro Linking. Consider an isochoric, homogeneous deformation governed by the deformation map

$$\bar{\varphi}_t = \bar{\mathcal{F}}(t)\bar{\mathbf{X}} : \bar{\mathbf{X}} \mapsto \bar{\mathbf{x}} = \bar{\varphi}_t \quad (4.1)$$

in terms of the prescribed macroscopic deformation tensor $\bar{\mathcal{F}}(t) = \nabla \bar{\varphi}_t \in \mathcal{SL}(3)$, where $\mathcal{SL}(3)$ is the special linear group of unimodular tensors with unit determinant $\det[\bar{\mathcal{F}}] = 1$. Here, macroscopic quantities are denoted with a bar. An overview with respect to micro-macro linking hypotheses is provided in Section 2.2, where the Taylor approach, according to TAYLOR [134], is used in the following. According to this assumption, each material element of the crystal grains is assumed to have equal volume and to undergo the deformation

$$\mathcal{F}(t) = \bar{\mathcal{F}}(t) \in \mathcal{SL}(3) \quad (4.2)$$

at any point in the reference configuration. Thus, the local deformation of the microstructure is affine to the macro deformation gradient (2.5) that does not allow for local displacement fluctuations.

4.1.2. Rigid-Plastic Decomposition of Crystal Deformation. The deformation (4.2) of a crystal at the point $\bar{\mathbf{X}} \in \mathcal{B}$ of the polycrystalline microstructure is multiplicatively decomposed by

$$\mathcal{F}(t) = \mathbf{R}^l(t) \mathbf{F}^p(t) \quad (4.3)$$

into a part $\mathbf{F}^p(t) \in \mathcal{SL}(3)$ solely due to plastic slip on given crystallographic slip systems and a rigid lattice rotation $\mathbf{R}^l(t)$ of the crystal lattice into its current configuration. In RASHID [122], DAFALIAS [40] or KUMAR & DAWSON [73, 74, 75] for instance elastic contributions are neglected and the model is considered as rigid-plastic. According to BUNGE [36] this assumption is reasonable for the determination of texture evolution in the range of fully developed plastic flow at large strains. The multiplicative decomposition of the deformation is visualized in Figure 4.1. Taking the time derivative of (4.3) gives

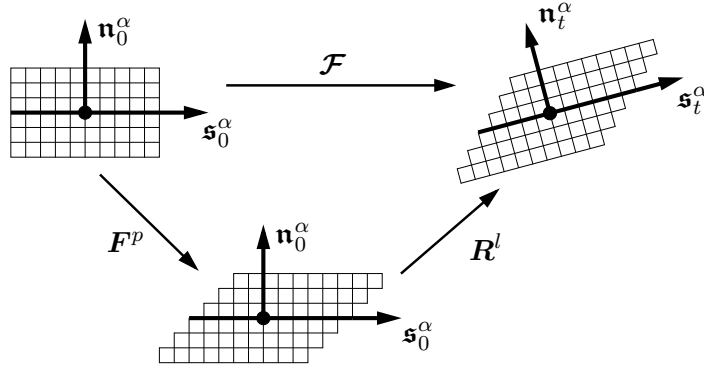


Figure 4.1: Basic geometry of rigid crystal plasticity. The plastic map $\mathbf{F}^p \in \mathcal{SL}(3)$ describes the dislocation flow as a simple shear mode. The lattice rotation $\mathbf{R}^l \in \mathcal{SO}(3)$ rotates the crystal into its current position.

the additive decomposition of the velocity gradient

$$\dot{\bar{\mathcal{F}}}(t) \bar{\mathcal{F}}^{-1}(t) = \dot{\mathbf{R}}^l(t) \mathbf{R}^{lT}(t) + \mathbf{R}^l(t) \left[\dot{\mathbf{F}}^p(t) \mathbf{F}^{p-1}(t) \right] \mathbf{R}^{lT}(t) , \quad (4.4)$$

by means of the Taylor assumption (4.2). Observe the decoupled contributions due to rigid rotation and plastic slip on the right hand side of this equation, which appears in the geometric representation of this rate relative to the intermediate configuration of the crystal. As derived in (3.13), the classical flow rule of crystal plasticity

$$\dot{\mathbf{F}}^p(t) \mathbf{F}^{p-1}(t) = \sum_{\alpha=1}^m \dot{\gamma}_t^\alpha \mathbf{s}_0^\alpha \otimes \mathbf{n}_0^\alpha \quad (4.5)$$

is written in terms of given crystallographic unit vectors $\{\mathbf{s}_0^\alpha, \mathbf{n}_0^\alpha\}$ for the slip directions and the slip plane normals of m slip systems $\alpha = 1, \dots, m$ in the initial configuration of the polycrystalline continuum. Recall, that $\dot{\gamma}_t^\alpha$ denotes the plastic slip on the system α and the plastic part \mathbf{F}^p of the deformation does not affect the slip system $\{\mathbf{s}_0^\alpha, \mathbf{n}_0^\alpha\}$. \mathbf{R}^l rotates the crystal lattice to its current configuration, see Figure 4.1, with the crystallographic structural vectors

$$\mathbf{s}_t^\alpha := \mathfrak{S}_i^\alpha \mathbf{g}_i^t \quad \text{and} \quad \mathbf{n}_t^\alpha := \mathfrak{N}_i^\alpha \mathbf{g}_i^t \quad (4.6)$$

in terms of the time-independent coordinates $\{\mathfrak{S}_i^\alpha, \mathfrak{N}_i^\alpha\}$ in the current lattice frame $\mathbf{g}_i^t = \mathbf{R}^l(t)\mathbf{e}_i$. (4.4) can be rewritten in the form

$$\dot{\mathcal{F}}\bar{\mathcal{F}}^{-1} = \dot{\mathbf{R}}^l(t)\mathbf{R}^{lT}(t) + \sum_{\alpha=1}^m \dot{\gamma}_t^\alpha \mathbf{s}_t^\alpha \otimes \mathbf{n}_t^\alpha. \quad (4.7)$$

4.1.3. Rate Equations of Rigid Crystal Plasticity. The macroscopic velocity gradient $\dot{\mathcal{F}}\bar{\mathcal{F}}^{-1} = \bar{\mathbf{D}}_t + \bar{\mathbf{W}}_t$ may be decomposed additively with

$$\bar{\mathbf{D}}_t := \text{sym}[\dot{\mathcal{F}}\bar{\mathcal{F}}^{-1}] \quad \text{and} \quad \bar{\mathbf{W}}_t := \text{skew}[\dot{\mathcal{F}}\bar{\mathcal{F}}^{-1}] \quad (4.8)$$

representing the macroscopic rate of deformation tensor $\bar{\mathbf{D}}_t$ and the macroscopic spin tensor $\bar{\mathbf{W}}_t$ as the symmetric and skew parts of the velocity gradient. Furthermore, current symmetric and skew second-order structural tensors

$$\mathfrak{P}_t^\alpha := \frac{1}{2} [\mathbf{s}_t^\alpha \otimes \mathbf{n}_t^\alpha + \mathbf{n}_t^\alpha \otimes \mathbf{s}_t^\alpha] \quad \text{and} \quad \mathfrak{Q}_t^\alpha := \frac{1}{2} [\mathbf{s}_t^\alpha \otimes \mathbf{n}_t^\alpha - \mathbf{n}_t^\alpha \otimes \mathbf{s}_t^\alpha]. \quad (4.9)$$

are defined. With these definitions at hand, a decomposition of (4.7) into symmetric and skew parts gives the two equations

$$\sum_{\alpha=1}^m \dot{\gamma}_t^\alpha \mathfrak{P}_t^\alpha = \underbrace{\text{sym}[\dot{\mathcal{F}}\bar{\mathcal{F}}^{-1}]}_{\bar{\mathbf{D}}_t} \quad \text{and} \quad \dot{\mathbf{R}}^l \mathbf{R}^{lT} = \underbrace{\text{skew}[\dot{\mathcal{F}}\bar{\mathcal{F}}^{-1}]}_{\bar{\mathbf{W}}_t} - \sum_{\alpha=1}^m \dot{\gamma}_t^\alpha \mathfrak{Q}_t^\alpha \quad (4.10)$$

corresponding to the two key rate equations of rigid crystal plasticity. These can be abbreviated by

$$\boxed{\mathbf{D}_t^p = \bar{\mathbf{D}}_t \quad \text{and} \quad \mathbf{W}_t^l = \bar{\mathbf{W}}_t - \mathbf{W}_t^p}, \quad (4.11)$$

i.e. the plastic rate of deformation $\mathbf{D}_t^p := \sum_{\alpha=1}^m \dot{\gamma}_t^\alpha \mathfrak{P}_t^\alpha$ can be identified with the macroscopic rate of deformation $\bar{\mathbf{D}}_t$ and the lattice spin $\mathbf{W}_t^l := \dot{\mathbf{R}}^l \mathbf{R}^{lT}$ is the difference between macroscopic spin $\bar{\mathbf{W}}_t$ and plastic spin $\mathbf{W}_t^p := \sum_{\alpha=1}^m \dot{\gamma}_t^\alpha \mathfrak{Q}_t^\alpha$. For a given macroscopic deformation of the polycrystal the plastic slip $\dot{\gamma}_t^\alpha$ can be calculated by (4.10)₁. With this at hand, the lattice spin, i.e. the reorientation velocity $\dot{\mathbf{R}}^l$, is determined with (4.10)₂, which is the key constitutive ingredient that governs the evolution of the crystal orientation distribution function. The solution of equations (4.11) is discussed in detail in the following two subsections. First, for the determination of the plastic slip two methods are presented. In Section 4.2.2 a power-type formulation is reviewed and in Section 4.2.3 the plastic slip of all active slip systems is determined, where the set of active slip systems is estimated by a purely kinematic argument. Afterwards the lattice spin and the crystal orientation are updated in an incremental setting, see Section 4.3.

4.2. Constitutive Formulation for the Determination of the Slip

4.2.1. Non-Uniqueness of Plastic Slip in Fcc and Bcc Crystals. Due to the deviatoric character of the structural tensors and the rate of deformation tensor $\text{tr}[\mathfrak{P}_t^\alpha] = 0$ and $\text{tr}[\bar{\mathbf{D}}_t] = 0$, the above system (4.10)₁ provides a maximum of $n = 5$ equations in the three-dimensional case and $n = 2$ equations in the two-dimensional case. As a consequence, this set of linear equations is non-unique for the case $m > n$ when the number m of slip systems exceeds the number n of independent degrees of $\bar{\mathbf{D}}_t$. Unfortunately, this is the

standard situation in crystal plasticity. Only for the case of planar crystals ($n = 2$) undergoing double slip ($m = 2$), the above purely kinematic condition (4.10)₁ yields a unique identification of the plastic slip and lattice rotation, see for example RASHID [122], DAFALIAS [40] and PRANTIL, JENKINS & DAWSON [114]. For the general case of three-dimensional crystal deformations through multislip, equation (4.10)₁ is not sufficient for a unique determination of the plastic slip, i.e. the $n = 5$ equations are not sufficient to determine the slip on the $m = 12$ or $m = 48$ slip systems of fcc or bcc crystals. To this end, additional constitutive assumptions which govern the slip activity of the plastically deforming crystal are necessary.

4.2.2. Standard Power-Type Formulation. For the determination of the plastic slip within a viscoplastic formulation, a classical Norton-type law

$$\dot{\gamma}_t^\alpha = a \frac{\tau_t^\alpha}{\tau_c} \left| \frac{\tau_t^\alpha}{\tau_c} \right|^{p-1} \quad \text{with} \quad \tau_t^\alpha := \mathfrak{P}_t^\alpha : \Sigma_t \quad (4.12)$$

is chosen as constitutive approach, cf. HUTCHINSON [62] and PEIRCE, ASARO & NEEDLEMAN [112]. τ_t^α is the resolved shear stress driving the plastic slip $\dot{\gamma}_t^\alpha$ on the $\alpha = 1, \dots, m$ slip systems. It is obtained by the symmetric second-order structural tensor \mathfrak{P}_t^α and the back-rotated Kirchhoff stress $\Sigma_t = \mathbf{R}_t^{l-1} \tau_t \mathbf{R}_t^l$ defined on the intermediate configuration. a , p and τ_c are parameters representing the reference slip rate, the power exponent and the critical resolved shear stress, respectively. With (4.11)₁ and (4.12) $2m + n$ equations are available for the determination of the plastic slip $\dot{\gamma}_t^\alpha$, the resolved shear stress τ_t^α and the stress Σ_t . Insertion of the constitutive approach (4.12) in (4.11)₁ yields the nonlinear system

$$\sum_{\alpha=1}^m a \frac{\tau_t^\alpha}{\tau_c} \left| \frac{\tau_t^\alpha}{\tau_c} \right|^{p-1} \mathfrak{P}_t^\alpha = \bar{D}_t \quad (4.13)$$

in Σ_t with n linear independent equations and the assumption of all m slip systems being active. For $p = 1$ the system is linear and the solution

$$\dot{\gamma}_t^\alpha = \mathfrak{P}_t^\alpha : \left[\sum_{\beta=1}^m \mathfrak{P}_t^\beta \otimes \mathfrak{P}_t^\beta \right]^{-1} : \bar{D}_t \quad (4.14)$$

for the plastic slip $\dot{\gamma}_t^\alpha$ does not depend on the parameters a , p and τ_c , i.e. it is purely geometric in nature. But as it provides $n < m$ equations, the choice $p = 1$ is not sufficient for the determination of the plastic slips. Otherwise, the assumption of all m slip systems being active is weighted by a large power exponent p resulting in dominant plastic slips for the resolved shear stress τ_t^α close to the critical shear stress τ_c . Hence, p serves as a parameter for a reasonable choice of an active set of slip systems. The resulting nonlinear system (4.13) needs to be solved by a Newton-type algorithm causing high computational costs.

4.2.3. Purely Geometric Approach. This purely geometric estimate for the determination of the plastic slip $\dot{\gamma}_t^\alpha$ for the case of multislip in crystals consists of three ingredients. In the first step, an active set of slip systems is obtained from the current rate of deformation by a purely kinematic argument. In the second step, the plastic slip on the active systems is determined by a quadratic optimization problem. As the kinematic constraint (4.10)₁ might be violated, the non-consistent active set needs to be enlarged in a third step.

4.2.3.1. First Estimate for Active Set of Slip Systems. In order to estimate a set of active slip systems based on a purely geometric argument, the rate of deformation tensor is projected onto the slip system, defining the pseudo-stresses

$$\tau_t^\alpha := \mathfrak{P}_t^\alpha : \bar{\mathbf{D}}_t \quad (4.15)$$

on the slip systems $\alpha = 1, \dots, m$. Pseudo-stresses means, that τ_t^α can be interpreted as fictitious resolved shear stress obtained from a viscous constitutive stress function $\bar{\Sigma}_t = \eta \bar{\mathbf{D}}_t$ with viscosity $\eta = 1$. Observe that these pseudo-stresses can be computed in a straightforward manner, because $\bar{\mathbf{D}}_t$ is prescribed. With these pseudo-stresses at hand, MIEHE & ROSATO [93] proposed a purely kinematic selection of an active set of slip systems in fcc crystals, which was expanded to bcc crystals by MIEHE, ROSATO & FRANKENREITER [94]. Let $\mathcal{S} := \{1, \dots, m\}$ denote the set of the $m = 12$ slip systems in a fcc crystal and $m = 48$ slip systems in a bcc crystal. This set can be subdivided into the m_G subgroups

$$\mathcal{S} = \bigcup_{p=1}^{m_G} \mathcal{S}^p, \quad (4.16)$$

with $m_G = 4$ for fcc crystals and $m_G = 16$ for bcc crystals, respectively. According to the definitions in Table 3.3, each of these subgroups

$$\mathcal{S}^1 := \{1, 2, 3\}, \quad \mathcal{S}^2 := \{4, 5, 6\}, \quad \mathcal{S}^3 := \{7, 8, 9\}, \quad \mathcal{S}^4 := \{10, 11, 12\} \quad (4.17)$$

consists of three slip systems for fcc crystals and the classification of slip systems in Table 3.4 yields

$$\begin{aligned} \mathcal{S}^1 &:= \{3, 7, 11\}, & \mathcal{S}^2 &:= \{16, 19, 22\}, & \mathcal{S}^3 &:= \{31, 36, 46\}, & \mathcal{S}^4 &:= \{28, 39, 42\}, \\ \mathcal{S}^5 &:= \{1, 6, 12\}, & \mathcal{S}^6 &:= \{15, 20, 21\}, & \mathcal{S}^7 &:= \{32, 35, 45\}, & \mathcal{S}^8 &:= \{27, 40, 41\}, \\ \mathcal{S}^9 &:= \{2, 8, 10\}, & \mathcal{S}^{10} &:= \{14, 17, 24\}, & \mathcal{S}^{11} &:= \{29, 34, 48\}, & \mathcal{S}^{12} &:= \{26, 37, 44\}, \\ \mathcal{S}^{13} &:= \{4, 5, 9\}, & \mathcal{S}^{14} &:= \{13, 18, 23\}, & \mathcal{S}^{15} &:= \{30, 33, 47\}, & \mathcal{S}^{16} &:= \{25, 38, 43\} \end{aligned} \quad (4.18)$$

for bcc crystals. These subgroups are chosen as for each of the subgroups $\{\mathcal{S}^p\}_{p=1, m_G}$, the sum $\sum_{\alpha \in \mathcal{S}^p} \mathfrak{P}^\alpha = \mathbf{0}$ vanishes and therefore $\sum_{\alpha \in \mathcal{S}^p} \tau_t^\alpha = 0$, see NEMAT NASSER [105]. Thus, the three pseudo stresses $\{\tau_t^\alpha\}_{\alpha \in \mathcal{S}^p}$ on a typical slip plane p are linear dependent. Assuming that some of the pseudo stresses reach a critical value where a plastic slip is activated, the above argument restricts the number of simultaneously possible active systems on a plane to two. Assuming at least two of the pseudo stresses to be non-zero in each subgroup, the relevant active systems are characterized by the subgroup criterion

$$\mathcal{A}_t^p := \{ \alpha \in \mathcal{S}^p \mid |\tau_t^\alpha| = \frac{3}{2} \bar{\tau}_t^p \} \subset \mathcal{S}^p \quad \text{with} \quad \bar{\tau}_t^p := \frac{1}{3} \sum_{\alpha \in \mathcal{S}^p} |\tau_t^\alpha|, \quad (4.19)$$

with the arithmetic average $\bar{\tau}_t^p$ of the absolute values of the pseudo stresses on the slip plane p . Considering for example the plane $p = 1$ of a fcc crystal, two important cases can appear. For (i) $\tau^1 = \tau^2 = k$, according to $\sum_{\alpha \in \mathcal{S}^p} \tau_t^\alpha = 0$ the third shear stress needs to be $\tau^3 = -2k$, for arbitrary $k \in \mathbb{R}$. Hence, only one system $\alpha = 3$ is active. If (ii) $\tau^1 = -\tau^2 = k$ and $\tau^3 = 0$, the two systems $\alpha = 1, 2$ are active. The same can be applied to the subgroups of bcc crystals. In order to weight the response of the full fcc crystal with simultaneous slip activity on the $p = 1, \dots, m_G$ planes, a criterion needs to take all

systems into account. Similar to the subgroup criterion (4.19), a global criterion for slip activity

$$\mathcal{A}_t := \{ \alpha \in \mathcal{S} \mid |\tau_t^\alpha| \geq \kappa \frac{3}{2} \bar{\tau}_t \} \subset \mathcal{S} \quad \text{with} \quad \bar{\tau}_t := \frac{1}{m_G} \sum_{p=1}^{m_G} \bar{\tau}_t^p \quad (4.20)$$

is formulated in terms of the arithmetic average $\bar{\tau}_t$ of the mean values of the pseudo stresses on the planes. The parameter κ influences the sharpness of the chosen active set. It is assumed to be in the range

$$\frac{2}{3} \leq \kappa \leq 1 . \quad (4.21)$$

The selection procedure picks out a number $m_{\mathcal{A}} \leq 2m_G < m$ of most loaded systems and ensures that a maximum of two systems can be active on each slip plane. Thus, a maximum number of $m_{\mathcal{A}} = 2m_G$ active slip systems is possible in the case of a fully developed plastic flow in fcc and bcc crystals.

In summary, the proposed estimate of a purely kinematic selection of an active set of slip systems in fcc and bcc crystals follows by combination of (4.19) and (4.20) in the compact statement

$$\mathcal{A}_t := \{ \alpha \in \mathcal{S} \mid |\tau_t^\alpha| \geq \kappa \frac{3}{2} \frac{1}{m} \sum_{\beta=1}^m |\tau_t^\beta| \} \subset \mathcal{S} . \quad (4.22)$$

Observe, that this definition of the selection procedure is purely geometric in nature and follows directly for a given rate of deformation tensor $\bar{\mathbf{D}}_t$ of the crystal. The performance of the selection procedure was demonstrated in MIEHE & ROSATO [93] for fcc crystals and in MIEHE, ROSATO & FRANKENREITER [94] for bcc crystals to give excellent texture estimates for representative deformation modes of polycrystalline aggregates.

4.2.3.2. Slip on Active Systems Obtained by Optimization. For a given first estimate of the active set (4.22), the current slip is computed from the optimization condition

$$\sum_{\alpha \in \mathcal{A}_t} |\dot{\gamma}_t^\alpha| \rightarrow \text{Min!} \quad (4.23)$$

Obviously, for the case of ideal plasticity with critical resolved shear stress τ_c such a solution minimizes the power $\sum_{\alpha \in \mathcal{A}_t} \tau_c |\dot{\gamma}_t^\alpha|$ needed for the plastic deformation of the crystal, see ANAND & KOTHARI [10]. Contrarily to TAYLOR [134] and BISHOP & HILL [24, 23], the criterion (4.23) is not used for the selection of the active slip systems, but in combination with the particular active set \mathcal{A}_t (4.22) for the determination of the plastic slip $\dot{\gamma}_t^\alpha$. The minimization problem (4.23) is subject to the constraint (4.10)₁, included in the penalty-type functional

$$\tilde{P}_t(\{\dot{\gamma}_t^\alpha\}_{\alpha \in \mathcal{A}_t}) = \frac{1}{2} \sum_{\alpha \in \mathcal{A}_t} |\dot{\gamma}_t^\alpha|^2 + \frac{1}{2\epsilon} \left[\sum_{\beta \in \mathcal{A}_t} \dot{\gamma}_t^\beta \mathfrak{P}_t^\beta - \bar{\mathbf{D}}_t \right]^2 \rightarrow \text{Stat!} \quad (4.24)$$

where $1/\epsilon$ is a constant penalty factor. The necessary condition of this stationary problem gives a linear system of equations of the dimension $\dim[\mathcal{A}_t] < m$ for the current slip

$$\sum_{\beta \in \mathcal{A}_t} \left[\epsilon \delta^{\alpha\beta} + \mathfrak{P}_t^\alpha : \mathfrak{P}_t^\beta \right] \dot{\gamma}_t^\beta = \mathfrak{P}_t^\alpha : \bar{\mathbf{D}}_t \quad \text{for } \alpha \in \mathcal{A}_t , \quad (4.25)$$

which can be solved for the non-zero slip $\dot{\gamma}_t^\beta$ with $\beta \in \mathcal{A}_t$. Clearly, the slip $\dot{\gamma}_t^\beta$ on the non-active systems $\beta \in \mathcal{S} \setminus \mathcal{A}_t$ is set to zero. Note, that the inverse penalty parameter ϵ plays in a natural way the role of a regularization of the singular matrix $\mathfrak{P}_t^\alpha : \mathfrak{P}_t^\beta$, with $\delta^{\alpha\beta}$ representing to the Kronecker-Delta. The matrix becomes well-posed due to diagonal regularization. A convenient choice is $\epsilon = 10^{-8}$ for double precision machines.

4.2.3.3. Enlargement of Non-Consistent Active Set. The fast estimate of the active set may in some situations not be consistent with the kinematic constraint (4.10)₁, i.e. the residual

$$\mathcal{R}_t := \bar{D}_t - \sum_{\alpha \in \mathcal{A}_t} \dot{\gamma}_t^\alpha \mathfrak{P}_t^\alpha \neq \mathbf{0} \quad (4.26)$$

is non-zero. In order to achieve consistency for the case $|\mathcal{R}_t| \neq \mathbf{0}$, the active set is enlarged by the maximum loaded system

$$\boxed{\mathcal{A}_t \leftarrow \mathcal{A}_t \cup \left\{ \text{Arg} \left[\max_{\alpha \in \mathcal{S}_{res}} [\tau_t^\alpha] \right] \right\}} \quad (4.27)$$

with the possible residual variables

$$\mathcal{S}_{res} := \{[\alpha \in \mathcal{S} \setminus \mathcal{A}_t] \wedge [\dim[\mathcal{S}^p(\alpha)] \leq 2]\} \quad (4.28)$$

for the non-active system such that no more than two systems are active on one plane p . With the new set \mathcal{A}_t the slip for the enlarged active set is recomputed via (4.25) until the condition $|\mathcal{R}_t| < tol$ is satisfied. The computational case of studies shows that only very few iterations for this consistency update are necessary. Note carefully, that in contrast to power-type formulations based on Norton-Bayley-type viscosity laws, the formulation is linear based on the reduced system size $\dim[\mathcal{A}_t] < m$ of the matrix with active systems. This is a key source for the fast solution of the proposed selection procedure.

4.3. Fast Incremental Updates of Crystal Orientation

In this subsection the determination of the crystal orientation is analyzed within an incremental formulation at discrete time steps. All internal variables at time t_n on a time interval $[t_n, t_{n+1}] \in \mathbb{R}_+$ are known. The subsequent steps concern the successive update of the crystal reorientation within the time increment under consideration.

4.3.1. Incremental Macroscopic Deformation. The first ingredient of the time-discrete setting concerns the definition of the incremental macroscopic deformation. To this end, consider a deformation-driven scenario where the last macroscopic deformation $\bar{\varphi}_n(\bar{\mathbf{X}})$ at time t_n and the current value $\bar{\varphi}_{n+1}(\bar{\mathbf{X}})$ at time t_{n+1} are given. Within a midpoint-type objective integration algorithm the deformation update of the polycrystal is related to the midpoint of these configurations, i.e.

$$\bar{\varphi}_{n+1/2}(\bar{\mathbf{X}}) = \frac{1}{2} [\bar{\varphi}_{n+1}(\bar{\mathbf{X}}) + \bar{\varphi}_n(\bar{\mathbf{X}})] . \quad (4.29)$$

In a typical time interval the macroscopic deformation gradient of the midpoint configuration reads

$$\bar{\mathcal{F}}_{n+1/2} := \nabla_{\bar{\mathbf{X}}} \bar{\varphi}_{n+1/2} = \frac{1}{2} [\bar{\mathcal{F}}_{n+1} + \bar{\mathcal{F}}_n] , \quad (4.30)$$

cf. Figure 4.2. The objective integration of the macroscopic spatial velocity gradient

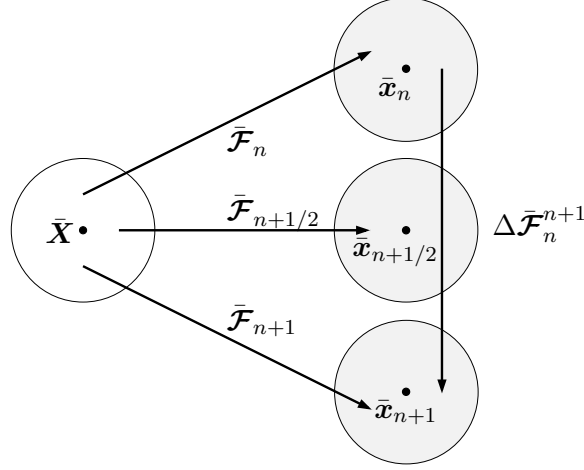


Figure 4.2: Algorithmic midpoint configuration of the polycrystalline aggregate. The incremental macroscopic deformation gradient $\Delta \bar{\mathcal{F}}_n^{n+1} := \bar{\mathcal{F}}_{n+1} \bar{\mathcal{F}}_n^{-1}$ along with the midpoint deformation gradient $\bar{\mathcal{F}}_{n+1/2} := [\bar{\mathcal{F}}_{n+1} + \bar{\mathcal{F}}_n]/2$ define the incremental spatial displacement gradient $\bar{\mathbf{H}}_{n+1/2} := [\bar{\mathcal{F}}_{n+1} - \bar{\mathcal{F}}_n] \bar{\mathcal{F}}_{n+1/2}^{-1}$ of the aggregate relative to the midpoint configuration.

$\bar{\mathbf{l}} = \dot{\bar{\mathcal{F}}} \bar{\mathcal{F}}^{-1}$ by a midpoint rule and the conversion $\bar{\mathcal{F}}_{n+1} - \bar{\mathcal{F}}_n = (\bar{\mathcal{F}}_{n+1} \bar{\mathcal{F}}_n^{-1} - \mathbf{1}) \bar{\mathcal{F}}_n$ gives the result

$$\bar{\mathbf{H}}_{n+1/2} \bar{\mathcal{F}}_{n+1/2} = \bar{\mathcal{F}}_{n+1} - \bar{\mathcal{F}}_n, \quad (4.31)$$

with the incremental macroscopic displacement gradient $\bar{\mathbf{H}}_{n+1/2} = \Delta t \bar{\mathbf{l}}_{n+1/2}$. This equation is solved for the incremental spatial displacement gradient

$$\bar{\mathbf{H}}_{n+1/2} = 2 [\bar{\mathcal{F}}_{n+1} - \bar{\mathcal{F}}_n] [\bar{\mathcal{F}}_{n+1} + \bar{\mathcal{F}}_n]^{-1} \quad (4.32)$$

that deforms the polycrystal in the time increment $[t_n, t_{n+1}]$. This is the gradient of the incremental displacement $\bar{\mathbf{u}}_n^{n+1} := [\bar{\varphi}_{n+1} - \bar{\varphi}_n] \circ \bar{\varphi}_{n+1/2}^{-1}(\bar{\mathbf{X}})$ with regard to the midpoint coordinates $\bar{\mathbf{x}}_{n+1/2} = \bar{\varphi}_{n+1/2}(\bar{\mathbf{X}})$, i.e.

$$\bar{\mathbf{H}}_{n+1/2} = \nabla_{\bar{\mathbf{x}}_{n+1/2}} \bar{\mathbf{u}}_n^{n+1}(\bar{\mathbf{x}}_{n+1/2}). \quad (4.33)$$

The symmetric and skew parts of the incremental displacement gradient

$$\bar{\mathbf{D}}_{n+1/2}^* := \text{sym}[\bar{\mathbf{H}}_{n+1/2}] \quad \text{and} \quad \bar{\mathbf{W}}_{n+1/2}^* := \text{skew}[\bar{\mathbf{H}}_{n+1/2}] \quad (4.34)$$

are then time-discrete counterparts of the continuous macroscopic rate of deformation and spin tensors in the sense $\bar{\mathbf{D}}_{n+1/2}^* = \bar{\mathbf{D}}_{n+1/2} \Delta t$ and $\bar{\mathbf{W}}_{n+1/2}^* = \bar{\mathbf{W}}_{n+1/2} \Delta t$. The definitions (4.34) are objective in the following sense. Assuming a pure incremental rotation $\Delta \bar{\mathcal{F}}_n^{n+1} = \bar{\mathcal{F}}_{n+1} \bar{\mathcal{F}}_n^{-1} = \mathbf{Q} \in \mathcal{SO}(3)$, the incremental displacement gradient is expected to vanish, i.e. $\bar{\mathbf{D}}_{n+1/2}^* = \mathbf{0}$. This reflects the demand of objectivity in the time increment $[t_n, t_{n+1}]$ under consideration. In this situation (4.32) yields the skew tensor

$$\bar{\mathbf{H}}_{n+1/2} = 2[\bar{\mathcal{F}}_{n+1} \bar{\mathcal{F}}_n^{-1} - \mathbf{1}][\bar{\mathcal{F}}_{n+1} \bar{\mathcal{F}}_n^{-1} + \mathbf{1}]^{-1} = 2[\mathbf{Q} - \mathbf{1}][\mathbf{Q} + \mathbf{1}]^{-1}, \quad (4.35)$$

which underlines the desired feature of the proposed integration algorithm.

4.3.2. Incremental Equations of Rigid Crystal Plasticity. With the above incremental macroscopic deformation at hand, the time discrete algorithmic counterpart of (4.10)

$$\sum_{\alpha=1}^m \Delta\gamma_{n+1/2}^{\alpha} \mathfrak{P}_n^{\alpha} = \bar{D}_{n+1/2}^* \quad (4.36)$$

is used for the update of the incremental slip $\Delta\gamma_{n+1/2}^{\alpha}$ and for the exponential update of the lattice rotation

$$\mathbf{R}_{n+1}^l = \exp[\mathbf{W}_{n+1/2}^{l*}] \mathbf{R}_n^l \quad \text{with} \quad \mathbf{W}_{n+1/2}^{l*} := \bar{\mathbf{W}}_{n+1/2}^* - \sum_{\alpha=1}^m \Delta\gamma_{n+1/2}^{\alpha} \mathfrak{Q}_n^{\alpha}, \quad (4.37)$$

compare (3.31). Note carefully, that an explicit dependence of the algorithm on the structural tensors \mathfrak{P}_n^{α} and \mathfrak{Q}_n^{α} at time t_n is considered. Thus, (4.36) is linear for given $\bar{D}_{n+1/2}^*$ in the deformation-driven context.

4.3.3. Algorithmic Determination of Plastic Slip. Two algorithmic treatments are presented for the determination of the plastic slip, i.e. the power-type formulation discussed in Section 4.2.2 and the formulation with a geometric estimate of the active slip presented in Section 4.2.3.

4.3.3.1. Power-Type Slip Law. The incremental form of equation (4.12) for the standard power-type slip law reads

$$\Delta\gamma_{n+1}^{\alpha} = \Delta t_{n+1} a \frac{\tau_{n+1}^{\alpha}}{\tau_c} \left| \frac{\tau_{n+1}^{\alpha}}{\tau_c} \right|^{p-1} \quad \text{with} \quad \tau_{n+1}^{\alpha} := \mathfrak{P}^{\alpha} : \Sigma_{n+1}, \quad (4.38)$$

with the incremental time step Δt_{n+1} . Similar to the continuous setting, by insertion of the discrete key equations (4.36), the nonlinear system

$$\mathfrak{R}_{n+1}(\Sigma_{n+1}) := \sum_{\alpha=1}^m \Delta t_{n+1} a \frac{\tau_{n+1}^{\alpha}}{\tau_c} \left| \frac{\tau_{n+1}^{\alpha}}{\tau_c} \right|^{p-1} \mathfrak{P}^{\alpha} - \bar{D}_{n+1/2}^* = \mathbf{0} \quad (4.39)$$

has to be solved for the stress deviator Σ_{n+1} for given $\bar{D}_{n+1/2}^*$. High values of p model dominant active slip systems α for τ^{α} close to τ_c causing a high nonlinear equation to be solved. Due to the deviatoric character of the rate of deformation and the stresses, this system provides five equations for the determination of the stress Σ , which is updated in a Newton iteration

$$\Sigma_{n+1} \leftarrow \Sigma_{n+1} - \mathbf{K}_{n+1}(\Sigma_{n+1})^{-1} \mathfrak{R}(\Sigma_{n+1}) \quad (4.40)$$

until convergence is reached, i.e. $|\mathfrak{R}_{n+1}| < tol$. Herein,

$$\mathbf{K}_{n+1}(\Sigma_{n+1}) := \frac{\partial \mathfrak{R}_{n+1}(\Sigma_{n+1})}{\partial \Sigma_{n+1}} = \sum_{\alpha=1}^m \Delta t_{n+1} a \frac{p}{\tau_c} \left| \frac{\tau_{n+1}^{\alpha}}{\tau_c} \right|^{p-1} \mathfrak{P}^{\alpha} \otimes \mathfrak{P}^{\alpha} \quad (4.41)$$

is the tangent. As \mathbf{K}_{n+1} is deviatoric, its inversion needs to be performed in the deviatoric space. The incremental plastic slip $\Delta\gamma_{n+1}^{\alpha}$ is then obtained for known current stresses Σ_{n+1} according to (4.38). Newtons method does not guaranty a convergence for any starting point. Therefore, PRESS, TEUKOLSKI, VETTERLING & FLANNERY [115] suggest a combination of Newtons method allowing a fast local convergence with a globally convergent method guarantying convergence from any starting point.

4.3.3.2. Geometric Estimate of Plastic Slip. For a given incremental Eulerian deformation $\bar{\mathbf{D}}_{n+1/2}^*$, (4.36) yields the incremental plastic slip by the procedure outlined in Section 4.2.3 for the continuous setting. In the algorithmic setting, the pseudo Schmid stress (4.15)

$$\tau_{n+1/2}^\alpha := \mathfrak{P}_n^\alpha : \bar{\mathbf{D}}_{n+1/2} \quad (4.42)$$

is defined to depend explicitly on the structural tensor \mathfrak{P}_n^α at time t_n . Thus, the pseudo Schmid stress is considered to be constant in the deformation-driven incremental process. As the symmetric structural tensor and axial vector of the skew structural tensor

$$\mathfrak{P}_n^\alpha := \text{sym}[\mathbf{s}_n^\alpha \otimes \mathbf{n}_n^\alpha] \quad \text{and} \quad \mathbf{q}_n^\alpha := \text{vect}\{\text{skew}[\mathbf{s}_n^\alpha \otimes \mathbf{n}_n^\alpha]\} \quad (4.43)$$

are obtained from the slip directions $\mathbf{s}_n^\alpha := \mathfrak{S}_i^\alpha \mathbf{g}_i^n$ and slip normals $\mathbf{n}_n^\alpha := \mathfrak{N}_i^\alpha \mathbf{g}_i^n$, these need to be transformed to the lattice frame \mathbf{g}_i^n . Therefore, the rotation is parametrized with Rodrigues parameters \mathbf{r} , discussed in detail in Section 3.3.1.5. The lattice frame

$$\mathbf{g}_i^n := \mathbf{e}_i + 2[\mathbf{r}_n \times \mathbf{e}_i + \mathbf{r}_n \times (\mathbf{r}_n \times \mathbf{e}_i)] / (1 + \mathbf{r}_n \cdot \mathbf{r}_n) \quad (4.44)$$

is then given by rotation of the sample frame \mathbf{e}_i by means of the Rodrigues parameters \mathbf{r}_n at time t_n . From the Schmid stresses, the active set

$$\mathcal{A}_{n+1/2} := \left\{ \alpha \in \mathcal{S} \mid |\tau_{n+1/2}^\alpha| \geq \kappa \frac{3}{2} \frac{1}{m} \sum_{\beta=1}^m |\tau_{n+1/2}^\beta| \right\} \quad (4.45)$$

can be estimated and the associated incremental slips

$$\Delta\gamma_{n+1/2}^\alpha = \sum_{\beta \in \mathcal{A}_{n+1/2}} [\epsilon \delta^{\alpha\beta} + \mathfrak{P}_n^\alpha : \mathfrak{P}_n^\beta]^{-1} [\mathfrak{P}_n^\beta : \bar{\mathbf{D}}_{n+1/2}] \quad (4.46)$$

are computed. For a non-consistent active set $|\mathcal{R}_{n+1/2}| > \text{tol}$ with $|\mathcal{R}_{n+1/2}| := \bar{\mathbf{D}}_{n+1/2} - \sum_{\alpha \in \mathcal{A}_{n+1/2}} \Delta\gamma_{n+1/2}^\alpha \mathfrak{P}_n^\alpha$ the active set is enlarged by the maximum loaded non-active system

$$\mathcal{A}_{n+1/2} \leftarrow \mathcal{A}_{n+1/2} \cup \left\{ \text{Arg} \left[\max_{\alpha \in \mathcal{S}_{res}^c} |\tau_{n+1/2}^\alpha| \right] \right\}, \quad (4.47)$$

otherwise the lattice rotation is updated. Recall, that a maximum of two systems can be active on one crystallographic plane.

4.3.4. Incremental Update of Orientation. With known plastic slip $\Delta\gamma_{n+1/2}^\alpha$, the incremental lattice rotation can be updated by the exponential algorithm (4.37). This update can be evaluated in closed-form by the Euler-Rodrigues formula. To this end, the axial vector

$$\boldsymbol{\omega}_{n+1/2}^{l*} = \text{vect}[\mathbf{W}_{n+1/2}^{l*}] \quad (4.48)$$

and similar to (3.28) the closed-form representation of the incremental rotation

$$\exp[\mathbf{W}_{n+1/2}^{l*}] = \mathbf{1} + \frac{\sin |\boldsymbol{\omega}_{n+1/2}^{l*}|}{|\boldsymbol{\omega}_{n+1/2}^{l*}|} \mathbf{W}_{n+1/2}^{l*} + \frac{1}{2} \left[\frac{\sin |\boldsymbol{\omega}_{n+1/2}^{l*}|/2}{|\boldsymbol{\omega}_{n+1/2}^{l*}|/2} \right]^2 \mathbf{W}_{n+1/2}^{l*2} \quad (4.49)$$

can be computed. With this at hand, the update of the rotation is then given in (4.37)₁. Alternatively, the incremental rotation can directly be formulated in terms of the Rodrigues vector parametrization. With the axial vector (4.48), equation (3.43) yields the straightforward result

$$\mathbf{r}_n^{n+1} = \tan[|\boldsymbol{\omega}_{n+1/2}^{l*}|/2] \frac{\boldsymbol{\omega}_{n+1/2}^{l*}}{|\boldsymbol{\omega}_{n+1/2}^{l*}|} \quad (4.50)$$

Box 4.1: *ALGO*: Incremental update of lattice orientation in fcc/bcc crystals.

1. *Initialization.* Let $\{\mathbf{r}_n^c\}_{c=1,\dots,E^h}$ be the known lattice orientations of E^h crystal grains at time t_n . Given are the macroscopic deformations of the polycrystal $\bar{\mathcal{F}}_n$ and $\bar{\mathcal{F}}_{n+1}$ at t_n and t_{n+1} , respectively. Initialize the crystal counter $c = 1$.

2. *Macro-deformation.* Get incremental gradient $\bar{\mathbf{H}}_{n+1/2} := (\bar{\mathcal{F}}_{n+1} - \bar{\mathcal{F}}_n) \left[\frac{1}{2} (\bar{\mathcal{F}}_{n+1} + \bar{\mathcal{F}}_n) \right]^{-1}$ and compute incremental deformation tensor and axial spin vector

$$\bar{\mathbf{D}}_{n+1/2} := \text{dev}\{\text{sym}[\bar{\mathbf{H}}_{n+1/2}]\} \quad \text{and} \quad \bar{\boldsymbol{\omega}}_{n+1/2} := \text{vect}\{\text{skew}[\bar{\mathbf{H}}_{n+1/2}]\}$$

3. *Structural tensors.* Get lattice frame $\mathbf{g}_i^{c_n} := \mathbf{e}_i + 2[\mathbf{r}_n^c \times \mathbf{e}_i + \mathbf{r}_n^c \times (\mathbf{r}_n^c \times \mathbf{e}_i)] / (1 + \mathbf{r}_n^c \cdot \mathbf{r}_n^c)$, the slip directions and normals $\mathbf{s}_n^{c\alpha} := \mathfrak{S}_i^\alpha \mathbf{g}_i^{c_n}$ and $\mathbf{n}_n^{c\alpha} := \mathfrak{N}_i^\alpha \mathbf{g}_i^{c_n}$ and compute $\alpha = 1, \dots, m$ structural tensors of crystal c at time t_n

$$\mathfrak{P}_n^{c\alpha} := \text{sym}[\mathbf{s}_n^{c\alpha} \otimes \mathbf{n}_n^{c\alpha}] \quad \text{and} \quad \mathbf{q}_n^{c\alpha} := \text{vect}\{\text{skew}[\mathbf{s}_n^{c\alpha} \otimes \mathbf{n}_n^{c\alpha}]\}$$

4. *Active set estimate.* Get pseudo stresses $\tau_{n+1/2}^{c\alpha} := \mathfrak{P}_n^{c\alpha} : \bar{\mathbf{D}}_{n+1/2}$ and set

$$\mathcal{A}_{n+1/2}^c := \left\{ \alpha \in \mathcal{S} \mid |\tau_{n+1/2}^{c\alpha}| \geq \kappa \frac{3}{2} \frac{1}{m} \sum_{\beta=1}^m |\tau_{n+1/2}^{c\beta}| \right\}$$

5. *Incremental slip.* Compute slip on active systems $\alpha \in \mathcal{A}_{n+1/2}^c$ by the linear update

$$\Delta\gamma_{n+1/2}^{c\alpha} = \sum_{\beta \in \mathcal{A}_{n+1/2}^c} \left[\epsilon \delta^{\alpha\beta} + \mathfrak{P}_n^{c\alpha} : \mathfrak{P}_n^{c\beta} \right]^{-1} \left[\mathfrak{P}_n^{c\beta} : \bar{\mathbf{D}}_{n+1/2} \right]$$

6. *Consistency check.* Define residual $\mathcal{R}_{n+1/2}^c := \bar{\mathbf{D}}_{n+1/2} - \sum_{\alpha \in \mathcal{A}_{n+1/2}^c} \Delta\gamma_{n+1/2}^{c\alpha} \mathfrak{P}_n^{c\alpha}$. For a consistent active set $|\mathcal{R}_{n+1/2}^c| \leq \text{tol}$, go to 8.

7. *Enlarge active set.* Enlarge active set by maximum loaded non-active system

$$\mathcal{A}_{n+1/2}^c \Leftarrow \mathcal{A}_{n+1/2}^c \cup \left\{ \text{Arg} \left[\max_{\alpha \in \mathcal{S}_{res}^c} |\tau_{n+1/2}^{c\alpha}| \right] \right\}$$

with $\mathcal{S}_{res}^c := \{[\alpha \in \mathcal{S} \setminus \mathcal{A}_{n+1/2}^c] \wedge [\dim[\mathcal{S}^p(\alpha)] \leq 2]\}$ and go to 5.

8. *Lattice rotation.* Compute the incremental lattice spin tensor

$$\boldsymbol{\omega}_{n+1/2}^{cl} := \bar{\boldsymbol{\omega}}_{n+1/2} - \sum_{\alpha \in \mathcal{A}_{n+1/2}^c} \Delta\gamma_{n+1/2}^{c\alpha} \mathbf{q}_n^{i\alpha}$$

and update the lattice orientation

$$\mathbf{r}_{n+1}^c = \frac{\mathbf{r}_n^{cn+1} + \mathbf{r}_n^c - \mathbf{r}_n^{cn+1} \times \mathbf{r}_n^c}{1 - \mathbf{r}_n^{cn+1} \cdot \mathbf{r}_n^c} \quad \text{with} \quad \mathbf{r}_n^{cn+1} := \tan \left[\frac{|\boldsymbol{\omega}_{n+1/2}^{cl}|/2}{\left| \frac{\boldsymbol{\omega}_{n+1/2}^{cl}}{|\boldsymbol{\omega}_{n+1/2}^{cl}|} \right|} \right]$$

9. *Advance crystal counter.* Set $c \Leftarrow c + 1$. For $c \leq E^h$, go to 3.

for the Rodrigues vector that parametrizes the incremental rotation. The update of the Rodrigues vectors dual to (4.37)₁ then follows from the standard composition rule of Rodrigues vectors as outlined for example in BECKER & PANCHANADEESWARAN [22],

i.e.

$$\mathbf{r}_{n+1} = \frac{\mathbf{r}_n^{n+1} + \mathbf{r}_n - \mathbf{r}_n^{n+1} \times \mathbf{r}_n}{1 - \mathbf{r}_n^{n+1} \cdot \mathbf{r}_n}, \quad (4.51)$$

analogous to the multiplication of quaternions, see equation (3.35). This update gives for known \mathbf{r}_n at time t_n directly the Rodrigues vector \mathbf{r}_{n+1} at time t_{n+1} . The algorithmic steps for the update of the lattice rotation of a polycrystalline aggregate is summarized in Box 4.1 for the purely geometric approach.

4.4. Representative Numerical Examples

In this subsection, the performance of the above discussed rigid-plastic active-set and rigid-plastic power-law models is demonstrated. For the sake of comparison several experimental results and simulation results serve as reference. With regard to the simulation results, the elastic-plastic active-set model of MIEHE & SCHOTTE [95] is chosen as a benchmark, as it is proven to yield good texture predictions. The subsection is divided in three parts, namely the texture development in planar crystals, face-centered cubic (fcc) crystals and body-centered cubic (bcc) crystals. For the first two parts, the reorientation process of single crystals is discussed before expanding to polycrystals. In a deformation-driven scenario, several deformation modes are chosen such as uniaxial compression, plane strain compression and simple shear modes. These are associated with the uniaxial compression, channel die compression and torsion used to examine large strain behavior of materials in industrial processes such as wire drawing, extrusion and rolling.

4.4.1. Texture Development in Planar Crystals. A descriptive representation of the above proposed method for orientation updates is obtained for the monotonic deformation of planar crystals exhibiting double slip. In this specific case, the reorientation θ_t is scalar and $m = 2$ slip systems exist. Here, the angle ξ specifies the separation angle between the two slip systems. For this planar double slip model, a closed form solution for the reorientation update is available. In the continuous setting it reads

$$\dot{\theta}_t = \Omega - [\sin(2\theta_t) \Lambda - \cos(2\theta_t) \Gamma] / \cos(2\xi) \quad \text{with} \quad \theta_t(t_0) = \theta_0 \quad (4.52)$$

in terms of the macroscopic rate of stretching Λ , rate of shearing Γ and spin Ω . A derivation of this continuous equation and its discrete counterpart can be found in Appendix A.

4.4.1.1. Reorientation of Planar Single Crystals. In order to point out the basic characteristics of deformation-induced lattice reorientations, the reorientation of a single crystal undergoing planar double slip is simulated. The subsequent investigations assume a slip system separation angle of $2\xi = 60^\circ$, corresponding to Asaro's planar double slip model, see ASARO [14]. Employing the closed-form algorithm of planar crystal plasticity

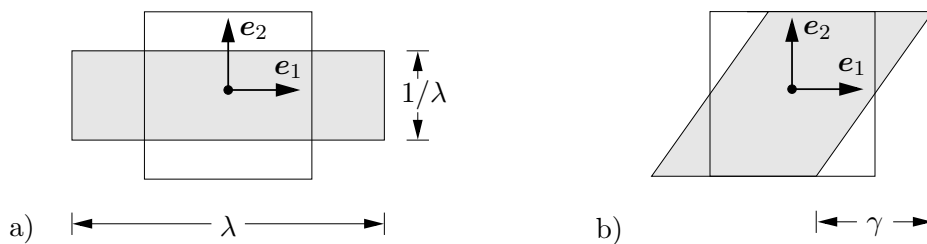


Figure 4.3: Homogeneous deformation tests. a) Pure shear test and b) simple shear test.

dual to (4.52) developed in Appendix A, a single crystal with an initial orientation of $\theta_0 = 80^\circ$ is deformed under pure shear up to a final deformation of $\lambda = 3.5$, cf. Figure 4.3a) for the definition of λ . The evolution of the crystal orientation θ_t throughout the subsequent deformation process is obtained by the closed-form update (A.11) and is visualized in Figure 4.4. It is observed that the crystal rotates from its initial orientation $\theta_0 = 80^\circ$ at $\lambda = 1.0$ towards the preferred orientation $\theta_t = 0^\circ$. The rotation saturates for

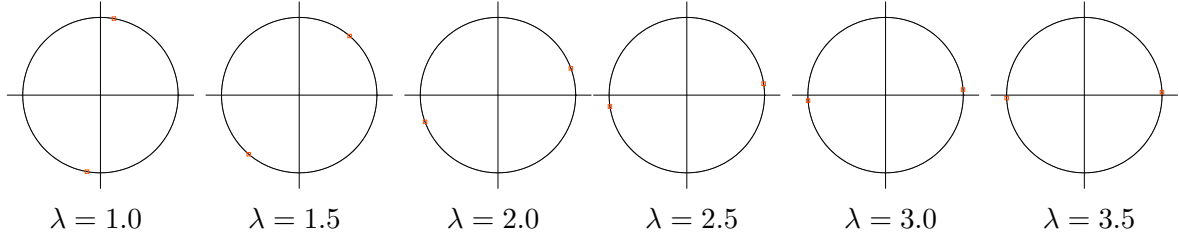


Figure 4.4: Planar single crystal undergoing double slip. Lattice reorientation under pure shear with initial orientation $\theta_0 = 80^\circ$. Rotation towards preferred orientation $\theta_t = 0^\circ$.

applied deformations beyond $\lambda = 3.0$. Another example is a homogeneous deformation test treating the simple shear of a single crystal, where the initial orientation is again chosen to $\theta_0 = 80^\circ$. The shear deformation is advanced from $\gamma = 0.0$ up to a final shear of $\gamma = 2.5$, see Figure 4.3b) for the definition of γ . The corresponding evolution of the lattice orientation is visualized in Figure 4.5. Here, the rotation saturates towards a final angle

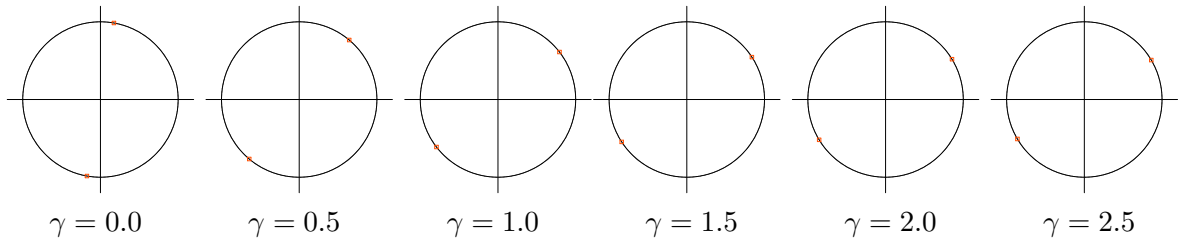


Figure 4.5: Planar single crystal undergoing double slip. Lattice reorientation under simple shear with initial orientation $\theta_0 = 80^\circ$. Rotation towards preferred orientation $\theta_t = 30^\circ$.

of $\theta_t = 30^\circ$ for the simple shear mode under consideration, which is directly correlated to the chosen slip separation angle $2\xi = 60^\circ$, compare PRANTIL, JENKINS & DAWSON [114]. These results are immediately observable from the closed form solution (4.52). For the pure shear test the saturation angle does not depend on the slip separation angle ξ , as $\Omega = \Gamma = 0$. In contrast, for the simple shear test $\Lambda = 0$ and $\Omega = -\Gamma$ holds and therefore the orientation saturates towards the slip separation angle ξ .

4.4.1.2. Reorientation of Planar Polycrystals. With the above basic mechanisms of single crystals at hand, the focus is now put on a comparative study of crystal reorientation for planar polycrystals undergoing the homogeneous deformation modes of pure and simple shear, illustrated in Figure 4.3. For the pure shear mode, the initial state is visualized in the first image of Figure 4.6 starting from an equidistant discretization of the orientation space, cf. (A.10). For the interval $[-\frac{\pi}{2}, \frac{\pi}{2}]$ of the orientation space, cf. Figure A.3, $E^h = 15$ orientations are chosen. The crystal orientations are updated using the closed-form solution (A.11). For all subsequent simulations, the slip system separation

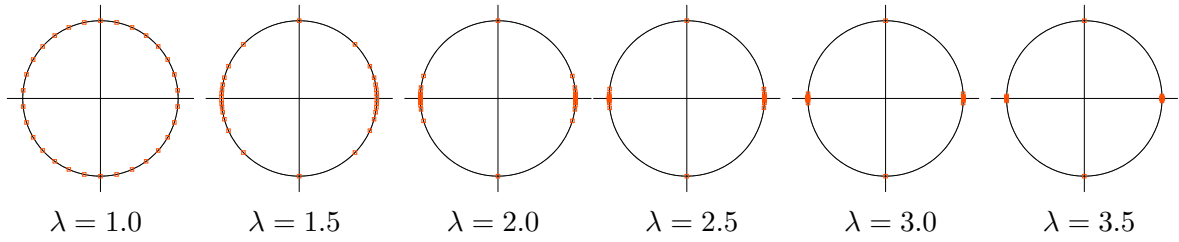


Figure 4.6: Planar polycrystal undergoing double slip. Lattice reorientation under pure shear with $E^h = 15$ orientations. Rotation towards preferred orientation $\theta_t = 0^\circ$.

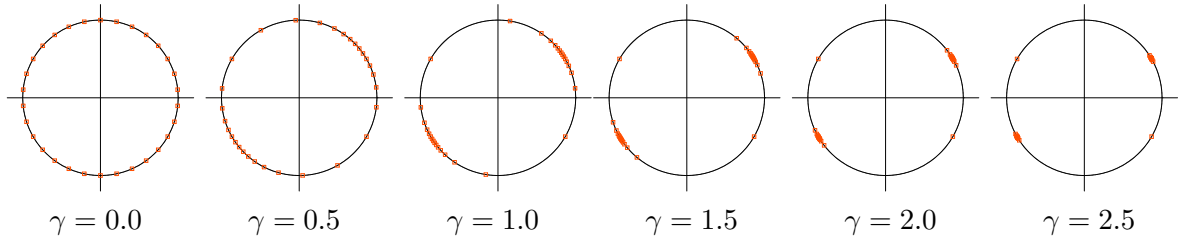


Figure 4.7: Planar polycrystal undergoing double slip. Lattice reorientation under simple shear with $E^h = 15$ orientations. Rotation towards preferred orientation $\theta_t = 30^\circ$.

angle is again taken to be $2\xi = 60^\circ$. Similar to the single crystals in the previous subsection, the polycrystal is subjected to homogeneous pure shear deformation up to $\lambda = 3.5$. Six levels of deformation are depicted in Figure 4.6. The initial configuration $\lambda = 1.0$ shows the equidistant partition of the orientation space with center points indicated by squares. As the deformation proceeds, the orientations move towards the preferred directions of 0° and 180° , similar to single crystals. For the simple shear test the evolution of the crystal orientations is shown in Figure 4.7. Again, six levels of deformation with a maximum shear of $\gamma = 2.5$ are depicted. Starting from an equidistant distribution of the orientations, a reorientation towards the preferred direction can be observed. Finally all grains are oriented at $30^\circ/210^\circ$, which results directly from the chosen slip separation angle $2\xi = 60^\circ$, as discussed above.

4.4.2. Texture Development in Fcc Crystals. In this subsection the two above outlined formulations are compared with regard to their capabilities of modeling the lattice reorientation in fcc single crystals and polycrystals with simulation and experimental results. As (i) reference, two different options are chosen. For the single crystal simulations, the elastic-plastic crystal plasticity model with active set search outlined in MIEHE, SCHOTTE & LAMBRECHT [96], MIEHE & SCHOTTE [95] serves as reference, as it is proven to predict the texture evolution in fcc crystals very well. For fcc polycrystalline aggregates experimental results are chosen as a sound reference. The (ii) geometric approach and the (iii) standard power-type setting have been derived in Section 4.2, while their algorithmic treatment has been presented in Section 4.3. For the deformation tests of single crystals a parametrization with Euler angles according to Section 3.3.1.2 is chosen, whereas for polycrystals a parametrization with Rodrigues vectors, presented in Section 3.3.1.5, is preferred. Fcc crystals are characterized by the 12 possible slip systems listed in Table 3.3, i.e. four $\{111\}$ planes with three $\langle 110 \rangle$ directions, see Figure 4.8 for an illustrative sketch. As discussed in Section 4.2.3 at the most 8 slip systems can be active at once. In

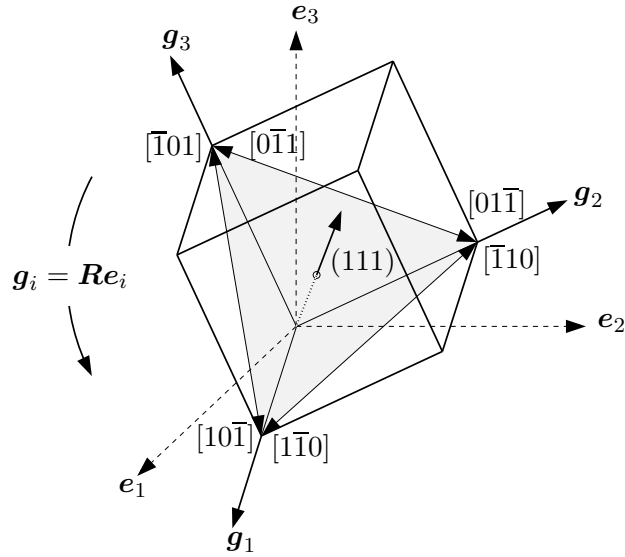


Figure 4.8: Orientation of the fcc unit cell. The standard Cartesian base $\{e_i\}_{i=1,2,3}$ is rotated to the base $\{g_i\}_{i=1,2,3}$ aligned to the fcc crystal. The (111) slip plane of the fcc crystal is marked by the shadow.

the subsequent simulations the parameters for the rigid-plastic active-set model with the update algorithm summarized in Box 4.1 are set to $\kappa = 1$, $\epsilon = 10^{-8}$ and $tol = 10^{-6}$ for the sharpness, regularization parameter and relative tolerance for the consistency check, respectively. The parameters for the rigid-plastic power-type model are chosen to $a = 1/s$ for the reference slip, $\tau_c = 7.17\text{MPa}$ for the critical resolved shear stress and $p = 20$ for the power exponent.

4.4.2.1. Deformation Tests for Fcc Single Crystals. Two different deformation modes are examined for single crystals. Initial and deformed configurations for simple compression and simple shear are illustrated in Figure 4.9.

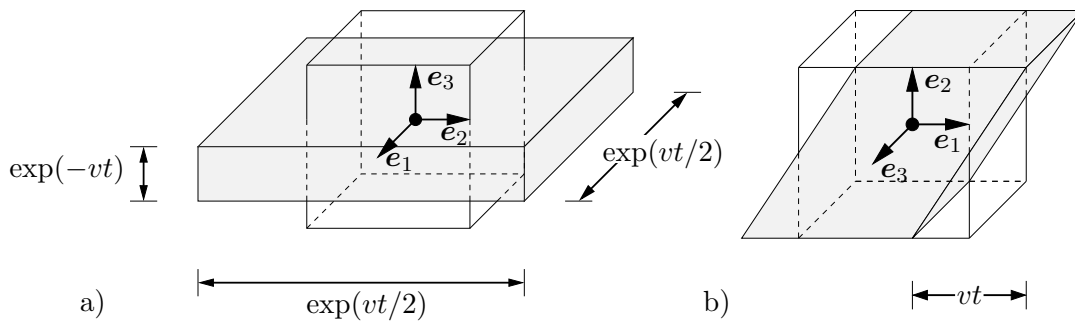


Figure 4.9: Homogeneous deformation tests and sample coordinate system $\{e_i\}_{i=1,2,3}$. a) Simple compression and b) simple shear test.

The elastic-plastic active-set model according MIEHE, SCHOTTE & LAMBRECHT [96], MIEHE & SCHOTTE [95] serves as a reference for the simulations. The results are represented in $\langle 111 \rangle$ pole figures obtained by stereographic projection. A single fcc crystal is subjected first to deformation-driven homogeneous simple compression specified by the

deformation gradient

$$\bar{\mathcal{F}}(t) = \begin{bmatrix} \exp(vt/2) & 0 & 0 \\ 0 & \exp(vt/2) & 0 \\ 0 & 0 & \exp(-vt) \end{bmatrix} \quad (4.53)$$

with $v = 1/s$ and augmenting time t by a step size $\Delta t = 0.01s$. Three different initial

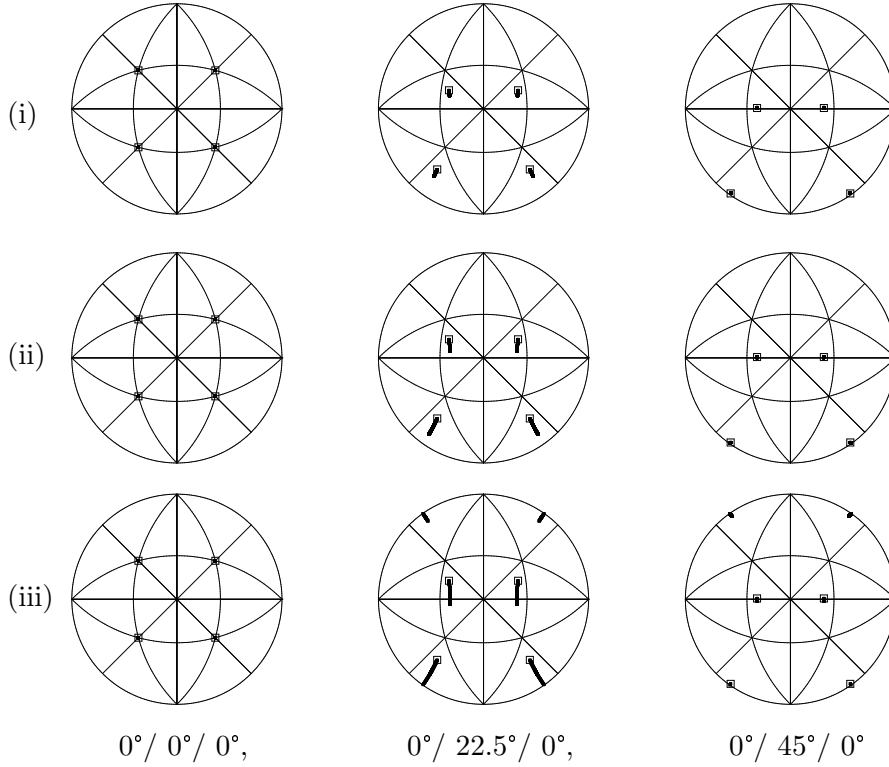


Figure 4.10: Simple compression of a fcc single crystal. Development of the $\langle 111 \rangle$ orientation for initial orientations $0^\circ/0^\circ/0^\circ$, $0^\circ/22.5^\circ/0^\circ$, $0^\circ/45^\circ/0^\circ$ with (i) elasto-plastic active-set model, (ii) rigid-plastic active-set model, (iii) rigid-plastic power-law model.

orientations $(0^\circ, 0^\circ, 0^\circ)$, $(0^\circ, 22.5^\circ, 0^\circ)$, $(0^\circ, 45^\circ, 0^\circ)$ parametrized by Euler angles are chosen. Consecutively, the whole reorientation process of a single crystal is visualized in Figure 4.10 until the final compression $vt = 2$. For an initial orientation $(0^\circ, 0^\circ, 0^\circ)$ the fcc unit cell remains unrotated for all three models. Contrarily, for $(0^\circ, 22.5^\circ, 0^\circ)$, the orientation tends with a small rotation to a saturated orientation. Especially for the power-type model, the rotation is overpredicted. Again, for the third initial orientation $(0^\circ, 45^\circ, 0^\circ)$, the orientation remains almost unrotated, which is similar in all models. The second test is dedicated to a homogeneous simple shear deformation driven by the deformation gradient

$$\bar{\mathcal{F}}(t) = \begin{bmatrix} 1 & vt & 0 \\ 0 & 1 & 0 \\ 0 & 0 & 1 \end{bmatrix} \quad (4.54)$$

with $v = 1/s$ and augmenting time t by a step size $\Delta t = 0.01s$ up to a total shear $vt = 2$. For the same initial orientations $(0^\circ, 0^\circ, 0^\circ)$, $(0^\circ, 22.5^\circ, 0^\circ)$, $(0^\circ, 45^\circ, 0^\circ)$ as above, the reorientation of a single crystal is shown in Figure 4.11. In all three tests, the orientation tends to a saturated value. For $(0^\circ, 0^\circ, 0^\circ)$ and $(0^\circ, 45^\circ, 0^\circ)$ on the one hand a rotation in

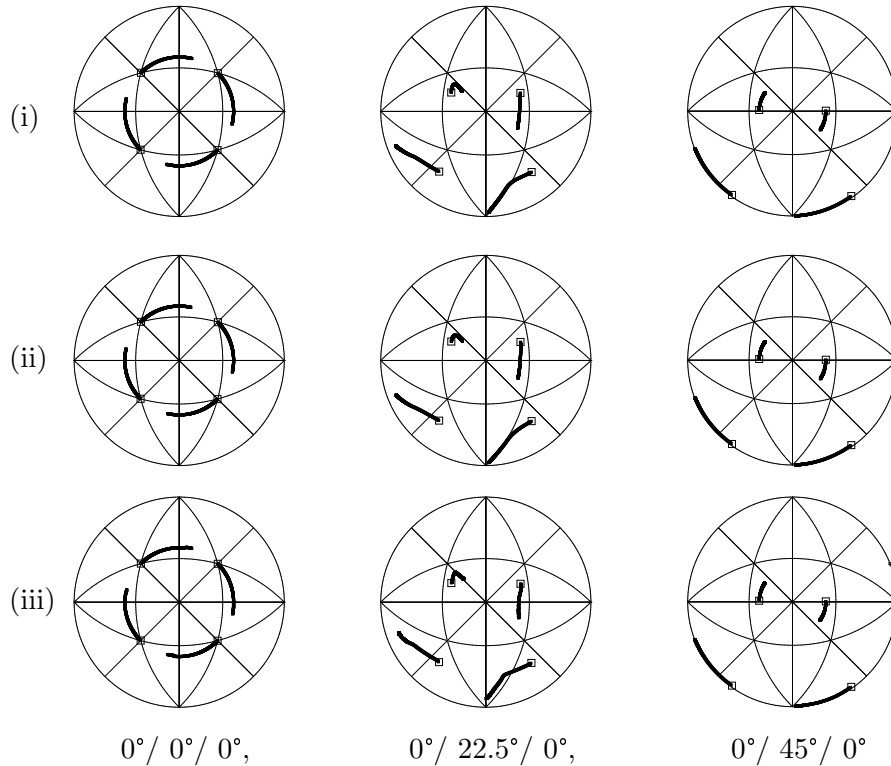


Figure 4.11: Simple shear of a fcc single crystal. Development of the $\langle 111 \rangle$ orientation for initial orientations $0^\circ/0^\circ/0^\circ$, $0^\circ/22.5^\circ/0^\circ$, $0^\circ/45^\circ/0^\circ$ with (i) elasto-plastic active-set model, (ii) rigid-plastic active-set model, (iii) rigid-plastic power-law model.

the 1-2 plane can be observed and on the other hand a perfect agreement of the three models is achieved. The results of the rigid-plastic active-set model and the elastic-plastic active-set model coincide for $(0^\circ, 22.5^\circ, 0^\circ)$ while the rigid-plastic power-type model shows some minor deviations. Recapitulatory, the models exhibit a good qualitative agreement for the modeling of texture reorientation in single crystals.

4.4.2.2. Deformation of Fcc Polycrystalline Aggregate. In contrast to the simulations in the previous subsection, Rodrigues vectors are chosen in the following examples. With regard to a parametrization of the orientations by means of Rodrigues parameters \mathbf{r} , recall, that all rotations can uniquely be represented within a truncated cube with the cube geometry discussed in Sections 3.3.1.5 and 3.3.2.2, respectively. A quasi-isotropic, initial orientation distribution of a polycrystal is obtained from a regular discretization of the truncated cube. Four different discretizations are considered, arising from the partition of the edges of the cube with 1, 2, 4 and 8 cells, respectively. In the subsequent treatment, these discretizations, illustrated in Figure 4.12, will be indicated by cube1, cube2, cube4 and cube8.

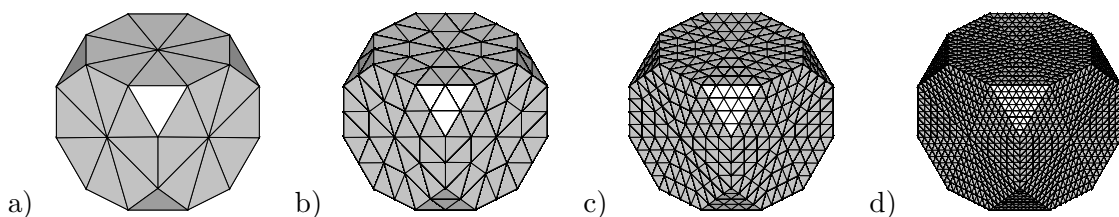


Figure 4.12: Discretizations of Rodrigues cube: a) cube1, b) cube2, c) cube4 and d) cube8.

and cube8, respectively. Let \mathcal{T}^h denote the triangulation of the Rodrigues space \mathcal{R} by E^h four-noded tetrahedral finite cells with N^h nodal points $\{\mathbf{r}_I\}_{I=1,\dots,N^h}$. Associated with this triangulation, the initial element volumes

$$|\mathcal{R}_0^e| := \frac{1}{6} |(\mathbf{r}_{\mathcal{T}^h(4,e)} - \mathbf{r}_{\mathcal{T}^h(1,e)}) \cdot (\mathbf{r}_{\mathcal{T}^h(3,e)} - \mathbf{r}_{\mathcal{T}^h(1,e)}) \times (\mathbf{r}_{\mathcal{T}^h(2,e)} - \mathbf{r}_{\mathcal{T}^h(1,e)})| \quad (4.55)$$

and the initial center rotation parameters

$$\mathbf{r}^e := \frac{1}{4} \sum_{i=1}^4 \mathbf{r}_{\mathcal{T}^h(i,e)} \quad (4.56)$$

of the elements $e = 1, \dots, E^h$ can be expressed in terms of the global topology map \mathcal{T}^h of the triangulation that assigns to the local nodes i of the cell e the global nodal number $I = \mathcal{T}^h(i, e)$. The pairs $\{|\mathcal{R}_0^e|, \mathbf{r}^e\}_{e=1,\dots,E^h}$ of volume fractions and center orientation parameters characterize the initial discretization of the Rodrigues space. These quantities are determined by the discrete values $\{\mathbf{r}_I\}_{I=1,\dots,N^h}$ at the nodes and the mesh topology. It is pointed out, that in this context the mesh is solely used for the specification of an initial distribution of orientations, i.e. the center rotation parameters shown in Figure 4.13. A stereographic projection of this quasi-isotropic initial distribution of

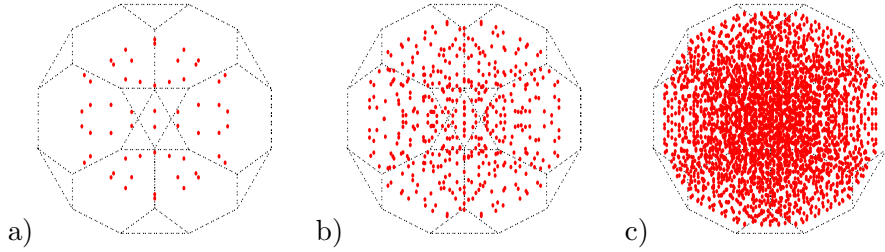


Figure 4.13: Initial orientations in the Rodrigues space: a) cube1, b) cube2 and c) cube4 (cube8 is not visualized).

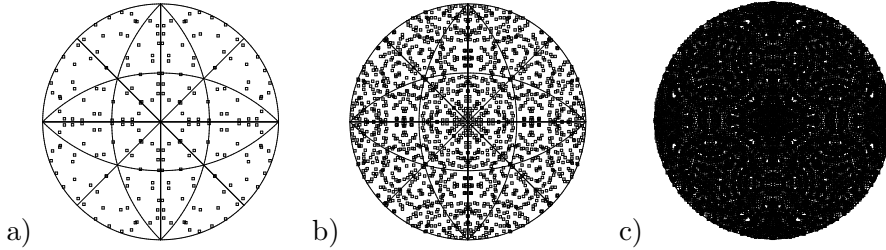


Figure 4.14: Pole figures of the discrete Rodrigues space: a) cube1, b) cube2 and c) cube4 (cube8 is not visualized).

orientations parametrized by Rodrigues vectors is shown in Figure 4.14. Cube1, cube2, cube4 and cube8 (not visualized) possess 56, 448, 3400 and 28672 cells/center orientations. The texture accuracy depends on the different discretizations of the Rodrigues cube, i.e. the amount of orientations. This will be of particular importance in Section 5.4 for the prediction of average quantities with regard to a multiscale modeling. For the graphical representation of the following simulations, pole figures of the cube2 discretization with 448 orientations are chosen for the comparison with experimental results. The reorientation process for the fcc polycrystal under plane strain compression, simple compression and simple shear is compared to experimental results taken from BRONKHORST, KALIDINDI & ANAND [33].

Fcc Crystals undergoing Plane Strain Compression First, the fcc polycrystalline material with 448 orientations is subjected to plane strain compression driven by the macroscopic deformation gradient

$$\bar{\mathcal{F}} = \begin{bmatrix} 1 & 0 & 0 \\ 0 & \exp(vt) & 0 \\ 0 & 0 & \exp(-vt) \end{bmatrix}. \quad (4.57)$$

For constant $v = 1/s$, the time $t \in [0, 1.54s]$ is linearly increased with a step size $\Delta t = 0.001s$ until a total compression of 78.6% in \mathbf{e}_3 direction. A deformation in \mathbf{e}_1 direction is disabled in order to guarantee plane strain conditions. For the rigid-plastic active set model the development of $\langle 111 \rangle$ pole figures at $vt_1 = 0.21$, $vt_2 = 0.52$, $vt_3 = 1.01$ and $vt_4 = 1.54$ in Figure 4.15 shows a reasonable agreement with experimental results. The same holds

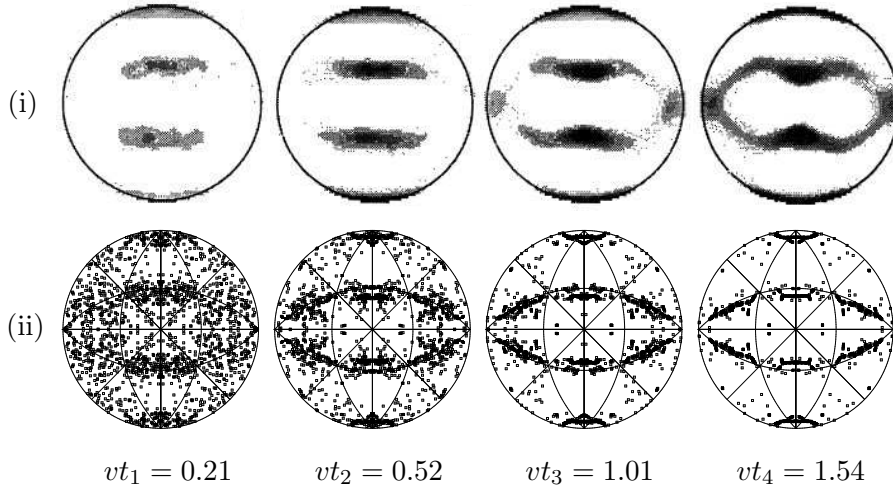


Figure 4.15: Plane strain compression of a fcc polycrystal. Development of $\langle 111 \rangle$ pole figures at different deformation states, i.e. $vt_1 = 0.21$, $vt_2 = 0.52$, $vt_3 = 1.01$ and $vt_4 = 1.54$. (i) Experimental results from BRONKHORST, KALIDINDI & ANAND [33] and (ii) simulation with rigid-plastic active-set model.

for the $\langle 111 \rangle$, $\langle 100 \rangle$ and $\langle 110 \rangle$ pole figures at the final deformation state $vt_4 = 1.54$ illustrated in Figure 4.16 for both models of rigid plasticity. While the experimental $\langle 111 \rangle$ pole figures show a dumbbell texture, the shapes of the simulated textures are rather elliptical, cf. BRONKHORST, KALIDINDI & ANAND [33]. Compared to the rigid-plastic active-set model the rigid-plastic power-law model shows a better agreement in the $\langle 100 \rangle$ pole figures. All pole figures are extracted from an equal area projection. They show a pronounced symmetry with respect to the perpendicular mirroring planes, which is a typical property of a material with orthotropic symmetry. In order to point out the capabilities of the rigid-plastic models with respect to their computational effort, the plane strain compression test was performed for cube1 with 56 orientations, cube2 with 448 orientations, cube4 with 3400 orientations and cube8 with 28672 orientations. Table 4.1 reports the CPU time (Intel Core2 Duo 3.0GHz), spent to run the plane strain compression test for polycrystals with different amount of grains, i.e. cube1, cube2, cube4 and cube8. The computation time of the standard power-law model is approximately 14 times higher than the computation time of the active-set model. This clearly emphasizes the computational attractiveness of the geometric approach.

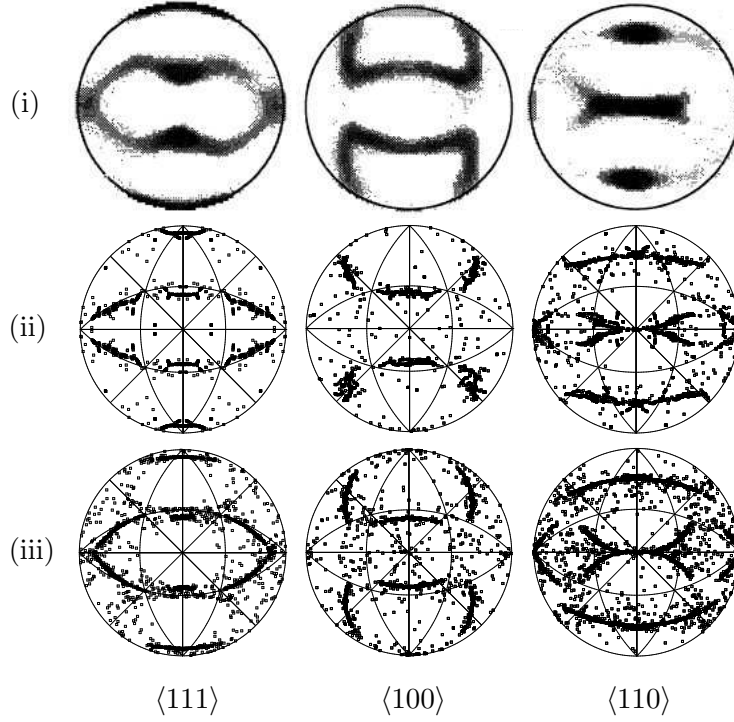


Figure 4.16: Plane strain compression of a fcc polycrystal. $\langle 111 \rangle$, $\langle 100 \rangle$ and $\langle 110 \rangle$ pole figures at $vt_4 = 1.54$. (i) Experimental results from [33] and simulation with (ii) rigid-plastic active-set model and (iii) rigid-plastic power-law model.

Table 4.1: Plane strain compression for fcc polycrystals. Comparison of CPU time [s] for rigid-plastic active-set and rigid-plastic power-law formulation.

orientations	rigid-plastic power-law	rigid-plastic active-set
56	18.40	1.51
448	146.44	10.07
3400	1134.35	74.55
28672	9378.51	625.52

Fcc Crystals undergoing Simple Compression A planar simple, isochoric compression test of a fcc polycrystalline material with 448 orientations described by the macroscopic deformation gradient

$$\bar{\mathcal{F}} = \begin{bmatrix} \exp(vt/2) & 0 & 0 \\ 0 & \exp(vt/2) & 0 \\ 0 & 0 & \exp(-vt) \end{bmatrix} \quad (4.58)$$

is performed. Initial and deformed configuration for this deformation mode are shown in Figure 4.9a). Again, the time $t \in [0, 1.53\text{s}]$ is linearly increased with a step size $\Delta t = 0.001\text{s}$ until a total compression of 78.4% in \mathbf{e}_3 direction accompanied by a transversal contraction in \mathbf{e}_1 and \mathbf{e}_2 direction. The simulation results of the rigid-plastic active-set model are

compared with experimental results at the deformation states $vt_1 = 0.20$, $vt_2 = 0.49$, $vt_3 = 0.99$ and $vt_4 = 1.53$. Figure 4.17 shows very good results for the texture evolution, represented by $\langle 111 \rangle$ pole figures. The same holds for the $\langle 111 \rangle$, $\langle 100 \rangle$ and $\langle 110 \rangle$ pole figures at the intermediate deformation state $vt_3 = 0.99$ illustrated in Figure 4.18 for experimental data, the rigid-plastic active-set as well as the rigid-plastic power-law model.

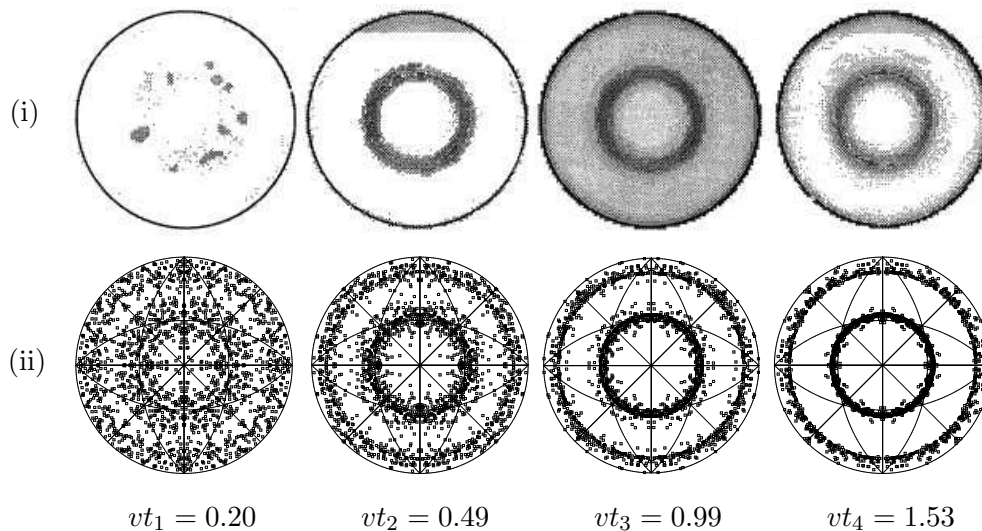


Figure 4.17: Planar simple compression of a fcc polycrystal. Development of $\langle 111 \rangle$ pole figures at different deformation states, i.e. $vt_1 = 0.20$, $vt_2 = 0.49$, $vt_3 = 0.99$ and $vt_4 = 1.53$. (i) Experimental results from BRONKHORST, KALIDINDI & ANAND [33] and (ii) simulation with rigid-plastic active-set model.

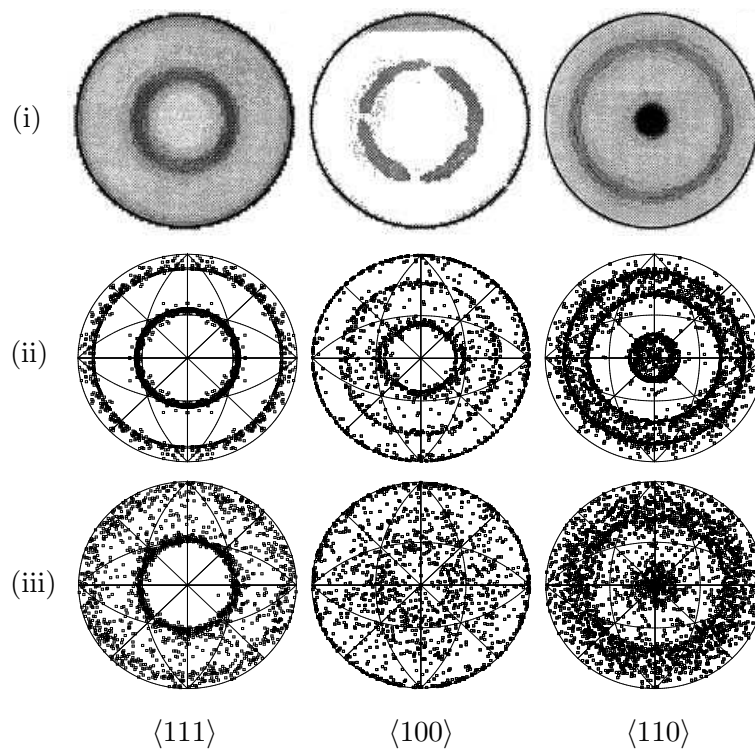


Figure 4.18: Planar simple compression of a fcc polycrystal. $\langle 111 \rangle$, $\langle 100 \rangle$ and $\langle 110 \rangle$ pole figures at $vt_3 = 0.99$. (i) Experimental results from [33] and simulation with (ii) rigid-plastic active-set model and (iii) rigid-plastic power-law model.

Simple compression yields an axis-symmetric texture with respect to the loading axis. All grains of the polycrystalline material rotate almost such that the $\{110\}$ planes become perpendicular to the loading axis, i.e. the $\{110\}$ directions take a preferred position almost parallel to the compression direction.

Fcc Crystals undergoing Simple Shear The last example for fcc polycrystalline materials with 448 orientations is dedicated to a simple shear test. Initial and deformed configuration for this deformation mode are shown in Figure 4.9b) and the deformation gradient within the deformation-driven scenario reads

$$\bar{\mathcal{F}} = \begin{bmatrix} 1 & vt & 0 \\ 0 & 0 & 0 \\ 0 & 0 & 0 \end{bmatrix}. \quad (4.59)$$

The $\langle 111 \rangle$ pole figures obtained by the rigid-plastic active-set model are illustrated for the deformation states $vt_1 = 0.26$, $vt_2 = 0.75$, $vt_3 = 1.40$ and $vt_4 = 1.50$ in Figure 4.19 and show an excellent agreement with experimental results. The same holds for the $\langle 111 \rangle$,

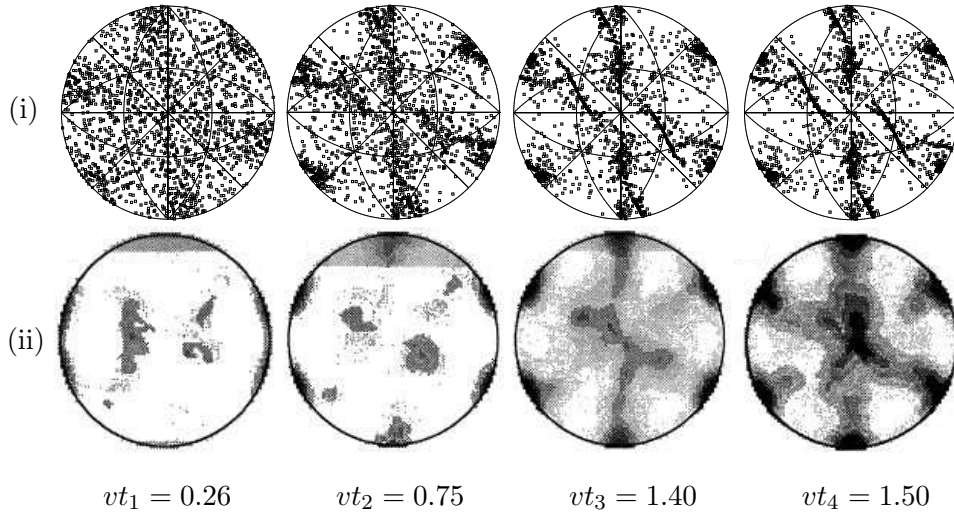


Figure 4.19: Simple shear of a fcc polycrystal. Development of $\langle 111 \rangle$ pole figures at different deformation states, i.e. $vt_1 = 0.26$, $vt_2 = 0.75$, $vt_3 = 1.40$ and $vt_4 = 1.50$. (i) Experimental results from BRONKHORST, KALIDINDI & ANAND [33] and (ii) simulation with rigid-plastic active-set model.

$\langle 100 \rangle$ and $\langle 110 \rangle$ pole figures at the last deformation state $vt_4 = 1.50$ illustrated in Figure 4.20. The rigid-plastic active-set model shows a better agreement compared to the rigid-plastic power-law model, which is not able to model the distinct texture evolution in an appropriate fashion.

4.4.3. Texture Development in Bcc Polycrystals. This subsection deals with the performance of the constitutive formulation for the reorientation of bcc crystals. The texture evolution of bcc crystals predicted with the active-set model, Section 4.2.3, is compared with the standard power-law model, Section 4.2.2, for rigid crystal plasticity and with experimental results. It is shown that the geometric approach provides an extremely fast estimate for texture developments in bcc polycrystals.

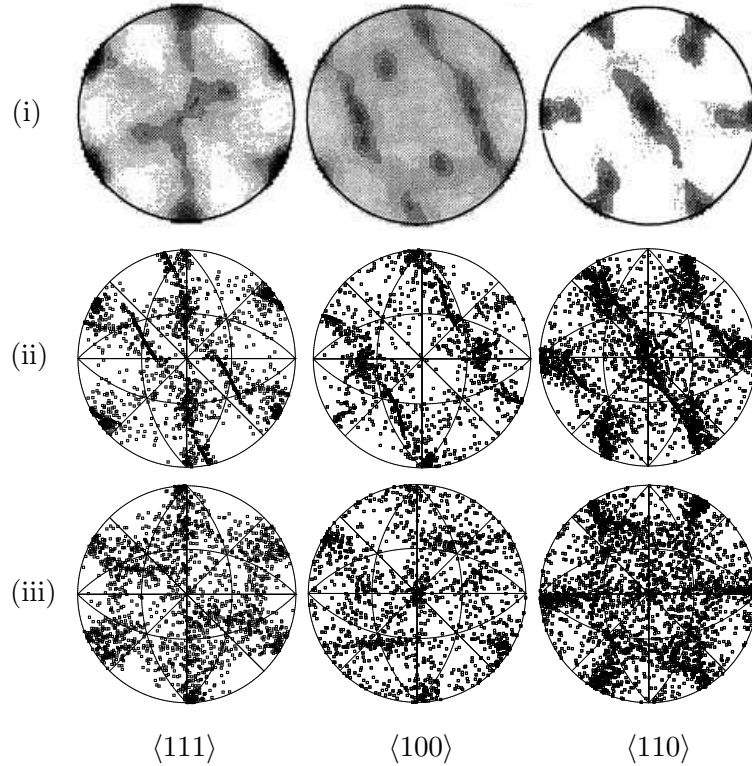


Figure 4.20: Simple shear of a fcc polycrystal. $\langle 111 \rangle$, $\langle 100 \rangle$ and $\langle 110 \rangle$ pole figures at $vt_3 = 1.40$. (i) Experimental results from [33] and simulation with (ii) rigid-plastic active-set model and (iii) rigid-plastic power-law model.

4.4.3.1. Geometric Representation of Bcc Crystals. In the subsequent numerical examples bcc polycrystals with $m = 48$ possible slip systems in each crystal are treated. The structure of bcc crystals is characterized by three families of slip planes $\{110\}$, $\{112\}$, and $\{123\}$, with $\langle 111 \rangle$ providing the corresponding family of slip directions, see Figure 4.21 for a graphical visualization. The slip systems $\alpha = 1, \dots, m$ are defined in Table 3.4 with respect to an orthogonal frame $\{\mathbf{g}_i\}_{i=1,2,3}$ aligned to the crystal with the slip plane normals \mathbf{n}^α and the slip directions \mathbf{s}^α . As discussed in Section 4.2.3 at the most 32 slip systems can be active at once. The orientation of the crystal is described by the rotation \mathbf{R} with respect to a fixed orthogonal frame $\{\mathbf{e}_i\}_{i=1,2,3}$. The local frame of the crystal $\mathbf{g}_i = \mathbf{R}\mathbf{e}_i$ is related to the given fixed orthogonal frame \mathbf{e}_i by the rotation \mathbf{R} , parametrized in the following by Rodrigues vectors \mathbf{r} , with the relationship (3.44).

4.4.3.2. Deformation of Bcc Polycrystalline Aggregates. A comparative numerical study for the texture evolution of the rigid-plastic active-set and power-law models with experimental results is carried out. The microstructure evolution is driven by a prescribed macro-deformation $\bar{\mathcal{F}}(t)$ according to the Taylor approach, see Section 4.1.1. A bcc polycrystalline material with 448 orientations is subjected to two macroscopic, isochoric deformation modes, namely plane strain compression and planar simple shear. These tests coincide with the experimental and computational benchmarks outlined in RAABE [116], KOCKS, TOMÉ & WENK [69], LI, HAN, JIANG, PI, WEI & TIEU [78] and WILLIAMS [142]. An initial distribution of the 448 orientations (cube2) is discussed in Section 4.4.2.2. The parameters for the rigid-plastic active-set model are set to $\kappa = 1$ for the sharpness parameter, $\epsilon = 10^{-4}$ for the regularization parameter and $tol = 5 \cdot 10^{-5}$

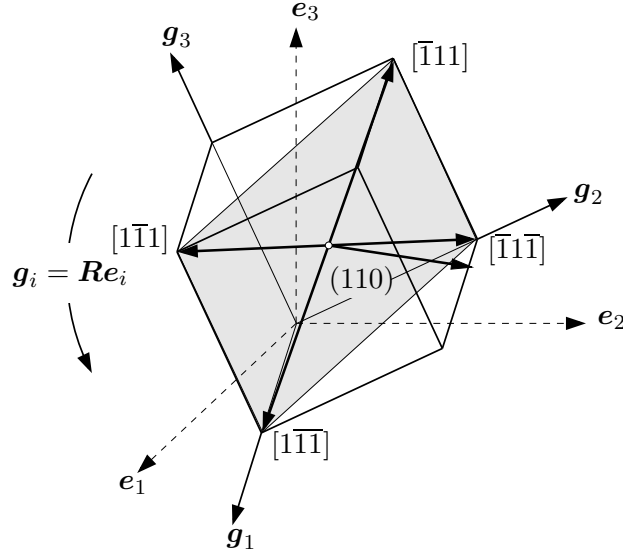


Figure 4.21: Orientation of the bcc unit cell. The standard cartesian base $\{e_i\}_{i=1,2,3}$ is rotated to the base $\{g_i\}_{i=1,2,3}$ aligned to the bcc crystal. The (111) slip plane of the bcc crystal is marked by the shadow.

for the relative tolerance for the consistency check. The parameters for the rigid-plastic power-type model are chosen to $a = 1/s$ for the reference slip, $\tau_c = 7.17\text{MPa}$ for the critical resolved shear stress and $p = 20$ for the power exponent.

Bcc Crystals undergoing Plane Strain Compression First, the polycrystalline microstructure is subjected to a plane strain compression mode. The macroscopic deformation is prescribed by

$$\bar{\mathcal{F}}(t) = \begin{bmatrix} 1 & 0 & 0 \\ 0 & \exp[vt] & 0 \\ 0 & 0 & \exp[-vt] \end{bmatrix} \quad (4.60)$$

with $v = 1/s$. During the simulation the time is linearly increased in an interval $t \in [0, 1.61\text{s}]$ in equal time steps $\Delta t = 0.001\text{s}$. Figure 4.22 presents the $\{100\}$ pole figures at different deformation states. The final state at time $t = 1.61\text{s}$ corresponds to a compression of the unit cube down to 20% of its initial height. The intermediate deformation states display a compression down to 70%, and 40% of the initial unit cube height. The deformed configuration is the one visualized in Figure 4.9a). The experimental results in Figure 4.22a) are taken from LI, HAN, JIANG, PI, WEI & TIEU [78] and those in Figure 4.22b) from RAABE [116]. Similar results are also obtained by KOCKS, TOMÉ & WENK [69]. LI, HAN, JIANG, PI, WEI & TIEU [78] compare their experimental results with a power-law model and test three possible combinations of slip systems: (1) 12 $\{110\}\langle 111\rangle$ slip systems, (2) 24 $\{110\}\langle 111\rangle$, $\{112\}\langle 111\rangle$ slip systems and (3) 48 $\{110\}\langle 111\rangle$, $\{112\}\langle 111\rangle$, $\{123\}\langle 111\rangle$ slip systems, using the same critical shear stress. Contrarily, RAABE [116] includes for the comparison with his experimental data 24 $\{110\}\langle 111\rangle$, $\{112\}\langle 111\rangle$ slip systems, choosing $k = 1$ and $k = 10$ for the ratio of the critical shear stresses

$$k := \frac{\tau_{\{110\}\langle 111\rangle}}{\tau_{\{112\}\langle 111\rangle}}. \quad (4.61)$$

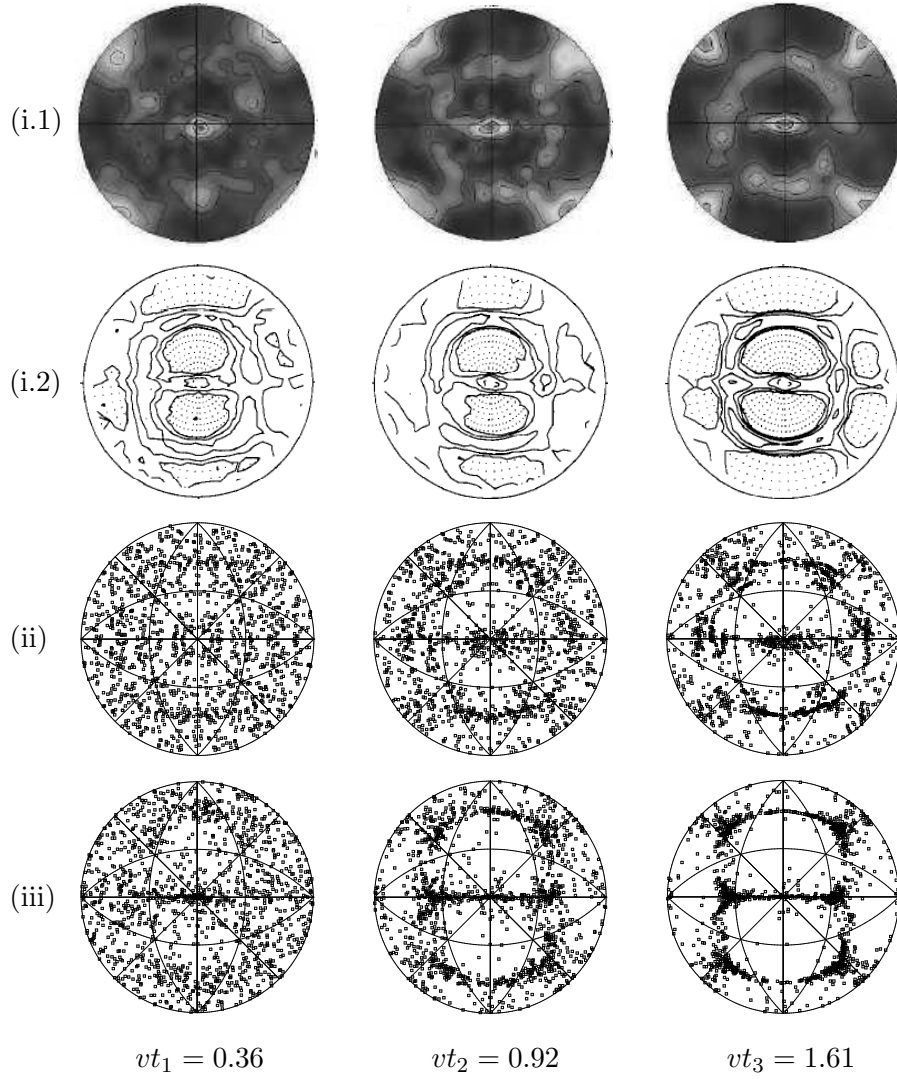


Figure 4.22: Plane strain compression of a bcc polycrystal. $\{100\}$ experimental pole figures taken from (i.1) LI, HAN, JIANG, PI, WEI & TIEU [78] and (i.2) RAABE [116] and simulation results of (ii) rigid-plastic active-set model and (iii) rigid-plastic power-law model at $vt_1 = 0.36$, $vt_2 = 0.92$ and $vt_3 = 1.61$.

For $k = 10$, the slip on $\{110\}\langle 111 \rangle$ is impeded and the slip on $\{112\}\langle 111 \rangle$ is favored. It was observed, that these 24 slip systems are sufficient to describe the texture evolution for the plane strain compression mode, see RAABE [116] and references therein. Accordingly, only the first 24 slip systems reported in Table 3.4 are used for the plane strain simulations that follow. The ratio k of the critical shear stresses can be related to a ratio between two different values of the parameter κ for the sharpness of the active set as introduced in (4.20). In order to consider different weights for the groups $\{110\}\langle 111 \rangle$, $\{112\}\langle 111 \rangle$ and $\{123\}\langle 111 \rangle$ of slip systems, (4.22) can be rewritten to

$$\mathcal{A} := \left\{ \alpha \in \mathcal{S} \mid |\tau^\alpha| \geq \mathcal{K}(\alpha) \frac{3}{2} \frac{1}{m} \sum_{\beta=1}^m |\tau^\beta| \right\} \subset \mathcal{S} \quad (4.62)$$

with the definition

$$\mathcal{K}(\alpha) = \begin{cases} \kappa_1 & \text{for } \alpha \in \{1 \dots 12\}, \\ \kappa_2 & \text{for } \alpha \in \{13 \dots 24\}, \\ \kappa_3 & \text{for } \alpha \in \{25 \dots 48\}. \end{cases} \quad (4.63)$$

Here, the ratio $\kappa_1/\kappa_2 = k$ corresponds to the parameter k defined in (4.61) by RAABE [116]. In order to consider only the first 24 systems, set $\kappa_3 \rightarrow \infty$. For the simulation with the rigid-plastic active-set model and the rigid-plastic power-law model the results for the $\langle 100 \rangle$ pole figures with $k = 1.1$ are plotted in Figure 4.22. A sharper texture is obtained for the power-law model, but nevertheless both simulations are in good qualitative agreement to the experimental results. With increasing deformation a strong α -fiber with $\{001\}\langle 110 \rangle$, $\{111\}\langle 110 \rangle$, $\{112\}\langle 110 \rangle$ texture components develops, whereas the γ -fiber with $\{111\}\langle 112 \rangle$ texture component degrades. In the power-law model, the $\{112\}\langle 110 \rangle$, and in the active-set model, the $\{001\}\langle 110 \rangle$ texture components are predominant. In Figure 4.23, the ratio for the critical shear stress is $k = 1$ for the active-set as well as the power-law model. In both models the $\{111\}\langle 112 \rangle$ texture component is

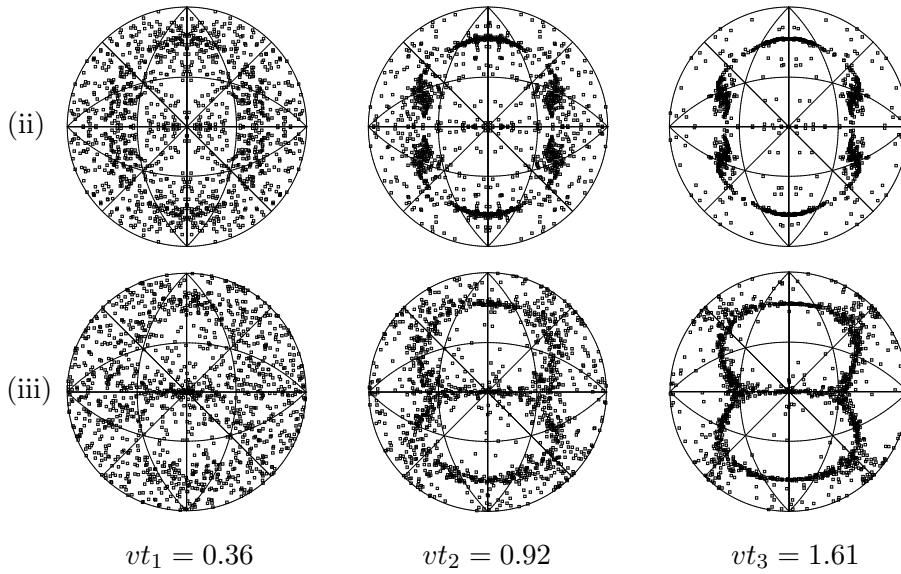


Figure 4.23: Plane strain compression of a bcc polycrystal. Comparison of $\{100\}$ pole figures of (ii) rigid-plastic active-set model and (iii) rigid-plastic power-law model at $vt_1 = 0.36$, $vt_2 = 0.92$ and $vt_3 = 1.61$.

overestimated compared to the experimental results. As observed by RAABE [116], the simulations for a larger ratio k , yield better texture results. The computational effort of the two models of rigid crystal plasticity is compared using the four different discretizations of the Rodrigues space, i.e. cube1, cube2, cube4 and cube8. In Table 4.2, the CPU time (Intel Core2 Duo 3.0GHz) spent to run the plane strain compression test for polycrystals with different amount of grains, i.e. 56 orientations for cube1, 448 orientations for cube2, 3400 orientations for cube4 and 28672 orientations for cube8, and using different material models is reported. Observe, that the computation time with the rigid-plastic active-set model is only a fraction of that with the rigid-plastic power-law model.

Bcc Crystals undergoing Planar Simple Shear The second example for texture development in bcc polycrystals is dedicated to a simple shear mode of the microstructure defined by the macro-deformation

$$\bar{\mathcal{F}}(t) = \begin{bmatrix} 1 & vt & 0 \\ 0 & 1 & 0 \\ 0 & 0 & 1 \end{bmatrix} \quad (4.64)$$

Table 4.2: Plane strain compression for bcc polycrystals. Comparison of CPU time [s] for rigid-plastic active-set and rigid-plastic power law formulation.

orientations	rigid-plastic power-law	rigid-plastic active-set
56	48.0	2.1
448	385.9	15.3
3400	2917.2	116.6
28672	22807.8	954.3

with $v = 1/s$. Again, the shear deformation is linearly increased up to a value $vt = 2.1$, corresponding to the same deformation state as discussed in WILLIAMS [142]. The experimental results for iron, taken from WILLIAMS [142], and the simulations of the rigid-plastic active-set model, are reported in Figure 4.24, for $\{100\}$ and $\{110\}$ pole figures. Contrarily to the plane strain compression mode, the ratio $k = 1$ is chosen. For planar

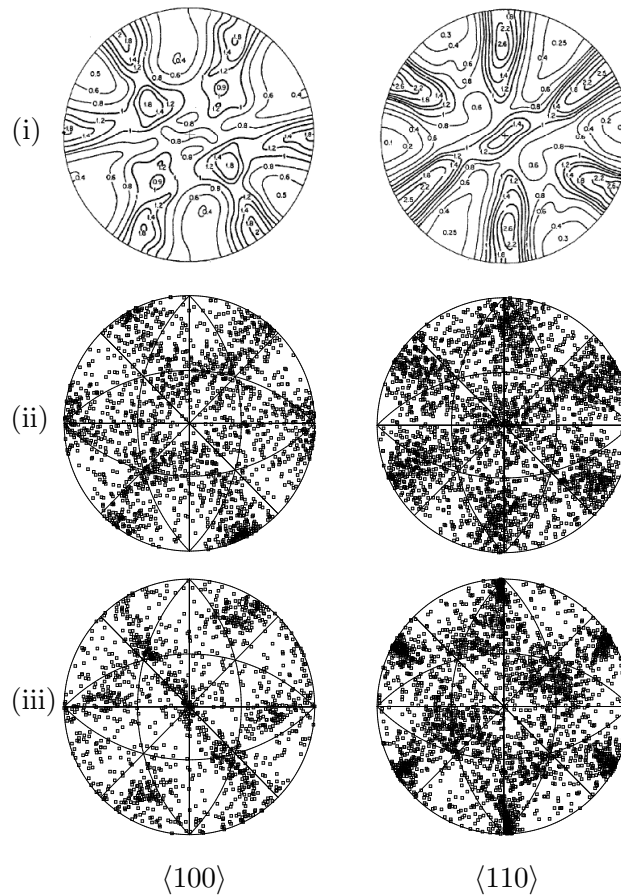


Figure 4.24: Planar simple shear test. $\langle 100 \rangle$ and $\langle 110 \rangle$ pole figures of (i) experimental results taken from WILLIAMS [142] for iron, (ii) rigid-plastic active-set model and (iii) rigid-plastic power-law model.

simple shear, the results obtained by using 24 $\{110\}\langle 111\rangle$, $\{112\}\langle 111\rangle$ slip systems are similar to the ones obtained by 48 $\{110\}\langle 111\rangle$, $\{112\}\langle 111\rangle$, $\{123\}\langle 111\rangle$ slip systems. The texture components $\{112\}\langle 111\rangle$ and $\{110\}\langle 111\rangle$ are observed, where the former dominates with increasing deformation, see MONTHEILLET, COHEN & JONAS [101]. This behavior can be observed for both the experimental as well as the simulated textures shown in Figure 4.24.

In summary, the two Taylor models of rigid crystal plasticity give reasonable results for the texture evolution undergoing characteristic deformation modes, i.e. plane strain compression also named rolling, planar simple compression and simple shear also named torsion, with the proposed active-set model being superior especially in terms of computational effort. The geometric estimate of the set of active slips and the geometrically exact finite-step-sized reorientation update produces reorientation estimates of large deformations with a speed up by a factor 20 when compared with standard power-law models at similar qualitative results.

5. Reorientation Continuum and Fourier Expansion

It is the objective of this section to idealize the polycrystalline microstructure as an orientation continuum with regard to the modeling of the crystal reorientations. This idealization results in a simple expression for crystal orientation distribution functions represented as a Fourier series and finally in so-called orientation averages, which can serve as input for a hybrid micro-macro approach. The section conceptually follows the recent publication of MIEHE, FRANKENREITER & ROSATO [91], with the just mentioned topics being extracted from this publication and some additional comments and explanations being given.

Polycrystalline models, which are more directed towards the macroscopic modeling, describe the texture evolution by crystal orientation distribution functions (codf), which express the distribution of the crystal orientations over the space of orientation parameters. The evolution of these distribution functions are typically governed by (i) a model of crystal plasticity and (ii) a crystal fraction conservation equation. The reader is referred in this context to the works of RASHID [122], DAFALIAS [40], KUMAR & DAWSON [75] and BÖHLKE, RISY & BERTRAM [30]. In the underlying contribution, fast estimates of crystal orientation distribution functions and orientation averages suitable for an incorporation into multiscale models are proposed. To this end, the geometrically-based, rate-independent approach for crystal reorientation, discussed in Section 4, is advanced to the computational treatment of codf evolutions on polycrystalline orientation continua. In Section 5.1 the kinematic equations which govern the evolution of the orientation continuum are outlined. Therefore, the polycrystalline microstructure is considered as a continuum of crystal orientations. This includes a precise definition of the Lagrangian and Eulerian orientation states, respectively associated with the initial and the reference orientations of single crystals. The reorientation process is governed by a reorientation map, whose time derivative defines the material reorientation velocity, locally prescribed by a constitutive assumption governed by the lattice spin of a model of rigid plasticity. With regard to a parameterization of the orientation continuum by Rodrigues vectors a precise definition of the parameter maps and its inverse, including the definition of a metric is given. The spatial discretization of the fundamental Rodrigues space, which exploits symmetry properties, is achieved by a triangulation in terms of tetrahedral cells. Crystal fraction conservation equations in both the Eulerian as well as the Lagrangian geometric setting, discussed in Section 5.2, determine the evolution of the crystal orientation distribution functions. These balances are driven by a constitutive assumption for the crystal lattice spin, which determines the current value of the crystal reorientation map on the orientation continuum. The constitutive input is given by an improved version of the geometric approach to rigid crystal plasticity proposed by MIEHE & ROSATO [93]. In contrast to the formulation of KUMAR & DAWSON [75] based on finite element discretization of the parameterized orientation continuum, a pointwise discretization is performed. The update of the codf at a particular point of the orientation continuum may alternatively be obtained within a Lagrangian or an Eulerian geometric setting. In Section 5.3 the performance of the proposed method is demonstrated by means of representative numerical examples. A simple representation is achieved by considering planar crystals. Here, closed form solutions for the codf evolution are available, see for example RASHID [122], DAFALIAS [40] and PRANTIL, JENKINS & DAWSON [114]. In this one-dimensional setting of the orientation continuum, the update methods of crystal orientation distribution functions respectively in the Lagrangian and Eulerian geometric setting are demonstrated

in a descriptive format. The Lagrangian approach is restricted to smooth reorientations, which is trivial in the one-dimensional setting but not guaranteed in 3D applications. The proposed Eulerian method gives rough estimates, but is very robust and well suited for the estimation of orientation averages, outlined in Section 5.4. With a modeling approach of the microstructure as orientation continuum, the evaluation of the crystal orientation distribution function is not explicitly necessary for the calculation of these orientation averages. Orientation averages can be applied to the development of a macroscopic yield function by distortional changes caused by the texture development. Following conceptually the works of MAN [80, 81] and BÖHLKE & BERTRAM [28], the coefficients which govern the distortion of the yield surface are obtained from a Fourier expansion of the codf and appear in the form of orientation averages. It turns out that already a rough discretization of the orientation space gives reasonable results for the macroscopic distortion of the yield surface. Basic features of the developing overall anisotropy of the polycrystalline aggregate can be described by a coarse discretization of the Rodrigues space. The evolving anisotropy described by the yield surfaces or the Lankford coefficients are shown to be in good qualitative agreement with results obtained by BÖHLKE, RISY & BERTRAM [30] and KOWALCZYK & GAMBIN [70]. Hence, the proposed method is considered to be an appropriate ingredient for a multiscale method with regard to the description of texture-induced anisotropy as will be shown in Section 6.

5.1. Kinematics of an Orientation Continuum

Consider polycrystalline microstructures with a very large number of single crystal grains as indicated in Figure 5.1. The orientation distribution of these grains is called the

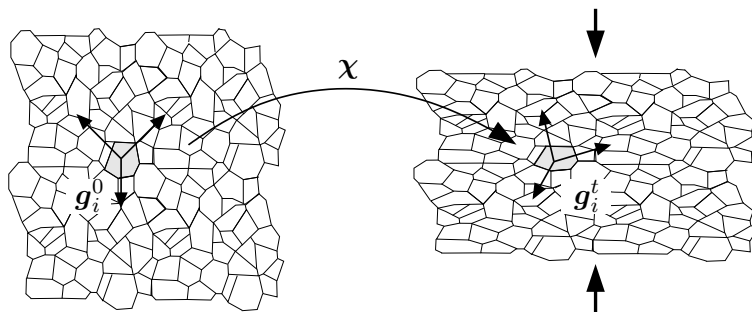


Figure 5.1: Orientation-texture microstructure. The macroscopic deformation of a polycrystalline microstructure causes a reorientation of the microscopic crystal grains. The microstructure is idealized by an orientation continuum where the reorientation map χ rotates crystal lattice frames from initial to current orientations, \mathbf{g}_i^0 and \mathbf{g}_i^t , respectively.

orientation texture of the polycrystal. This texture is a key ingredient for the macroscopic modeling of the overall response of the polycrystalline aggregate. Due to the large number of grains, the texture is statistically described by continuous crystal orientation distribution functions (codf). Comprehensive reviews of this classical viewpoint are given in BUNGE [36] and KUMAR & DAWSON [75].

5.1.1. Orientation Continuum of Crystals. The polycrystalline microstructure is idealized as an orientation continuum of crystals, schematically depicted in Figure 5.2, that occupies at a particular time a fundamental region in the orientation space of proper orthogonal tensors. Material points of the orientation continuum are the crystals itself which are placed in the orientation space by their individual orientation. During the

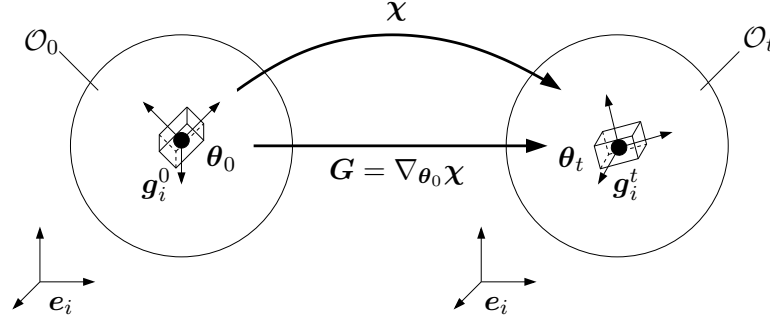


Figure 5.2: Deformation of an orientation continuum. $\mathcal{O}_0 \subset \mathcal{SO}(3)$ and $\mathcal{O}_t \subset \mathcal{SO}(3)$ are initial and current configurations of the orientation continuum. The smooth reorientation map $\chi : \theta_0 \mapsto \theta_t$ with gradient $\mathbf{G} = \nabla_{\theta_0} \chi$ maps initial crystal orientations $\theta_0 \in \mathcal{O}_0$ onto current crystal orientations $\theta_t \in \mathcal{O}_t$, defining the lattice frames $\mathbf{g}_i^0 = \theta_0 \mathbf{e}_i$ and $\mathbf{g}_i^t = \theta_t \mathbf{e}_i$.

deformation of the polycrystalline aggregate, the texture develops due to distortions and rigid rotations of the grains. This causes a deformation of the orientation continuum of crystals in time accompanied by the change of the crystal orientation distribution function.

5.1.1.1. Initial Configuration. Similar to formulations of standard continuous media, the crystal orientation continuum is defined in a referential description by its placement in a reference or initial configuration as visualized in Figures 5.1 and 5.2. Let $\mathcal{O}_0 \subset \mathcal{SO}(3)$ be a given initial configuration of the orientation continuum of crystals at a reference time $t_0 \in \mathbb{R}_+$. Elements $\theta_0 \in \mathcal{O}_0$ are rotations which relate in a unique format the reference orientation of the lattice frame $\{\mathbf{g}_i^0\}_{i=1,3}$ aligned to a crystal grain of the polycrystalline aggregate to the fixed sample frame $\{\mathbf{e}_i\}_{i=1,3}$

$$\mathbf{g}_i^0 = \theta_0 \mathbf{e}_i \quad \text{with} \quad \theta_0 \in \mathcal{O}_0 \subset \mathcal{SO}(3) \quad (5.1)$$

as depicted in Figures 5.1 and 5.2. θ_0 is called the initial or Lagrangian orientation of a crystal grain. \mathcal{O}_0 may also be denoted as the Lagrangian configuration of the orientation continuum. It is a fundamental subset of the set $\mathcal{SO}(3)$ of proper orthogonal tensors that reflects the symmetry of the single crystal grains under consideration.

5.1.1.2. Current Configuration. Let $\mathcal{O}_t \subset \mathcal{SO}(3)$ be the current configuration of the orientation continuum of crystals at a time $t \in \mathbb{R}_+$. Elements $\theta_t \in \mathcal{O}_t$ are rotations which relate the current orientation of the lattice frame to the fixed sample frame

$$\mathbf{g}_i^t = \theta_t \mathbf{e}_i \quad \text{with} \quad \theta_t \in \mathcal{O}_t \subset \mathcal{SO}(3) . \quad (5.2)$$

θ_t is the current or Eulerian orientation of a crystal grain. \mathcal{O}_t is also called the Eulerian configuration of the orientation continuum. It is a fundamental subset of the set $\mathcal{SO}(3)$ that reflects the symmetry of the single crystal grains.

5.1.2. Crystal Reorientation Map, Gradient and Velocity. In order to describe the evolving texture, it is necessary to follow the orientation of individual grains as the deformation proceeds, i.e. the current orientation $\theta_t \in \mathcal{O}_t$ of a crystal at time t depends on its initial orientation $\theta_0 \in \mathcal{O}_0$ at time t_0 . This is achieved by the introduction of a crystal lattice reorientation map

$$\chi : \begin{cases} \mathcal{O}_0 \times [t_0, T] \rightarrow \mathcal{O}_t \\ (\theta_0, t) \mapsto \theta_t = \chi(\theta_0, t) , \end{cases} \quad (5.3)$$

which maps at a current time $t \in [t_0, T]$ the initial orientation $\boldsymbol{\theta}_0$ of a crystal onto its current orientation $\boldsymbol{\theta}_t$. This fundamental kinematic function determines the motion of the orientation continuum of crystal grains in the orientation space $\mathcal{SO}(\beta)$ by mapping at time t its reference configuration \mathcal{O}_0 onto the current configuration \mathcal{O}_t . The map is such that it gives the identity $\boldsymbol{\theta}_0 = \boldsymbol{\chi}(\boldsymbol{\theta}_0, t_0)$ at the initial time t_0 of the deformation process. The continuous reorientation map is assumed to be smooth and differentiable. Its gradient with respect to the initial orientation

$$\mathbf{G}(\boldsymbol{\theta}_0, t) := \nabla_{\boldsymbol{\theta}_0} \boldsymbol{\chi}(\boldsymbol{\theta}_0, t) \quad (5.4)$$

is called the reorientation gradient which determines the relationships between infinitesimal volume elements

$$d\mathcal{O}_t = J(\boldsymbol{\theta}_0, t) d\mathcal{O}_0 \quad \text{with} \quad J(\boldsymbol{\theta}_0, t) := \det[\mathbf{G}(\boldsymbol{\theta}_0, t)] > 0 \quad (5.5)$$

of the orientation continuum in its initial and current configurations \mathcal{O}_0 and \mathcal{O}_t , respectively, similar to (2.11). As outlined in Section 5.2, the Jacobian J governs the Lagrangian formulation of a crystal orientation distribution function. The constraint (5.5)₂ on the Jacobian expresses the assumption that the reorientation map (5.3) is one-to-one and such that crystals do not penetrate in the orientation space. The time derivative of the reorientation map defines the material reorientation velocity

$$\mathbf{V}(\boldsymbol{\theta}_0, t) := \frac{\partial}{\partial t} \boldsymbol{\chi}(\boldsymbol{\theta}_0, t), \quad (5.6)$$

which is parameterized by the initial orientation of the crystal $\boldsymbol{\theta}_0 \in \mathcal{O}_0$. The material reorientation velocity is related to the spatial reorientation velocity $\mathbf{v}(\boldsymbol{\theta}_t, t)$ parameterized by the current orientation $\boldsymbol{\theta}_t \in \mathcal{O}_t$ of the crystal by

$$\mathbf{V}(\boldsymbol{\theta}_0, t) = \mathbf{v}(\boldsymbol{\theta}_t, t) \circ \boldsymbol{\chi}(\boldsymbol{\theta}_0, t) = \mathbf{v}(\boldsymbol{\chi}(\boldsymbol{\theta}_0, t), t). \quad (5.7)$$

The spatial reorientation velocity field \mathbf{v} plays a critical role in the subsequent linking of the crystal reorientation to the macroscopic deformation of the polycrystalline aggregate. Its spatial reorientation velocity gradient is defined by

$$\nabla_{\boldsymbol{\theta}_t} \mathbf{v}(\boldsymbol{\chi}(\boldsymbol{\theta}_0, t), t) = \left[\frac{\partial}{\partial t} \mathbf{G}(\boldsymbol{\theta}_0, t) \right] \mathbf{G}^{-1}(\boldsymbol{\theta}_0, t). \quad (5.8)$$

Using $\partial_{\mathbf{G}} \det[\mathbf{G}] = \det[\mathbf{G}] \mathbf{G}^{-T}$, the time evolution of the Jacobian of the reorientation gradient reads

$$\frac{\partial}{\partial t} J(\boldsymbol{\theta}_0, t) = \text{tr}[\nabla_{\boldsymbol{\theta}_t} \mathbf{v}(\boldsymbol{\chi}(\boldsymbol{\theta}_0, t), t)] J(\boldsymbol{\theta}_0, t). \quad (5.9)$$

5.1.3. Parameterization of Rotations by Rodrigues Vectors. The manifold $\mathcal{SO}(\beta)$ of rotations may be parameterized in a singular-free format by quaternions

$$\mathcal{Q} := (q, \mathbf{q}) := (\cos[\vartheta/2], \sin[\vartheta/2] \mathbf{e}) \in \mathbb{R}^4 \quad (5.10)$$

as pseudo-vectors in the four-dimensional Euclidean space \mathbb{R}^4 , cf. Section 3.3.1. Here, $\vartheta \in \mathbb{R}^1$ is the rotation angle and $\mathbf{e} \in \mathbb{R}^3$ the axis of the rotation. The four coordinates of the quaternion are called the Euler-Rodrigues parameters of the rotation, see for example ANGELES [11]. From the definition (5.10), it is clear that \mathcal{Q} satisfies the normalization

condition, i.e. $q^2 + \mathbf{q} \cdot \mathbf{q} = 1$. Thus, rotations may be considered as points on the unit sphere $S^3 \subset \mathbb{R}^4$ in the four-dimensional space \mathbb{R}^4 of quaternions. Elements of the Hamiltonian algebra of quaternions are reviewed for example in ALTMANN [9]. A projection of the quaternion space \mathbb{R}^4 onto a three-dimensional space \mathbb{R}^3 is provided by the so-called Rodrigues vectors

$$\mathbf{r} := \frac{\mathbf{q}}{q} = \tan[\vartheta/2] \mathbf{e} \in \mathbb{R}^3 \quad (5.11)$$

for $q = \cos[\vartheta/2] \neq 0$. Though the parameterization with Rodrigues vectors has a singularity at $\vartheta = \pi$, it has strong advantages with regard to the representation of orientation textures, see for example FRANK [42], BECKER & PANCHANADEESWARAN [22], HEINZ & NEUMANN [49] and KUMAR & DAWSON [75, 76]. In the subsequent treatment, exclusively the Rodrigues vector parameterization of the rotations is used.

Let $\mathcal{R}_0 \subset \mathbb{R}^3$ and $\mathcal{R}_t \subset \mathbb{R}^3$ denote the Lagrangian and Eulerian parameter manifolds with Lagrangian and Eulerian rotation parameters $\mathbf{r}_0 \in \mathcal{R}_0$ and $\mathbf{r}_t \in \mathcal{R}_t$, respectively. The Lagrangian and Eulerian parameter maps are defined as

$$\hat{\boldsymbol{\theta}}_0 : \begin{cases} \mathcal{R}_0 \rightarrow \mathcal{O}_0 \\ \mathbf{r}_0 \mapsto \boldsymbol{\theta}_0 = \hat{\boldsymbol{\theta}}_0(\mathbf{r}_0) \end{cases} \quad \text{and} \quad \hat{\boldsymbol{\theta}}_t : \begin{cases} \mathcal{R}_t \rightarrow \mathcal{O}_t \\ \mathbf{r}_t \mapsto \boldsymbol{\theta}_t = \hat{\boldsymbol{\theta}}_t(\mathbf{r}_t) \end{cases} . \quad (5.12)$$

As conceptually outlined in ANGELES [11] and derived in Section 3.3.1.5, the parameterization with Rodrigues vectors gives the closed form of these mappings

$$\boldsymbol{\theta}_t = \hat{\boldsymbol{\theta}}_t(\mathbf{r}_t) = \frac{1}{1 + \mathbf{r}_t \cdot \mathbf{r}_t} [(1 - \mathbf{r}_t \cdot \mathbf{r}_t) \mathbf{1} + 2(\mathbf{1} \times \mathbf{r}_t + \mathbf{r}_t \otimes \mathbf{r}_t)] . \quad (5.13)$$

With the linear invariants

$$\text{tr}[\boldsymbol{\theta}_t] = \frac{1}{1 + \mathbf{r}_t \cdot \mathbf{r}_t} [(1 - \mathbf{r}_t \cdot \mathbf{r}_t) 3 + 2(\mathbf{r}_t \cdot \mathbf{r}_t)] \quad \text{and} \quad \text{vect}[\boldsymbol{\theta}_t] = \frac{1}{1 + \mathbf{r}_t \cdot \mathbf{r}_t} 2\mathbf{r}_t \quad (5.14)$$

the inverse representation for the Rodrigues vector reads

$$\mathbf{r}_t = \hat{\mathbf{r}}_t(\boldsymbol{\theta}_t) = 2\text{vect}[\boldsymbol{\theta}_t] / (1 + \text{tr}[\boldsymbol{\theta}_t]) . \quad (5.15)$$

Here $\mathbf{1} \times \mathbf{r}_t$ is a second-order tensor \mathbf{A} with components $A_{jk} = \epsilon_{ijk} \delta_{im} (r_t)_m$, where ϵ_{ijk} is the permutation operator. The current lattice frame may directly be expressed in terms of the Rodrigues vector. Inserting (5.13) into (5.2) gives the closed form result

$$\mathbf{g}_i^t = \frac{1}{1 + \mathbf{r}_t \cdot \mathbf{r}_t} [(1 - \mathbf{r}_t \cdot \mathbf{r}_t) \mathbf{e}_i + 2(\mathbf{r}_t \times \mathbf{e}_i + (\mathbf{r}_t \cdot \mathbf{e}_i) \mathbf{r}_t)] . \quad (5.16)$$

With the above parameterization of the Lagrangian and Eulerian rotation manifolds at hand, the modified crystal reorientation map

$$\tilde{\boldsymbol{\chi}} : \begin{cases} \mathcal{R}_0 \times [t_0, T] \rightarrow \mathcal{R}_t \\ (\mathbf{r}_0, t) \mapsto \mathbf{r}_t = \tilde{\boldsymbol{\chi}}(\mathbf{r}_0, t) \end{cases} \quad (5.17)$$

maps the Lagrangian rotation parameters $\mathbf{r}_0 \in \mathcal{R}_0$ directly onto the Eulerian rotation parameters $\mathbf{r}_t \in \mathcal{R}_t$. This map is defined by the composition

$$\boxed{\tilde{\boldsymbol{\chi}} = \hat{\mathbf{r}}_t \circ \boldsymbol{\chi} \circ \hat{\boldsymbol{\theta}}_0 .} \quad (5.18)$$

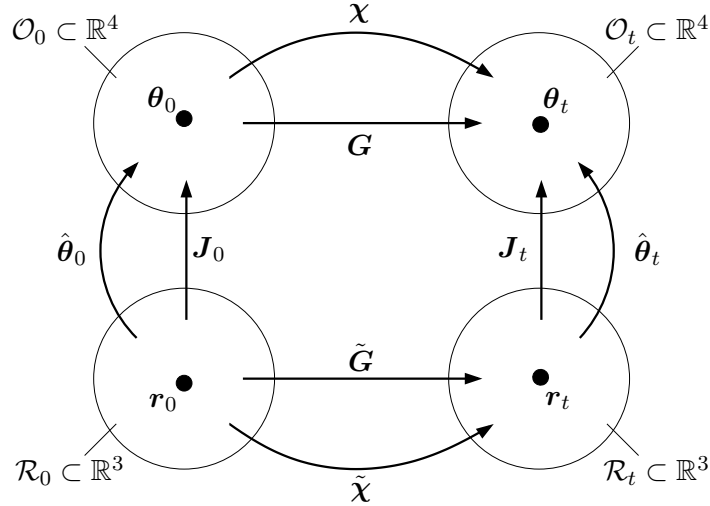


Figure 5.3: Parametrization of orientation manifolds. The configurations $\mathcal{O}_0 \subset \mathbb{R}^4$ and $\mathcal{O}_t \subset \mathbb{R}^4$ of the orientation continuum are parametrized by $\hat{\theta}_0 : r_0 \mapsto \theta_0$ and $\hat{\theta}_t : r_t \mapsto \theta_t$. Then $\tilde{\chi} := \hat{r}_t \circ \chi \circ \hat{\theta}_0 : r_0 \mapsto r_t$ is the parameter reorientation map that links the parameter manifolds $\mathcal{R}_0 \subset \mathbb{R}^3$ and $\mathcal{R}_t \subset \mathbb{R}^3$.

As visualized in Figure 5.3, this composition first parameterizes the Lagrangian initial orientation θ_0 by the Lagrangian rotation parameter r_0 , then evaluates the current orientation θ_t via the reorientation map χ in terms of the initial orientation θ_0 and finally computes the Eulerian rotation parameter r_t in terms of the current orientation θ_t . Recall, that the current crystal orientation θ_t can be considered as an element of a three-dimensional manifold of quaternions that characterizes the unit sphere $\mathcal{O}_t \subset \mathbb{R}^4$ in the four-dimensional space. In order to compute metric tensors associated with the manifold \mathcal{O}_t , the gradient of the parameter map

$$\mathbf{J}_t(\mathbf{r}_t) := \nabla_{\mathbf{r}_t} \hat{\theta}_t(\mathbf{r}_t) \quad (5.19)$$

is introduced. This gradient induces the current metric tensor

$$\mathbf{C}_t(\mathbf{r}_t) := \mathbf{J}_t^T(\mathbf{r}_t) \mathbf{J}_t(\mathbf{r}_t) \quad (5.20)$$

of the orientation manifold \mathcal{O}_t in its convected representation with respect to the parameter manifold \mathcal{R}_t . For a parameterization in terms of Rodrigues vectors, the current metric appears in the closed form representation

$$\mathbf{C}_t(\mathbf{r}_t) = \frac{1}{(1 + \mathbf{r}_t \cdot \mathbf{r}_t)^2} [(1 + \mathbf{r}_t \cdot \mathbf{r}_t) \mathbf{1} - \mathbf{r}_t \otimes \mathbf{r}_t], \quad (5.21)$$

see also KUMAR & DAWSON [75, 76]. With these definitions at hand, the volume elements of the orientation manifolds and the rotation parameter spaces

$$d\mathcal{O}_t = \sqrt{\det[\mathbf{C}_t(\mathbf{r}_t)]} d\mathcal{R}_t = \frac{d\mathcal{R}_t}{(1 + \mathbf{r}_t \cdot \mathbf{r}_t)^2} \quad (5.22)$$

are related in a very simple form for the parameterization with Rodrigues parameters.

5.1.4. Spatial Discretization of Orientation Space.

5.1.4.1. Discrete Lagrangian Parameter Space. Consider now the spatial discretization of the Lagrangian rotation space. Let \mathcal{T}^h denote a triangulation of the three-dimensional Lagrangian parameter space \mathcal{R}_0 by E^h four-noded tetrahedral finite cells $\{\mathcal{R}_0^e\}_{e=1,\dots,E^h}$ with N^h nodal points $\{\mathbf{R}_I\}_{I=1,\dots,N^h}$. Associated with this triangulation, the initial element volumes

$$|\mathcal{R}_0^e| := \frac{1}{6} |(\mathbf{R}_{\mathcal{T}^h(4,e)} - \mathbf{R}_{\mathcal{T}^h(1,e)}) \cdot (\mathbf{R}_{\mathcal{T}^h(3,e)} - \mathbf{R}_{\mathcal{T}^h(1,e)}) \times (\mathbf{R}_{\mathcal{T}^h(2,e)} - \mathbf{R}_{\mathcal{T}^h(1,e)})| \quad (5.23)$$

and the initial center rotation parameter of the elements

$$\mathbf{R}^e := \frac{1}{4} \sum_{i=1}^4 \mathbf{R}_{\mathcal{T}^h(i,e)} \quad (5.24)$$

for $e = 1, \dots, E^h$ are defined. Here, \mathcal{T}^h is the global topology map of the triangulation that assigns to the local nodes i of the cell e the global nodal number $I = \mathcal{T}^h(i, e)$. The pairs $\{|\mathcal{R}_0^e|, \mathbf{R}^e\}_{e=1,\dots,E^h}$ of volume fractions and average orientation parameters characterize the initial discretization of the Rodrigues space. These quantities are determined by the discrete values $\{\mathbf{R}_I\}_{I=1,\dots,N^h}$ at the nodes and the mesh topology. Taking into account (5.22), the initial cell volumes in the orientation space are

$$|\mathcal{O}_0^e| = \frac{|\mathcal{R}_0^e|}{(1 + \mathbf{R}^e \cdot \mathbf{R}^e)^2} \quad (5.25)$$

for a parameterization with Rodrigues vectors.

5.1.4.2. Discrete Eulerian Parameter Space. In the Lagrangian description the reorientation of the discrete grains is determined. For a known reorientation process, the Eulerian rotation parameters at the discrete nodal points of the triangulation are obtained by the modified reorientation map defined in (5.18), i.e.

$$\mathbf{r}_I = \tilde{\chi}_t(\mathbf{R}_I) \quad \text{for } I = 1, \dots, N^h. \quad (5.26)$$

These parameters define a deformed mesh in the Rodrigues space with deformed cell domains $\mathcal{R}_t^e = \tilde{\chi}_t(\mathcal{R}_0^e)$. Thus, the current volumes

$$|\mathcal{R}_t^e| := \frac{1}{6} |(\mathbf{r}_{\mathcal{T}^h(4,e)} - \mathbf{r}_{\mathcal{T}^h(1,e)}) \cdot (\mathbf{r}_{\mathcal{T}^h(3,e)} - \mathbf{r}_{\mathcal{T}^h(1,e)}) \times (\mathbf{r}_{\mathcal{T}^h(2,e)} - \mathbf{r}_{\mathcal{T}^h(1,e)})| \quad (5.27)$$

and the current center rotation parameter

$$\mathbf{r}^e := \frac{1}{4} \sum_{i=1}^4 \mathbf{r}_{\mathcal{T}^h(i,e)} \quad (5.28)$$

of the cells $e = 1, \dots, E^h$ can be computed. Following (5.22), the volume of the deformed cell is

$$|\mathcal{O}_t^e| = \frac{|\mathcal{R}_t^e|}{(1 + \mathbf{r}^e \cdot \mathbf{r}^e)^2}. \quad (5.29)$$

5.1.5. Constitutive Formulation of Crystal Reorientations.

5.1.5.1. Continuous Formulation. The lattice reorientation of the crystal is assumed to be governed by a constitutive assumption for the spatial reorientation velocity defined in (5.7)

$$\mathbf{v}(\boldsymbol{\theta}_t, t) = \mathbf{W}^l(\boldsymbol{\theta}_t, t)\boldsymbol{\theta}_t. \quad (5.30)$$

The constitutive function $\mathbf{W}^l(\boldsymbol{\theta}_t, t)$ for the lattice spin incorporates the plastic slip mechanisms of a local crystal and its link to the macroscopic deformation of the polycrystalline aggregate, as discussed in detail in Section 4.1. With this constitutive function at hand, the reorientation function is defined by the initial-value-problem

$$\frac{\partial}{\partial t}\boldsymbol{\chi}(\boldsymbol{\theta}_0, t) = \mathbf{W}^l(\boldsymbol{\chi}(\boldsymbol{\theta}_0, t), t)\boldsymbol{\chi}(\boldsymbol{\theta}_0, t) \quad \text{with} \quad \boldsymbol{\chi}(\boldsymbol{\theta}_0, t_0) = \boldsymbol{\theta}_0. \quad (5.31)$$

This ordinary differential equation with the initial condition determines the orientation of the crystal at current time $t \in [t_0, T]$.

5.1.5.2. Discrete Formulation. The spatial discretization of the orientation space considers a finite number of evolution equations (5.31) at the E^h center points of the mesh introduced above. Thus, simply consider E^h time-dependent reorientations associated with the representative initial orientations $\boldsymbol{\theta}_0^e = \hat{\boldsymbol{\theta}}_0(\mathbf{r}_0^e)$ for $e = 1, \dots, E^h$. The time discretization then gives an incremental update of the center orientations in the form

$$\boldsymbol{\theta}_{n+1}^e = \exp[\mathbf{W}^{l*}] \boldsymbol{\theta}_n^e \quad (5.32)$$

for $e = 1, \dots, E^h$, where $\mathbf{W}^{l*}/(t_{n+1} - t_n)$ is a time-discrete algorithmic approximation of \mathbf{W}^l in the time interval $[t_n, t_{n+1}]$ under consideration. The details of this algorithm are outlined in Box 4.1.

5.2. Evolution of Crystal Orientation Distribution Function

In this subsection alternative formulations for the evolution of orientation distribution functions in an Eulerian and a Lagrangian geometric setting are outlined. The spatial discretization of these equations provides simple Eulerian and Lagrangian updates of the codfs, which are used for the computation of orientation averages based on a homogenization of state variables over the orientation space.

5.2.1. Eulerian Formulation of Crystal Fraction Conservation.

5.2.1.1. Eulerian Codf. Consider a crystal reorientation process in a fixed control space $\mathcal{O} \subset \mathcal{SO}(3)$ of possible crystal orientations. Define the spatial (Eulerian) crystal orientation distribution function

$$f : \begin{cases} \mathcal{O} \times [t_0, T] \rightarrow \mathcal{R}_+ \\ (\boldsymbol{\theta}, t) \mapsto f(\boldsymbol{\theta}, t) \end{cases} \quad (5.33)$$

as a function of the spatially fixed crystal orientation $\boldsymbol{\theta} \in \mathcal{O}$ at the current time $t \in [t_0, T]$. The function has the following physical meaning. Let $\mathcal{P} \subset \mathcal{O}$ be an arbitrary part of the crystal orientation space \mathcal{O} , referred to as the control orientation sector. Then

$$\nu_E(\mathcal{P}, t) := \int_{\mathcal{P} \subset \mathcal{O}} f(\boldsymbol{\theta}, t) d\mathcal{O} \quad (5.34)$$

is the probability that the current orientation $\boldsymbol{\theta} \in \mathcal{SO}(\mathcal{B})$ of crystals falls into the sector \mathcal{P} . Based on this physical meaning, the codf is constrained to be positive and normalized to one, when integrated over the full domain of the orientation continuum

$$f(\boldsymbol{\theta}, t) \geq 0 \quad \text{and} \quad \int_{\mathcal{O}} f(\boldsymbol{\theta}, t) d\mathcal{O} = 1. \quad (5.35)$$

5.2.1.2. Eulerian Conservation Equation. The physical basis for the evolution of the crystal orientation distribution function in time is a mass-type conservation law for the probability of crystal orientations. The balance of crystal orientations for the control orientation sector \mathcal{P} reads

$$\boxed{\frac{d}{dt} \nu_E(\mathcal{P}, t) = -t_E(\partial\mathcal{P}, t)} \quad (5.36)$$

in terms of the flux of crystal orientations out of the control volume

$$t_E(\partial\mathcal{P}, t) := \int_{\partial\mathcal{P}} f(\boldsymbol{\theta}, t) \mathbf{v}(\boldsymbol{\theta}, t) \cdot \mathbf{n}(\boldsymbol{\theta}) d\mathcal{O} \quad (5.37)$$

for a given spatial reorientation velocity field \mathbf{v} . Here, \mathbf{n} is the outward normal on the surface $\partial\mathcal{P}$ of the control sector as depicted in Figure 5.4a). Application of the Gauss

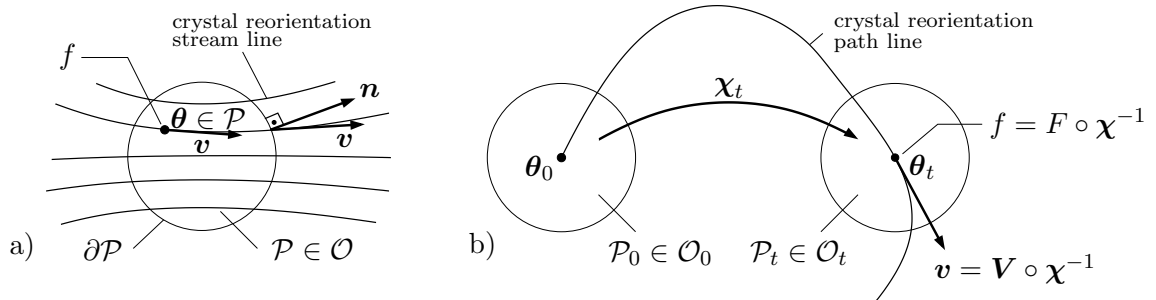


Figure 5.4: Eulerian and Lagrangian description of reorientation. a) Eulerian formulation based on a fixed control volume $\mathcal{P} \in \mathcal{O}$ in orientation space \mathcal{O} , where the reorientation velocity \mathbf{v} is tangential to crystal reorientation streamlines. b) Lagrangian formulation based on moving crystal fraction \mathcal{P}_t in orientation space, where \mathbf{v} is tangential to crystal reorientation path lines. $f(\boldsymbol{\theta}_t, t)$ and $F(\boldsymbol{\theta}_0, t)$ are the Eulerian and Lagrangian codfs, respectively.

theorem

$$\int_{\partial\mathcal{P}} f(\boldsymbol{\theta}, t) \mathbf{v}(\boldsymbol{\theta}, t) \cdot \mathbf{n}(\boldsymbol{\theta}) d\mathcal{O} = \int_{\mathcal{P}} f(\boldsymbol{\theta}, t) \text{tr}[\nabla_{\boldsymbol{\theta}} \mathbf{v}(\boldsymbol{\theta}, t)] d\mathcal{O} \quad (5.38)$$

transforms the surface integral in a volume integral. The local Eulerian form of the crystal fraction conservation equation

$$\frac{\partial}{\partial t} f(\boldsymbol{\theta}, t) + \nabla_{\boldsymbol{\theta}} f(\boldsymbol{\theta}, t) \cdot \mathbf{v}(\boldsymbol{\theta}, t) + f(\boldsymbol{\theta}, t) \text{tr}[\nabla_{\boldsymbol{\theta}} \mathbf{v}(\boldsymbol{\theta}, t)] = 0 \quad (5.39)$$

in \mathcal{O} follows from the material time derivative $df/dt := \partial f/\partial t + \nabla_{\boldsymbol{\theta}} f \cdot \mathbf{v}$ of the codf with the second term being a typical convective part. For a given reorientation velocity \mathbf{v} , the Eulerian conservation equation (5.39) is a linear hyperbolic differential equation. It has been derived by CLEMENT [38] in the context for a parameterization of the rotations by Euler angles and in the general context by KUMAR & DAWSON [75].

5.2.2. Lagrangian Formulation of Crystal Fraction Conservation.

5.2.2.1. Lagrangian Codf. Consider now a volume $\mathcal{P}_t \subset \mathcal{O}_t$ with a fixed fraction of crystals that moves through the spatial orientation space. Again, f is the spatial (Eulerian) crystal orientation distribution function. In contrast to (5.33), the function is now defined on the time-dependent moving orientation space \mathcal{O}_t . Let $\mathcal{P}_t \subset \mathcal{O}_t$ be a part of the orientation space \mathcal{O}_t which is currently occupied by the crystal fraction. Then this moving fraction is defined by

$$\nu_L(\mathcal{P}_t, t) := \int_{\mathcal{P}_t \subset \mathcal{O}_t} f(\boldsymbol{\theta}_t, t) d\mathcal{O}_t . \quad (5.40)$$

When taking into account the Lagrangian reorientation function $\boldsymbol{\chi}$ and the relationship between initial and current volume elements in (5.5), (5.40) can be recast into the form

$$\nu_L(\mathcal{P}_0, t) := \int_{\mathcal{P}_0 \subset \mathcal{O}_0} F(\boldsymbol{\theta}_0, t) \det[\nabla_{\boldsymbol{\theta}_0} \boldsymbol{\chi}(\boldsymbol{\theta}_0, t)] d\mathcal{O}_0 \quad (5.41)$$

with respect to the time-independent initial configuration \mathcal{O}_0 of the orientation space. Here,

$$F : \begin{cases} \mathcal{O}_0 \times [t_0, T] \rightarrow \mathcal{R}_+ \\ (\boldsymbol{\theta}_0, t) \mapsto F(\boldsymbol{\theta}_0, t) \end{cases} \quad (5.42)$$

is the material (Lagrangian) crystal orientation distribution function. The Lagrangian codf

$$F(\boldsymbol{\theta}_0, t) = f(\boldsymbol{\theta}_t, t) \circ \boldsymbol{\chi}(\boldsymbol{\theta}_0, t) = f(\boldsymbol{\chi}(\boldsymbol{\theta}_0, t), t) \quad (5.43)$$

is related to the Eulerian codf by a composition with the crystal reorientation function in analogy to the material reorientation velocity in (5.7). Due to (5.35), the Lagrangian codf is constrained to be positive and normalized to one when integrated over the full orientation domain, i.e.

$$F(\boldsymbol{\theta}_0, t) \geq 0 \quad \text{and} \quad \int_{\mathcal{O}_0} F(\boldsymbol{\theta}_0, t) \det[\nabla_{\boldsymbol{\theta}_0} \boldsymbol{\chi}(\boldsymbol{\theta}_0, t)] d\mathcal{O}_0 = 1 . \quad (5.44)$$

5.2.2.2. Lagrangian Conservation Equation. The constant crystal fraction associated with the moving sector \mathcal{P}_t in the orientation space is defined by the Lagrangian form of the conservation

$$\boxed{\frac{d}{dt} \nu_L(\mathcal{P}_0, t) = 0.} \quad (5.45)$$

This gives with the time evolution of the Jacobian (5.9) and the localization $\mathcal{P}_0 \rightarrow dV$ of the local field equation

$$\frac{\partial}{\partial t} F(\boldsymbol{\theta}_0, t) + F(\boldsymbol{\theta}_0, t) \operatorname{tr}[\nabla_{\boldsymbol{\theta}_t} \mathbf{v}(\boldsymbol{\chi}(\boldsymbol{\theta}_0, t), t)] = 0 \quad (5.46)$$

in \mathcal{O}_0 . In contrast to the Eulerian form (5.39), this evolution equation for the Lagrangian codf is for given reorientation velocity \mathbf{v} a simple ordinary differential equation. An alternative formulation is based on the statement

$$\nu_L(\mathcal{P}_0, t) = \nu_L(\mathcal{P}_0, t_0) , \quad (5.47)$$

which states explicitly that the number of crystals remains constant in the moving domain as an immediate consequence of (5.45). The localization $\mathcal{P}_0 \rightarrow dV$ gives the field equation

$$F(\boldsymbol{\theta}_0, t) \det[\nabla_{\boldsymbol{\theta}_0} \boldsymbol{\chi}(\boldsymbol{\theta}_0, t)] - F(\boldsymbol{\theta}_0, t_0) = 0, \quad (5.48)$$

which determines for a given reorientation map $\boldsymbol{\chi}(\boldsymbol{\theta}_0, t)$ at time t and the initial orientation function $F(\boldsymbol{\theta}_0, t_0)$ at time t_0 directly the current orientation function $F(\boldsymbol{\theta}_0, t)$. Clearly, (5.46) is the rate form of (5.48).

5.2.3. Discrete Formulation of Crystal Fraction Conservation.

5.2.3.1. Eulerian Formulation.

An elementary simple discrete representation of the Eulerian codf is obtained by projecting the moving discrete orientations onto fixed control volumes of the orientations space. To this end, the Eulerian orientation space is discretized by the control volumes $\{\mathcal{O}^e\}_{e=1, \dots, E^h}$, where the mesh is constructed such that the cell volumes

$$|\mathcal{O}^e| = |\mathcal{O}^h|/E^h \quad (5.49)$$

are equal in the orientation space. The cells represent a fraction of crystals with orientation $\boldsymbol{\theta}^e \in \mathcal{O}^e$ associated with the center of the cell. From (5.35), the constant initial orientation distribution function $f^h(\boldsymbol{\theta}^e, t_0) = f_0$ characterizes a uniform virgin state of the polycrystal at time t_0 . Hence, the discretization

$$\int_{\mathcal{O}} f(\boldsymbol{\theta}, t_0) d\mathcal{O} \approx \sum_{e=1}^{E^h} f^h(\boldsymbol{\theta}^e, t_0) |\mathcal{O}^e| = 1 \quad (5.50)$$

gives the value of the initial orientation distribution function

$$f^h(\boldsymbol{\theta}^e, t_0) = 1 / \sum_{e=1}^{E^h} |\mathcal{O}^e| =: 1/|\mathcal{O}^h| \quad (5.51)$$

with the same value at all center points $\boldsymbol{\theta}^e \in \mathcal{O}^e$ of the $e = 1, \dots, E^h$ fixed control element domains \mathcal{O}^e . Assigning to each center point of the control volume the Lagrangian initial orientation $\boldsymbol{\theta}_0^e = \boldsymbol{\theta}^e$ of a representative crystal, there exists one representative orientation associated with the control volume \mathcal{O}^e . Thus, the initial codf reads

$$f^h(\boldsymbol{\theta}^e, t_0) = N(\mathcal{O}^e, t_0)/|\mathcal{O}^h| \quad \text{with} \quad N(\mathcal{O}^e, t_0) = 1. \quad (5.52)$$

If the process time proceeds, the representative cell orientations reorientate according to (5.32) to the current value $\boldsymbol{\theta}_t^e = \boldsymbol{\chi}(\boldsymbol{\theta}_0^e, t) = \boldsymbol{\chi}(\boldsymbol{\theta}^e, t)$ at time t . Projecting this current orientation onto the fixed Eulerian mesh gives the current number $N(\mathcal{O}^e, t)$ of representative orientations which fall into the control segment \mathcal{O}^e . Hence, the current crystal orientation distribution function can be estimated as

$$\boxed{f^h(\boldsymbol{\theta}^e, t) = N(\mathcal{O}^e, t)/|\mathcal{O}^h|.} \quad (5.53)$$

The projection is realized by a search algorithm that assigns for each current orientation the associated control cell, discussed below. This search is performed in the Rodrigues

space. The procedure automatically preserves the normalization constraint due to the conservation property

$$\sum_{e=1}^{E^h} N(\mathcal{O}^e, t) = E^h \quad (5.54)$$

of moving representative orientations. Clearly, such a strong approximation of the current codf is for coarse meshes only useful for a rough visualization. The evolution of the discrete codf f^h in time is non-smooth due to the counting procedure that is related to finite control spaces. However, the estimate is straightforward and avoids completely the differentiation. As a consequence, the method is applicable to non-smooth reorientation processes.

5.2.3.2. Lagrangian Formulation. An approximative formulation of the Lagrangian form of crystal fraction conservation can be obtained as a discrete counterpart of (5.48). To this end, a constant initial orientation distribution function $F^h(\boldsymbol{\theta}_0^e, t_0) = F_0$ that characterizes a uniform virgin state of the polycrystal at time t_0 is determined. The discretization of (5.44) reads with $\boldsymbol{\chi}(\boldsymbol{\theta}_0, t_0) = \boldsymbol{\theta}_0$

$$\int_{\mathcal{O}_0} F(\boldsymbol{\theta}_0, t_0) d\mathcal{O}_0 \approx \sum_{e=1}^{E^h} F^h(\boldsymbol{\theta}_0^e, t_0) |\mathcal{O}_0^e| = 1. \quad (5.55)$$

This gives the value of the initial orientation distribution function

$$F^h(\boldsymbol{\theta}_0^e, t_0) = 1 / \sum_{e=1}^{E^h} |\mathcal{O}_0^e| =: 1 / |\mathcal{O}_0^h| \quad (5.56)$$

with the same value at all center points $\boldsymbol{\theta}_0^e \in \mathcal{O}_0^e$ of the $e = 1, \dots, E^h$ Lagrangian element domains \mathcal{O}_0^e . With known initial orientation function, the current orientation function immediately follows by applying the balance (5.47) to a discrete element volume, yielding the element conservation statement

$$F^h(\boldsymbol{\theta}_0^e, t) |\mathcal{O}_t^e| - F^h(\boldsymbol{\theta}_0^e, t_0) |\mathcal{O}_0^e| = 0. \quad (5.57)$$

This is the discrete counterpart of (5.48), yielding the simple update equation

$$\boxed{F^h(\boldsymbol{\theta}_0^e, t) = F^h(\boldsymbol{\theta}_0^e, t_0) |\mathcal{O}_0^e| / |\mathcal{O}_t^e|.} \quad (5.58)$$

Note, that the initial and current volumes $|\mathcal{O}_0^e|$ and $|\mathcal{O}_t^e|$ of the cells are given by the discrete reorientation updates discussed in Section 5.1.4. The above equation satisfies exactly the normalization constraint (5.44). However, such an update that includes the computation of deformed cell volumes \mathcal{O}_t^e is intrinsically related to smooth crystallization processes. This smoothness is not guaranteed in three-dimensional applications, if active-set selection procedures are used for rate-independent problems. Furthermore, in these situations, the mesh distortion plays a major role and Lagrangian schemes must be enhanced by mesh update procedures. This is in particular for three-dimensional reorientation processes, where discontinuities develop. In these situations, the above outlined robust Eulerian formulation should be applied.

5.3. Numerical Examples

5.3.1. Evolution of Codf in Planar Polycrystals. The reorientation process of Section 4.4.1.2 is now expanded by the evolution of crystal orientation distribution functions for planar polycrystals exhibiting double slip. Again, the polycrystal is subjected to the homogeneous deformation modes of pure and simple shear, illustrated in Figure 4.3. The Lagrangian conservation equation (5.46) appears with the scalar reorientation (4.52) in the closed form

$$\dot{F} - F [2 \cos(2\chi) \Lambda + 2 \sin(2\chi) \Gamma] / \cos(2\xi) = 0 \quad \text{with} \quad F(\theta_0, t_0) = 1/\pi. \quad (5.59)$$

The two equations (4.52) and (5.59) govern the reorientation and the codf evolution in the planar double slip model in terms of the macroscopic rate of stretching Λ , rate of shearing Γ and spin Ω .

Starting point for the simulations of pure shear and simple shear deformation test is an equidistant discretization of the orientation space and an isotropic initial orientation distribution, see (5.49), (5.51) and (5.56) as visualized in the left images of Figure 5.5 and 5.6, respectively. Here, the center points are highlighted by red squares and the initial isotropic codf is plotted in blue on the unit circle. In the Eulerian approach the discrete center orientations are projected onto a fixed control volume of the orientation space, see Figure 5.5, whereas in the Lagrangian approach the cell size changes due to moving nodes, see Figure 5.6. The crystal reorientations, represented by the nodes in the Lagrangian approach and the center points in the Eulerian approach, are updated via equation (A.11) and (A.12)₂. For given current orientations, the codf for the Eulerian approach at the nodes I and $I + 1$, of the fixed control volume in which the current orientation θ_J lies, are computed according to

$$f_I^h = \frac{1}{\pi} \frac{\theta_{I+1} - \theta_J}{\Delta\theta} \quad \text{and} \quad f_{I+1}^h = \frac{1}{\pi} \left[1 - \frac{\theta_{I+1} - \theta_J}{\Delta\theta} \right] \quad (5.60)$$

with $\Delta\theta = \theta_{I+1} - \theta_I$. This update is performed for all current center orientations and summed up at the global nodes of the mesh. The ratio of the initial and current volumes $|\mathcal{O}_0^e|$ and $|\mathcal{O}_t^e|$ yields the codf for the Lagrangian approach

$$F_t^h = F_0^h |\mathcal{O}_0^e| / |\mathcal{O}_t^e| \quad (5.61)$$

at the center point of the deformed control segment. This value is projected onto the nodes for the visualization. $N^h = 15$ orientations for one half of the unit circle are chosen. For all subsequent simulations, the slip system separation angle is taken to be $2\xi = 60^\circ$.

5.3.1.1. Codf Evolution in Planar Polycrystals: Pure Shear. In the first example, the polycrystal is subjected to homogeneous pure shear mode shown in Figure 4.3a) up to $\lambda = 2.5$. Four levels of deformation are depicted in Figure 5.5 for the Eulerian approach and in Figure 5.6 for the Lagrangian approach. In both cases, first the equidistant partition of the orientation space with center points highlighted by red squares and the initial isotropic codf plotted in blue on the unit circle can be observed. As the deformation proceeds, the orientations move towards the preferred directions of 0° and 180° . With increasing deformation, the isotropic initial codf of the single crystalline constituents evolves into a strongly anisotropic codf. In order to obtain an appropriate illustration, the maximum value of the codf has been scaled to a constant value. For the Lagrangian

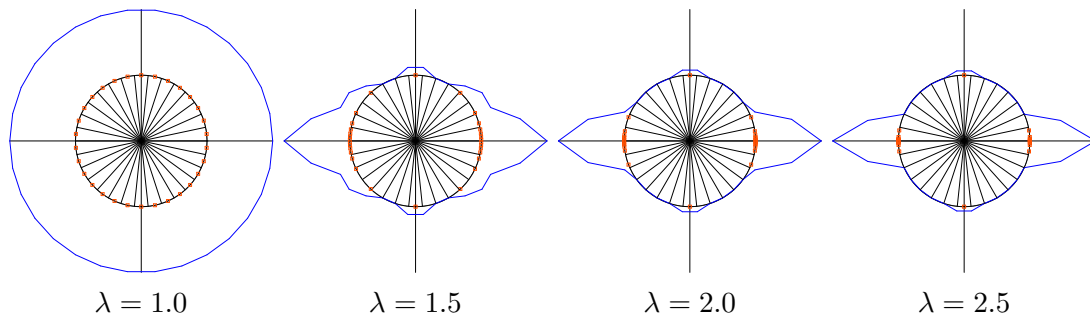


Figure 5.5: Evolution of the codf in planar crystals under pure shear for the Eulerian approach with an initial isotropic codf and $N^h=15$ discrete orientations.

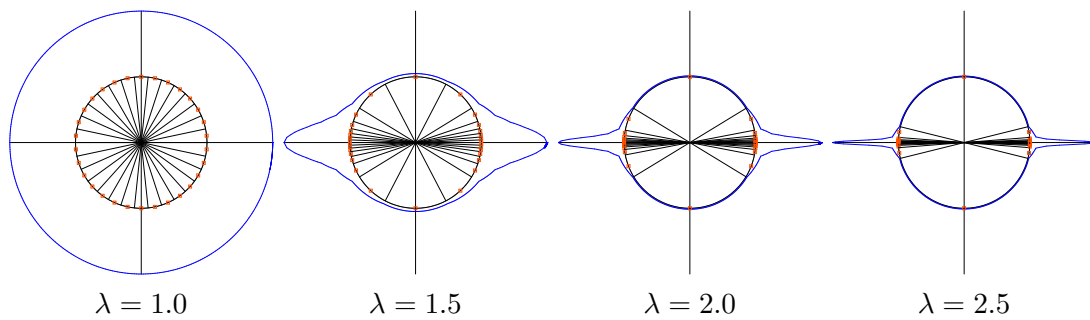


Figure 5.6: Evolution of the codf in planar crystals under pure shear for the Lagrangian approach with an initial isotropic codf and $N^h=15$ discrete orientations.

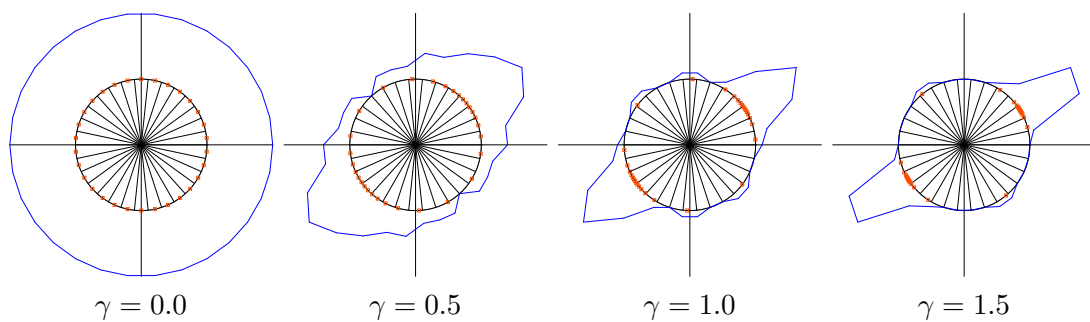


Figure 5.7: Evolution of the codf in planar crystals under simple shear for the Eulerian approach with an initial isotropic codf and $N^h=15$ discrete orientations.

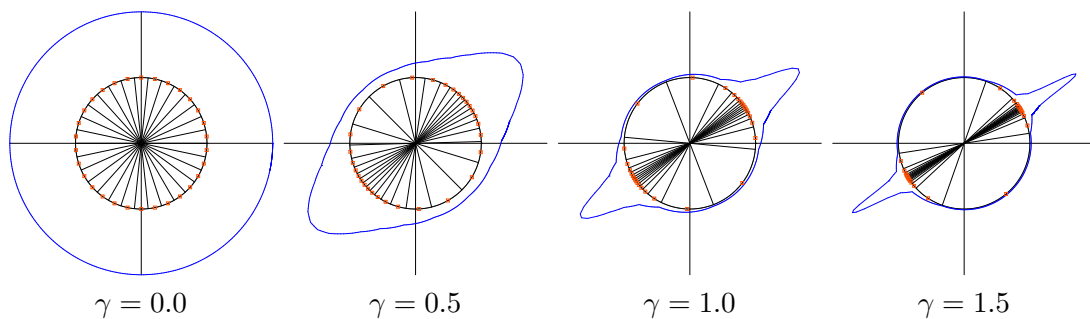


Figure 5.8: Evolution of the codf in planar crystals under simple shear for the Lagrangian approach with an initial isotropic codf and $N^h=15$ discrete orientations.

approach, smoother results are obtained. Here, in contrast to the Eulerian approach, a sharply varying codf can be resolved. Such a resolution cannot be achieved within the Eulerian approach, because of the projection of the codf onto the nodes of a coarse partition of the orientation space. However, the qualitative overall picture is the same for both approaches.

5.3.1.2. Codf Evolution in Planar Polycrystals: Simple Shear. The second example treats the simple shear test, with the initial and deformed configurations shown in Figure 4.3b). Reorientations and the evolution of the codf for the Eulerian and the Lagrangian approaches are shown in Figures 5.7 and 5.8, respectively. Again, four levels of deformation with a maximum shear of $\gamma = 1.5$ are depicted. Starting from an equidistant distribution of the orientations, a reorientation towards the preferred direction can be observed. The isotropic initial codf evolves into a strongly anisotropic codf, where finally all grains are oriented at $30^\circ/210^\circ$.

For the two approaches the resolution of the codf is compared for different discretizations. At $\gamma = 0.0, 1.0, 2.0$ the reorientation and the codf are illustrated in Figure 5.9 for the Eulerian approach and in Figure 5.10 for the Lagrangian approach, with $N^h = 15, 25, 45$ cells, respectively. One observes that with increasing number of orientations, the Eulerian approach shows improved results with regard to the resolution of sharp codfs. In contrast,

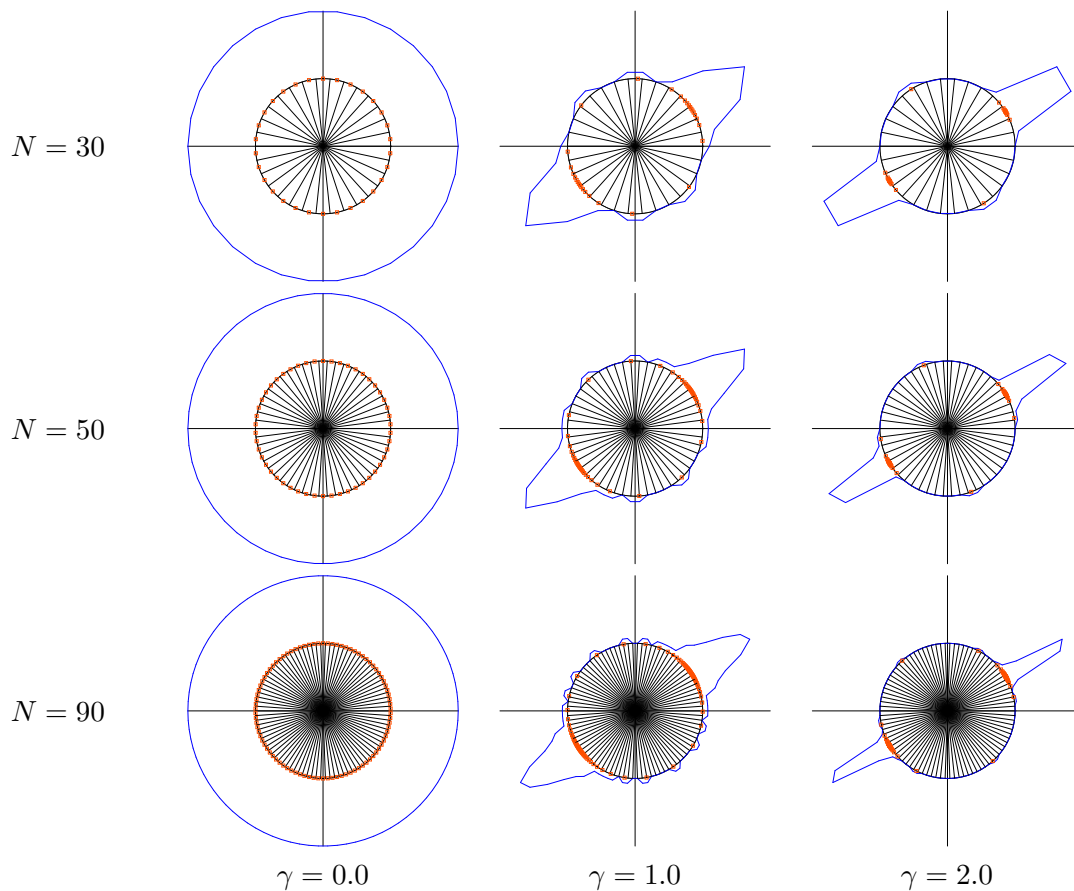


Figure 5.9: Evolution of the discretized codf in planar crystals for the simple shear mode within the Eulerian approach, obtained for different discretizations of the orientation space.

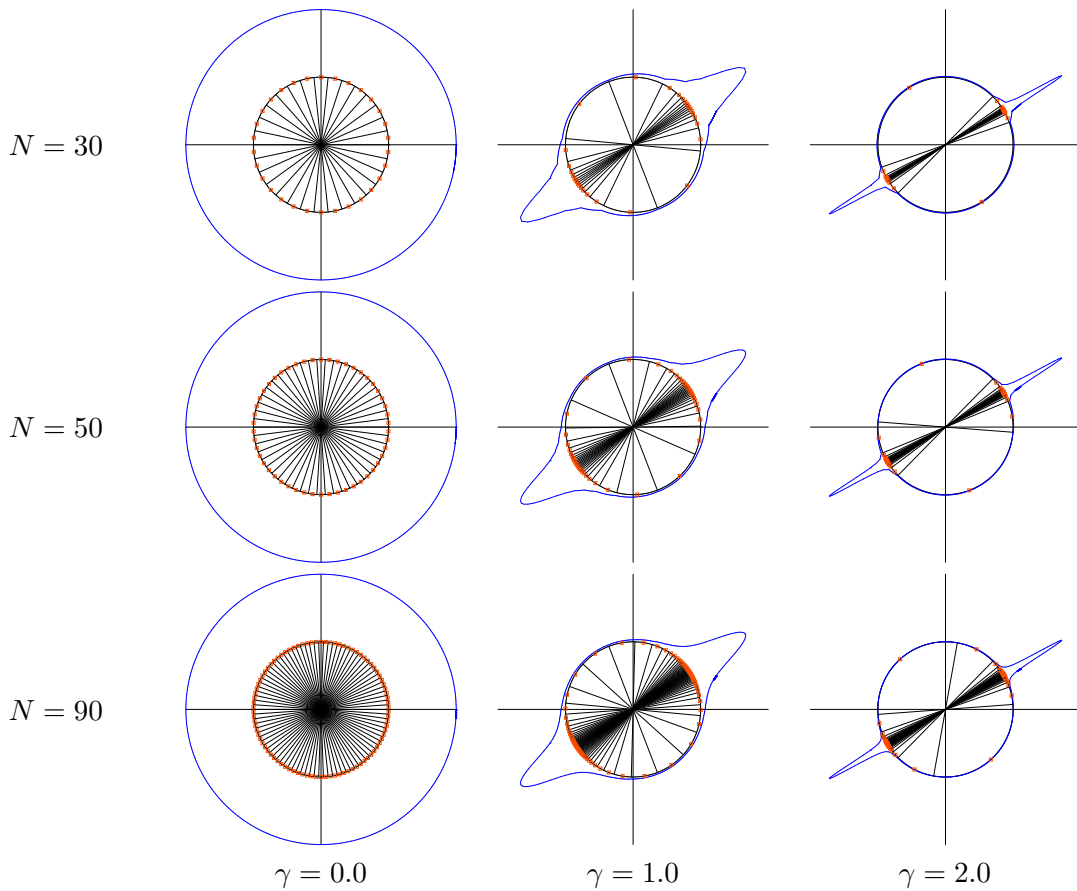


Figure 5.10: Evolution of the discretized codf in planar crystals for the simple shear mode within the Lagrangian approach, obtained for different discretizations of the orientation space.

the influence of the number of orientations N^h on the codf within the Lagrangian approach is insignificant. The number of orientations N^h is directly related to the computational effort. Since the amount of center points and nodes coincide in the planar examples, the computation time does not differ for the two approaches. Even though the computation time is relatively insignificant in the simple one-dimensional case under consideration, it increases with the number of orientations. For $N^h = 15$ the CPU time is $t = 0.120$ s, for $N^h = 25$ it is $t = 0.155$ s and for $N^h = 45$ it is $t = 0.210$ s.

5.3.2. Evolution of Codf in Fcc Crystals. Similar to the previous subsection, the reorientation process of fcc polycrystals in Section 4.4.2.2 is now expanded by the evolution of crystal orientation distribution functions for fcc polycrystals. As mentioned above, due to developing discontinuities in three-dimensional reorientation processes in the following solely the robust Eulerian formulation is applied. As homogeneous deformation modes plane strain compression and simple compression modes have been chosen for this investigation, as performed by KUMAR & DAWSON [72, 76] and ACHARJEE & ZABARAS [6]. Recall, that all orientations can be represented inside the fundamental cube. Hence, if there are orientations leaving the cube during deformation, they must be projected back into the cube on the diametrically opposite face, see FRANK [42]. This requires the identification of the associated face of the truncated cube, where an orientation leaves the

fundamental Rodrigues space. Within the Eulerian approach to fcc crystals, the computation of the codf is performed similar to the procedure for planar polycrystals. Again, the cell of the initial mesh must be determined in which the considered orientation \mathbf{r}_e lies. To this end, the linear set of equations

$$\mathbf{r}_e = \mathbf{A}_e \cdot \boldsymbol{\xi}_e \quad \text{with} \quad e = 1, \dots, E^h \quad (5.62)$$

must be solved for the volume coordinates $\boldsymbol{\xi}_e$. The transformation matrix \mathbf{A}_e is constant for every cell e during the deformation process and needs to be set up and inverted just once. For all Rodrigues vectors \mathbf{r}_e the parameter coordinates $\boldsymbol{\xi}_e$ are computed at every time step. If the coordinate condition

$$|\xi_e^{\mathcal{T}^h(1,e)} + \xi_e^{\mathcal{T}^h(2,e)} + \xi_e^{\mathcal{T}^h(3,e)} + \xi_e^{\mathcal{T}^h(4,e)} - 1| \leq \text{tol}_\xi \quad (5.63)$$

is satisfied, the cell $e^* = e$ is detected. Finally, the contribution of the codf at the nodes of cell e^* is accumulated according to

$$\boxed{f_{\mathcal{T}^h(k,e^*)}^h \leftarrow f_{\mathcal{T}^h(k,e^*)}^h + \frac{1}{E^h} \xi_{e^*}^{\mathcal{T}^h(k,e^*)}} \quad (5.64)$$

for the $k = 1, \dots, 4$ local nodes of the cell. As in the one-dimensional case, this procedure is performed for all center orientations and summed up as shown above at the global nodes by use of the topology field. Notice that the codf is weighted by the volume coordinates ξ_{e^*} . In order to optimize the search algorithm, the truncated cube is partitioned into eight sections for $\pm \mathbf{x}$ i.e. $[(+x, +y, +z), (+x, -y, +z), (+x, +y, -z), (+x, -y, -z), (-x, +y, +z), (-x, -y, +z), (-x, +y, -z), (-x, -y, -z)]$. It should be pointed out, that the mesh is solely used for the specification of an initial distribution of orientations and for the search algorithm discussed above.

5.3.2.1. Codf Evolution in Fcc Crystals: Plane Strain Compression. Focus is put on the deformation-induced reorientation of the crystals represented in the Rodrigues space and the associated orientation distribution functions for the plane strain compression test based on the macro-deformation gradient (4.57). The computation of the reorientation follows from the procedure summarized in Box 4.1 and discussed in Section 4.4.2.2. In Figure 5.11, the reorientations of the cell center points in the Rodrigues space are shown, considering cube2 at four deformation states $vt_1 = 0.25$, $vt_2 = 0.50$, $vt_3 = 0.75$ and $vt_4 = 1.00$. The codf on the boundary of the Rodrigues space is illustrated in Figure 5.12 for the four established deformation states of cube2. At $vt_2 = 0.5$ the cube is sliced and the codf on these slices ($z = -0.368$, $z = -0.276$, $z = -0.184$, $z = -0.095$, $z = 0.0$, $z = 0.095$, $z = 0.184$, $z = 0.276$, $z = -0.368$) is displayed in Figure 5.13. The comparison with KUMAR & DAWSON [76] shows a very good qualitative agreement. Recall, that in KUMAR & DAWSON [76] a finite element procedure with a very fine discretization was used to resolve the codf. Clearly, in the coarse discretization of the Rodrigues space under consideration, sharp codfs cannot be resolved.

5.3.2.2. Codf Evolution in Fcc Crystals: Simple Compression. The second test considers a simple compression with the macro-deformation gradient (4.58). As in the plane strain compression case examined above, the reorientation and the evolution of the codf are computed. For cube2 the evolution of the orientations in Rodrigues space

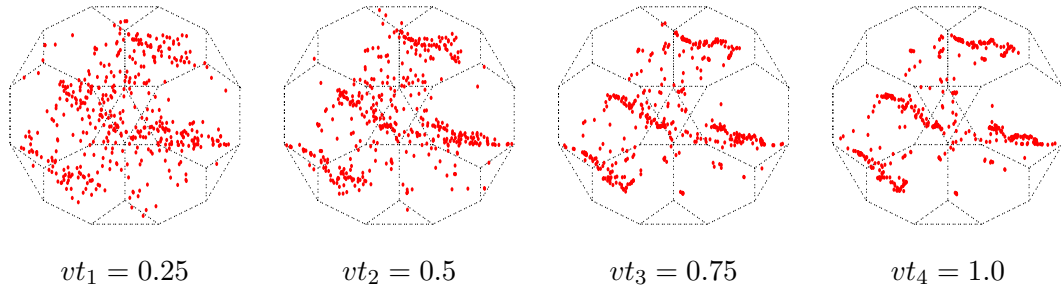


Figure 5.11: Codf evolution in fcc crystals under plane strain compression. Discrete reorientations at $vt_1 = 0.25$, $vt_2 = 0.5$, $vt_3 = 0.75$ and $vt_4 = 1.0$, plotted in the Rodrigues space.

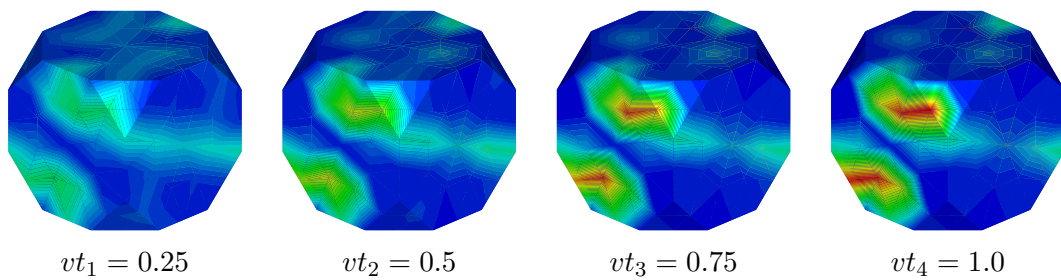


Figure 5.12: Codf evolution in fcc crystals under plane strain compression. Codf on the surface of the Rodrigues space at $vt_1 = 0.25$, $vt_2 = 0.5$, $vt_3 = 0.75$ and $vt_4 = 1.0$.

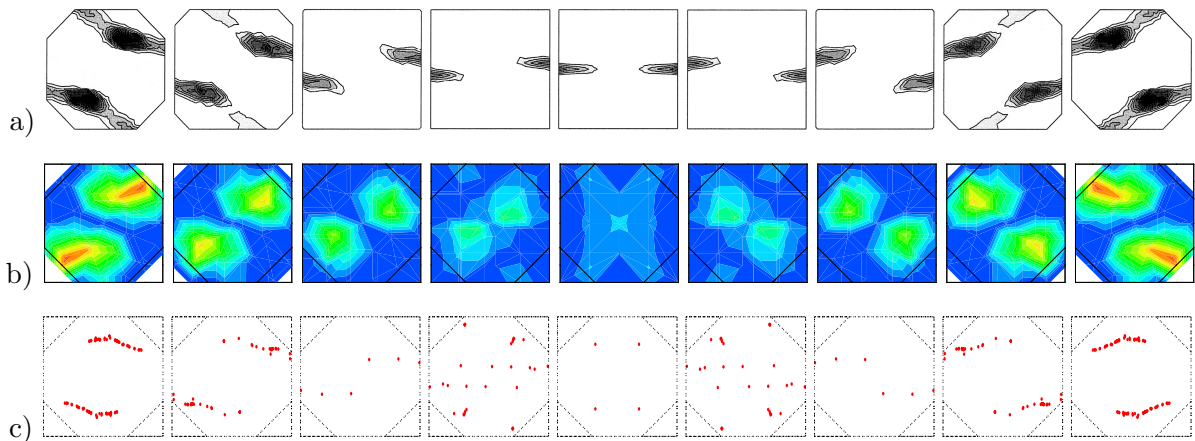


Figure 5.13: Codf evolution in fcc crystals under plane strain compression. Comparison of discrete reorientations and codf on slices through the Rodrigues space. a) Results taken from KUMAR & DAWSON [76], b) codf and c) orientations with cube2 discretization.

is shown in Figure 5.14. With these reorientations at hand, the codf is computed in a post-processing manner as described above. The codf on the boundary of the truncated cube and on slices through the cube are illustrated in Figures 5.15 and 5.16. The results match those of KUMAR & DAWSON [76].

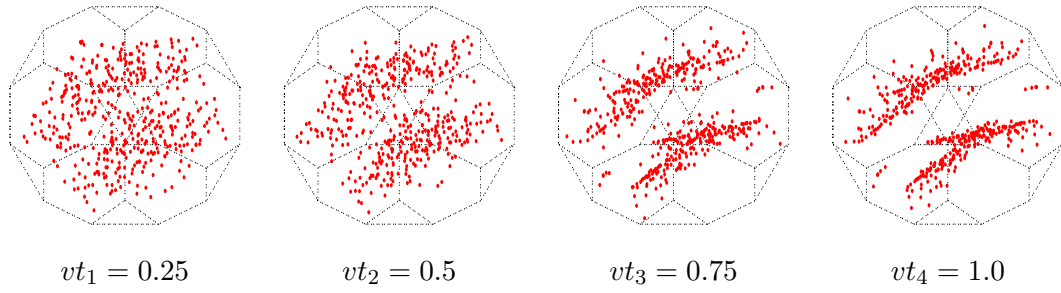


Figure 5.14: Codf evolution in fcc crystals under simple compression. Discrete reorientations at $vt_1 = 0.25$, $vt_2 = 0.5$, $vt_3 = 0.75$ and $vt_4 = 1.0$, plotted in the Rodrigues space.

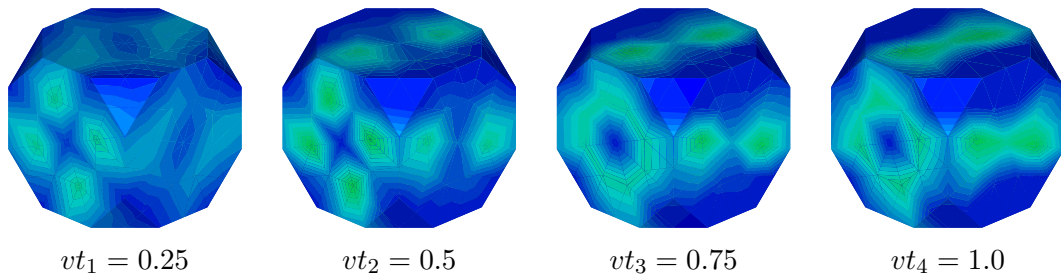


Figure 5.15: Codf evolution in fcc crystals under simple compression. Codf on the surface of the Rodrigues space at $vt_1 = 0.25$, $vt_2 = 0.5$, $vt_3 = 0.75$ and $vt_4 = 1.0$.

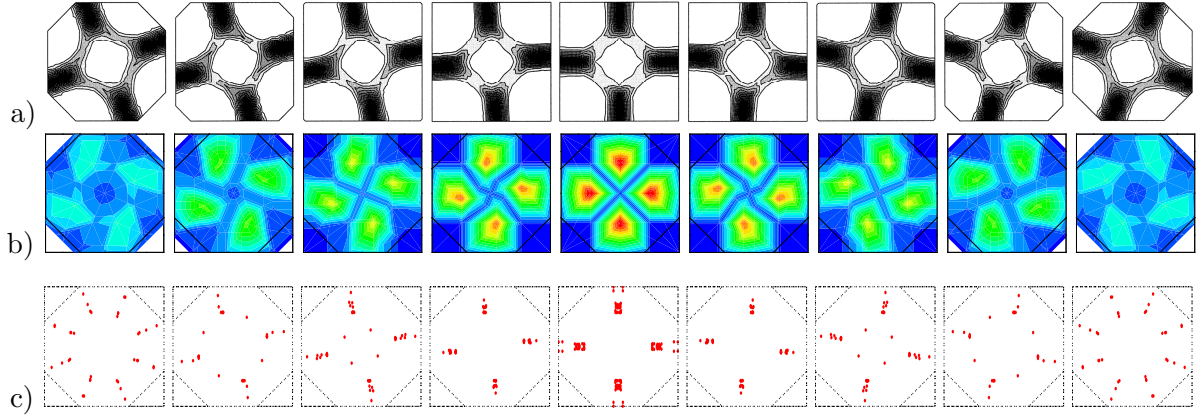


Figure 5.16: Codf evolution in fcc crystals under simple compression. Comparison of discrete reorientations and codf on slices through the Rodrigues space. a) Results taken from KUMAR & DAWSON [76], b) codf and c) orientations with cube2 discretization.

5.4. Orientation Averages and Homogenization

5.4.1. Continuous Formulation. With the above formulation at hand, orientation averages of quantities on the orientation space can be defined. The Eulerian definition of an orientation average is

$$\bar{s}(t) := \int_{\mathcal{O}_t} f(\boldsymbol{\theta}_t, t) \mathbf{s}(\boldsymbol{\theta}_t, t) d\mathcal{O}_t, \quad (5.65)$$

compare (3.53). Here, $\mathbf{s}(\boldsymbol{\theta}_t, t)$ may be a time-dependent scalar or tensor-valued state function defined on the orientation space. $\bar{\mathbf{s}}$ is the homogenized quantity of values \mathbf{s} defined on the orientation space, weighted by the codf f . Pulling back this integral to the Lagrangian setting gives

$$\bar{\mathbf{s}}(t) := \int_{\mathcal{O}_0} F(\boldsymbol{\theta}_0, t) \mathbf{s}(\boldsymbol{\chi}(\boldsymbol{\theta}_0, t), t) \det[\nabla_{\boldsymbol{\theta}_0} \boldsymbol{\chi}(\boldsymbol{\theta}_0, t)] d\mathcal{O}_0 \quad (5.66)$$

with (5.43) and the relationship between initial and current volume elements in (5.5). The insertion of the local Lagrangian conservation equation (5.48) results in

$$\bar{\mathbf{s}}(t) := \int_{\mathcal{O}_0} F(\boldsymbol{\theta}_0, t_0) \mathbf{s}(\boldsymbol{\chi}(\boldsymbol{\theta}_0, t), t) d\mathcal{O}_0 \quad (5.67)$$

with the uniform initial codf $F(\boldsymbol{\theta}_0, t_0) = 1/|\mathcal{O}_0|$, yielding the Lagrangian expression

$$\boxed{\bar{\mathbf{s}}(t) := \frac{1}{|\mathcal{O}_0|} \int_{\mathcal{O}_0} \mathbf{s}(\boldsymbol{\chi}(\boldsymbol{\theta}_0, t), t) d\mathcal{O}_0 .} \quad (5.68)$$

Note carefully, that in the Lagrangian expression the current crystal orientation distribution function is not needed for the computation of the orientation averages, if the values are evaluated with known reorientation function $\boldsymbol{\chi}$ at the current orientations $\boldsymbol{\theta}_t = \boldsymbol{\chi}(\boldsymbol{\theta}_0, t)$.

5.4.2. Discrete Formulation. In the discrete setting, the counterpart of the Eulerian definition (5.65) of an orientation average

$$\bar{\mathbf{s}}(t) := \sum_{e=1}^{E^h} f^h(\boldsymbol{\theta}_t^e, t) \mathbf{s}(\boldsymbol{\theta}_t^e, t) |\mathcal{O}_t^e| \quad (5.69)$$

is obtained based on the cell discretization outlined above in terms of the discrete Eulerian codf, introduced in (5.50). The insertion of the discrete function (5.53) with constant Eulerian control volumes (5.49) results in the simple formulation

$$\bar{\mathbf{s}}(t) := \frac{1}{E^h} \sum_{e=1}^{E^h} N(\mathcal{O}^e, t) \mathbf{s}(\boldsymbol{\theta}^e, t) \quad (5.70)$$

in terms of the number $N(\mathcal{O}^e, t)$ of crystal orientations which fall currently into the sector $\mathcal{O}^e \subset \mathcal{O}^h$. However, such a formulation is non-smooth due to the elementary counting procedure and only suitable for a rough estimate. A smooth formulation is achieved by pulling back the integral (5.69) to the Lagrangian setting

$$\bar{\mathbf{s}}(t) := \sum_{e=1}^{E^h} F^h(\boldsymbol{\theta}_0^e, t_0) \mathbf{s}(\boldsymbol{\chi}(\boldsymbol{\theta}_0^e, t), t) |\mathcal{O}_0^e| . \quad (5.71)$$

With the uniform initial orientation distribution function (5.56), the discrete counterpart of (5.68) reads

$$\boxed{\bar{\mathbf{s}}(t) := \frac{1}{|\mathcal{O}_0^h|} \sum_{e=1}^{E^h} \mathbf{s}(\boldsymbol{\chi}(\boldsymbol{\theta}_0^e), t) |\mathcal{O}_0^e| .} \quad (5.72)$$

A particular simple result is obtained for a Lagrangian mesh with equal cell size $|\mathcal{O}_0^e| = |\mathcal{O}_0^h|/E^h$, yielding the arithmetic average

$$\bar{\mathbf{s}}(t) := \frac{1}{E^h} \sum_{e=1}^{E^h} \mathbf{s}(\boldsymbol{\chi}(\boldsymbol{\theta}_0^e, t), t). \quad (5.73)$$

Again, note carefully that the explicit representation of the crystal orientation distribution function is not needed for the evaluation of the averages (5.72) and (5.73), respectively.

5.4.3. Evolution of Texture-Induced Anisotropy. Definition of Anisotropy Coefficients. This subsection considers the numerical evaluation of evolving yield surfaces in fcc polycrystals based on the ingredients outlined above. The approach follows conceptually the works MAN [80, 81] and BÖHLKE & BERTRAM [28]. In order to describe the evolving anisotropy, texture-dependent parameters introduced in Section 3.3.4 are included in the yield criterion.

The tensorial coefficients of each rank can be computed for given codf $f(\boldsymbol{\theta}, t)$ by the scaled orientation averages

$$\mathbf{c}^m = (2m + 1) \int_{\mathcal{O}} f(\boldsymbol{\theta}, t) \mathbf{b}^m(\boldsymbol{\theta}, t) d\mathcal{O}, \quad (5.74)$$

compare (3.64). Thus, \mathbf{c}^m represents a homogenized quantity as defined in general in equation (5.65). Comparison of (5.74) with (5.65) yields, together with the procedure described above, the discrete evaluation for the anisotropy coefficients

$$\mathbf{c}^m = \frac{(2m + 1)}{E^h} \sum_{e=1}^{E^h} \mathbf{b}^m(\boldsymbol{\theta}, t) \quad (5.75)$$

as an application of the general representation (5.73). Note again, that this representation is independent of the codf and will be one of the key ingredients for a hybrid micro-macro model to be discussed in Section 6.

5.4.4. Numerical Study.

5.4.4.1. Distortional Evolution of Yield Surfaces. The evolving anisotropy due to texture development can be illustrated by distortional changes of a yield surface. To this end, a classical Hill-type yield function of metal plasticity

$$\phi = \|\mathbf{S}\|_{\mathbb{H}} - \sqrt{\frac{2}{3}} y_0 \leq 0 \quad (5.76)$$

is considered, where $\|\mathbf{S}\|_{\mathbb{H}} := \sqrt{\mathbf{S} : \mathbb{H} : \mathbf{S}}$ is the norm of the second Piola stress tensor \mathbf{S} with respect to the fourth-order Hill tensor \mathbb{H} . To simplify matters, isotropic and kinematic hardening are not considered so far. For $\mathbb{H} = \mathbb{P} := \mathbb{I} - \frac{1}{3} \mathbf{1} \otimes \mathbf{1}$, (5.76) gives the classical isotropic von Mises yield criterion with the fourth order projection tensor \mathbb{P} , the fourth order identity tensor \mathbb{I} and the second order identity tensor $\mathbf{1}$. Simply assume that the yield criterion is governed by the fourth-order anisotropy coefficient tensor \mathbf{c}_4 . Thus, the Hill tensor

$$\mathbb{H} = \mathbb{P} + \zeta_4 \mathbf{c}_4 \quad (5.77)$$

is texture-dependent through the evolving fourth-order anisotropy coefficient \mathbf{c}_4 . This is considered to be the simplest representation accounting for an evolving anisotropy. The macroscopic material parameter ζ_4 scales the microstructural influence on the macroscopic anisotropy and consequently the shape of the yield surface.

The evolution of the yield surfaces for fcc polycrystals under a plane strain compression mode, usually called a rolling mode is examined with the associated deformation gradient defined in (4.57). For the discretizations cube1, cube2, cube4 and cube8, the yield surfaces for plane strain compression are shown on top in Figure 5.17 for $vt_0 = 0.0$ and $vt_4 = 1.0$. In a) the scaling parameter is chosen to be $\zeta_4 = 0.2$. Observe initially a von Mises ellipse related to the isotropic initial state for all discretizations. At $vt_4 = 1.0$, the yield stress during the deformation process increases and a rotation of the yield surface occurs, comparable to the observations reported in KOWALCZYK & GAMBIN [70] and KOCKS, TOMÉ & WENK [69]. A very good agreement for cube2, cube4 and cube8 is observed. For the coarse discretization cube1, however, the yield surface is larger. As pointed out before, the important task under consideration is the determination of the shape of the yield surface. Using different values of the macroscopic parameter ζ_4 , the yield surface can be scaled appropriately. For $\zeta_4 = 0.15$, the yield surface for cube1 is in good agreement to the yield surface for cube8 obtained with $\zeta_4 = 0.2$, see top of Figure 5.17b). Hence, the most coarse discretization of the microstructural orientation space already describes the main features of the texture-induced anisotropy on the macroscopic level. This is a consequence of the hybrid micro-macro modeling of the evolving texture-induced anisotropy governed by the ansatz (5.77).

5.4.4.2. Normalized Yield Stress and Lankford Coefficient. In order to examine the evolved anisotropy, uniaxial tension tests are performed on the sheet plane $\mathbf{e}_1 - \mathbf{e}_2$ of Figure 5.18. Here different directions parameterized by the angle ϕ with respect to the rolling direction \mathbf{e}_2 are examined. With these uniaxial tension tests, the yield stress S_ϕ and the so-called Lankford coefficient R_ϕ can be determined as a function of the angle ϕ . The vector \mathbf{e}_{ϕ_1} in Figure 5.18 characterizes the uniaxial tension direction. As discussed in KOWALCZYK & GAMBIN [70], the specimen under uniaxial tension is subject to a stress

$$\mathbf{S} = S_\phi \mathbf{e}_{\phi_1} \otimes \mathbf{e}_{\phi_1} \quad \text{with} \quad \mathbf{e}_{\phi_1} = \sin \phi \mathbf{e}_1 + \cos \phi \mathbf{e}_2 \quad (5.78)$$

in terms of the rolling direction \mathbf{e}_2 and the transverse direction \mathbf{e}_1 . Using the yield criterion (5.76) and $\|\mathbf{S}\|_{\mathbb{H}} = S_\phi \|\text{dev}[\mathbf{e}_{\phi_1} \otimes \mathbf{e}_{\phi_1}]\|_{\mathbb{H}}$, a normalized yield stress reads

$$\frac{S_\phi}{y_0} = \frac{\sqrt{2/3}}{\|\text{dev}[\mathbf{e}_{\phi_1} \otimes \mathbf{e}_{\phi_1}]\|_{\mathbb{H}}}. \quad (5.79)$$

For the isotropic case with $\zeta_4 = 0$ the denominator on the right hand side is equal to $\sqrt{2/3}$ and hence $S_\phi/y_0 = 1$. In Figure 5.17, S_ϕ/y_0 is plotted as a function of ϕ in correspondence with two different deformation stages and different discretizations. In the right column the adaption of cube1 to cube8 is shown by using $\zeta_4 = 0.15$ and $\zeta_4 = 0.2$, respectively. Observe, that the relative yield stress at $\pi/4$ falls below the initial value. The obtained result exhibits a very good qualitative agreement compared to the corresponding results presented e.g. in BÖHLKE, RISY & BERTRAM [30]. For the same deformation mode, they plotted a normalized yield stress for an initially anisotropic texture, where the normalization is performed with respect to the maximum value of the yield stress. Furthermore, the Lankford coefficients, also called r -values, as a function of the angle to

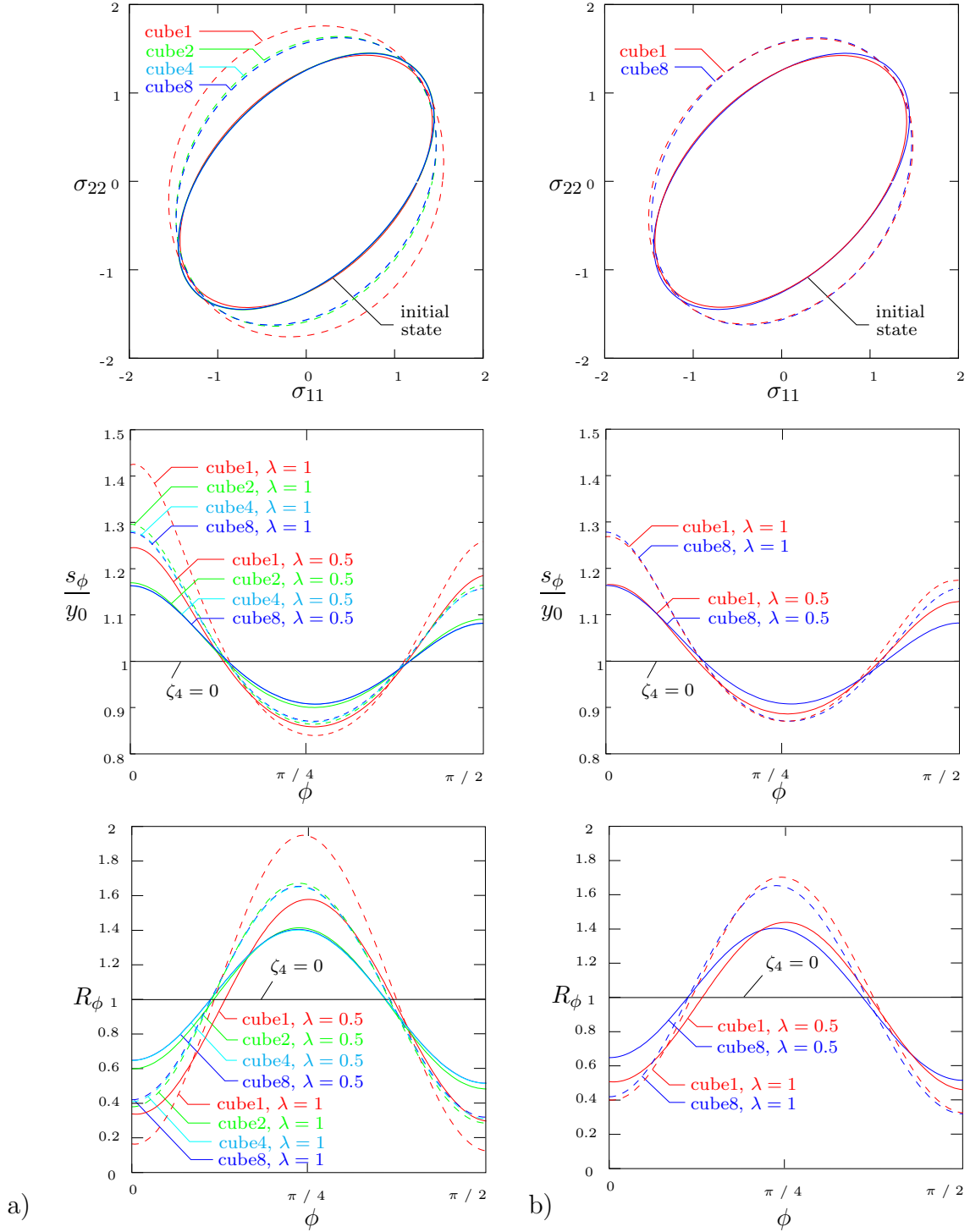


Figure 5.17: Yield surfaces, normalized yield stresses and r -values plotted for different discretizations of the orientation space cube1, cube2, cube4 and cube8 for plane strain compression mode at $\lambda = 0$, $\lambda = 0.5$ and $\lambda = 1$. The macroscopic scaling in the hybrid approach is set to a) $\zeta_4 = 0.2$ and b) $\zeta_4 = 0.15$.

the rolling direction are plotted in Figure 5.17. It is a measure for the anisotropy and defined as

$$R_\phi = \frac{d_{22}^{p,\phi}}{d_{33}^{p,\phi}} = \frac{\mathbf{e}_{\phi 2} \cdot \mathbf{d}^p \cdot \mathbf{e}_{\phi 2}}{\mathbf{e}_{\phi 3} \cdot \mathbf{d}^p \cdot \mathbf{e}_{\phi 3}}, \quad (5.80)$$

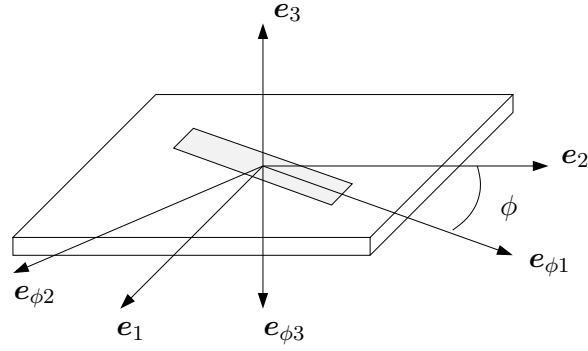


Figure 5.18: Uniaxial tension test in the direction ϕ of a metal sheet for the characterization of anisotropy.

where $d_{22}^{p,\phi}$ and $d_{33}^{p,\phi}$ are the components of the plastic strain rate tensor $\mathbf{d}^p = \lambda \partial_S \phi$. Making use of the yield function (5.76) it follows

$$R_\phi = \frac{\mathbf{e}_{\phi 2} \cdot (\mathbb{H} : \text{dev} [\mathbf{e}_{\phi 1} \otimes \mathbf{e}_{\phi 1}]) \cdot \mathbf{e}_{\phi 2}}{(\mathbb{H} : \text{dev} [\mathbf{e}_{\phi 1} \otimes \mathbf{e}_{\phi 1}])_{33}}. \quad (5.81)$$

For the isotropic case $\zeta_4 = 0$ the Lankford coefficient is $R_\phi = 1$, i.e. the material yields isotropically in all directions. For an r -value less/greater than 1 the behavior is anisotropic whereas more material yields in thickness/width under tension. The sheet has more resistance against a decrease in width/thickness. In a deep-drawing process an inhomogeneous deformation called earing appears whose behavior depends on the r -value. Ears develop in locations of maximum r -value. The results obtained for the r -value are in a very good qualitative agreement for instance with the ones in BÖHLKE, RISY & BERTRAM [30] and KOWALCZYK & GAMBIN [70].

6. Hybrid Modeling of Texture-Induced Anisotropy

The underlying goal of this section is the embedding of the microscopic mechanism of grain reorientation into a hybrid micro-macro modeling by means of tensorial texture components. As outlined in Section 2.2, there exist a lot of approaches in crystal plasticity to incorporate microstructural information directly into a macroscopic material model. With regard to two-scale descriptions of texture-induced anisotropies in polycrystals e.g. MATHUR & DAWSON [84], BRONKHORST, KALIDINDI & ANAND [33] and MIEHE, SCHRÖDER & SCHOTTE [98] assume a microstructure with discretized grains. Unfortunately such a modeling is computationally extremely demanding and less interesting for large-scale applications. Phenomenological anisotropic approaches based on anisotropic yield surfaces are indeed computationally less expensive but neglect the texture evolution during the deformation process. In polycrystalline materials the texture evolves during large strain deformations such as in deep drawing processes and hence this effect needs to be accounted for. Another possibility to reduce the computational effort is the use of texture components, which goes back to WASSERMANN & GREWEN [141] using discrete texture components for the interpretation of pole figures with regard to its physical significance. For the modeling of the crystal orientation distribution functions, representing the texture effect of the microstructure, RAABE, ZHAO & ROTERS [119] suggest a so-called texture component crystal plasticity method, cf. Section 2.2 for more details. This method was adopted by RAABE & ROTERS [118] and BÖHLKE, RISY & BERTRAM [29, 30] to overcome the overestimated anisotropy, i.e. to adopt the arising earing height. Contrarily to these Taylor-type polycrystal models, ENGLER & KALZ [41] derive earing profiles from texture data by means of a visco-plastic self-consistent polycrystal plasticity approach. The microstructural effects discussed in the previous sections can be used within a multi-scale framework in order to improve the macroscopic description with regard to evolving texture-induced macroscopic anisotropy. Therefore, the response of individual crystals has to be put into a relationship to the macroscopic response of the material. This coupling is provided by a linking hypothesis governed by specific homogenization assumptions. In contrast to the definition of macroscopic overall stresses by straightforward computational homogenization methods such as FE^2 methods, cf. MIEHE, SCHRÖDER & SCHOTTE [98] and BALZANI, SCHRÖDER & BRANDS [18], or Taylor-type methods, the hybrid approach presented in this contribution consists of a coupled micro-macro modeling based on three ingredients:

- A microscopic plasticity model outlined in Section 4 is formulated in a simplified manner for rigid-plastic grain reorientations. The key aspect with regard to the computational efficiency is a fast, purely geometric estimate of crystal reorientations.
- A homogenization-based bridging concept couples the micro-mechanism of grain orientation with the evolution of structural anisotropy tensors presented in Section 5.4. These macroscopic structural tensors are governed by a specific homogenization procedure of the crystal orientation distribution functions, cf. Section 5.
- A macroscopic plasticity model includes the afore calculated evolving structural tensors and describes the evolution of the macroscopic anisotropy.

The proposed fast reorientation update and homogenization procedure of the reorientation continuum are perfect ingredients for the description of evolving texture-induced

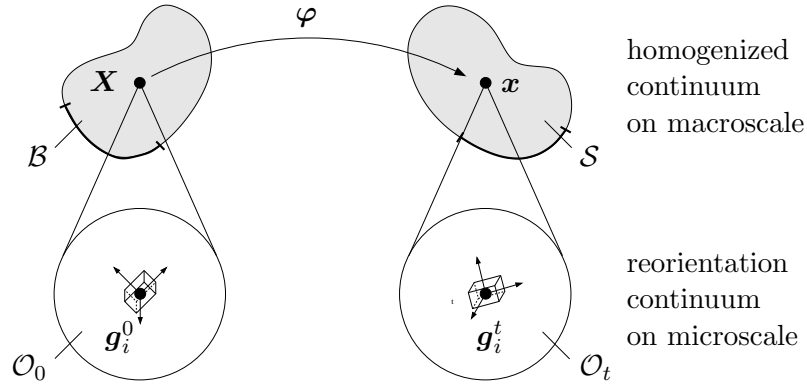


Figure 6.1: Homogenized continuum on the macroscale with locally, i.e. pointwise, attached polycrystalline aggregates idealized as reorientation continua on the microscale in both the undeformed state \mathcal{B} as well as the deformed state \mathcal{S} .

anisotropy and computationally efficient micro-macro scenarios for polycrystalline plasticity can be developed. To each material point a polycrystalline aggregate idealized as reorientation continuum is attached, cf. Figure 6.1. In a deformation-driven scenario, the macroscopic deformation causes a reorientation process of the microstructure, which in turn induces the macroscopic anisotropy resulting among others in the evolution of earings and varying thickness distribution of metal sheets during deep drawing. As deep drawing processes undergo large strain deformations, the material model needs to be formulated in a finite strain context. Following MIEHE, APEL & LAMBRECHT [90], an additive formulation of finite plasticity in the logarithmic strain space is used in this work.

In Section 6.1 the continuous formulation of the hybrid micro-macro model in finite polycrystal plasticity is presented. The corresponding algorithmic treatment is discussed in Section 6.2 and summarized in Box 6.3. In Section 6.3 representative numerical examples are presented. Here, the local texture evolution within a shearband of a 2D strip with initial isotropic and anisotropic texture and within the necking region of a 3D metallic rod is examined. Furthermore, the earing development within a circular and a square deep drawing process is simulated. Therefore, the material model is implemented in the user subroutine UEL of the finite element software package ABAQUS STANDARD 6.9-2.

6.1. Framework for Hybrid Micro-Macro Modeling in Finite Crystal Plasticity

The proposed hybrid micro-macro model in finite crystal plasticity is based on purely geometric transformations relating large and small strain settings. This additive approach of finite plasticity in the logarithmic strain space is proven to be in good agreement with the multiplicative approach, cf. MIEHE, APEL & LAMBRECHT [90]. Therefore, the hybrid micro-macro model to be developed in the following comprises the three major steps

- Preprocessor: $\bar{\boldsymbol{\varepsilon}} = \frac{1}{2} \ln[\bar{\mathbf{F}}^T \bar{\mathbf{g}} \bar{\mathbf{F}}]$
- **Hybrid Micro-Macro Model:** $\{\bar{\boldsymbol{\varepsilon}}, \bar{\mathbf{q}}_n\} \Rightarrow \{\bar{\boldsymbol{\sigma}}, \bar{\mathbf{q}}\}$
 - Input: current logarithmic strains $\bar{\boldsymbol{\varepsilon}}$ and historic state of micro-macro internal variables $\bar{\mathbf{q}}_n$, with subscript n indicating the last time step.
 - Output: current logarithmic stresses $\bar{\boldsymbol{\sigma}}$ and current internal variables $\bar{\mathbf{q}}$.
- Postprocessor: $\bar{\mathbf{g}} \bar{\mathbf{P}} = \bar{\boldsymbol{\sigma}} : \bar{\mathbf{Q}}$

Within the preprocessing step logarithmic strains $\bar{\boldsymbol{\varepsilon}}$ are computed from the finite macroscopic deformation gradient $\bar{\mathbf{F}}$. The hybrid micro-macro material model is formulated in terms of these logarithmic strains $\bar{\boldsymbol{\varepsilon}}$ and an additional set of internal variables $\bar{\mathbf{q}}$, namely the plastic strains and variables governing both macroscopic and microscopic hardening effects, in a format similar to the geometric linear theory. The macroscopic stresses $\bar{\boldsymbol{\sigma}}$ and moduli $\bar{\mathbb{E}}^{ep}$ obtained from the hybrid model in the logarithmic strain space are transformed in the postprocessing step to their nominal counterparts $\bar{\mathbf{P}}$ and $\bar{\mathbb{C}}^{ep}$, respectively.

6.1.1. Kinematic Approach in terms of a Plastic Metric. With regard to a hybrid modeling technique, the microstructural orientation continuum is linked via the in Section 5.4 outlined homogenization method to a macroscopic plasticity model. The macroscopic fundament is formed by a purely phenomenological framework of plasticity based on a plastic metric, developed in MIEHE [85]. Due to the plastic metric being a symmetric and positive definite second-order tensor with six linear independent components, the macroscopic plastic rotations are a priori excluded. In the following macroscopic quantities are denoted with a bar. Let $\bar{\mathcal{B}} \subset \mathcal{R}^3$ be the reference configuration of the macro-continuum of the solid, $\bar{\boldsymbol{\varphi}}(\bar{\mathbf{X}}, t)$ the nonlinear deformation map at time $t \in \mathcal{R}_+$ and $\bar{\mathbf{F}}$ the macroscopic deformation gradient, introduced in (2.4) and (2.5). According to (2.12), $\bar{\mathbf{g}}$ and $\bar{\mathbf{G}}$ are the standard covariant metric tensors on the current configuration and the reference configuration, respectively. The right and left Cauchy-Green tensors $\bar{\mathbf{C}}$ and $\bar{\mathbf{c}}$ introduced in (2.15) are denoted by MIEHE [85] as convected current metric and convected reference metric, respectively. For the modeling, the classical concept of internal variables is applied. These internal variables are additional quantities dual to the primary macroscopic variables describing the history and the current state of the inelastic deformation. The description of plastic deformations is based on the so-called covariant Lagrangian plastic metric $\bar{\mathbf{G}}^p = \bar{\mathbf{F}}^{pT} \bar{\mathbf{G}} \bar{\mathbf{F}}^p$ with $\bar{\mathbf{G}}^p(t = t_0) = \bar{\mathbf{G}}$ identified with the standard covariant metric on the reference configuration at the beginning $t = t_0$ of an elasto-plastic deformation. The evolution of $\bar{\mathbf{G}}^p$ is governed by the plastic flow rule (3.13). The stress power

$$\mathcal{P} := \bar{\mathbf{g}} \bar{\mathbf{P}}(t) : \dot{\bar{\mathbf{F}}}(t) \quad (6.1)$$

with respect to the unit volume of the reference configuration of the material is defined in terms of the non-symmetric first Piola or nominal stress $\bar{\mathbf{P}}$ introduced in Section 2.1.2. This tensor is said to be work-conjugate to the rate $\dot{\bar{\mathbf{F}}}$ of deformation. The non-symmetric tensors $\bar{\mathbf{P}}$ and $\bar{\mathbf{F}}$ are considered as the canonical pair of dual external variables of the local elastic-plastic material element.

6.1.2. Geometric Preprocessing into the Logarithmic Strain Space. A particular dependence of a Lagrangian elastic strain variable $\bar{\boldsymbol{\varepsilon}}^e := \bar{\boldsymbol{\varepsilon}}^e(\bar{\mathbf{C}}, \bar{\mathbf{G}}^p)$ on both the current metric $\bar{\mathbf{C}}$ and the plastic metric $\bar{\mathbf{G}}^p$ is provided by the additive decomposition

$$\bar{\boldsymbol{\varepsilon}}^e := \bar{\boldsymbol{\varepsilon}} - \bar{\boldsymbol{\varepsilon}}^p \quad (6.2)$$

in the logarithmic strain space as suggested in MIEHE, APEL & LAMBRECHT [90]. Here,

$$\bar{\boldsymbol{\varepsilon}} := \frac{1}{2} \ln \bar{\mathbf{C}} \quad \text{and} \quad \bar{\boldsymbol{\varepsilon}}^p := \frac{1}{2} \ln \bar{\mathbf{G}}^p, \quad (6.3)$$

are Hencky-type total and plastic strains, respectively. Due to the one-to-one relationship between $\bar{\boldsymbol{\varepsilon}}^p$ and $\bar{\mathbf{G}}^p$, in what follows the logarithmic plastic strains $\bar{\boldsymbol{\varepsilon}}^p$ are considered as

internal variable which describes the local plastic deformation. The volume change due to plastic deformation is described by the plastic Jacobi determinant

$$\bar{J}^p := \sqrt{\det[\bar{\mathbf{G}}^p]} = \{\det[\exp[2\bar{\boldsymbol{\varepsilon}}^p]]\}^{1/2} = \exp[\text{tr}[\bar{\boldsymbol{\varepsilon}}^p]] \quad (6.4)$$

with the identity $\det[\exp(\mathbf{A})] = \exp[\text{tr}(\mathbf{A})]$ of a quadratic tensor \mathbf{A} . The plastic incompressibility constraint $\bar{J}^p = 1$ as a basic feature in metal plasticity yields

$$\det[\bar{\mathbf{G}}^p] = 1 \quad \leftrightarrow \quad \text{tr}[\bar{\boldsymbol{\varepsilon}}^p] = 0 \quad (6.5)$$

in the logarithmic strain space in analogy to the geometric linear theory.

6.1.3. Hybrid Constitutive Model the Logarithmic Strain Space.

6.1.3.1. Micro-Macro Bridging. In the hybrid micro-macro modeling, the macroscopic plastic strains $\bar{\mathbf{G}}^p$ introduced above are assumed to determine the deformation (4.2) of the microscopic orientation continuum via

$$\bar{\mathcal{F}} := \sqrt{\bar{\mathbf{G}}^p} = \exp[\bar{\boldsymbol{\varepsilon}}^p]. \quad (6.6)$$

Thus, the microstructural aggregate is driven by a macroscopic plastic stretch of the plastic metric theory. For the typical scenario in metal forming the elastic strains are small compared to the large plastic strains. i.e. $\bar{\mathcal{F}} \approx \bar{\mathbf{U}}$, where $\bar{\mathbf{U}}$ is the stretch tensor from the polar decomposition (2.19), $\bar{\mathbf{F}} = \bar{\mathbf{R}}\bar{\mathbf{U}}$, of the macroscopic deformation gradient. As a consequence, the aggregate deformation $\bar{\mathcal{F}} \approx \bar{\mathbf{R}}^{-1}\bar{\mathbf{F}}$ is related to the macroscopic deformation by the macroscopic rigid rotation $\bar{\mathbf{R}}$. The definition of the aggregate deformation (6.6) independent from the macroscopic rigid rotation is a key ingredient of an objective constitutive modeling. Hence, the macroscopic plastic stretch $\bar{\mathbf{U}}$ drives the reorientation, parametrized by Rodrigues vectors \mathbf{r} , of the crystal grains on the microstructure. The specific homogenization of this reorientation process results in structural tensors

$$\mathbf{c}^m = \frac{(2m+1)}{E^h} \sum_{e=1}^{E^h} \mathbf{b}^m(\mathbf{r}, t), \quad (6.7)$$

discussed in detail in Section 5.4. These tensors represent the averaged anisotropy of the microstructure on the macro-scale and reflect the texture-induced orientation dependence

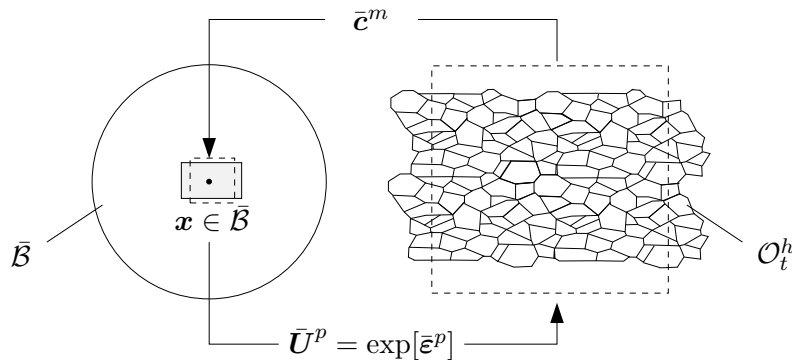


Figure 6.2: Deformation-driven homogenization. A macro-plastic strain $\bar{\boldsymbol{\varepsilon}}^p$ deforms the microstructure. Homogenization over the orientation space determines the macroscopic structural tensors $\bar{\mathbf{c}}^m$.

of the material. This deformation-driven homogenization procedure is visualized in Figure 6.2 with the macroscopic continuum $\bar{\mathcal{B}}$ and the microscopic orientation continuum \mathcal{O}_t^h representing the different scales. A key assumption is, that for the underlying work, this homogenization is performed in an operator splitting. Hence, the macroscopic problem is solved for frozen microstructure and afterwards the microstructure is updated at frozen macrostructure.

6.1.3.2. Energy Storage and Elastic Stress Response. With the logarithmic total and plastic strains (6.3) at hand, a constitutive model restricted to the logarithmic strain space is to be formulated. The state of the material at a local material point is assumed to be described by the total Hencky strains $\bar{\boldsymbol{\varepsilon}}$ together with a set of macroscopic internal variables $\bar{\mathbf{q}}$. These internal variables consist of the plastic strains $\bar{\boldsymbol{\varepsilon}}^p$, and strain-like internal variables modeling hardening effects. The free energy function

$$\bar{\Psi} = \bar{\Psi}(\bar{\boldsymbol{\varepsilon}}, \bar{\mathbf{q}}) \quad (6.8)$$

is a function of the state of the material, i.e. it depends on the total strains $\bar{\boldsymbol{\varepsilon}}$ and the set $\bar{\mathbf{q}}$ of internal variables. Recall, that this definition is similar to a geometric linear formulation. To link explicitly the macroscopic constitutive response with the microscopic resolution of grain-reorientation, distortional hardening and the anisotropy of the macroscopic material behavior due to texture development is taken into account according to Section 5 by the structural tensors defined in (6.7). Thus, the model problem is defined by the reduced set of macroscopic internal variables

$$\bar{\mathbf{q}} := \{\bar{\boldsymbol{\varepsilon}}^p, \bar{\boldsymbol{\alpha}}, \bar{\alpha}, \bar{\mathbb{A}}\} \quad (6.9)$$

with the plastic strains $\bar{\boldsymbol{\varepsilon}}^p$ introduced in (6.3), the second-order tensor $\bar{\boldsymbol{\alpha}}$, the scalar $\bar{\alpha}$ and the fourth-order tensor $\bar{\mathbb{A}}$ representing strain-like internal variables modeling kinematic, isotropic and distortional hardening effects. In the following formulation the fourth-order tensor $\bar{\mathbb{A}} = \bar{\mathbb{A}}(\bar{\boldsymbol{c}}^m)$ is assumed to be frozen within a typical time increment $[t_n, t]$, which reduces the set of internal variables $\bar{\mathbf{q}}^r := \{\bar{\boldsymbol{\varepsilon}}^p, \bar{\boldsymbol{\alpha}}, \bar{\alpha}\}$. The macroscopic constitutive response is governed by the free energy function $\bar{\Psi} = \bar{\Psi}^e + \bar{\Psi}^p$, which is in metal plasticity usually decomposed into elastic and plastic parts. The elastic part $\bar{\Psi}^e$ covers the energy storage due to macroscopic lattice deformations whereas the plastic part $\bar{\Psi}^p$ covers the energy storage due to micro-stress fields associated with dislocations or point defects, see RICE [123]. In the following, a fully decoupled representation of the free energy function

$$\bar{\Psi} = \bar{\Psi}^e(\bar{\boldsymbol{\varepsilon}} - \bar{\boldsymbol{\varepsilon}}^p; \bar{\boldsymbol{c}}^m) + \bar{\Psi}^k(\bar{\boldsymbol{\alpha}}) + \bar{\Psi}^i(\bar{\alpha}) \quad (6.10)$$

is considered with the specific form in the logarithmic strain space

$$\bar{\Psi}(\bar{\boldsymbol{\varepsilon}}, \bar{\mathbf{q}}^r; \bar{\boldsymbol{c}}^m) = \frac{1}{2} \|\bar{\boldsymbol{\varepsilon}} - \bar{\boldsymbol{\varepsilon}}^p\|_{\bar{\mathbb{E}}}^2 + \frac{\bar{c}_k}{2} \bar{\boldsymbol{\alpha}} : \bar{\boldsymbol{\alpha}} + \frac{\bar{c}_i}{2} \bar{\alpha}^2 \quad (6.11)$$

at frozen texture. Herein, \bar{c}_k , and \bar{c}_i are kinematic and isotropic hardening moduli. $\|\bar{\boldsymbol{\varepsilon}} - \bar{\boldsymbol{\varepsilon}}^p\|_{\bar{\mathbb{E}}}^2 := (\bar{\boldsymbol{\varepsilon}} - \bar{\boldsymbol{\varepsilon}}^p) : \bar{\mathbb{E}} : (\bar{\boldsymbol{\varepsilon}} - \bar{\boldsymbol{\varepsilon}}^p)$ is the norm of the elastic strains with respect to the fourth-order macroscopic elasticity tensor. This tensor is assumed to have the major and minor symmetries

$$\bar{\mathbb{E}}^{ABCD} = \bar{\mathbb{E}}^{BACD} = \bar{\mathbb{E}}^{ABDC} = \bar{\mathbb{E}}^{CDAB} . \quad (6.12)$$

$\bar{\mathbb{E}}$ is assumed here to consist of an isotropic and an anisotropic part according to

$$\bar{\mathbb{E}} := \bar{\mathbb{E}}_0 + \bar{\zeta}_e \bar{\mathbb{E}}_a(\bar{\boldsymbol{c}}^m) . \quad (6.13)$$

The isotropic initial modulus $\bar{\mathbb{E}}_0 := \bar{\lambda} \mathbf{1} \otimes \mathbf{1} + 2\bar{\mu} \mathbb{I}$ is written in terms of the macroscopic Lamé parameters $\bar{\lambda}$ and $\bar{\mu}$ and the second- and fourth-order identities $\mathbf{1}$ and \mathbb{I} , respectively. $\bar{\zeta}_e$ is a macroscopic material parameter that scales the effect of texture-based anisotropy on the elastic moduli and $\bar{\mathbb{E}}_a(\bar{\mathbf{c}}^m)$ is a fourth-order tensor function of the structural tensors $\bar{\mathbf{c}}^m$, see BÖHLKE & BERTRAM [27].

6.1.3.3. Dissipation and Plastic Flow Response with Hill-Type Yield Condition. With the functional dependence of the free energy on the total strains and a set of internal variables at hand, the local dissipation for the isothermal case is obtained from the Clausius-Planck inequality (2.52)₁

$$\rho_0 \mathcal{D} := \bar{\mathbf{g}} \bar{\mathbf{P}} : \dot{\bar{\mathbf{F}}} - \dot{\bar{\Psi}}(\bar{\boldsymbol{\varepsilon}}, \bar{\mathbf{q}}) \geq 0 \quad (6.14)$$

defined per unit of reference volume. Incorporation of the time derivative of the free energy gives the expression

$$\mathcal{D} := (\bar{\mathbf{g}} \bar{\mathbf{P}} - \partial_{\bar{\boldsymbol{\varepsilon}}} \bar{\Psi}(\bar{\boldsymbol{\varepsilon}}, \bar{\mathbf{q}}) : \bar{\mathbb{Q}}) : \dot{\bar{\mathbf{F}}} - \partial_{\bar{\mathbf{q}}} \bar{\Psi}(\bar{\boldsymbol{\varepsilon}}, \bar{\mathbf{q}}) \cdot \dot{\bar{\mathbf{q}}} \geq 0, \quad (6.15)$$

with the fourth-order nominal transformation tensor $\bar{\mathbb{Q}} := \partial_{\bar{\mathbf{F}}} \bar{\boldsymbol{\varepsilon}}$. Following standard arguments, the constitutive expression for the nominal stress tensor $\bar{\mathbf{P}}$ can be determined by the free energy $\bar{\Psi}(\bar{\boldsymbol{\varepsilon}}, \bar{\mathbf{q}})$, i.e.

$$\bar{\mathbf{g}} \bar{\mathbf{P}} = \partial_{\bar{\boldsymbol{\varepsilon}}} \bar{\Psi}(\bar{\boldsymbol{\varepsilon}}, \bar{\mathbf{q}}) : \bar{\mathbb{Q}}. \quad (6.16)$$

Note, that the nominal stresses can be written in the form $\bar{\mathbf{g}} \bar{\mathbf{P}} = \bar{\boldsymbol{\sigma}} : \bar{\mathbb{Q}}$, in terms of the logarithmic stresses

$$\bar{\boldsymbol{\sigma}} = \partial_{\bar{\boldsymbol{\varepsilon}}} \bar{\Psi}(\bar{\boldsymbol{\varepsilon}}, \bar{\mathbf{q}}) \quad (6.17)$$

dual to $\bar{\boldsymbol{\varepsilon}}$, which are mapped by the transformation tensor $\bar{\mathbb{Q}}$ to the nominal stresses. The identification (6.16) reduces the Clausius-Planck inequality (6.14) to the form

$$\mathcal{D} := \bar{\mathbf{p}} \cdot \dot{\bar{\mathbf{q}}} \geq 0 \quad \text{with} \quad \bar{\mathbf{p}} := -\partial_{\bar{\mathbf{q}}} \bar{\Psi}(\bar{\boldsymbol{\varepsilon}}, \bar{\mathbf{q}}) \quad (6.18)$$

representing the dissipative forces dual to the set of macroscopic internal variables $\bar{\mathbf{q}}$. To complete the constitutive setting, evolution equations need to be specified for the set of macroscopic internal variables $\bar{\mathbf{q}}$. These equations can be formulated by postulating the existence of a dissipation potential $\bar{\Phi}(\dot{\bar{\mathbf{q}}})$ depending on the flux $\dot{\bar{\mathbf{q}}}$ of the internal variables, cf. Biot equation (2.57). Here, the particular representation of the evolution equations for the internal variables are derived by invoking the principle of maximum dissipation

$$\bar{\Phi}(\dot{\bar{\mathbf{q}}}) = \sup_{\bar{\mathbf{p}} \in \bar{\mathcal{E}}} \{ \bar{\mathbf{p}} \cdot \dot{\bar{\mathbf{q}}} \} \quad (6.19)$$

where $\bar{\mathcal{E}}$ models a reversible domain usually called the elastic domain in the space of the dissipative macroscopic forces $\bar{\mathbf{p}}$

$$\bar{\mathcal{E}} := \{ \bar{\mathbf{p}} \mid \bar{\chi}(\bar{\mathbf{p}}) \leq 0 \} \quad (6.20)$$

defined in terms of the threshold function $\bar{\chi}(\bar{\mathbf{p}})$. This threshold function $\bar{\chi}(\bar{\mathbf{p}}) = \bar{f}(\bar{\mathbf{p}}) - \bar{c}$ can be expressed in terms of a level set function \bar{f} and a constant threshold parameter $\bar{c} \in \mathcal{R}^+$. The level set function is restricted to be convex, positively homogeneous of degree

one, zero at the origin and always positive. Consider an approximate penalty-type solution of the maximum problem (6.19)

$$\bar{\Phi}(\dot{\mathbf{q}}) = \sup_{\bar{\mathbf{p}}} \left\{ \bar{\mathbf{p}} \cdot \dot{\mathbf{q}} - \frac{1}{2\bar{\eta}} \langle \bar{\chi}(\bar{\mathbf{p}}) \rangle^2 \right\} \quad (6.21)$$

where the penalty parameter $\bar{\eta} > 0$ is interpreted as material parameter associated with the viscosity of the macroscopic material response. $\langle x \rangle = \frac{1}{2}(x + |x|)$ is the ramp function expressed by the McAuley brackets. The necessary conditions for the maximum problem (6.21) provides the non-linear evolution equations for the macroscopic internal variables

$$\dot{\mathbf{q}} = \frac{1}{\bar{\eta}} \langle \bar{\chi}(\bar{\mathbf{p}}) \rangle \partial_{\bar{\mathbf{p}}} \bar{\chi}(\bar{\mathbf{p}}) . \quad (6.22)$$

Having the internal variables at hand, the current stress $\bar{\boldsymbol{\sigma}}$ dual to the logarithmic strains and the associated elastic-plastic tangent moduli $\bar{\mathbb{E}}^{ep}$ are computed. These quantities are the main output of the constitutive model with regard to an algorithmic implementation. Note, that the underlying representation in the logarithmic strain space is very attractive as it makes the additive structure of the small strain theory applicable to the finite strain context.

Adopting the penalty solution (6.21) of the principle of maximum dissipation (6.19), the dissipation

$$\bar{\Phi}(\dot{\mathbf{q}}^r; \bar{\mathbf{c}}^m) = \sup_{\bar{\mathbf{p}}^r} \left\{ \bar{\mathbf{p}}^r \cdot \dot{\mathbf{q}}^r - \frac{1}{2\bar{\eta}} \langle \bar{\chi}(\bar{\mathbf{p}}^r; \bar{\mathbf{c}}^m) \rangle^2 \right\} \quad (6.23)$$

can be formulated in terms of the reduced set of dissipative forces

$$\bar{\mathbf{p}}^r := \{\bar{\boldsymbol{\sigma}}, \bar{\boldsymbol{\beta}}, \bar{\beta}\} = \{-\partial_{\bar{\boldsymbol{\varepsilon}}^p} \bar{\Psi}, -\partial_{\bar{\boldsymbol{\alpha}}} \bar{\Psi}, -\partial_{\bar{\alpha}} \bar{\Psi}\} \quad (6.24)$$

dual to the reduced set $\bar{\mathbf{q}}^r$ of internal variables (6.9). The internal force driving the plastic strains corresponds to the logarithmic stress (6.17), i.e. $\bar{\boldsymbol{\sigma}} = -\partial_{\bar{\boldsymbol{\varepsilon}}^p} \bar{\Psi} = \partial_{\bar{\boldsymbol{\varepsilon}}} \bar{\Psi}$, which again is a typical feature of the small strain theory. The threshold function is specified by

$$\bar{\chi}(\bar{\mathbf{p}}^r; \bar{\mathbf{c}}^m) = \|\bar{\boldsymbol{\sigma}} - \bar{\boldsymbol{\beta}}\|_{\bar{\mathbb{H}}} - \bar{c}_\chi(\bar{y}_0 + \bar{\beta}) . \quad (6.25)$$

Here \bar{y}_0 is the initial yield stress, $\bar{c}_\chi > 0$ a scaling factor for the isotropic hardening contribution and $\|\bar{\boldsymbol{\sigma}} - \bar{\boldsymbol{\beta}}\|_{\bar{\mathbb{H}}} := [(\bar{\boldsymbol{\sigma}} - \bar{\boldsymbol{\beta}}) : \bar{\mathbb{H}} : (\bar{\boldsymbol{\sigma}} - \bar{\boldsymbol{\beta}})]^{1/2}$ the norm of the relative stress with respect to the Hill tensor

$$\bar{\mathbb{H}} := \mathbb{P} + \bar{\zeta}_p \bar{\mathbb{H}}_a(\bar{\mathbf{c}}^m) , \quad (6.26)$$

which is assumed here to consist of an isotropic and anisotropic part. It is a fourth-order irreducible tensor with the major and minor symmetries, i.e.

$$\bar{\mathbb{H}}^{ABCD} = \bar{\mathbb{H}}^{BACD} = \bar{\mathbb{H}}^{ABDC} = \bar{\mathbb{H}}^{CDAB} \quad \text{and} \quad \bar{\mathbb{H}} : \mathbf{1} = \mathbf{0} . \quad (6.27)$$

In (6.26), $\mathbb{P} = \mathbb{I} - \frac{1}{3} \mathbf{1} \otimes \mathbf{1}$ represents the fourth-order deviatoric projection tensor and $\bar{\zeta}_p$ is a macroscopic parameter that scales the texture effects on the yield surface. The texture effects are taken into account by the fourth-order tensor function $\bar{\mathbb{H}}_a(\bar{\mathbf{c}}^m)$. Note, that the key constitutive equations (6.11), (6.23) and (6.25) in the logarithmic strain space have a structure similar to the geometric linear theory, which is considered as an important

advantage of the proposed framework. The hybrid coupling of the macro model to the polycrystalline microstructure is governed by (6.13) and (6.26). The necessary conditions (6.22) for the maximum problem (6.23) provide the non-linear evolution equations for the macroscopic internal variables $\bar{\mathbf{q}}^r$

$$\dot{\bar{\boldsymbol{\varepsilon}}^p} = \frac{1}{\bar{\eta}} \langle \bar{\chi}(\bar{\mathbf{p}}; \mathbf{c}_n^m) \rangle \frac{\bar{\mathbb{H}} : \bar{\boldsymbol{\xi}}}{\|\bar{\boldsymbol{\xi}}\|_{\bar{\mathbb{H}}}}, \quad \dot{\bar{\boldsymbol{\alpha}}} = -\frac{1}{\bar{\eta}} \langle \bar{\chi}(\bar{\mathbf{p}}; \mathbf{c}_n^m) \rangle \frac{\bar{\mathbb{H}} : \bar{\boldsymbol{\xi}}}{\|\bar{\boldsymbol{\xi}}\|_{\bar{\mathbb{H}}}}, \quad \dot{\bar{\alpha}} = -\frac{1}{\bar{\eta}} \langle \bar{\chi}(\bar{\mathbf{p}}; \mathbf{c}_n^m) \rangle \bar{c}_\chi \quad (6.28)$$

with the definition of the relative stress $\bar{\boldsymbol{\xi}} := (\bar{\boldsymbol{\sigma}} - \bar{\boldsymbol{\beta}})$ and the internal forces $\bar{\mathbf{p}}^r$

$$\bar{\boldsymbol{\sigma}} = \bar{\mathbb{E}} : (\bar{\boldsymbol{\varepsilon}} - \bar{\boldsymbol{\varepsilon}}^p), \quad \bar{\boldsymbol{\beta}} = -\bar{c}_k \bar{\boldsymbol{\alpha}}, \quad \bar{\beta} = -\bar{c}_i \bar{\alpha} \quad (6.29)$$

derived with the definitions (6.24) and the specific free energy function (6.11). Note, that the evolution equations for the kinematic hardening strains $\bar{\boldsymbol{\alpha}}$ and the plastic strains $\bar{\boldsymbol{\varepsilon}}^p$ are identical except for the sign. Due to the irreducibility (6.27) of the Hill tensor, it holds $\text{tr}[\bar{\boldsymbol{\varepsilon}}^p] = 0$, satisfying the incompressibility constraint (6.5).

Alternatively to the penalty-type solution (6.23), the maximum problem (6.19) can be solved by a Lagrangian multiplier method

$$\bar{\Phi}(\bar{\mathbf{q}}^r; \bar{\mathbf{c}}^m) = \sup_{\bar{\mathbf{p}}^r} \{ \bar{\mathbf{p}}^r \cdot \dot{\bar{\mathbf{q}}}^r + \bar{\lambda} \bar{\chi}(\bar{\mathbf{p}}^r; \bar{\mathbf{c}}^m) \}, \quad (6.30)$$

yielding a rate-independent formulation. The dissipation is here extended by the threshold function $\bar{\chi}$ weighted with the Lagrangian multiplier $\bar{\lambda}$. This multiplier is constraint by the well-known Karush-Kuhn-Tucker loading/unloading conditions

$$\bar{\lambda} \geq 0, \quad \bar{\chi} \leq 0 \quad \text{and} \quad \bar{\lambda} \bar{\chi} = 0 \quad (6.31)$$

being equivalent to

$$\bar{\lambda} = \begin{cases} \frac{1}{\bar{\eta}} \langle \bar{\chi}(\bar{\mathbf{p}}; \mathbf{c}_n^m) \rangle & \text{if } \bar{\chi} = 0 \\ 0 & \text{if } \bar{\chi} < 0 \end{cases} \quad (6.32)$$

in the rate-independent case. Hence, in rate-independent plasticity, the Lagrangian multiplier is governed by the Karush-Kuhn-Tucker conditions, whereas in viscoplasticity it is determined by an additional constitutive equation.

6.1.3.4. Continuous Elastic-Plastic Tangent Moduli. The derivation of the elastic-plastic tangent moduli starts with the rate expressions for the internal forces

$$\dot{\bar{\boldsymbol{\sigma}}} = \bar{\mathbb{E}} : \dot{\bar{\boldsymbol{\varepsilon}}}^e = \bar{\mathbb{E}} : [\dot{\bar{\boldsymbol{\varepsilon}}} - \dot{\bar{\boldsymbol{\varepsilon}}^p}], \quad \dot{\bar{\boldsymbol{\beta}}} = -\bar{c}_k \dot{\bar{\boldsymbol{\alpha}}} \quad \text{and} \quad \dot{\bar{\beta}} = -\bar{c}_i \dot{\bar{\alpha}} \quad (6.33)$$

dual to the macroscopic internal variables $\bar{\mathbf{q}}^r$ in terms of the second-order derivatives of the free energy function $\bar{\mathbb{E}} = \partial_{\bar{\boldsymbol{\varepsilon}}^e \bar{\boldsymbol{\varepsilon}}^e}^2 \Psi$, $\bar{c}_k = \partial_{\bar{\boldsymbol{\alpha}} \bar{\boldsymbol{\alpha}}}^2 \Psi$ and $\bar{c}_i = \partial_{\bar{\alpha} \bar{\alpha}}^2 \Psi$. The consistency condition demands that in case of plastic loading $\bar{\chi} = 0$ the stress state remains on the border of the elastic domain $\bar{\mathcal{E}}$, i.e. $\dot{\bar{\chi}} = 0$. This gives the expression

$$\partial_{\bar{\boldsymbol{\sigma}}} \bar{\chi} : \dot{\bar{\boldsymbol{\sigma}}} + \partial_{\bar{\boldsymbol{\beta}}} \bar{\chi} : \dot{\bar{\boldsymbol{\beta}}} + \partial_{\bar{\beta}} \bar{\chi} \cdot \dot{\bar{\beta}} = 0. \quad (6.34)$$

With the rate forms (6.33) and the evolution equations for the macroscopic internal variables (6.28), the consistency can be rewritten in

$$\partial_{\bar{\boldsymbol{\sigma}}} \bar{\chi} : \bar{\mathbb{E}} : \dot{\bar{\boldsymbol{\varepsilon}}} - \frac{1}{\bar{\eta}} \langle \bar{\chi} \rangle \bar{\boldsymbol{\xi}} = 0 \quad \text{with} \quad \bar{\boldsymbol{\xi}} := \partial_{\bar{\boldsymbol{\sigma}}} \bar{\chi} : \bar{\mathbb{E}} : \partial_{\bar{\boldsymbol{\sigma}}} \bar{\chi} + \partial_{\bar{\boldsymbol{\beta}}} \bar{\chi} : \bar{c}_k \partial_{\bar{\boldsymbol{\beta}}} \bar{\chi} + \partial_{\bar{\beta}} \bar{\chi} \cdot \bar{c}_i \partial_{\bar{\beta}} \bar{\chi} \quad (6.35)$$

and resolved for $\langle \bar{\chi} \rangle / \bar{\eta}$. Insertion of the resulting term into the rate expression (6.33)₁ yields the rate of the stress tensor

$$\dot{\bar{\sigma}} = \bar{\mathbb{E}}^{ep} : \dot{\bar{\epsilon}} \quad (6.36)$$

in terms of the elastic-plastic tangent moduli

$$\boxed{\bar{\mathbb{E}}^{ep} := \bar{\mathbb{E}} - \mathfrak{k}^{-1}(\bar{\mathbb{E}} : \partial_{\bar{\sigma}} \bar{\chi}) \otimes (\partial_{\bar{\sigma}} \bar{\chi} : \bar{\mathbb{E}})} \quad (6.37)$$

Clearly, for the case of plastic loading, i.e. $\langle \bar{\chi} \rangle / \bar{\eta} > 0$, a plastic softening term appears in the elastic-plastic tangent moduli.

6.1.4. Geometric Postprocessing from the Logarithmic Strain Space. In a post-processing step, the stresses and moduli obtained by the constitutive model in the logarithmic strain space need to be transformed back to the nominal stresses $\bar{\mathbf{P}}$ and moduli $\bar{\mathbb{C}}^{ep}$ in a purely geometric way. These stresses and moduli

$$\bar{\mathbf{g}}\bar{\mathbf{P}} = \bar{\sigma} : \bar{\mathbb{Q}} \quad \text{and} \quad \bar{\mathbb{C}}^{ep} = \bar{\mathbb{Q}}^T : \bar{\mathbb{E}}^{ep} : \bar{\mathbb{Q}} + \bar{\sigma} : \bar{\mathbb{L}} \quad (6.38)$$

are obtained in terms of the fourth-order and sixth-order nominal transformation tensors

$$\bar{\mathbb{Q}} := \partial_{\bar{\mathbf{F}}}\bar{\epsilon} \quad \text{and} \quad \bar{\mathbb{L}} := \partial_{\bar{\mathbf{F}}\bar{\mathbf{F}}}\bar{\epsilon} \quad (6.39)$$

For the explicit forms of the transformation tensors of the stresses and tangent in the logarithmic strain space to their nominal, Lagrangian or Eulerian counterparts, see MIEHE & LAMBRECHT [92]. The nominal elastic-plastic moduli $\bar{\mathbb{C}}^{ep}$ govern the rate of the nominal stresses with respect to the rate of deformation. For a more detailed discussion on additive plasticity in the logarithmic strain space and a comparison to multiplicative plasticity, the reader is referred to MIEHE, APEL & LAMBRECHT [90] and APEL [12]. The continuous setting of the proposed hybrid micro-macro model in finite crystal plasticity is summarized in Figure 6.3.

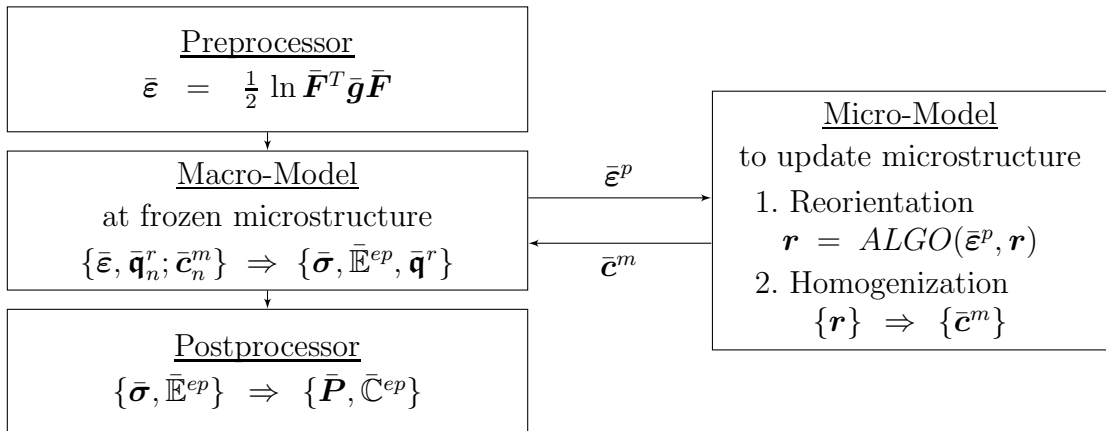


Figure 6.3: Hybrid micro-macro modeling in the logarithmic strain space

6.2. Algorithmic Formulation at Frozen Texture

The objective of this subsection is the algorithmic treatment of the proposed hybrid micro-macro model in the finite strain context. Consider a time interval $[t_n, t_{n+1}]$, where all variables without a subscript are to be evaluated at time t_{n+1} . The logarithmic strains are computed according to

$$\bar{\boldsymbol{\varepsilon}} = \frac{1}{2} \ln \left[\nabla_{\bar{\mathbf{X}}}^T \bar{\boldsymbol{\varphi}} \bar{\mathbf{g}} \nabla_{\bar{\mathbf{X}}} \bar{\boldsymbol{\varphi}} \right] \quad (6.40)$$

for known deformation $\bar{\boldsymbol{\varphi}}$. An implicit integration algorithm is performed for the evolution of the macroscopic internal variables $\bar{\mathbf{q}}^r = \{\bar{\boldsymbol{\varepsilon}}^p, \bar{\boldsymbol{\alpha}}, \bar{\alpha}\}$. The internal variables $\bar{\boldsymbol{\varepsilon}}_n^p$, $\bar{\boldsymbol{\alpha}}_n = -\bar{\boldsymbol{\varepsilon}}_n^p$ and $\bar{\alpha}_n$ at time t_n are known. Recall, that the structural tensor $\bar{\mathbf{c}}_n^m$ is assumed to be frozen, i.e. evaluated at time t_n .

An implicit integration scheme of the evolution equations (6.28) for the internal variables gives the discrete equations

$$\begin{aligned} \bar{\boldsymbol{\varepsilon}}^p &= \bar{\boldsymbol{\varepsilon}}_n^p + \Delta\bar{\gamma} \partial_{\bar{\boldsymbol{\sigma}}} \bar{\chi} \\ \bar{\boldsymbol{\alpha}} &= \bar{\boldsymbol{\alpha}}_n + \Delta\bar{\gamma} \partial_{\bar{\boldsymbol{\beta}}} \bar{\chi} \\ \bar{\alpha} &= \bar{\alpha}_n + \Delta\bar{\gamma} \partial_{\bar{\beta}} \bar{\chi} \end{aligned} \quad (6.41)$$

in terms of the incremental plastic parameter $\Delta\bar{\gamma} := \bar{\lambda} \Delta t$ with the plastic multiplier $\bar{\lambda}$ according to (6.32). In order to first check for plastic loading, an elastic trial state at time t is introduced. The logarithmic trial strains

$$\bar{\boldsymbol{\varepsilon}}^{e*} := \bar{\boldsymbol{\varepsilon}} - \bar{\boldsymbol{\varepsilon}}_n^p = \bar{\boldsymbol{\varepsilon}} - (\bar{\boldsymbol{\varepsilon}}^p - \Delta\bar{\gamma} \partial_{\bar{\boldsymbol{\sigma}}} \bar{\chi}) = \bar{\boldsymbol{\varepsilon}}^e + \Delta\bar{\gamma} \partial_{\bar{\boldsymbol{\sigma}}} \bar{\chi}, \quad (6.42)$$

the internal strain-like variables associated with this trial state as well as the dual forces

$$\begin{aligned} \bar{\boldsymbol{\varepsilon}}^{p*} &:= \bar{\boldsymbol{\varepsilon}}_n^p = \bar{\boldsymbol{\varepsilon}}^p - \Delta\bar{\gamma} \partial_{\bar{\boldsymbol{\sigma}}} \bar{\chi} & \bar{\boldsymbol{\sigma}}^* &:= \partial_{\bar{\boldsymbol{\varepsilon}}^{e*}} \Psi^* = -\partial_{\bar{\boldsymbol{\varepsilon}}^{p*}} \Psi^* \\ \bar{\boldsymbol{\alpha}}^* &:= \bar{\boldsymbol{\alpha}}_n = \bar{\boldsymbol{\alpha}} - \Delta\bar{\gamma} \partial_{\bar{\boldsymbol{\beta}}} \bar{\chi} & \bar{\boldsymbol{\beta}}^* &:= -\partial_{\bar{\boldsymbol{\alpha}}^*} \Psi^* \\ \bar{\alpha}^* &:= \bar{\alpha}_n = \bar{\alpha} - \Delta\bar{\gamma} \partial_{\bar{\beta}} \bar{\chi} & \bar{\beta}^* &:= -\partial_{\bar{\alpha}^*} \Psi^*, \end{aligned} \quad (6.43)$$

and the free energy $\Psi^* = \Psi(\bar{\boldsymbol{\varepsilon}}^{e*}, \bar{\boldsymbol{\alpha}}^*, \bar{\alpha}^*)$ are furnished by $(\cdot)^*$ indicating a variable associated with the trial state. Insertion of the trial forces into the threshold function (6.25) yields elastic loading for the threshold function $\bar{\chi}^*(\bar{\boldsymbol{\sigma}}^*, \bar{\boldsymbol{\beta}}^*, \bar{\beta}^*) \leq 0$ and plastic loading else. For plastic loading the nonlinear system of equations (6.41) and the loading condition (6.31) at frozen total deformation need to be solved iteratively with a Newton algorithm for the internal variables and the incremental plastic parameter. Therefore, named equations are rewritten in the residual format

$$\begin{aligned} \mathbf{r}_{\bar{\boldsymbol{\varepsilon}}} &:= -\bar{\boldsymbol{\varepsilon}}^p + \bar{\boldsymbol{\varepsilon}}^{p*} + \Delta\bar{\gamma} \partial_{\bar{\boldsymbol{\sigma}}} \bar{\chi} = \mathbf{0} \\ \mathbf{r}_{\bar{\boldsymbol{\alpha}}} &:= -\bar{\boldsymbol{\alpha}} + \bar{\boldsymbol{\alpha}}^* + \Delta\bar{\gamma} \partial_{\bar{\boldsymbol{\beta}}} \bar{\chi} = \mathbf{0} \\ r_{\bar{\alpha}} &:= -\bar{\alpha} + \bar{\alpha}^* + \Delta\bar{\gamma} \partial_{\bar{\beta}} \bar{\chi} = 0 \\ r_{\bar{\chi}} &:= \bar{\chi} = 0. \end{aligned} \quad (6.44)$$

For the set of internal variables $\bar{\mathbf{p}}^r = \{\bar{\boldsymbol{\sigma}}, \bar{\boldsymbol{\beta}}, \bar{\beta}\}$ the linearization of (6.44)

$$\begin{aligned} \text{Lin}[\mathbf{r}_{\bar{\boldsymbol{\varepsilon}}}] &= \mathbf{r}_{\bar{\boldsymbol{\varepsilon}}} - \Delta\bar{\boldsymbol{\varepsilon}}^p + \Delta\Delta\bar{\gamma} \partial_{\bar{\boldsymbol{\sigma}}} \bar{\chi} + \Delta\bar{\gamma} \partial_{\bar{\boldsymbol{\sigma}} \bar{\mathbf{p}}}^2 \bar{\chi} \cdot \Delta\bar{\mathbf{p}} = \mathbf{0} \\ \text{Lin}[r_{\bar{\boldsymbol{\alpha}}}] &= r_{\bar{\boldsymbol{\alpha}}} - \Delta\bar{\boldsymbol{\alpha}} + \Delta\Delta\bar{\gamma} \partial_{\bar{\boldsymbol{\beta}}} \bar{\chi} + \Delta\bar{\gamma} \partial_{\bar{\boldsymbol{\beta}} \bar{\mathbf{p}}}^2 \bar{\chi} \cdot \Delta\bar{\mathbf{p}} = 0 \\ \text{Lin}[r_{\bar{\chi}}] &= r_{\bar{\chi}} + \partial_{\bar{\mathbf{p}}} \bar{\chi} \cdot \Delta\bar{\mathbf{p}} = 0 \end{aligned} \quad (6.45)$$

has to vanish at the solution point. The linearization $\text{Lin}[r_{\bar{\boldsymbol{\alpha}}}]$ can be dropped due to the relationships of the plastic strains and the kinematic hardening for the increments

$\Delta\bar{\alpha} = -\Delta\bar{\varepsilon}^p$ and the corresponding derivatives of the threshold function. Note, that within the Newton iteration the total strains are constant, i.e. $\Delta\bar{\varepsilon} = \mathbf{0}$ holds. With the incremental forms $\Delta\bar{\sigma} = -\partial_{\bar{\varepsilon}^e\bar{\varepsilon}^e}\bar{\Psi} : \Delta\bar{\varepsilon}^p$, $\Delta\bar{\beta} = -\partial_{\bar{\alpha}\bar{\alpha}}\bar{\Psi} : \Delta\bar{\alpha}$, $\Delta\bar{\beta} = -\partial_{\bar{\alpha}\bar{\alpha}}\bar{\Psi}\Delta\bar{\alpha}$ and the specific threshold function (6.25), (6.45) can be solved for the increments

$$\begin{aligned}\Delta\bar{\varepsilon}^p &= \bar{\mathbb{F}}^{-1} : (\bar{\mathbb{E}} + \bar{\mathbb{E}}_k)^{-1} : \{\mathbf{r}_{\bar{\varepsilon}} + \Delta\Delta\bar{\gamma}\partial_{\bar{\sigma}}\bar{\chi}\} & \text{with} & \quad \bar{\mathbb{F}} := (\bar{\mathbb{E}} + \bar{\mathbb{E}}_k)^{-1} + \bar{\mathbb{N}} \\ \Delta\bar{\alpha} &= \bar{F}^{-1}\bar{E}_i^{-1} \{r_{\bar{\alpha}} + \Delta\Delta\bar{\gamma}\partial_{\bar{\beta}}\bar{\chi}\} & \text{with} & \quad \bar{F} := \bar{E}_i^{-1} + \bar{N} .\end{aligned}\quad (6.46)$$

Here, the elasticity tensor $\bar{\mathbb{E}} := \partial_{\bar{\varepsilon}\bar{\varepsilon}}^2\bar{\Psi}$, the kinematic modulus $\bar{\mathbb{E}}_k := \partial_{\bar{\alpha}\bar{\alpha}}^2\bar{\Psi}\mathbb{I}$, the isotropic modulus $\bar{E}_i := \partial_{\bar{\alpha}\bar{\alpha}}^2\bar{\psi}$ and $\bar{\mathbb{N}} := \Delta\bar{\gamma}\partial_{\bar{\sigma}\bar{\sigma}}^2\bar{\chi}$, $\bar{N} := \Delta\bar{\gamma}\partial_{\bar{\beta}\bar{\beta}}^2\bar{\chi}$ are defined, respectively. The linearized discrete consistency condition (6.45)₃ yields with these incremental internal variables the increment of the incremental plastic parameter

$$\Delta\Delta\bar{\gamma} = \frac{1}{\bar{g}} [r_{\bar{\chi}} - (\partial_{\bar{\sigma}}\bar{\chi} : \bar{\mathbb{F}}^{-1} : \mathbf{r}_{\bar{\varepsilon}} + \partial_{\bar{\beta}}\bar{\chi}\bar{F}^{-1}r_{\bar{\alpha}})] \quad (6.47)$$

with $\bar{g} := \partial_{\bar{\sigma}}\bar{\chi} : \bar{\mathbb{F}}^{-1} : \partial_{\bar{\sigma}}\bar{\chi} + \partial_{\bar{\beta}}\bar{\chi}\bar{F}^{-1}\partial_{\bar{\beta}}\bar{\chi}$. Then the incremental plastic parameter can be updated according to

$$\Delta\bar{\gamma} \leftarrow \Delta\bar{\gamma} + \Delta\Delta\bar{\gamma} . \quad (6.48)$$

The incremental internal variables can then be calculated from (6.46). Furthermore, the residual $\bar{r} = \sqrt{|\mathbf{r}_{\bar{\varepsilon}}|^2 + |r_{\bar{\alpha}}|^2 + |r_{\bar{\alpha}}|^2 + |r_{\bar{\chi}}|^2}$ is evaluated and the plastic parameter is updated within the Newton algorithm (6.41) - (6.48) until $\bar{r} < tol$. In Box 6.1 this so-called general return algorithm for frozen texture is summarized.

With (6.6), the evaluation of the texture-based structural tensors (6.7) in a typical time increment $[t_n, t]$ are assumed to be an algorithmic function

$$\bar{\mathbf{c}}^m = \frac{(2m+1)}{E^h} \sum_{e=1}^{E^h} \hat{\boldsymbol{\theta}}(\bar{\varepsilon}^p, \bar{\varepsilon}_n^p, \mathbf{r}_n^e) \star \mathbf{t}^m \quad (6.49)$$

of the plastic macro-deformation and the microstructural state at time t_n , i.e. the set of $e = 1, \dots, E^h$ grain orientations parametrized by Rodrigues vectors \mathbf{r}_n^e . This deformation-driven homogenization procedure is visualized in Figure 6.2 and summarized in Box 6.2. It includes the fast reorientation update *ALGO*, discussed in Section 4 and summarized in Box 4.1.

The algorithmic formulation of the algorithmic elasto-plastic tangent moduli connects the incremental stress with the incremental strain

$$\Delta\bar{\sigma} = \bar{\mathbb{E}}^{ep} : \Delta\bar{\varepsilon} . \quad (6.50)$$

Starting point for the derivation of the elasto-plastic tangent moduli is the additive decomposition $\bar{\varepsilon} = \bar{\varepsilon}^e + \bar{\varepsilon}^p$ of the strain and the incremental elasticity law

$$\Delta\bar{\sigma} = \bar{\mathbb{E}} : \Delta\bar{\varepsilon}^e = \bar{\mathbb{E}} : (\Delta\bar{\varepsilon} - \Delta\bar{\varepsilon}^p) . \quad (6.51)$$

The incremental form of (6.43) yields the incremental plastic strains and the incremental isotropic hardening

$$\begin{aligned}\Delta\bar{\varepsilon}^p &= \Delta\Delta\bar{\gamma}\partial_{\bar{\sigma}}\bar{\chi} + \Delta\bar{\gamma}\partial_{\bar{\sigma}\bar{\sigma}}^2\bar{\chi} \cdot \Delta\mathbf{p} = (\bar{\mathbb{E}} + \bar{\mathbb{E}}_k)^{-1} : \bar{\mathbb{F}}^{-1} : [\Delta\Delta\bar{\gamma}\partial_{\bar{\sigma}}\bar{\chi} + \bar{\mathbb{N}} : \bar{\mathbb{E}} : \Delta\bar{\varepsilon}] \\ \Delta\bar{\alpha} &= \Delta\Delta\bar{\gamma}\partial_{\bar{\beta}}\bar{\chi} + \Delta\bar{\gamma}\partial_{\bar{\beta}\bar{\beta}}^2\bar{\chi} \cdot \Delta\mathbf{p} = \bar{E}_i^{-1}\bar{F}^{-1}\Delta\Delta\bar{\gamma}\partial_{\bar{\beta}}\bar{\chi}\end{aligned}\quad (6.52)$$

Box 6.1: General return algorithm for hybrid micro-macro model.

1. *Set initial values.* Given are the current macroscopic strains $\bar{\boldsymbol{\varepsilon}}$ at t_{n+1} and the macroscopic internal variables $\bar{\mathbf{q}}_n = \{\bar{\boldsymbol{\varepsilon}}_n^p, \bar{\boldsymbol{\alpha}}_n, \bar{\alpha}_n\}$ at time t_n . Set trial variables and initialize incremental plastic parameter

$$\bar{\boldsymbol{\varepsilon}}^{e*} := \bar{\boldsymbol{\varepsilon}} - \bar{\boldsymbol{\varepsilon}}_n^p, \quad \bar{\boldsymbol{\varepsilon}}^{p*} := \bar{\boldsymbol{\varepsilon}}_n^p, \quad \bar{\boldsymbol{\alpha}}^* := \bar{\boldsymbol{\alpha}}_n, \quad \bar{\alpha}^* := \bar{\alpha}_n, \quad \Delta\bar{\gamma} = 0.$$

2. *Elasticity tensor and Hill tensor.* The elasticity tensor and the Hill tensor are split into an isotropic and an anisotropic part

$$\bar{\mathbb{E}} := \bar{\mathbb{E}}_0 + \bar{\zeta}_c \bar{\mathbb{E}}_a(\bar{\mathbf{c}}_n^m) \quad \text{and} \quad \bar{\mathbb{H}} := \mathbb{P} + \bar{\zeta}_p \bar{\mathbb{H}}_a(\bar{\mathbf{c}}_n^m),$$

with frozen texture $\bar{\mathbf{c}}_n^m$.

3. *Trial state and plastic loading.* Compute trial forces $\bar{\mathbf{p}}^{r*} := -\partial_{\bar{\mathbf{q}}^{r*}} \Psi^*$ with trial free energy function $\Psi^* = \Psi(\bar{\boldsymbol{\varepsilon}}^{e*}, \bar{\boldsymbol{\alpha}}^*, \bar{\alpha}^*)$. Determine threshold function

$$\bar{\chi}^*(\bar{\mathbf{p}}^{r*}; \bar{\mathbf{c}}_n^m) = \|\bar{\boldsymbol{\sigma}}^* - \bar{\boldsymbol{\beta}}^*\|_{\bar{\mathbb{H}}} - \bar{c}_\chi(\bar{y}_0 + \bar{\beta}^*).$$

Check criterion for plastic loading: For $\bar{\chi}^* < 0$ the response is elastic \rightarrow EXIT.

4. *Residuals.* Compute residuals and check tolerance

$$\mathbf{r}_{\bar{\boldsymbol{\varepsilon}}} := -\bar{\boldsymbol{\varepsilon}}^p + \bar{\boldsymbol{\varepsilon}}^{e*} + \Delta\bar{\gamma} \partial_{\bar{\boldsymbol{\sigma}}} \bar{\chi}, \quad \mathbf{r}_{\bar{\boldsymbol{\alpha}}} := -\bar{\boldsymbol{\alpha}} + \bar{\boldsymbol{\alpha}}^* + \Delta\bar{\gamma} \partial_{\bar{\boldsymbol{\beta}}} \bar{\chi}, \quad \mathbf{r}_{\bar{\alpha}} := -\bar{\alpha} + \bar{\alpha}^* + \Delta\bar{\gamma} \partial_{\bar{\beta}} \bar{\chi}$$

For $\bar{r} = \sqrt{|\mathbf{r}_{\bar{\boldsymbol{\varepsilon}}}|^2 + |\mathbf{r}_{\bar{\boldsymbol{\alpha}}}|^2 + |\mathbf{r}_{\bar{\alpha}}|^2 + |\mathbf{r}_{\bar{\chi}}|^2} < \text{tol} \rightarrow$ EXIT.

5. *Plastic parameter.* Linearization of residuals gives the increment of the incremental plastic parameter

$$\Delta\Delta\bar{\gamma} = \frac{1}{\bar{g}} [r_{\bar{\chi}} - (\partial_{\bar{\boldsymbol{\sigma}}} \bar{\chi} : \bar{\mathbb{F}}^{-1} \bar{\mathbf{r}}_{\bar{\boldsymbol{\varepsilon}}} + \partial_{\bar{\beta}} \bar{\chi} : \bar{F}^{-1} \bar{r}_{\bar{\alpha}})].$$

6. *Internal variables and dual forces.* Update plastic parameter $\Delta\bar{\gamma} \Leftarrow \Delta\bar{\gamma} + \Delta\Delta\bar{\gamma}$ and evaluate internal variables and incremental internal forces

$$\begin{aligned} \bar{\boldsymbol{\varepsilon}}^p &\Leftarrow \bar{\boldsymbol{\varepsilon}}^p + \bar{\mathbb{F}}^{-1} : (\bar{\mathbb{E}} + \bar{\mathbb{E}}_k)^{-1} : \{\mathbf{r}_{\bar{\boldsymbol{\varepsilon}}} + \Delta\Delta\bar{\gamma} \partial_{\bar{\boldsymbol{\sigma}}} \bar{\chi}\} & \bar{\boldsymbol{\sigma}} &= \bar{\mathbb{E}} : (\bar{\boldsymbol{\varepsilon}} - \bar{\boldsymbol{\varepsilon}}^p) \\ \bar{\boldsymbol{\alpha}} &\Leftarrow \bar{\boldsymbol{\alpha}} + \bar{F}^{-1} \bar{E}_i^{-1} \{\mathbf{r}_{\bar{\boldsymbol{\alpha}}} + \Delta\Delta\bar{\gamma} \partial_{\bar{\boldsymbol{\beta}}} \bar{\chi}\} & \bar{\beta} &= -\bar{c}_i \bar{\alpha}, \end{aligned}$$

GOTO 4

Insertion of the incremental internal forces $\Delta\bar{\boldsymbol{\sigma}}$ according to (6.51), $\Delta\bar{\boldsymbol{\beta}}$, $\Delta\bar{\beta}$ and the incremental internal variables (6.52) into the incremental plastic consistency condition $\Delta\bar{\chi} = \partial_{\bar{\mathbf{p}}} \bar{\chi} \Delta\bar{\mathbf{p}}$ gives the increment of the incremental plastic parameter in the form

$$\Delta\Delta\bar{\gamma} = \frac{1}{\bar{g}} \partial_{\bar{\boldsymbol{\sigma}}} \bar{\chi} : (\bar{\mathbb{I}} - \bar{\mathbb{F}}^{-1} : \bar{\mathbb{N}}) : \bar{\mathbb{E}} : \Delta\bar{\boldsymbol{\varepsilon}}. \quad (6.53)$$

Box 6.2: Deformation-driven reorientation and homogenization of texture.

Driving macro-deformation. Given are the current macroscopic plastic deformations $\bar{\boldsymbol{\varepsilon}}^p$ at time t . Compute aggregate deformation

$$\mathbf{F} := \exp[\bar{\boldsymbol{\varepsilon}}^p]$$

1. *Microstructural reorientation.* The lattice orientations $\{\mathbf{r}_n^c\}_{c=1,\dots,E^h}$ and the aggregate deformation \mathbf{F}_n at time t_n are given. Compute current grain orientations

$$(\mathbf{r}^1, \dots, \mathbf{r}^{E^h}) = \text{ALGO}(\mathbf{F}; \mathbf{F}_n, \mathbf{r}_n^1, \dots, \mathbf{r}_n^{E^h})$$

by the fast orientation update algorithm *ALGO* in Box 4.1

2. *Homogenization.* Compute texture-based macroscopic structural tensors by homogenization over the orientation space

$$\bar{\mathbf{c}}^m = \frac{(2m+1)}{E^h} \sum_{e=1}^{E^h} \hat{\boldsymbol{\theta}}(\mathbf{r}^e) \star \mathbf{t}^m$$

With this formulation for the increment of the incremental plastic parameter $\Delta\Delta\bar{\gamma}$, (6.51) yields the incremental stresses in terms of the incremental total strains. Comparison with (6.50) results in the algorithmic elasto-plastic tangent moduli

$$\bar{\mathbb{E}}^{ep} = \bar{\mathbb{E}} - \bar{\mathbb{E}} : (\bar{\mathbb{N}}^{-1} + \bar{\mathbb{E}} + \bar{\mathbb{E}}_k)^{-1} : \bar{\mathbb{E}} - \frac{1}{\bar{g}} \bar{\mathbb{T}} : \partial_{\bar{\boldsymbol{\sigma}}} \bar{\chi} \otimes \partial_{\bar{\boldsymbol{\sigma}}} \bar{\chi} : \bar{\mathbb{T}} \quad (6.54)$$

in terms of the abbreviation of the fourth-order tensor

$$\bar{\mathbb{T}} := \bar{\mathbb{E}} : \bar{\mathbb{F}}^{-1} : (\bar{\mathbb{E}} + \bar{\mathbb{E}}_k)^{-1} = (\bar{\mathbb{I}} - \bar{\mathbb{F}}^{-1} : \bar{\mathbb{N}}) : \bar{\mathbb{E}} . \quad (6.55)$$

Finally, the stresses and moduli are transformed to the nominal stresses and moduli via

$$\bar{\mathbf{g}}\bar{\mathbf{P}} = \bar{\boldsymbol{\sigma}} : \bar{\mathbb{Q}} \quad \text{and} \quad \bar{\mathbb{C}}^{ep} = \bar{\mathbb{Q}}^T : \bar{\mathbb{E}}^{ep} : \bar{\mathbb{Q}} + \bar{\boldsymbol{\sigma}} : \bar{\mathbb{L}} . \quad (6.56)$$

An overview of the algorithmic treatment for the hybrid micro-macro model of finite anisotropic plasticity in the logarithmic strain space is given in Box 6.3, representing the algorithmic counterpart of the procedure sketched in Figure 6.3.

6.3. Representative Numerical Examples

The capability of the above outlined hybrid micro-macro model in the logarithmic strain space is presented by means of representative numerical examples. These are concerned with the simulation of shearband developments in a 2D strip at plane strain conditions, the necking of a 3D metallic rod and the deep drawing of metal sheets. The local texture evolution within the shearband of the 2D strip and the necking region of the 3D rod is analyzed. With regard to the material testing, so-called earrings develop during the deep drawing process of a circular sheet due to the texture-induced anisotropy. As a typical forming process, the deep drawing of a square metal sheet is simulated. For all simulations the underlying microstructure consists of 448 fcc crystals obtained by a cube2 discretization, see Section 4.

Box 6.3: Algorithmic hybrid micro-macro-model of finite anisotropic plasticity

1. *Geometric preprocessor.* Let $\bar{\varphi}(\bar{\mathbf{X}}, t)$ be the current deformation map. At each $\bar{\mathbf{X}} \in \bar{\mathcal{B}}$, define Lagrangian logarithmic strains

$$\bar{\boldsymbol{\varepsilon}} := \frac{1}{2} \ln \left[\nabla_{\bar{\mathbf{X}}}^T \bar{\varphi} \bar{\mathbf{g}} \nabla_{\bar{\mathbf{X}}}^T \bar{\varphi} \right]$$

2. *Macro model in the logarithmic strain space at frozen microstructure.*

<i>internal variables</i>	$\bar{\mathbf{q}}^r := \{\bar{\boldsymbol{\varepsilon}}^p, \bar{\boldsymbol{\alpha}}, \bar{\alpha}\}$
<i>free energy</i>	$\bar{\Psi} := \frac{1}{2} \ \bar{\boldsymbol{\varepsilon}} - \bar{\boldsymbol{\varepsilon}}^p\ _{\bar{\mathbb{E}}}^2 + \frac{\bar{c}_k}{2} \bar{\boldsymbol{\alpha}} : \bar{\boldsymbol{\alpha}} + \frac{\bar{c}_i}{2} \bar{\alpha}^2$
<i>anisotropic elasticity modulus</i>	$\bar{\mathbb{E}} := \bar{\mathbb{E}}_0 + \bar{\zeta}_e \bar{\mathbb{H}}_a(\bar{\mathbf{c}}_n^m)$
<i>internal forces</i>	$\bar{\mathbf{p}}^r := \{\bar{\boldsymbol{\sigma}}, \bar{\boldsymbol{\beta}}, \bar{\beta}\} = -\partial_{\bar{\mathbf{q}}^r} \bar{\Psi}$
<i>threshold function</i>	$\bar{\chi} := \ \bar{\boldsymbol{\sigma}} - \bar{\boldsymbol{\beta}}\ _{\bar{\mathbb{H}}} - \bar{c}_\chi(\bar{y}_0 + \bar{\beta})$
<i>anisotropic Hill tensor</i>	$\bar{\mathbb{H}} := \mathbb{P} + \bar{\zeta}_p \bar{\mathbb{H}}_a(\bar{\mathbf{c}}_n^m)$

Update internal variables and internal forces according to Box 6.1

$$\{\bar{\boldsymbol{\varepsilon}}, \bar{\mathbf{q}}^r, \bar{\mathbf{p}}^r; \bar{\mathbf{c}}_n^m\} \Rightarrow \{\bar{\mathbf{q}}^r, \bar{\mathbf{p}}^r\}$$

3. *Microstructure update.* For given plastic strains $\bar{\boldsymbol{\varepsilon}}^p$ and microstructural data base $\{\mathbf{r}_n^1, \dots, \mathbf{r}_n^{E^h}\}$ at t_n ,

1. Update reorientation

$$(\mathbf{r}^1, \dots, \mathbf{r}^{E^h}) = \text{ALGO}(\mathbf{F}; \mathbf{F}_n, \mathbf{r}_n^1, \dots, \mathbf{r}_n^{E^h})$$

2. Update structural tensors

$$\bar{\mathbf{c}}^m = \frac{(2m+1)}{E^h} \sum_{e=1}^{E^h} \hat{\boldsymbol{\theta}}(\mathbf{r}^e) \star \mathbf{t}^m$$

4. *Geometric postprocessor.* Compute nominal stresses and moduli

$$\bar{\mathbf{g}}\bar{\mathbf{P}} = \bar{\boldsymbol{\sigma}} : \bar{\mathbb{Q}} \quad \text{and} \quad \bar{\mathbb{C}}^{ep} = \bar{\mathbb{Q}}^T : \bar{\mathbb{E}}^{ep} : \bar{\mathbb{Q}} + \bar{\boldsymbol{\sigma}} : \bar{\mathbb{L}}$$

6.3.1. Localization of a rectangular strip in tension. As a first numerical example the localization of a two-dimensional rectangular strip under tension is investigated. The system and boundary conditions of the polycrystalline strip with the ratio of height to width $h/w = 2.8$ are illustrated in Figure 6.4a). Exploiting the symmetry of the problem, only one quarter of the macroscopic continuum has been discretized using 450 four-noded elements. Here, a Q1/E4 enhanced incompatible mode element formulation with bilinear compatible and quadratic incompatible interpolations has been employed, cf. SIMO & ARMERO [130] for more details. The chosen Lamé parameters are the bulk modulus $\kappa = 164.21\text{kN/mm}^2$ and the shear modulus $\mu = 89.194\text{kN/mm}^2$. The linear hardening

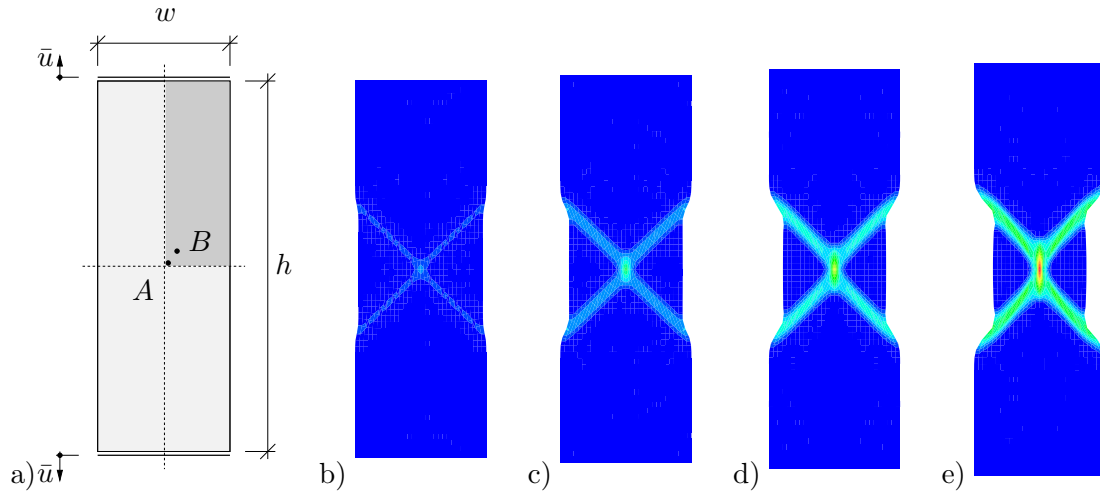


Figure 6.4: Localization of a 2D strip. a) System and boundary conditions. Due to symmetry, only a quarter of the specimen is discretized. Deformed specimen and distribution of equivalent plastic strains at b) 2%, c) 5%, d) 8% and e) 11.5% deformation.

is governed by the hardening (softening) modulus $h = -0.129\text{kN/mm}^2$ and an initial yield stress $y_0 = 0.45\text{kN/mm}^2$. In order to trigger the development of a shear band, the initial yield stress in the center of the strip is attenuated by 10%. Furthermore, the factor $\zeta_4 = 0.3$ scales the microstructural influence on the macroscopic anisotropy. The specimen is deformed within a deformation controlled process up to a total elongation of $\bar{u} = 0.115h$ in vertical direction, where free contraction of the strip is allowed. Concerning the microstructure, a quasi-isotropic distribution of crystal orientations is obtained from a regular cube2 discretization of the truncated cube containing 448 fcc crystals, see Figure 4.12. The evolving shape of the 2D rectangular strip and the distribution of equivalent plastic strains are visualized in Figure 6.4, where a pronounced shear band develops. Here, the deformation states correspond to 2%, 5%, 8% and 11.5% deformation with respect to the initial height h . At the beginning of the loading process, the specimen shows a homogeneous state of deformation. At around 2% deformation, a symmetrical necking starts

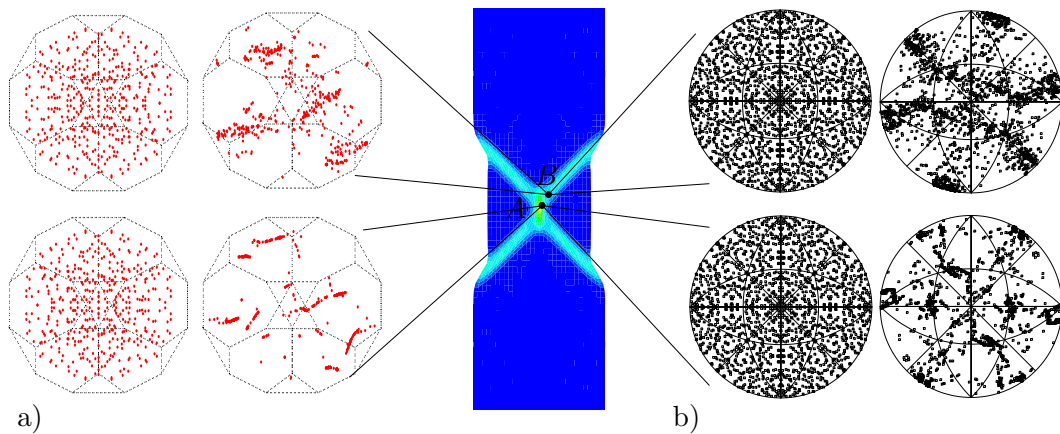


Figure 6.5: Localization of a 2D strip. a) Discrete reorientations and b) $\{111\}$ pole figures of a tensile test at initial state and 11.5% deformation.

to develop and at a further state, the deformation mode changes to a pattern involving shearbands. The discrete orientations in the Rodrigues space as well as the $\{111\}$ pole figures at both the initial state and the final state, i.e. 11.5% deformation, are compared at points A and B in the shearband, see Figure 6.5. A pronounced texture develops with increasing deformation, especially within the shearband. The texture evolution in the two points A and B is shown in Figure 6.6 for the same deformation states as above, i.e. for 2%, 5%, 8% and 11.5% deformation, where the texture aligns with the prevailing orientation corresponding to the one of the shear mode, compare Section 4.4.2.2. A less sharp

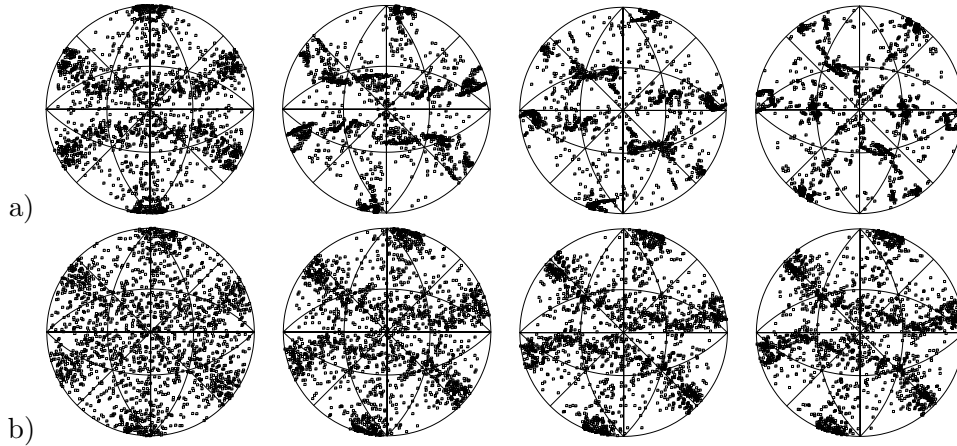


Figure 6.6: Localization of a 2D strip. $\{111\}$ pole figures at 2%, 5%, 8% and 11.5% deformation at a) point A and b) point B in the evolving shearband.

and rotated texture at point B in the shearband is observed in contrast to point A , which can be ascribed to a rigid body rotation. In BOVE [31] the influence of the specimen discretization, the number of crystal orientations and the anisotropy scaling factor on the texture evolution and the load deflection behavior is analyzed. Note, that there is no major deflection for a coarse discretization of the Rodrigues cube on the global material response but a much lower computation time as discussed in Section 4.4.2.2.

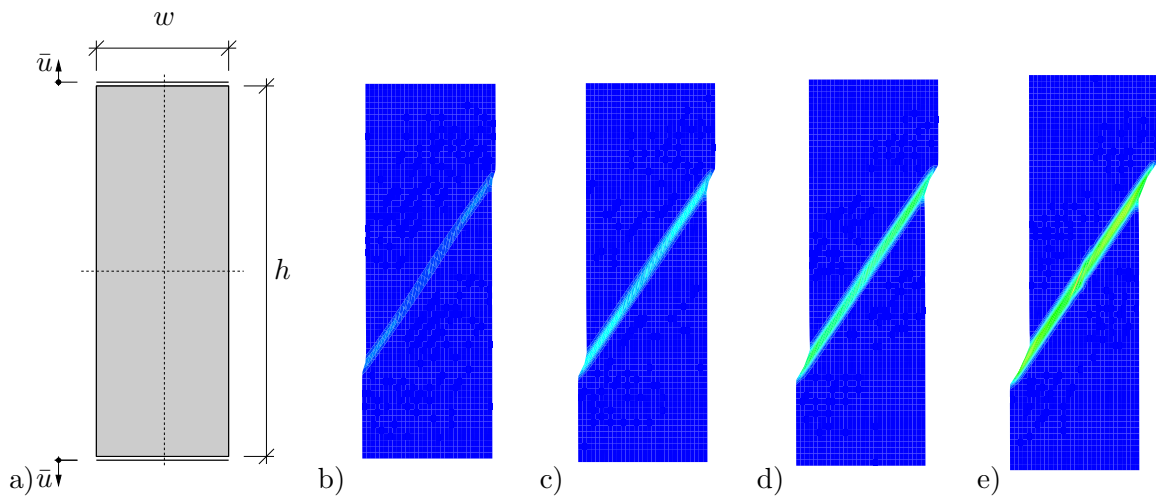


Figure 6.7: Localization of a 2D strip with initial anisotropic material behavior. a) System and boundary conditions. Deformed specimen and distribution of equivalent plastic strains at b) 2%, c) 4%, d) 6% and e) 8.5% deformation.

By consideration of an initial anisotropic distribution of crystal orientations the whole specimen, illustrated in Figure 6.7a) needs to be discretized with 1800 four-noded Q1/E4 elements. An initial anisotropy is obtained by a prior shear deformation, i.e. to each Gauss point a microstructure with a shear texture obtained by the (ii) rigid-plastic active set model, cf. Figure 4.19(ii). In a deformation-driven scenario, the specimen is deformed up to a total state of $\bar{u} = 0.085h$ with the evolution of the shape and the distribution of equivalent plastic strains shown in Figure 6.7. The deformation states correspond to 2%, 4%, 6% and 8.5% deformation with respect to the original height. Due to the pretexture of the specimen an anisotropic shear band evolves, which shows the influence of the texture on the macroscopic material behavior.

6.3.2. Necking of a 3D rod in tension. The second boundary value problem is devoted to the tension of a circular metallic rod, illustrated in Figure 6.8, where the relation between height and diameter is $h = 4.2d$. Due to symmetry considerations, only one eighth of the rod is analyzed.

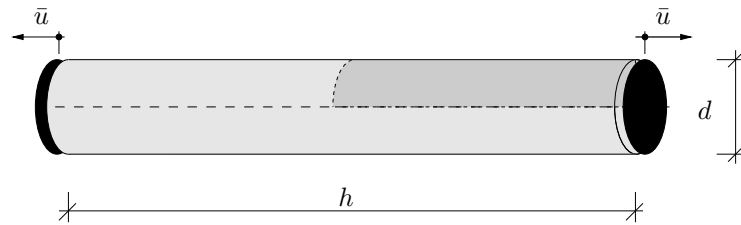


Figure 6.8: Necking of a 3D rod: System and boundary conditions. Due to symmetry only one eighth of the rod is analyzed.

of the specimen has been discretized with 120 eight-noded Q1/P0 elements. The finite element formulation with mixed interpolations for the Jacobian and the pressure has been proposed by SIMO, TAYLOR & PISTER [131] based on ideas from NAGTEGAAL, PARKS & RICE [104]. The Lamé parameters $\kappa = 164.21\text{kN/mm}^2$, $\mu = 89.194\text{kN/mm}^2$ and the anisotropy scaling factor in the Hill tensor $\zeta_4 = 0.3$ remain unchanged. The nonlinear hardening response is governed by the hardening modulus $h = 0.129\text{kN/mm}^2$, the initial yield stress $y_0 = 0.45\text{kN/mm}^2$ and the infinite yield stress $y_\infty = 1.165\text{kN/mm}^2$ with the saturation parameter $\omega = 16.93$. Necking describes the decrease of the area in the cross section at the middle of the strip under tensile loading. To achieve this behavior, the initial and saturation flow stresses in the center of the rod are attenuated by 10%. The specimen is elongated in a deformation-driven simulation in constant increments up to a maximum prescribed displacement $\bar{u} = 0.3h$. Figure 6.9 depicts the initial and three

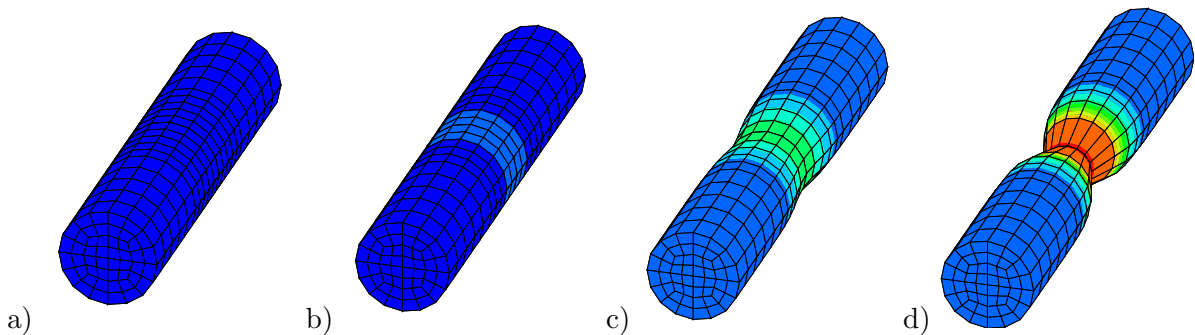


Figure 6.9: Necking of a 3D rod. Deformed specimen and distribution of equivalent plastic strains at a) initial configuration and b) 10%, c) 20% and d) 30% deformation.

deformed configurations with the distribution of the equivalent plastic strains. The deformation states correspond to 10%, 20% and 30% deformation with respect to the original height. Up to a deformation of around $\bar{u} = 0.1h$, i.e. 10%, the load increases and the whole rod contracts uniformly. As the load is increased further, necking starts at the center of the rod, where the material is weak. In the center of the rod the deformation mechanism can be compared to a simple tension test. The $\{111\}$, $\{100\}$ and $\{110\}$ pole figures in a Gauss point near the center of the rod are illustrated in Figure 6.10 and compared to experimental results for simple tension tests taken from BRONKHORST, KALIDINDI & ANAND [33]. The pole figures of the simulation show a very good qualitative agreement

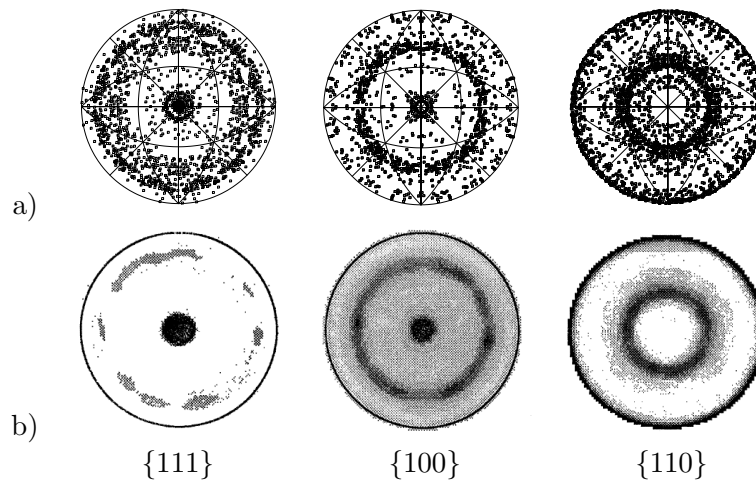


Figure 6.10: Necking of a 3D rod. a) $\{111\}$, $\{100\}$ and $\{110\}$ pole figures in the center of the rod compared with b) experimental results for simple tension taken from BRONKHORST, KALIDINDI & ANAND [33].

with those of the experiment. As one proceeds to Gauss points in x - and y -direction from the center of the rod towards the outer surface, similar pole figures are observed, see Figure 6.11, but they are clearly offset from the pole figure normal. Focusing attention

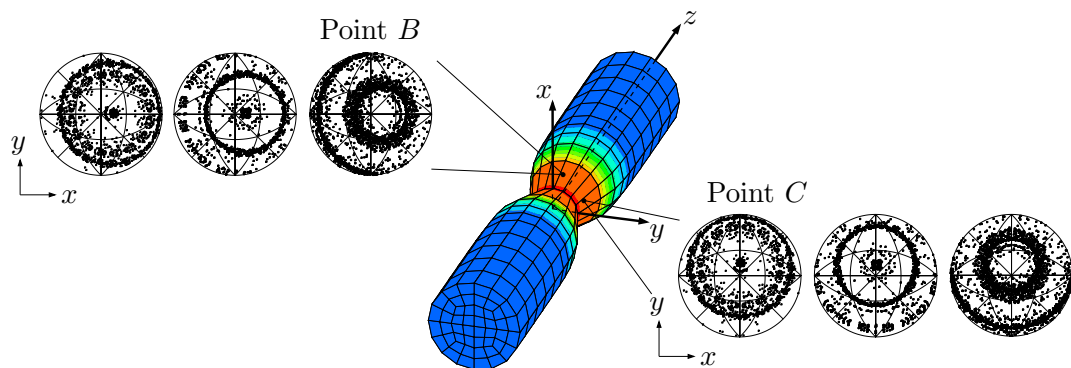


Figure 6.11: Necking of a 3D rod. Discrete reorientations, $\{111\}$, $\{100\}$ and $\{110\}$ pole figures of a tensile test at 30 % deformation and in two different points within the specimen.

to a fiber within the rod with the fiber axis lying on the z -axis, this fiber deforms solely in z -direction, i.e. the fiber is stretched. In contrast, a second fiber that connects two points within the necking region and runs parallel to the z -axis at the beginning of the

deformation process, experiences a rotation in addition to a change in length during the deformation progress. The overall growth direction of the rod is not aligned to the growth direction of this second fiber. Hence, the pole figures at points within the necking region and not lying on the z -axis show an offset with respect to the pole figure normal. As can be seen in Figure 6.11 the offset direction of the pole figure depends on the position of the considered Gauss point. Here, the $\{111\}$, $\{100\}$ and $\{110\}$ pole figures are plot for two different points, B and C respectively. For point B , near the x/z -plane, an above mentioned fiber running through B rotates during deformation from the z -axis towards the x -axis. Therefore, the pole figure for point B moves right compared to the point near the center of the rod shown in Figure 6.10, i.e. towards the x -axis. The same holds for point C towards the y -axis and similar for other points lying in-between. The amount of offset depends on the distance of the considered Gauss point from the z -axis. Cutting a plane perpendicular to the z -axis, for all points on this plane with same distance from the z -axis, the pole figures are related to each other due to the rotational symmetry of the metallic rod. For the specific case of point B and C , the pole figures of the points in-between rotate from the one of point B towards the one of point C .

6.3.3. Circular Deep Drawing of a Metallic Sheet. The modeling of anisotropy effects is extremely important for industrial applications such as sheet metal forming. This simulation example is meaningful as it is widely discussed in the literature both from simulation and experimental points of view. Furthermore, fundamental phenomena can be modeled which appear in typical industry processes. Due to the texture of the microstructure metallic sheets exhibit an anisotropic behavior, which results on the one hand in the evolution of earings and on the other hand in an inhomogeneous sheet thickness. To capture those phenomena, the anisotropy formation and the development of earings in a deep drawing process is discussed. In this context, the influence of the anisotropy scaling factor $\bar{\zeta}_4$, the amount of pretexture, the microstructure discretization and the so-called drawing ratio is studied. In Figure 6.12a) the setup and dimensions for the subsequent

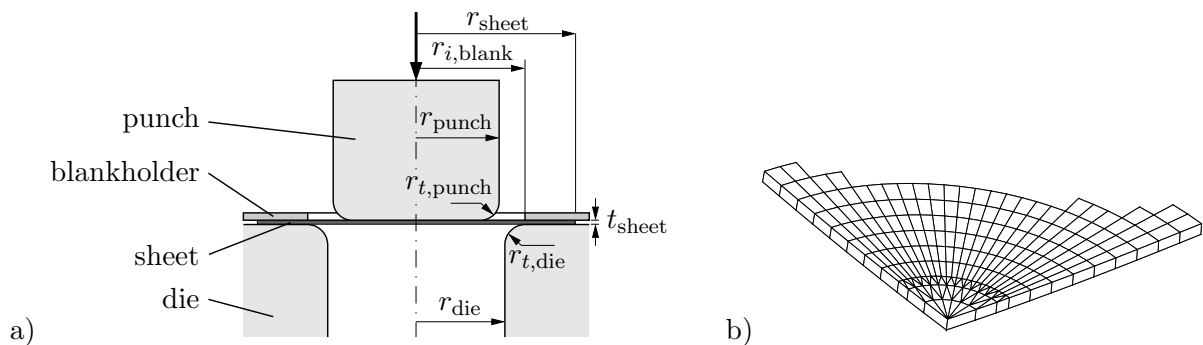


Figure 6.12: Deep drawing of a metal sheet. a) Geometry and boundary condition. Lengths in mm. b) Detail of meshed sheet with six-noded linear triangular prisms and eight-noded Q1/P0 elements.

deep drawing processes are sketched. For the circular deep drawing process the radius of the circular sheet is $r_{\text{sheet}} = 39.5\text{mm}$, its thickness is $t_{\text{sheet}} = 0.8\text{mm}$ and the radius of the punch is $r_{\text{punch}} = 20.6\text{mm}$ with corresponding transition radius $r_{t,\text{punch}} = 4.6\text{mm}$. The outer radius $r_{o,\text{blank}} = 39.5\text{mm}$ of the blankholder corresponds to the sheet radius and the inner radius is chosen to $r_{i,\text{blank}} = 27.0\text{mm}$. Finally, the die is characterized by its radius $r_{\text{die}} = 22.0\text{mm}$ and corresponding transition radius $r_{t,\text{die}} = 5.1\text{mm}$. The configuration is axisymmetric with respect to the punch direction. A flat, circular sheet is placed

between a rigid die and a rigid, so-called blankholder. The latter one is fixed at a distance equal to the thickness of the sheet and prevents the raising of the sheet during the deformation process as well as a possible wrinkling. The material parameters correspond to the ones in the previous subsection, i.e. $\kappa = 164.21\text{kN/mm}^2$, $\mu = 89.194\text{kN/mm}^2$, $\zeta_4 = 0.3$, $h = 0.129\text{kN/mm}^2$, $y_0 = 0.45\text{kN/mm}^2$, $y_\infty = 1.165\text{kN/mm}^2$ and $\omega = 16.93$. In a deformation-driven scenario the rigid punch descends into the die up to a total punch deformation of $\bar{u} = 45\text{mm}$, i.e. the circular sheet is formed as a cup. In order to circumvent a rigid body motion of the sheet after being hold by the blankholder, a friction coefficient of 1% is chosen. It has a minor influence on the cup height and shape, see RAABE & ROTERS [118] and TIKHOVSKIY, RAABE & ROTERS [136] and references therein. The whole sheet is discretized with 2160 finite elements, namely 240 ABAQUS six-noded linear triangular prisms and 1920 eight-noded Q1/P0 elements, with one element over the sheet thickness. A detail of the mesh discretization of one quarter of the sheet is shown in Figure 6.12b). For an ideal isotropic material, the cup needs to keep the axisymmetry with respect to the punch direction, hence the rim of the produced cup would be level. But usually, distinct high points, so-called ears, and low points, so-called troughs, occur. This is due to the fact of planar anisotropy resulting from the texture in the sheet and varying plastic flow in the sheet. Usually, four ears and troughs evolve for commercially processed aluminum sheets, cf. ENGLER & KALZ [41]. As sheets and plates used for material forming operations are prerolled, an initial anisotropy exists prior to the deep drawing operation. Therefore, the sheet is subjected to plane strain compression, i.e. rolling, with 26% thickness reduction, see MIEHE, FRANKENREITER & ROSATO [91] and Section 4.4.2.2. For the subsequent examples the cube2 discretization with 448 orientations is chosen. A sequence of deformation states at $\bar{u} = 0\text{mm}$, $\bar{u} = 15.3\text{mm}$, $\bar{u} = 18.7\text{mm}$, $\bar{u} = 21.5\text{mm}$, $\bar{u} = 26.9\text{mm}$, $\bar{u} = 45.0\text{mm}$ shown in Figure 6.13 reports the evolution of equivalent plastic strains throughout the sheet. In the first picture, the undeformed

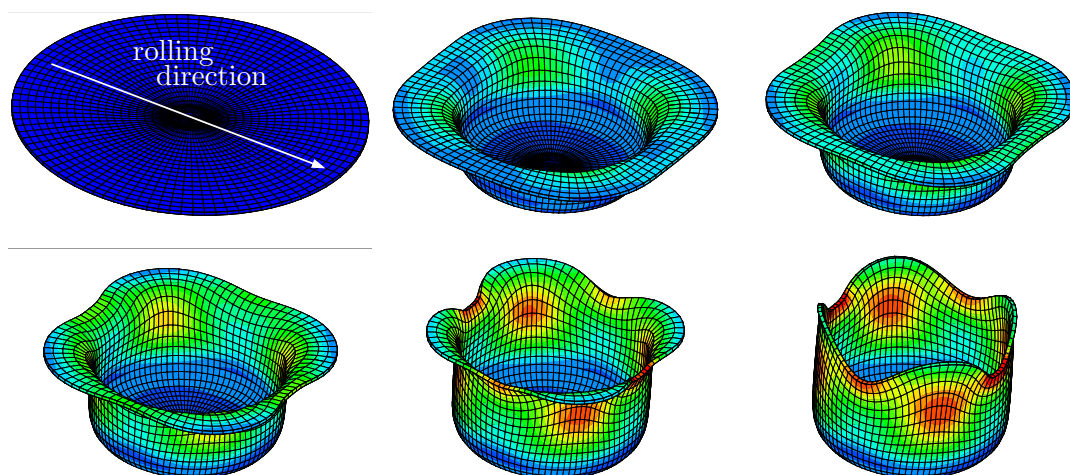


Figure 6.13: Circular deep drawing of a metal sheet. Evolution of four ears in deep drawing of a polycrystalline sheet with rolling texture (26% thickness reduction) and anisotropy factor $\bar{\zeta}_p = 0.3$.

configuration as well as the rolling direction is indicated. Four ears develop, where the shape and distribution of equivalent plastic strains of opposite ears are equal. As it is clearly visible in Figure 6.13 the deformed structure exhibits a distinct symmetry. Thus,

only one quarter of the circular sheets needs to be simulated. The plastic strains concentrate in the regions right below the ears as well as in the troughs. Similar results are obtained in experiments and simulations by TUCKER [139], WILSON & BUTLER [143], KANETAKE, TOZAWA & OTANI [66], BALASUBRAMANIAN & ANAND [16], ENGLER & KALZ [41], BÖHLKE, RISY & BERTRAM [30], TIKHOVSKIY, RAABE & ROTERS [136], VLADIMIROV, SCHWARZE & REESE [140].

To obtain different initial textures, the sheet is subjected to plane strain compression, i.e. rolling, with 18%, 26% and 40% thickness reduction. The $\{111\}$ pole figures and the final

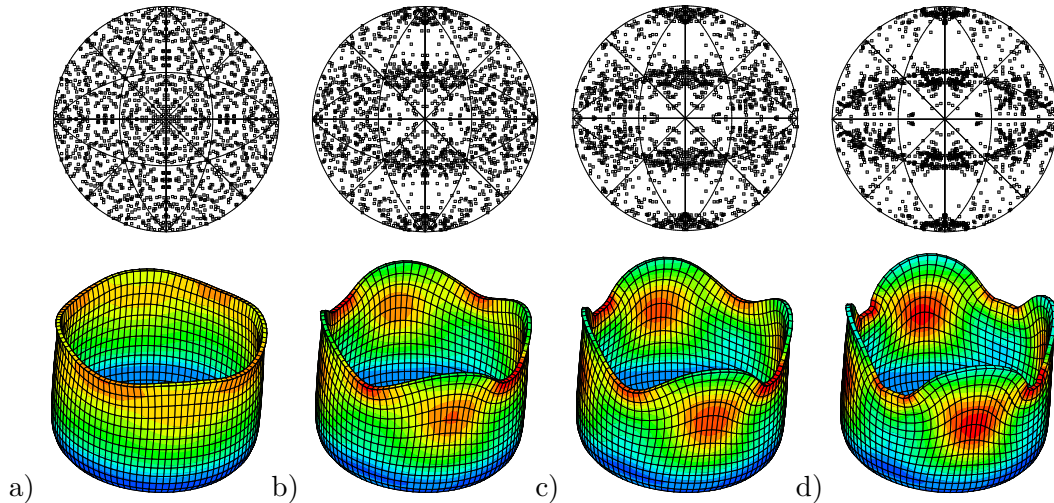


Figure 6.14: Circular deep drawing of a metal sheet. $\{111\}$ pole figures at a) initial configuration, b) 18%, c) 26% and d) 40% thickness reduction due to rolling deformation are starting textures for the deep drawing simulation and cause texture-induced anisotropy. The earing developments are shown at a total punch deformation of $u = 45\text{mm}$ and for an anisotropy factor $\bar{\zeta}_4 = 0.3$.

deformation states with the equivalent plastic strains are shown for the different initial textures in Figure 6.14. For all starting textures four ears develop while with increasing initial texture more distinctive ears develop as well as the level of equivalent plastic strains increases. For the in Figure 6.14 illustrated deep drawn cups with different initial texture the normalized cup height

$$\bar{h} = \frac{1}{N} \sum_{I=1}^N h_I \quad (6.57)$$

is plot over the angle with respect to the rolling direction in Figure 6.15. Herein, N is the total number of nodes at the boundary of the sheet and h_I the cup height at a specific node I . According to BALDWIN, HOWALD & ROSS [17] and ROBERTS [125] cube texture results in $0^\circ/90^\circ$ earing and 45° earing occurs for rolling texture. In our simulations the troughs form in rolling direction 0° and perpendicular to this direction, i.e. $90^\circ, 180^\circ, 270^\circ$. The ears develop under $45^\circ, 135^\circ, 225^\circ, 315^\circ$ with respect to the rolling direction, as discussed by ROBERTS [125] for rolling texture. Note, that the cup without pretexture does not have an even rim, implying a non-isotropic initial microstructure. However, as no rolling has been applied the microstructure in deed is isotropic and the anisotropy effect is solely caused by the discretization of the microstructure, implying a non-isotropic initial microstructure. A study concerning the impact of the anisotropy factor $\bar{\zeta}_4$ is shown in Figure 6.16. More

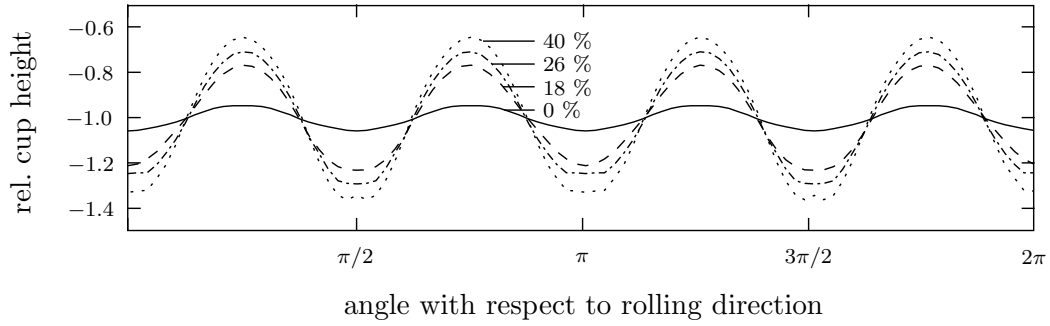


Figure 6.15: Circular deep drawing of a metal sheet. Texture induced earing yields two equal pairs of ears. The relative cup height at a total punch deformation of $\bar{u} = 45\text{mm}$ is given for different pretextures with 0%, 18%, 26% and 40% thickness reduction.

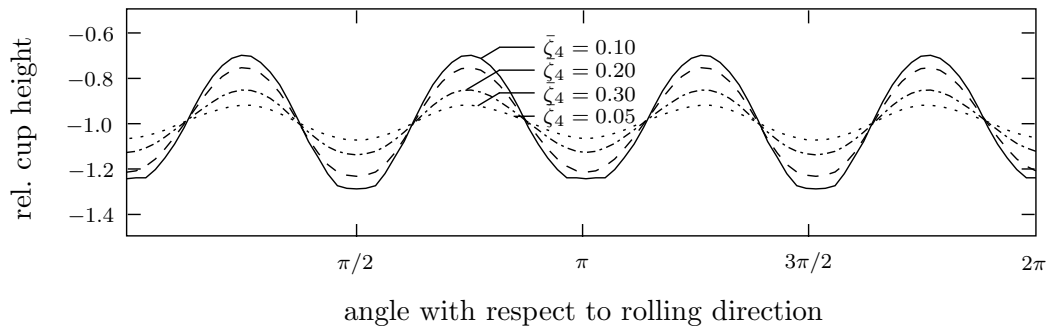


Figure 6.16: Circular deep drawing of a metal sheet. Texture induced earing yields two equal pairs of ears. The relative cup height at a total punch deformation of $\bar{u} = 45\text{mm}$ is given for different anisotropy scaling factors $\bar{\zeta}_4 = 0.3$, $\bar{\zeta}_4 = 0.2$, $\bar{\zeta}_4 = 0.1$ and $\bar{\zeta}_4 = 0.05$.

distinctive earings develop with increasing anisotropy factor. This is in line with the scaling of the yield surface, Section 5.4.4.1, representing the texture-induced macroscopic anisotropy. For the different microstructures cube1 and cube2, the relative earing heights are illustrated in Figure 6.17 as a function of the angle with respect to the rolling direction. Due to the discretization of the microstructure with 56 orientations for cube1 and 448

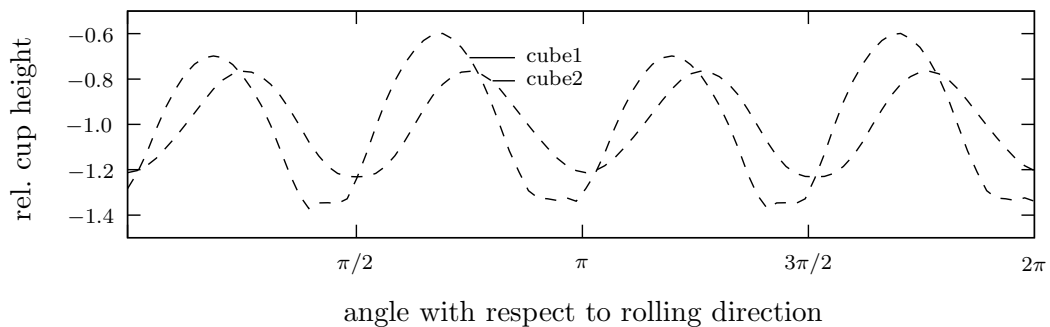


Figure 6.17: Circular deep drawing of a metal sheet. Texture induced earing yields two equal pairs of ears. The relative cup height at a total punch deformation of $\bar{u} = 45\text{mm}$ is given for the different microstructures cube1 with 56 orientations and cube2 with 448 orientations.

orientations for cube2, the relative earing heights differ. On the one hand an overestimation of the anisotropy is obtained by a coarse discretization, which can be scaled by a smaller anisotropy factor $\bar{\zeta}_4$. But on the other hand, a significant shift of the earing position from \approx

45° towards lower angles is observed. This does not agree with experimental observations for rolled sheets. The calculation of the metal sheet with cube2 microstructure takes about 2.5 times longer compared to the cube1 microstructure. Although the cube2 discretization is computationally more expensive, a certain amount of crystal orientations is necessary as the coarse cube1 discretization does not give physically reasonable results.

As outlined in ENGLER & KALZ [41] the final earing height depends on the drawing ratio $r_d = r_{\text{sheet}}/r_{\text{punch}}$ of the sheet radius to the punch radius, the sheet thickness, the transition radius of the punch and the previous rolling reduction. An increasing drawing ratio yields to more distinctive ears and an increasing overall cup height, see Figure 6.18.

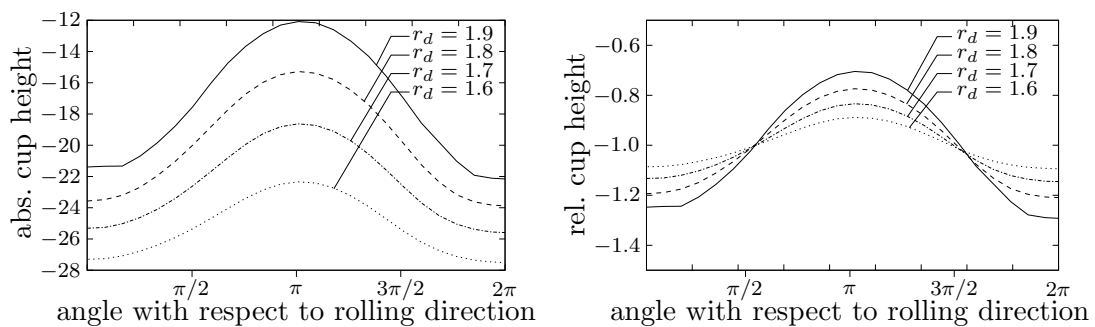


Figure 6.18: Circular deep drawing of a metal sheet. Texture induced earing yields two equal pairs of ears. The relative cup height at a total punch deformation of $\bar{u} = 45\text{mm}$ is given for different drawing ratios $r_d = 1.6$, $r_d = 1.7$, $r_d = 1.8$ and $r_d = 1.9$.

Recapitulatory, the proposed hybrid micro-macro model simulates the earing development and the earing position of a prerolled metallic sheet in a very good manner. The studies with regard to the degree of pretexture, anisotropy scaling and drawing ratio give reasonable results compared to relevant experimental and numerical benchmarks. A microstructure with a small amount of grains is not able to predict the right earing position and therefore an appropriate number of grains, in the underlying analysis a cube2 discretization, has to be chosen.

6.3.4. Square Deep Drawing of a Metallic Sheet. Finally the deep drawing of a square cup is simulated. The square deep drawing process is a fundamental forming operation in industrial applications and in contrast to the circular deep drawing process not axisymmetric. The setup corresponds to the one illustrated in Figure 6.12a). The half width of the quadratic sheet is $r_{\text{sheet}} = 50.0\text{mm}$, its thickness is $t_{\text{sheet}} = 0.8\text{mm}$ and the half width of the punch is $r_{\text{punch}} = 25.0\text{mm}$ with corresponding transition radius $r_{t,\text{punch}} = 5.0\text{mm}$. The dimensions of the blankholder are $r_{o,\text{blank}} = 50.0\text{mm}$ and $r_{i,\text{blank}} = 26.4\text{mm}$. Finally, the die is characterized by $r_{\text{die}} = 26.7\text{mm}$ and corresponding transition radius $r_{t,\text{die}} = 4.7\text{mm}$. The material parameters agree with the ones in the circular deep drawing test and the punch is pressed in a deformation-driven process into the die up to a total deformation of $\bar{u} = 30\text{mm}$. Again, the blankholder is fixed at a distance equal to the thickness of the sheet and prevents the raising of the sheet during the deformation process as well as a possible wrinkling. Different metal flow and uneven material distribution in the corners, flanges and faces of the sheet cause wrinkles in the flange. A natural evolution of ears is induced by the square geometry, with the quadratic sheet being discretized with 2601 eight-noded Q1/P0 elements with one element over the sheet thickness. Figure 6.19 shows the upper and lower perspective of the deep drawn

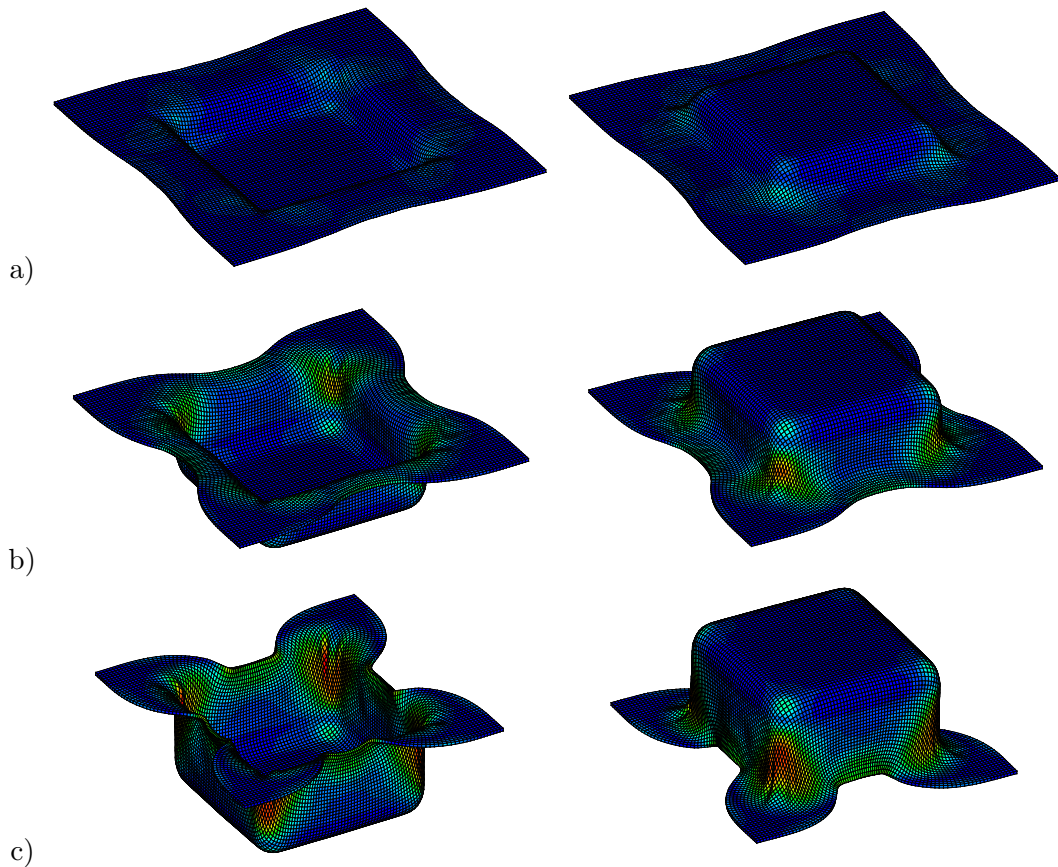


Figure 6.19: Deep drawing of a square sheet. Top and bottom view of square sheet with evolution of plastic strains at a) $\bar{u} = 10\text{mm}$, b) $\bar{u} = 20\text{mm}$ and c) $\bar{u} = 30\text{mm}$.

specimen with the distribution of plastic strains at the intermediate states $\bar{u} = 10\text{mm}$, $\bar{u} = 20\text{mm}$ and the final deformation state $\bar{u} = 30\text{mm}$. It can be observed that the maximum of accumulated plastic strains occurs at the corners of the die. Furthermore, wrinkles form at the flanges of the deformed sheet. A study concerning the thickness distribution is shown in Figure 6.20a). A localized thinning can be observed in the lower edges of the

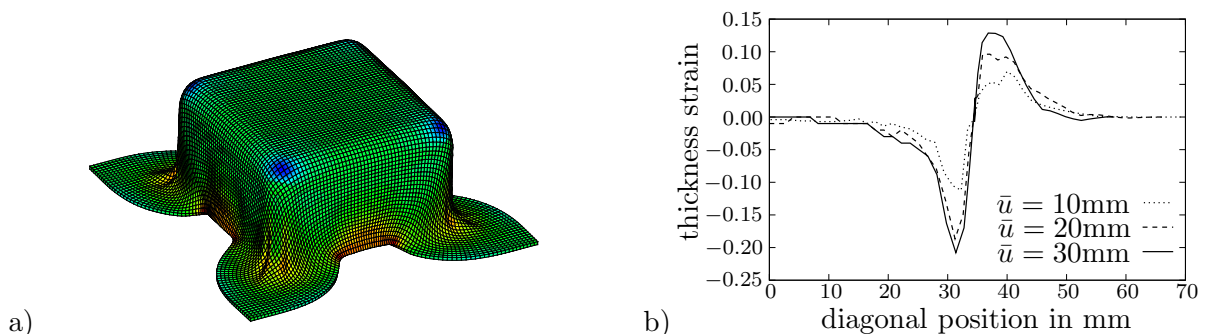


Figure 6.20: Deep drawing of a square sheet. a) Bottom view of square sheet with thickness strains at $\bar{u} = 30\text{mm}$ and b) thickness strain distribution along the sheet diagonal for $\bar{u} = 10\text{mm}$, $\bar{u} = 20\text{mm}$ and $\bar{u} = 30\text{mm}$.

sheet increasing with the deformation. The thickness strain along the blank diagonal at

the same deformation states $\bar{u} = 10\text{mm}$, $\bar{u} = 20\text{mm}$ and $\bar{u} = 30\text{mm}$ is documented in Figure 6.20b). These results qualitatively agree with the experimental and simulation results in YOON, YANG, CHUNG & BARLAT [144]. A study concerning the influence of an initial anisotropic texture is documented in Figure 6.21. The simulation is performed for a metal

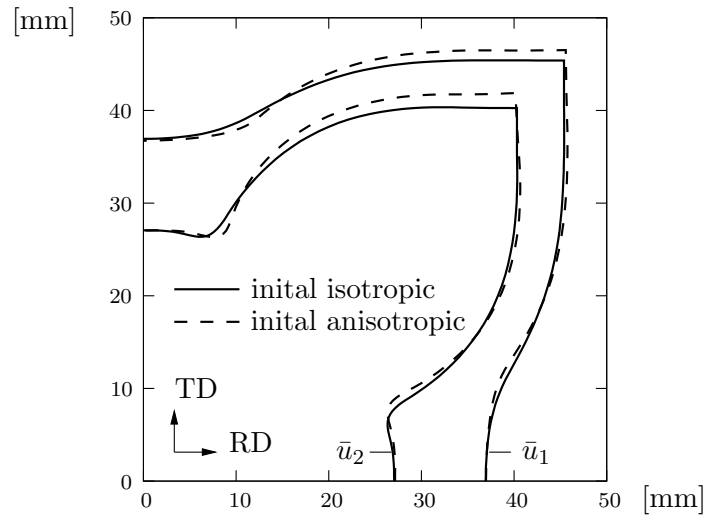


Figure 6.21: Deep drawing of a square sheet. Draw-in profile at intermediate state $\bar{u}_1 = 19\text{mm}$ and final deformation state $\bar{u}_2 = 30\text{mm}$ for initial isotropic texture and initial pretexture due to rolling with 18% thickness reduction. TD and RD represent the transverse and rolling direction, respectively.

sheet with quasi-isotropic initial texture and an initial anisotropic texture obtained by a predeformation. Here, the metal sheet is deformed by rolling to 18% thickness reduction, see MIEHE, FRANKENREITER & ROSATO [91] and Section 4.4.2.2. Figure 6.21 shows an upper view of the rim of a quarter of the square sheet at the intermediate deformation state $\bar{u}_1 = 19\text{mm}$ and the final deformation state $\bar{u}_2 = 30\text{mm}$. For both initial textures, the amount of draw-in in rolling and transverse direction does not show a major difference, in agreement with YOON, YANG, CHUNG & BARLAT [144]. For the initial isotropic texture, the profile is nearly symmetric to the bisecting line. In contrast, the simulation with the prerolled texture shows a clear deflection from this symmetry.

Hence, the modeling of texture-induced anisotropy within a hybrid micro-macro approach influences the macroscopic response towards a direction dependence. It is crucial to take into account the microstructure and its impact with respect to an anisotropic macroscopic material behavior.

7. Conclusion

The underlying work is concerned with microstructure-based modeling of texture-induced anisotropy in finite polycrystal plasticity. A short overview on general modeling aspects and a concise description of fundamental characteristics of crystalline materials is given. With this background information at hand, a microstructural material model is developed, which governs the texture evolution in rigid crystal plasticity. The polycrystalline aggregate is idealized as reorientation continuum and the crystal orientation distribution function is approximated as a Fourier series. The Fourier coefficients enter as evolving structural tensors the hybrid micro-macro model capable of covering the simulation of texture-induced anisotropy in polycrystalline materials at finite plastic deformation. This hybrid model is a mixture of the earlier introduced rigid-plastic crystal plasticity model including the microscopic effect of grain reorientation on the microscale and a purely macroscopic material model of finite plasticity in the logarithmic strain space on the macroscale. Specific homogenization assumptions bridge the gap between these two scales and permit the simulation of macroscopic anisotropy induced by a heterogeneous microstructure.

The microstructural texture modeling in rigid crystal plasticity comprises a theoretical and computational framework for the analysis of evolving textures in crystals. The key result is a purely geometric approach to rigid-plasticity of single crystals and polycrystalline aggregates, which provides an extremely fast and robust computation of the developing texture. For planar crystals undergoing double slip the crystal reorientation is purely geometric in nature, which serves as basic idea for a similar ansatz with respect to three-dimensional crystals. Therefore, arithmetic values of suitable defined pseudo-stresses are chosen for a geometric estimate of the active set of slip systems in a rate-independent setting. With this set of active slip systems at hand, an optimality condition results in a closed-form expression for the lattice rotation in terms of the overall deformation of the aggregate. Details of the algorithmic implementation are outlined, which updates in a typical time increment of an objective mid-point scheme the lattice rotations parameterized by Rodrigues vectors. The excellent modeling capacity of the formulation was documented for planar single crystals and polycrystals as well as for face-centered and body-centered cubic crystals. With regard to qualitative texture estimates and a computational efficiency, the proposed geometric rigid-plastic active-set model is compared to numerical and experimental results. For characteristic, industry-relevant deformation processes the proposed rigid-plastic active-set model yields very good qualitative results at a fraction of time compared to an alternative rigid-plastic power-law model for face-centered as well as body-centered cubic crystals. It turns out to be extremely robust and is considered to be an attractive ingredient with regard to the description of evolving anisotropy in polycrystals within multiscale models.

With these results at hand, the estimation of evolving crystal orientation distribution functions in finite plasticity of polycrystals bases on the geometric approach to rate-independent rigid-plasticity of crystals, allowing a fast and robust determination of local crystal reorientations. The crystal orientations are represented by material points of an idealized orientation continuum. A crystal reorientation map describes the reorientation of the crystal grains, i.e. the deformation of the orientation continuum. Therefore, Lagrangian and Eulerian configurations are introduced in the orientation as well as in the Rodrigues space involving the definition of a metric as a relation between volume elements

of the two spaces. The reorientation process is governed by a crystal fraction conservation equation yielding a Lagrangian and an Eulerian form of the crystal orientation distribution function. In the Lagrangian setting, the crystal orientations and its corresponding crystal fractions are associated with moving sectors, whereas in the Eulerian setting the crystal reorientations are projected onto fixed control volumes. Thus, the Lagrangian approach is restricted to a smooth reorientation process and in the Eulerian approach a simple count of orientations directly determines discrete values of the crystal orientation distribution function. Such an estimate is rough but very robust and applicable to non-smooth reorientation processes. Furthermore, a numerical method for the computation of orientation averages in the Eulerian setting is developed. This method recasts the homogenization over the orientation space into arithmetic averages associated with the discrete crystal orientations and providing a very robust scheme for a possible embedding of structural anisotropy tensors into multiscale methods. It is shown that the discrete evaluation of orientation averages does not need the explicit computation of crystal orientation distribution function. For several deformation modes of polycrystalline aggregates the proposed geometric model is proven to predict the evolution of the crystal orientation distribution function and the overall anisotropy very good in the range of large strains. Even for a coarse discretization of the orientation continuum, the main characteristics of the anisotropy development are captured very well. This is documented by a comparison of simulated anisotropy evolution with data available in the literature for the yield surface, the normalized yield stress and the Lankford coefficient. Being very fast and robust, the proposed algorithm is an attractive feature for the design of fast multiscale models of anisotropic metal plasticity.

The microscopic effect of grain reorientation with its corresponding homogenization procedure is incorporated into a purely macroscopic model of finite polycrystal plasticity. Within this hybrid micro-macro model the structural tensors govern the evolving texture and result in an anisotropic macroscopic material behavior. The finite strain framework is realized by an additive approach in the logarithmic strain space, which allows a formulation of the constitutive model in a format similar to the geometric linear theory. Two scalar-valued tensor functions, i.e. the free energy and dissipation function, govern this constitutive hybrid micro-macro model. Hereby, the microstructure enters the macroscopic material model by structural tensors. The algorithmic treatment solves the micro-macro problem in an efficient operator splitting. By means of academic and engineering-relevant simulations the texture and anisotropy evolution is qualitatively analyzed and successfully compared to the literature. Hence the proposed hybrid micro-macro model is shown to be very attractive for the description of finite deformation processes with the numerically efficient and robust microstructure update, its corresponding homogenization procedure and its embedding in a framework of finite plasticity in the logarithmic strain space.

A. Planar Crystals undergoing Double Slip

This appendix is dedicated to planar crystals undergoing double slip. A closed-form solution of the crystal reorientation and the evolution of crystal orientation distribution functions in both the continuous as well as the discrete setting is investigated. For a detailed discussion on planar polycrystals see e.g. RASHID [122], DAFALIAS [40] or PRANTIL, JENKINS & DAWSON [114].

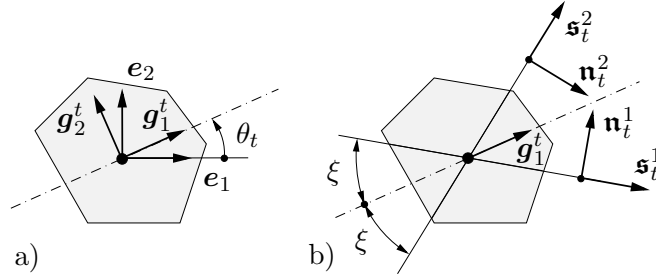


Figure A.1: Planar crystal undergoing double slip. a) The lattice frame $\{g_i^t\}_{i=1,2,3}$ is oriented by the angle θ_t relative to a fixed sample frame $\{e_i\}_{i=1,2,3}$. b) The two slip systems $\alpha = 1, 2$ are symmetrically oriented by the slip system separation angle ξ relative to the lattice orientation vectors.

A.1. Continuous Formulation

For the planar double slip system depicted in Figure A.1, the rotation occurs in the 1-2 slip plane of the sample frame $\{e_i\}_{i=1,2,3}$. Thus, $\mathcal{SO}(3)$ reduces to $\mathcal{SO}(1)$ and the polycrystalline microstructure is one-dimensional. The reorientation of the crystal can be described by the coordinate representation

$$\mathbf{R}_t = \begin{bmatrix} \cos(\theta_t) & -\sin(\theta_t) \\ \sin(\theta_t) & \cos(\theta_t) \end{bmatrix} \quad (\text{A.1})$$

with respect to the sample frame $\{e_i\}_{i=1,2}$ in terms of the scalar angle θ_t . The reference configuration is defined by $\theta_0 \in \mathbb{R} \mid -\frac{\pi}{2} \leq \theta_0 < \frac{\pi}{2}$, which defines the fundamental range of orientations of the double slip model. For the planar double slip model the reorientation is scalar in nature. This simplifies the general formulation tremendously. As depicted in Figure A.1, only $m = 2$ effective slip systems exist. The coordinates of the slip directions and slip plane normals, defined in (4.6) relative to the rotated lattice system $\{g_i^t\}_{i=1,2}$, are

$$\mathbf{s}_i^{1,2} = \begin{bmatrix} \cos(\xi) \\ \mp \sin(\xi) \end{bmatrix} \quad \text{and} \quad \mathbf{n}_i^{1,2} = \begin{bmatrix} \sin(\xi) \\ \pm \cos(\xi) \end{bmatrix}, \quad (\text{A.2})$$

yielding the coordinates of the structural tensors (4.9)

$$\mathfrak{P}_{ij}^{1,2} = \frac{1}{2} \begin{bmatrix} \sin(2\xi) & \pm \cos(2\xi) \\ \pm \cos(2\xi) & -\sin(2\xi) \end{bmatrix} \quad \text{and} \quad \mathfrak{Q}_{ij}^{1,2} = \frac{1}{2} \begin{bmatrix} 0 & \pm 1 \\ \mp 1 & 0 \end{bmatrix}, \quad (\text{A.3})$$

in terms of the slip system separation angle ξ . In order to obtain a unique solution for the crystallographic slip problem in the subsequent development, the slip system separation angle is restricted to the range of $0 < \xi < \frac{\pi}{2}$. Since the two systems are always active, the evaluation of the pseudo-stress τ^α in (4.15) is not needed and the selection criterion (4.22) always gives $\mathcal{A} = \mathcal{S}$, where $\mathcal{S} := \{1, 2\}$ is the full set of slip systems. Based on the

introduced definitions $\mathbf{D}_t^p := \sum_{\alpha=1}^m \dot{\gamma}^\alpha \mathfrak{P}_t^\alpha$ and $\mathbf{W}_t^p := \sum_{\alpha=1}^m \dot{\gamma}^\alpha \mathfrak{Q}_t^\alpha$ in Section 4.1.3, the plastic rate of deformation and the plastic spin are

$$\begin{aligned} \mathbf{D}_t^p &= \frac{1}{2} (\dot{\gamma}^1 + \dot{\gamma}^2) \begin{bmatrix} \sin(2\xi) & 0 \\ 0 & -\sin(2\xi) \end{bmatrix} + \frac{1}{2} (\dot{\gamma}^1 - \dot{\gamma}^2) \begin{bmatrix} 0 & \cos(2\xi) \\ \cos(2\xi) & 0 \end{bmatrix} \\ \mathbf{W}_t^p &= \frac{1}{2} (\dot{\gamma}^1 - \dot{\gamma}^2) \begin{bmatrix} 0 & 1 \\ -1 & 0 \end{bmatrix}. \end{aligned} \quad (\text{A.4})$$

Figure A.2 shows the response of two active systems in the planar double slip model. For an isochoric macroscopic deformation of the planar polycrystalline aggregate, the spatial rate of deformation and spin tensors defined in (4.8) have the coordinate representation

$$\bar{\mathbf{D}}_t = \begin{bmatrix} \Lambda & \Gamma \\ \Gamma & -\Lambda \end{bmatrix} \quad \text{and} \quad \bar{\mathbf{W}}_t = \begin{bmatrix} 0 & -\Omega \\ \Omega & 0 \end{bmatrix} \quad (\text{A.5})$$

in the sample frame $\{\mathbf{e}_i\}_{i=1,2}$ in terms of the macroscopic rate of stretching Λ , rate of shearing Γ and spin Ω . For this macroscopic rate of deformation (4.25) yields the closed-

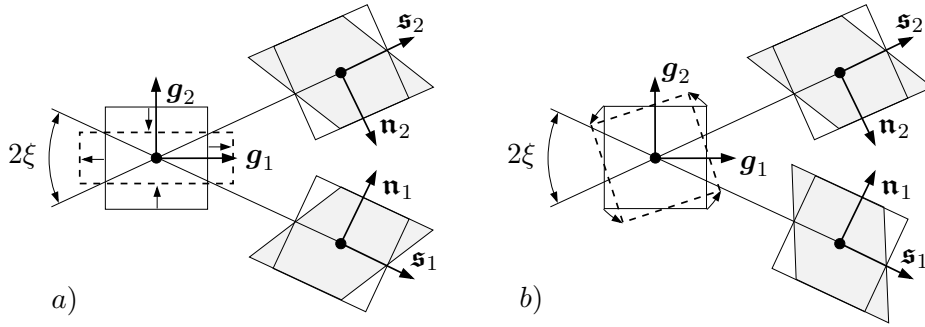


Figure A.2: Double slip system response. Simultaneous activity of both slip systems produce a) a *pure shearing mode* for $\dot{\gamma}^2 = \dot{\gamma}^1 > 0$ and b) a *pure plastic rotation* for $\dot{\gamma}^2 = -\dot{\gamma}^1 > 0$.

form result

$$\dot{\gamma}^{1,2} = [\cos(2\theta_t) \Lambda + \sin(2\theta_t) \Gamma] / \sin(2\xi) \pm [\cos(2\theta_t) \Gamma - \sin(2\theta_t) \Lambda] / \cos(2\xi) \quad (\text{A.6})$$

for the plastic slip in the current configuration in terms of the prescribed coordinates Λ and Γ of the macroscopic rate of deformation tensor. By insertion of the plastic slip into equation (4.11)₂ and the expressions (A.4)₂ and (A.5)₂ for the plastic and the total spin, the crystal reorientation has the simple scalar representation

$$\dot{\theta}_t = \Omega - [\sin(2\theta_t) \Lambda - \cos(2\theta_t) \Gamma] / \cos(2\xi) \quad \text{with} \quad \theta_t(t_0) = \theta_0 \quad (\text{A.7})$$

with the prescribed spin Ω . The Lagrangian conservation equation (5.46) appears with the scalar reorientation (A.7) in the closed form

$$\dot{F} - F [2 \cos(2\chi) \Lambda + 2 \sin(2\chi) \Gamma] / \cos(2\xi) = 0 \quad \text{with} \quad F(\theta_0, t_0) = 1/\pi. \quad (\text{A.8})$$

The two equations (A.7) and (A.8) govern the reorientation and the codf evolution in the planar double slip model.

A.2. Discrete Algorithmic Formulation

In the algorithmic setting at finite time steps, the incremental deformation and spin tensors defined in (4.34) have the coordinate representation

$$\bar{\mathbf{D}}_{n+1/2}^* = \begin{bmatrix} \Lambda_{n+1/2}^* & \Gamma_{n+1/2}^* \\ \Gamma_{n+1/2}^* & -\Lambda_{n+1/2}^* \end{bmatrix} \quad \text{and} \quad \bar{\mathbf{W}}_{n+1/2}^* = \begin{bmatrix} 0 & -\Omega_{n+1/2}^* \\ \Omega_{n+1/2}^* & 0 \end{bmatrix} \quad (\text{A.9})$$

in the sample coordinate system. These tensors drive the reorientation process of the polycrystal for the time step under consideration. The initial or Lagrangian orientation space of planar crystals $\mathcal{O}_0 := [-\frac{\pi}{2}, \frac{\pi}{2}]$ is discretized by $e = 1, \dots, E^h$ equal elements $\mathcal{O}_0^e := [\theta_0^e, \theta_0^{e+1}]$ with local nodal positions $\theta_0^e := \pi(e-1)/E^h$ and $\theta_0^{e+1} := \pi e/E^h$. Thus, the finite element mesh is characterized by the pair of element sizes and center positions

$$|\mathcal{O}_0^e| = |\theta_0^{\mathcal{T}^h(1,e)} - \theta_0^{\mathcal{T}^h(2,e)}| \quad \text{and} \quad \theta_0^e := \frac{1}{2}[\theta_0^{\mathcal{T}^h(1,e)} + \theta_0^{\mathcal{T}^h(2,e)}], \quad (\text{A.10})$$

where i is an element of the mesh topology $\mathcal{T}^h(i, e)$. The Lagrangian mesh is used in the Eulerian formulation as a fixed assembly of control volumes, see Figure A.3. With the incremental deformation (A.9) at hand, integration of (A.7) yields the updates

$$\theta_{n+1}^I = \theta_n^I + \Omega_{n+1/2}^* - [\sin(2\theta_n^I)\Lambda_{n+1/2}^* - \cos(2\theta_n^I)\Gamma_{n+1/2}^*] / \cos(2\xi) \quad (\text{A.11})$$

of the orientation at the global nodes $I = 1, \dots, N^h$ of the mesh. With known orientations at the nodes, a pair of deformed element sizes and center positions is defined in analogy to (A.10) by

$$|\mathcal{O}_{n+1}^e| = |\theta_{n+1}^{\mathcal{T}^h(1,e)} - \theta_{n+1}^{\mathcal{T}^h(2,e)}| \quad \text{and} \quad \theta_{n+1}^e := \frac{1}{2}[\theta_{n+1}^{\mathcal{T}^h(1,e)} + \theta_{n+1}^{\mathcal{T}^h(2,e)}] \quad (\text{A.12})$$

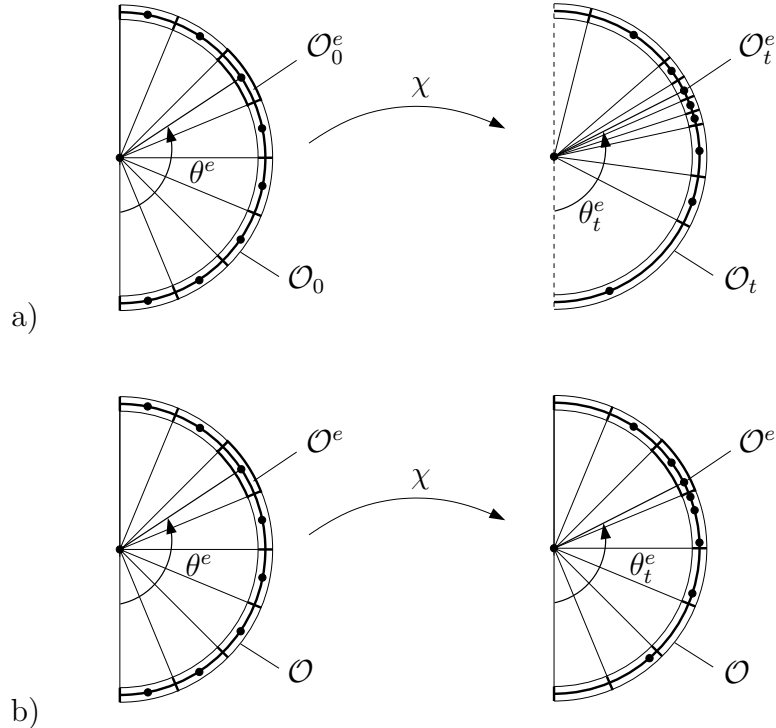


Figure A.3: Reorientation for planar crystals. a) Lagrangian formulation with deforming cells. b) Eulerian formulation with fixed cells representing control volumes

for $e = 1, \dots, E^h$. The Lagrangian update of the codf, based on equation (5.58), is visualized in Figure A.3a) with deforming element sizes and center positions according to (A.12). With $F^h(\theta_0^e, t_0) = 1/\pi$ and $|\mathcal{O}_0^e| = \pi/E^h$ the discrete Lagrangian codf reads

$$F^h(\theta_0^e, t_{n+1}) = F^h(\theta_0^e, t_0) |\mathcal{O}_0^e|/|\mathcal{O}_{n+1}^e| = [E^h |\mathcal{O}_{n+1}^e|]^{-1} . \quad (\text{A.13})$$

The Eulerian update of the codf based on equation (5.53) is visualized in Figure A.3b). It is based on the count of the representative center orientations which fall into the control cells, i.e.

$$f^h(\theta^e, t_{n+1}) = N(\mathcal{O}^e, t_{n+1})/|\mathcal{O}^h| = N(\mathcal{O}^e, t_{n+1})/\pi , \quad (\text{A.14})$$

by means of $|\mathcal{O}^h| = \pi$. Clearly, such a definition only gives a rough and discontinuous estimate, in particular for the coarse mesh depicted in Figure A.3.

References

- [1] www.aluminium.matter.org.uk/content/html/eng/default.asp?catid=84&pageid=-1941055071 [August 14, 2012].
- [2] www.schulergroup.com/technologien/produkte/pressenlinien_hydraulisch/Bauteile/index.html [August 14, 2012].
- [3] www.thomasnet.com/articles/custom-manufacturing-fabricating/wrinkling-during-deep-drawing [August 14, 2012].
- [4] www-hrem.msm.cam.ac.uk/gallery/index.shtml [August 14, 2012].
- [5] www.en.wikipedia.org/wiki/grain_boundary [August 14, 2012].
- [6] ACHARJEE, S.; ZABARAS, N. [2003]: *A proper orthogonal decomposition approach to microstructure model reduction in Rodrigues space with applications to optimal control of microstructure-sensitive properties*. *Acta Materialia*, 51: 5627–5646.
- [7] ACHARYA, A.; BEAUDOIN, A. J. [2000]: *Grain-size effect in viscoplastic polycrystals at moderate strains*. *Journal of the Mechanics and Physics of Solids*, 48: 2213–2230.
- [8] ADAMS, B. L.; BOEHLER, J. P.; GUIDI, M.; ONAT, E. T. [1992]: *Group theory and representation of microstructure and mechanical behavior of polycrystals*. *Journal of the Mechanics and Physics of Solids*, 40: 723–737.
- [9] ALTMANN, S. L. [1986]: *Rotations, quaternions and double groups*. Oxford Science Publications.
- [10] ANAND, L.; KOTHARI, M. [1996]: *A computational procedure for rate-independent crystal plasticity*. *Journal of the Mechanics and Physics of Solids*, 44: 525–558.
- [11] ANGELES, J. [1988]: *Rational kinematics*. Springer-Verlag.
- [12] APEL, N. [2004]: *Approaches to the description of anisotropic material behaviour at finite elastic and plastic deformations, theory and numerics*. Report No. I-12, Institute of Applied Mechanics (CE) Chair I, University of Stuttgart.
- [13] ARGYRIS, J. [1982]: *An excursion into large rotations*. *Computer Methods in Applied Mechanics and Engineering*, 32: 85–155.
- [14] ASARO, R. [1983]: *Micromechanics of crystals and polycrystals*. *Advances in Applied Mechanics*, 23: 1–115.
- [15] ASARO, R. J.; NEEDLEMAN, A. [1985]: *Texture development and strain hardening in rate dependent polycrystals*. *Acta Metallurgica*, 33: 923–953.
- [16] BALASUBRAMANIAN, S.; ANAND, L. [1998]: *Polycrystalline plasticity: Application to earing in cup drawing of AL2008-T4 sheet*. *Journal of Applied Mechanics*, 65: 268–271.
- [17] BALDWIN, W. M.; HOWALD, T. S.; ROSS, A. W. [1946]: *Relative triaxial deformation rates*. *Transactions of the American Institute of Mining and Metallurgical Engineers*, 166: 86–113.
- [18] BALZANI, D.; SCHRÖDER, J.; BRANDS, D. [2010]: *FE²-simulation of micro-heterogeneous steels based on statistically similar RVE's*. In *IUTAM-symposium on variational concepts with applications to the mechanics of materials*, Vol. 21, pp. 15–28.

- [19] BANABIC, D. [2000]: *Formability of metallic materials: Plastic anisotropy, formability testing, forming limits*. Springer Verlag, Berlin.
- [20] BARGEL, H. J.; SCHULZE, G. [2008]: *Werkstoffkunde*. Springer, Berlin.
- [21] BARRETT, C. S.; MASSALSKI, T. B. [1980]: *Structure of metals*. Pergamon Press, Oxford.
- [22] BECKER, R.; PANCHANADEESWARAN, S. [1989]: *Crystal rotations represented as Rodrigues vectors*. Textures and Microstructures, 10: 167–194.
- [23] BISHOP, J. F. W.; HILL, R. [1951]: *A theoretical deviation of the plastic properties of a polycrystalline face-centered metal*. Philosophical Magazine, 42: 1298–1307.
- [24] BISHOP, J. F. W.; HILL, R. [1951]: *A theory of plastic distortion of a polycrystalline aggregate under combined stresses*. Philosophical Magazine, 42: 414–427.
- [25] BÖHLKE, T. [2005]: *Application of the maximum entropy method in texture analysis*. Computational Materials Science, 32: 276–283.
- [26] BÖHLKE, T. [2006]: *Texture simulation based on tensorial Fourier coefficients*. Computers and Structures, 84: 1086–1094.
- [27] BÖHLKE, T.; BERTRAM, A. [2001]: *The evolution of Hooke's law due to texture development in fcc polycrystals*. International Journal of Solids and Structures, 38: 9437–9459.
- [28] BÖHLKE, T.; BERTRAM, A. [2003]: *Crystallographic texture induced anisotropy in copper: an approach based on a tensorial Fourier expansion of the codf*. Journal De Physique IV, 105: 167–174.
- [29] BÖHLKE, T.; RISY, G.; BERTRAM, A. [2005]: *A texture component model for anisotropic polycrystal plasticity*. Computational Materials Science, 32: 284–293.
- [30] BÖHLKE, T.; RISY, G.; BERTRAM, A. [2006]: *Finite element simulation of metal forming operations with texture based material models*. Modelling and Simulation in Materials Science and Engineering, 14: 365–387.
- [31] BOVE, S. [2011]: *Hybrid micro-macro modeling of texture-induced anisotropy in finite polycrystal plasticity*. Technical report, Institute of Applied Mechanics (CE) Chair I, University of Stuttgart.
- [32] BRAVAIS, A. [1859]: *Mémoire sur les systèmes des points distribués régulièrement sur un plan ou dans l'espace*. Journal de l'Ecole Polytechnique, 19: 1–128.
- [33] BRONKHORST, C. A.; KALIDINDI, S. R.; ANAND, L. [1992]: *Polycrystalline plasticity and the evolution of crystallographic texture in fcc metals*. Philosophical Transactions: Physical Sciences and Engineering, 341, No. 1662: 443–477.
- [34] BUERGER, M. J. [1977]: *Kristallographie: Eine Einführung in die geometrische und röntgenographische Kristallkunde*. Walter de Gruyter, Berlin.
- [35] BUNGE, H. J. [1965]: *Zur Darstellung allgemeiner Texturen*. Zeitschrift für Metallkunde, 56: 872–874.
- [36] BUNGE, H. J. [1969]: *Texture analysis in materials science. Mathematical methods*. Butterworth & Co Publishers.
- [37] CHADWICK, P. [1999]: *Continuum mechanics: Concise theory and problems*. Courier Dover Publications.

- [38] CLEMENT, A. [1982]: *Prediction of deformation texture using a physical principle of conservation*. Materials Science and Engineering, 55: 203–210.
- [39] CUITIÑO, A. M.; ORTIZ, M. [1992]: *Computational modelling of single crystals*. Modelling and Simulation in Materials Science and Engineering, 1: 225–263.
- [40] DAFALIAS, Y. F. [1993]: *Planar double-slip micromechanical model for polycrystal plasticity*. Journal of Engineering Mechanics, 119: 1260–1284.
- [41] ENGLER, O.; KALZ, S. [2004]: *Simulation of earing profiles from texture data by means of a visco-plastic self-consistent polycrystal plasticity approach*. Materials Science and Engineering A, 373: 350–362.
- [42] FRANK, F. C. [1988]: *Orientation mapping*. Metallurgical Transactions A, 19A: 403–408.
- [43] FRENKEL, J. [1926]: *Zur Theorie der Elastizitätsgrenze und der Festigkeit kristallinischer Körper*. Zeitschrift für Physik, 37: 572–609.
- [44] GELFAND, I. M.; MINLOS, R. I.; SHAPIRO, Z. Y. [1963]: *Representation of the rotation and Lorentz groups and their applications*. Pergamon Press, Oxford.
- [45] GUIDI, M.; ADAMS, B. L.; ONAT, E. T. [1992]: *Tensorial representation of the orientation distribution function in cubic polycrystals*. Textures of Microstructures, 19: 147–167.
- [46] HABRAKEN, A. M. [2004]: *Modelling the plastic anisotropy of metals*. Archives of Computational Methods in Engineering, 11: 3–96.
- [47] HARREN, S.; ASARO, R. [1989]: *Nonuniform deformations in polycrystals and aspects of the validity of the Taylor model*. Journal of the Mechanics and Physics of Solids, 37: 191–232.
- [48] HAUPT, P. [2000]: *Continuum mechanics and theory of materials*. Springer Verlag, Berlin.
- [49] HEINZ, A.; NEUMANN, P. [1991]: *Representation of orientation and disorientation data for cubic, hexagonal, tetragonal and orthorhombic crystals*. Acta Cryst., A47: 780–789.
- [50] HILL, R. [1948]: *A theory of the yielding and plastic flow of anisotropic metals*. Proceedings of the Royal Society of London. Series A, Mathematical and Physical Sciences, 193: 281–297.
- [51] HILL, R. [1966]: *Generalized constitutive relations for incremental deformation of metal crystals by multislip*. Journal of the Mechanics and Physics of Solids, 14: 95–102.
- [52] HILL, R. [1968]: *On constitutive inequalities for simple materials – I*. Journal of the Mechanics and Physics of Solids, 16: 229–242.
- [53] HILL, R. [1985]: *On the micro-to-macro transition in constitutive analyses of elasto-plastic response at finite strains*. Mathematical Proceedings of the Cambridge Philosophical Society, 98: 579–590.
- [54] HOLZAPFEL, G. A. [2000]: *Nonlinear solid mechanics. A continuum approach for engineering*. John Wiley & Sons.

- [55] HONEYCOMBE, R. W. K. [1984]: *The plastic deformation of metals*. Edward Arnold, London.
- [56] HONNEF, H.; MECKING, H. [1978]: *A method for the determination of the active slip systems and orientation changes during single slip deformation*. In GOTSTEIN, G.; LÜCKE, K. (Editors): *Textures of Materials*, pp. 265–275.
- [57] HOSFORD, W. F. [1993]: *The mechanics of crystals and textured polycrystals*. Oxford Engineering Science Series.
- [58] HOUTTE, P. VAN [1987]: *Calculation of the yield locus of textures polycrystals using the Taylor and the relaxed Taylor theory*. *Textures and Microstructures*, 72: 7–29.
- [59] HOUTTE, P. VAN; MOLS, K.; BAEL, A. VAN ; AERNOUDT, E. [1989]: *Application of yield loci calculated from texture data*. *Textures and Microstructures*, pp. 23–39.
- [60] HULL, D.; BACON, D. J. [1984]: *Introduction to dislocations*. Pergamon Press, Oxford.
- [61] HUTCHINSON, J. W. [1970]: *Elastic-plastic behaviour of polycrystalline metals and composites*. *Proceedings of the Royal Society London A*, 319: 247–272.
- [62] HUTCHINSON, J. W. [1976]: *Bounds and self-consistent estimates for creep of polycrystalline materials*. *Proceedings of the Royal Society London A*, 348: 101–127.
- [63] ILSCHNER, B.; SINGER, R. F. [2010]: *Werkstoffwissenschaften und Fertigungstechnik*. Springer, Berlin.
- [64] JAGODZINSKI, H. [1955]: *Kristallographie*. In *Handbuch der Physik VII/1*, pp. 1–103. Springer, Berlin.
- [65] KALIDINDI, S. R.; BRONKHORST, C. A.; ANAND L. [1992]: *Crystallographic texture development in bulk deformation processing of fcc metals*. *Journal of the Mechanics and Physics of Solids*, 40: 537–569.
- [66] KANETAKE, N.; TOZAWA, Y.; OTANI, T. [1983]: *Calculations from texture of earing in deep drawing for fcc metal sheets*. *International Journal of Mechanical Sciences*, 25: 337–345.
- [67] KHORASHADIZADEH, A.; RAABE, D.; ZAEFFERER, S.; ROHRER, G. S.; ROLLETT, A. D.; WINNING, M. [2011]: *Five-parameter grain boundary analysis by 3D EBSD of an ultra fine grained CuZr alloy processed by equal channel angular pressing*. *Advanced Engineering Materials*, 13: 237–244.
- [68] KLEBER, W.; BAUTSCH, H. J.; BOHM, J. [1998]: *Einführung in die Kristallographie*. Verlag Technik, Berlin.
- [69] KOCKS, U. F.; TOMÉ, C. N.; WENK, H. R. [1998]: *Texture and anisotropy*. Cambridge University Press.
- [70] KOWALCZYK, K.; GAMBIN, W. [2004]: *Model of plastic anisotropy evolution with texture-dependent yield surface*. *International Journal of Plasticity*, 20: 19–54.
- [71] KRÖNER, E. [1960]: *Allgemeine Kontinuumstheorie der Versetzungen und Eigenspannungen*. *Archive for Rational Mechanics and Analysis*, 4: 273–334.
- [72] KUMAR, A.; DAWSON, P. R. [1995]: *Polycrystal plasticity modeling of bulk forming with finite elements over orientation space*. *Computational Mechanics*, 17: 10–25.

- [73] KUMAR, A.; DAWSON, P. R. [1996]: *The simulation of texture evolution with finite elements over orientation space I. Development*. Computer Methods in Applied Mechanics and Engineering, 130: 227–246.
- [74] KUMAR, A.; DAWSON, P. R. [1996]: *The simulation of texture evolution with finite elements over orientation space II. Application to planar crystals*. Computer Methods in Applied Mechanics and Engineering, 130: 247–261.
- [75] KUMAR, A.; DAWSON, P. R. [1998]: *Modeling crystallographic texture evolution with finite elements over neo-Eulerian orientation spaces*. Computer Methods in Applied Mechanics and Engineering, 153: 259–302.
- [76] KUMAR, A.; DAWSON, P. [2000]: *Computational modeling of fcc deformation textures over Rodrigues' space*. Acta Materialia, 48: 2719–2736.
- [77] LEBENSOHN, R. A.; TOMÉ, C. N. [1993]: *A self-consistent anisotropic approach for the simulation of plastic deformation and texture development of polycrystals: Application to zirconium alloys*. Acta Metallurgica et Materialia, 41: 2611–2624.
- [78] LI, H.J.; HAN, J.; JIANG, Z.; PI, H.; WEI, D.; TIEU, A. [2008]: *Crystal plasticity finite element modelling of bcc deformation texture in cold rolling*. Advanced Materials Research, 32: 251–254.
- [79] MALVERN, L. E. [1969]: *Introduction to the mechanics of a continuous medium*. Prentice-Hall Inc., New Jersey.
- [80] MAN, C.-S. [1998]: *On the constitutive equations of some weakly-textured materials*. Archive for Rational Mechanics and Analysis, 143: 77–103.
- [81] MAN, C.-S. [2002]: *On the r -value of textured sheet metals*. International Journal of Plasticity, 18: 1683–1706.
- [82] MANDEL, J. [1972]: *Plasticité classique et viscoplasticité*. In *CISM Courses and Lectures, No. 97*. Springer.
- [83] MARSDEN, J. E.; HUGHES, T. J. R. [1983]: *Mathematical foundation of elasticity*. Dover Publications Inc., New Jersey.
- [84] MATHUR, K. K.; DAWSON, P. R. [1989]: *On modeling the development of crystallographic texture in bulk forming processes*. International Journal of Plasticity, 5: 67–94.
- [85] MIEHE, C. [1998]: *A constitutive frame of elastoplasticity at large strains based on the notion of a plastic metric*. International Journal of Solids and Structures, 35: 3859–3897.
- [86] MIEHE, C. [2002]: *Strain-driven homogenization of inelastic microstructures and composites based on an incremental variational formulation*. International Journal for Numerical Methods in Engineering, 55: 1285–1322.
- [87] MIEHE, C. [2003]: *Computational micro-to-macro transitions for discretized microstructures of heterogeneous materials at finite strains based on the minimization of averaged incremental energy*. Computer Methods in Applied Mechanics and Engineering, 192: 559–591.
- [88] MIEHE, C. [2007]: *Geometrical methods of nonlinear continuum mechanics*. Lecture Notes, University of Stuttgart.

- [89] MIEHE, C. [2008]: *Theoretical and computational mechanics of materials at large strains*. Lecture Notes, University of Stuttgart.
- [90] MIEHE, C.; APEL, N.; LAMBRECHT, M. [2002]: *Anisotropic additive plasticity in the logarithmic strain space: modular kinematic formulation and implementation based on incremental minimization principles for standard materials*. Computer methods in applied mechanics and engineering, 191: 5383–5425.
- [91] MIEHE, C.; FRANKENREITER, I.; ROSATO, D. [2011]: *Codf-evolutions on polycrystalline orientation continua obtained by fast geometric estimates of plastic slip*. International Journal for Numerical Methods in Engineering, 85: 1103–1139.
- [92] MIEHE, C.; LAMBRECHT, M. [2001]: *Algorithms for computation of stresses and elasticity moduli in terms of Seth-Hill's family of generalized strain tensors*. Communications in Numerical Methods in Engineering, 17: 337–353.
- [93] MIEHE, C.; ROSATO, D. [2007]: *Fast texture updates in fcc polycrystal plasticity based on a linear active-set-estimate of the lattice spin*. Journal of the Mechanics and Physics of Solids, 55: 2687–2716.
- [94] MIEHE, C.; ROSATO, D.; FRANKENREITER, I. [2010]: *Fast estimates of evolving orientation microstructures in textured bcc polycrystals at finite plastic strains*. Acta Materialia, 58: 4911–4922.
- [95] MIEHE, C.; SCHOTTE, J. [2004]: *Crystal plasticity and evolution of polycrystalline microstructure*. Encyclopedia of Computational Mechanics, 2: 267–289.
- [96] MIEHE, C.; SCHOTTE, J.; LAMBRECHT, M. [2002]: *Homogenization of inelastic solid materials at finite strains based on incremental minimization principles*. Journal of the Mechanics and Physics of Solids, 50: 2123–2167.
- [97] MIEHE, C.; SCHOTTE, J.; SCHRÖDER, J. [1999]: *Computational micro-macro transitions and overall moduli in the analysis of polycrystals at large strains*. Computational Materials Science, 16: 372–382.
- [98] MIEHE, C.; SCHRÖDER, J.; SCHOTTE, J. [1999]: *Computational homogenization analysis in finite plasticity. Simulation of texture development in polycrystalline materials*. Computer Methods in Applied Mechanics and Engineering, 171: 387–418.
- [99] MISES, R. VON [1928]: *Mechanik der plastischen Formänderung von Kristallen*. Zeitschrift für Angewandte Mathematik und Mechanik, 8: 161–185.
- [100] MOLINARI, A.; CANOVA, G. R.; AHZI, S. [1987]: *A self consistent approach of the large deformation polycrystal viscoplasticity*. Acta Metallurgica, 35, No.12: 2983–2994.
- [101] MONTHEILLET, F.; COHEN, M.; JONAS, J. J. [1984]: *Axial stresses and texture development during the torsion testing of Al, Cu and α -Fe*. Acta Metallurgica, 32: 2077–2089.
- [102] MORAWIEC, A. [2004]: *Orientations and rotations: Computations in crystallographic textures*. Springer.
- [103] MÜLLER, M. [1993]: *Plastische Anisotropie polykristalliner Materialien als Folge der Texturentwicklung*. Ph.D. Thesis, Universität Hannover, Fakultät für Maschinenwesen, Hannover.

- [104] NAGTEGAAL, J. C., PARKS D. M.; RICE, J. R. [1985]: *On numerically accurate finite element solutions in the fully plastic range*. Computer Methods in Applied Mechanics and Engineering, 4: 153–177.
- [105] NEMAT-NASSER, S. [2004]: *Plasticity - A treatise on the finite deformation of heterogeneous inelastic materials*. Cambridge University Press, Cambridge.
- [106] NEUMANN, P. [1991]: *Representation of orientations of symmetrical objects by Rodrigues vectors*. Textures and Microstructures, 14-18: 53–58.
- [107] NYE, J. F. [1953]: *Some geometrical relations in dislocated crystals*. Acta Metallurgica, 1: 153–162.
- [108] OROWAN, E. [1934]: *Zur Kristallplastizität*. Zeitschrift für Physik, 89: 605–659.
- [109] ORTIZ, M.; REPETTO, E. A. [1999]: *Nonconvex energy minimization and dislocation structures in ductile single crystals*. Journal of the Mechanics and Physics of Solids, 47: 397–462.
- [110] ORTIZ, M.; STAINIER, L. [1999]: *The variational formulation of viscoplastic constitutive updates*. Computer Methods in Applied Mechanics and Engineering, 171: 419–444.
- [111] PEIRCE, D.; ASARO, R.; NEEDLEMAN, A. [1982]: *An analysis of nonuniform and localized deformation in ductile single crystals*. Acta Metallurgica, 30: 1087–1119.
- [112] PEIRCE, D.; ASARO, R.; NEEDLEMAN, A. [1983]: *Material rate dependence and localized deformation in crystalline solids*. Acta Metallurgica, 31: 1951–1976.
- [113] POLANYI, M. [1934]: *Über eine Art Gitterstörung, die einen Kristall plastisch machen könnte*. Zeitschrift für Physik, 89: 660–664.
- [114] PRANTIL, V. C.; JENKINS, J. T.; DAWSON, P. R. [1993]: *An analysis of texture and plastic spin for planar polycrystals*. Journal of Mechanics and Physics of Solids, 41, No. 8: 1357–1382.
- [115] PRESS, W. H.; TEUKOLSKI, S. A.; VETTERLING, W. T.; FLANNERY, B. P. [1992]: *Numerical Recipes in Fortran 77*. Cambridge University Press, Cambridge.
- [116] RAABE, D. [1996]: *Taylor simulation and experimental investigation of rolling textures of polycrystalline iron aluminides with special regard to slip on {112} planes*. Acta Metallurgica, 44: 937–951.
- [117] RAABE, D.; KLOSE, P.; ENGL, B.; IMLAU, K.-P.; FRIEDEL, F.; ROTERS, F. [2002]: *Concepts for integrating plastic anisotropy into metal forming simulations*. Advanced Engineering Materials, 4: 169–180.
- [118] RAABE, D.; ROTERS, F. [2004]: *Using texture components in crystal plasticity finite element simulations*. International Journal of Plasticity, 20: 339–361.
- [119] RAABE, D.; ZHAO, Z.; ROTERS, F. [2001]: *A finite element method on the basis of texture components for fast predictions of anisotropic forming operations*. Steel Research, 72: 421–426.
- [120] RAAZ, F.; TERTSCH, H. [1958]: *Kristallographie*. Springer, Wien.
- [121] RANDLE, V.; ENGLER, O. [2000]: *Texture analysis. Macrotexture, microtexture and orientation mapping*. Overseas Publishers Association.

- [122] RASHID, M. M. [1992]: *Texture evolution and plastic response of two-dimensional polycrystals*. Journal of Mechanics and Physics of Solids, 40, No.5: 1009–1029.
- [123] RICE, J.R. [1971]: *Inelastic constitutive relations for solids: an internal-variable theory and its application to metal plasticity*. Journal of the Mechanics and Physics of Solids, 19: 433–455.
- [124] RISY, G. [2007]: *Modellierung der texturinduzierten plastischen Anisotropie auf verschiedenen Skalen*. Ph.D. Thesis, Otto-von-Guericke-Universität, Fakultät für Maschinenbau, Magdeburg.
- [125] ROBERTS, W. T. [1966]: *Texture control in sheet metal*. Sheet Metal Industries, pp. 237–245.
- [126] ROE, R.-J. [1965]: *Description of crystallite orientation in polycrystalline materials. III. General solution to pole figure inversion*. Journal of Applied Physics, 36, No. 6: 2024–2031.
- [127] SCHMID, E.; BOAS, W. [1935]: *Kristallplastizität*. SpringerVerlag, Berlin.
- [128] SCHWARTZ, A. J.; KUMAR, M.; FIELD, D. P.; ADAMS, B. L. [2009]: *Electron Backscatter Diffraction in Materials*. Springer.
- [129] SETH, B. R. [1964]: *Generalized strain measure with application to physical problems*. In REINER, M. AND ABIR, D. (Editor): *Second-Order Effects in Elasticity, Plasticity and Fluid Dynamics*, pp. 162–172. Pergamon Press, Oxford.
- [130] SIMO, J. C.; ARMERO, F. [1992]: *Geometrically non-linear enhanced strain mixed methods and the method of incompatible modes*. International Journal for Numerical Methods in Engineering, 33: 1413–1449.
- [131] SIMO, J. C., TAYLOR R. L.; PISTER, K. S. [1985]: *Variational and projection methods for the volume constraint in finite deformation elasto-plasticity*. Computer Methods in Applied Mechanics and Engineering, 51: 177–208.
- [132] SUQUET, P. M. [1986]: *Elements of homogenization for inelastic solid mechanics*. In SANCHEZ-PALENZIA, E.; ZAOU, A. (Editors): *Homogenization Techniques for Composite Materials*, pp. 193–278.
- [133] TAYLOR, G. I. [1934]: *The mechanism of plastic deformation of crystals. Part I – Theoretical*. Proceedings of the Royal Society London A, 145: 362–387.
- [134] TAYLOR, G. I. [1938]: *Plastic strain in metals*. Journal of the Institute of Metals, 62: 307–324.
- [135] TEODOSIU, C. [1970]: *A dynamic theory of dislocations and its applications to the theory of the elastic-plastic continuum*. In *Fundamental Aspects of Dislocation Theory*, pp. 837–876. U. S. National Bureau of Standards, Washington.
- [136] TIKHOVSKIY, I.; RAABE, D.; ROTERS, F. [2008]: *Simulation of earing of a 17% Cr stainless steel considering texture gradients*. Materials Science and Engineering, A 488: 382–490.
- [137] TROOST, A. [1980]: *Einführung in die allgemeine Werkstoffkunde metallischer Werkstoffe*. Bibliographisches Institut, Mannheim.
- [138] TRUESDELL, C. A.; NOLL, W. [1965]: *The non-linear field theories of mechanics*. In FLÜGGE, S. (Editor): *Handbuch der Physik, Vol. III (3)*. Springer Verlag, Berlin.

-
- [139] TUCKER, G. E. G [1961]: *Texture and earing in deep drawing of aluminium*. Acta Metallurgica, 9: 275–286.
- [140] VLADIMIROV, I. N.; SCHWARZE, M.; REESE, S. [2010]: *Earing prediction by a finite strain multiplicative formulation for anisotropic elastoplastic materials*. GAMM Mitteilungen, 33: 116–129.
- [141] WASSERMANN, G.; GREWEN, J. [1962]: *Texturen metallischer Werkstoffe*. Springer-Verlag, Berlin.
- [142] WILLIAMS, R. O. [1962]: *Shear textures in copper, brass, aluminium, iron and zirconium*. Transactions of the Metallurgical Society of AIME, 224: 129–1391.
- [143] WILSON, D.; BUTLER, R. [1962]: *The role of cup-drawing tests in measuring drawability*. Journal of the Institute of Metals/Metals and Metallurgy Trust of the Institute of Metals and the Institution of Metallurgists, 90: 473–483.
- [144] YOON, J. W.; YANG, D. Y.; CHUNG, K.; BARLAT, F. [1999]: *A general elastoplastic finite element formulation based on incremental deformation theory for planar anisotropy and its application to sheet metal forming*. International Journal of Plasticity, 15: 35–67.
- [145] ZHENG, Q.-S.; FU, Y.-B. [2001]: *Orientation distribution functions for microstructures of heterogeneous materials (II) - Crystal distribution functions and irreducible tensors restricted to various material symmetries*. Applied Mathematics and Mechanics, 22, No.8: 885–903.
- [146] ZHENG, Q.-S.; ZOU, W.-N. [2001]: *Orientation distribution functions for microstructures of heterogeneous materials (I) - Directional distribution functions and irreducible tensors*. Applied Mathematics and Mechanics, 22, No.8: 865–884.

Curriculum Vitae

Personal Data

Name: Ilona Zimmermann, nee Frankenreiter
Date of Birth: May 13, 1980
Place of Birth: Ellwangen/Jagst, Germany
Nationality: German
Parents: Josef Frankenreiter and Helene Frankenreiter, nee Rettenmaier
Siblings: Sonja Frankenreiter and Tobias Frankenreiter
Marital Status: Married to Dominik Zimmermann, one child

School Education

1986 – 1990 Elementary School: Deutschordenschule, Lauchheim
1990 – 1999 Secondary School: Ostalbgymnasium, Bopfingen
June 1999 University Entrance Certificate (Abitur)
1999 – 2001 Apprenticeship at Karl-Heinz Geiger GmbH & Co.KG, Aalen

University Education

2002 – 2007 Studies of Civil Engineering, Universität Stuttgart
October 2007 Graduation as Diplom-Ingenieur

Professional Occupation

2001 – 2002 Employee at Karl-Heinz Geiger GmbH & Co.KG, Aalen
2005 – 2006 Trainee at Freyssinet LLC in Toledo, Ohio, USA
Since 2007 Research Associate and Lecturer, Institute of Applied Mechanics
(Civil Engineering), Universität Stuttgart
On parental leave 08/2011 - 05/2012 and 08/2012 - 11/2012

In dieser Schriftenreihe bisher erschienene Berichte:

- I-1(1996) *Theoretische und algorithmische Konzepte zur phänomenologischen Beschreibung anisotropen Materialverhaltens*, J. Schröder, Dissertation, 1996.
- I-2(1996) *Zur Theorie und Numerik finiter elastoplastischer Deformationen von Schalentragwerken*, B. Seifert, Dissertation, 1996.
- I-3(1996) *Zur Modellierung des künstlichen Infrarot-Dichroismus in Polymerfolien bei großen Verformungen*, J. Buhler, Dissertation, 1996.
- I-4(1998) *Verfahren zur Ermittlung der Erdbebenlasten mit Berücksichtigung des stochastischen Charakters des Bebens*, S. Zhang, Dissertation, 1998.
- I-5(1998) *Zur Beschreibung finiter Deformationen von Polymeren: Experimente, Modellbildung, Parameteridentifikation und Finite-Elemente-Formulierung*, J. Keck, Dissertation, 1998.
- I-6(1999) *Berechnungsverfahren instationär erregter Systeme im Frequenzbereich*, A. Jaworek, Dissertation, 1999.
- I-7(2000) *Homogenisierungsmethoden der nichtlinearen Kontinuumsmechanik unter Beachtung von Stabilitätsproblemen*, J. Schröder, Habilitation, 2000.
- I-8(2002) *Theorie und Numerik von Materialinstabilitäten elastoplastischer Festkörper auf der Grundlage inkrementeller Variationsformulierungen*, M. Lambrecht, Dissertation, 2002.
- I-9(2002) *Mikromechanisch motivierte Modelle zur Beschreibung finiter Deformationen gummiartiger Polymere: physikalische Modellbildung und numerische Simulation*, F. Lulei, Dissertation, 2002.
- I-10(2003) *Adaptive Finite-Elemente-Berechnungen der nichtlinearen Festkörpermechanik bei kleinen und großen Verzerrungen*, A. Koch, Dissertation, 2003.
- I-11(2003) *Theorie und Numerik der Parameteridentifikation von Materialmodellen der finiten Elastizität und Inelastizität auf der Grundlage optischer Feldmeßmethoden*, G. Scheday, Dissertation, 2003.
- I-12(2004) *Approaches to the Description of Anisotropic Material Behaviour at Finite Elastic and Plastic Deformations, Theory and Numerics*, N. Apel, Dissertation, 2004.
- I-13(2004) *Temperaturabhängige Beschreibung visko-elasto-plastischer Deformationen kurzglasfaserverstärkter Thermoplaste: Modellbildung, Numerik und Experimente*, S. Rieger, Dissertation, 2004.
- I-14(2005) *Zur Parameteridentifikation komplexer Materialmodelle auf der Basis realer und virtueller Testdaten*, A. Rieger, Dissertation, 2005.
- I-15(2005) *Viskoelastisches Verhalten von Elastomeren bei finiten Verzerrungen: Experimente, Modellierung und Simulationen*, H. Zecha, Dissertation, 2005.

- I-16(2005) *Mehrskalenmodelle in der Festkörpermechanik und Kopplung von Mehrgittermethoden mit Homogenisierungsverfahren*, C.G. Bayreuther, Dissertation, 2005.
- I-17(2005) *Static and Dynamic Homogenization Analyses of Discrete Granular and Atomistic Structures on Different Time and Length Scales*, J. Dettmar, Dissertation, 2005.
- I-18(2006) *Incompatibility and Instability Based Size Effects in Crystals and Composites at Finite Elastoplastic Strains*, M. Becker, Dissertation, 2006.
- I-19(2007) *Aspects of Energy Minimization in Solid Mechanics: Evolution of Inelastic Microstructures and Crack Propagation*, E. Gürses, Dissertation, 2007.
- I-20(2007) *Micro-Macro Approaches to Rubbery and Glassy Polymers: Predictive Micromechanically-Based Models and Simulations*, S. Göktepe, Dissertation, 2007.
- I-21(2008) *Material Forces in Finite Inelasticity and Structural Dynamics: Topology Optimization, Mesh Refinement and Fracture*, D. Zimmermann, Dissertation, 2008.
- I-22(2010) *Thermoviscoplasticity of Glassy Polymers: Experimental Characterization, Parameter Identification and Model Validation*, J. Méndez Diez, Dissertation, 2010.
- I-23(2010) *On the Formulation and Numerical Implementation of Dissipative Electro-Mechanics at Large Strains*, D. Rosato, Dissertation, 2010.
- I-24(2011) *A Variational Framework for Gradient-Extended Dissipative Continua: Application to Damage Mechanics, Fracture, and Plasticity*, F. Welschinger, Dissertation, 2011.
- I-25(2013) *Variational Multifield Modeling of the Formation and Evolution of Laminate Microstructure*, F. Hildebrand, Dissertation, 2013.
- I-26(2013) *On the Computational Modeling of Micromechanical Phenomena in Solid Materials*, C. Linder, Habilitation, 2013.
- I-27(2013) *Hybrid Micro-Macro Modeling of Texture Evolution in Polycrystal Plasticity Based on Microstructural Reorientation Continua*, Ilona Zimmermann, Dissertation, 2013.